# Investigations on the Oxidation Behaviour of Silica and Borosilica Forming Materials

A Thesis Submitted

In Partial Fulfillment of the Requirements

for the Degree of

#### **DOCTOR OF PHILOSOPHY**

by

Jhalak

(2020MMZ0010)



## DEPARTMENT OF METALLURGICAL AND MATERIALS ENGINEERING

#### INDIAN INSTITUTE OF TECHNOLOGY ROPAR

June 2025

Jhalak: Investigations on the Oxidation Behaviour of Silica and Borosilica Forming Materials	
Copyright © 2025, Indian Institute of Technology Ropar	
All Rights Reserved	

#### **Declaration of Originality**

I hereby declare that the work which is being presented in the thesis entitled 'Investigations on the Oxidation Behaviour of Silica and Borosilica Forming Materials' has been authored by me. It presents the results of my own independent investigation/research conducted during the time period from January 2021 to *January* 2025 under the supervision of *Dr. Pratik K. Ray (Assistant Professor, Dept.* of Metallurgical and Materials Engineering, IIT Ropar). To the best of my knowledge, it is an original work, both in terms of research content and narrative, and has not been submitted or accepted elsewhere, in part or in full, for the award of any degree, diploma, fellowship, associateship, or similar title of any university or institution. Further, due credit has been attributed to the relevant state-of-the-art and collaborations with appropriate citations and acknowledgments, in line with established ethical norms and practices. I also declare that any idea/data/fact/source stated in my thesis has not been fabricated/falsified/misrepresented. All the principles of academic honesty and integrity have been followed. I fully understand that if the thesis is found to be unoriginal, fabricated, or plagiarized, the Institute reserves the right to withdraw the thesis from its archive and revoke the associated Degree conferred. Additionally, the Institute also reserves the right to appraise all concerned sections of society of the matter for their information and necessary action. If accepted, I hereby consent for my thesis to be available online in the Institute's Open Access repository, inter-library loan, and the title & abstract to be made available to outside organizations.

Name: Jhalak

Entry Number: 2020MMZ0010

Program: PhD

Department: Metallurgical and Materials Engineering

Indian Institute of Technology Ropar

Rupnagar, Punjab 140001

Date: 25th June 2025

#### Certificate

This is to certify that the thesis entitled 'Investigations on the Oxidation Behaviour of Silica and Borosilica Forming Materials', submitted by Jhalak (Entry No.: 2020MMZ0010) for the award of the degree of 'Doctor of Philosophy' of Indian Institute of Technology Ropar, is a record of bonafide research work carried out under my guidance and supervision. To the best of my knowledge and belief, the work presented in this thesis is original and has not been submitted, either in part or full, for the award of any other degree, diploma, fellowship, associateship or similar title of any university or institution. In my opinion, the thesis has reached the standard fulfilling the requirements of the regulations relating to the Degree.

91 9

Dr. Pratik K. Ray

Department of Metallurgical and Materials Engineering

Indian Institute of Technology Ropar

Rupnagar, Punjab 140001

Date: 25th June 2025



## Acknowledgement

I am deeply indebted to many people who helped me throughout my PhD journey. First and foremost, I would express my sincere gratitude to my supervisor Dr. Pratik K Ray for his unwavering support, encouragement, invaluable advice and patience during my PhD study. His immense knowledge, experience and meticulous attention to detail have significantly helped me in shaping my thesis. His valuable insights and perspective of looking at any problem are inspiring and his contributions towards my professional growth were significant. He has been an exceptional mentor and words cannot adequately express my gratitude.

I am very thankful to the members of my doctoral committee, Dr. Ravi Mohan Prasad, Dr. Prince Singh, Dr. Abhishek Tiwari and Prof. Harpreet Singh for their constructive feedback and suggestions throughout my PhD. I am deeply thankful to Dr. Srikant Sekhar Padhee who introduced me to the course on atomistic simulations and provided recommendations which contributed immensely to my professional growth. I am extremely grateful to our collaborator Dr. Ganesh Balasubramanian and his group at Lehigh University, USA for providing access to computational resources for carrying out computational work. I am also grateful to Dr. S. Mula and his group at IIT Roorkee for their help in the fabrication of UHTC samples. I am thankful to Dr. Imteyaz Ahmed who allowed me to visit his lab at IIT BHU. The discussions with him and his group were enlightening and it was a great learning experience.

I am thankful to the Department Metallurgical and Materials Engineering at IIT Ropar and IIT Ropar itself for allowing me to pursue my doctoral research there. I am thankful to IIT Ropar for providing the central research facilities including SEM, EDS and XRD facilities that I have used extensively for my

research. I am thankful to the Prime Minister's Research Fellowship Scheme by Govt. of India which financially supported my PhD research.

I am extremely thankful to the IDEAs Lab members at IIT Ropar -Dishant, Rudraksha, Sagarika, Santosh, Maitreya all of whom have been wonderful friends and a constant support throughout my PhD journey. I am also thankful to all the fellow PhD research scholars at the Department of Metallurgical and Materials Engineering, IIT Ropar who made for a wonderful work environment.

I am extremely grateful to my husband Dishant, without whose support my work would have taken even longer to complete. He is my best friend and an amazing person. I am thankful to him for always being there in every phase of my life. I would like to express my gratitude to my grandmother and parents who always encouraged me to pursue my dreams. Their unconditional love and sacrifices since my childhood have been the foundation of whatever I am today. I am thankful to my sisters for sharing responsibilities and taking care of my father that allowed me to focus on my work.

## Lay Summary

High temperature materials can maintain their properties such as creep and oxidation resistance at elevated temperatures. For many high temperature applications stainless steels and superalloys are commonly used as they form protective Cr<sub>2</sub>O<sub>3</sub> scales on their surface during their oxidation. These scales start to volatilize ~900 °C. Some high temperature materials including Alumina-Forming Austenitic (AFA) steels form protective Al<sub>2</sub>O<sub>3</sub> layer. At temperatures greater than 1100 °C, Al<sub>2</sub>O<sub>3</sub> grows fast and thick generating high Pilling-Bedworth stresses resulting in cracking and spallation of scale. Therefore, these materials are limited for applications up to 1100 °C. For higher temperatures, silica forming materials are favorable candidates. Silica forms a glassy scale which has liquid-like nature and can flow into the cracks that are generated during thermal cycling. It acts as self-healing scale under high temperature conditions. For excellent oxidation resistance, an oxide scale must have an optimum viscosity to flow, spread and cover the surface effectively. Additionally, the oxide scale must resist the oxygen diffusion through it. The flow and spread of scale depend on viscosity which is a function of temperature and scale composition. In this work, the alloys and ceramics that form silica or borosilica scales during oxidation at extreme temperature conditions were studied using computational and experimental approaches. Computational simulations were used to study diffusion through various glass compositions and to simulate how oxide scale will grow on certain alloy compositions. This

helps in designing compositions for experimental studies. The selected compositions were fabricated for studying oxidation behaviour of the alloys and ceramics. After fabrication oxidation studies were conducted to measure how much the samples have deteriorated in terms of the oxide scale thickness and the change in mass with time.

#### **Abstract**

Mo-Si-B alloys and Ultra-high temperature ceramics are potential materials for high temperatures beyond Ni based superalloys. In Mo-Si-B based systems and with SiC addition to ZrB<sub>2</sub>, protective SiO<sub>2</sub>-rich glassy scale is formed at the surface. Diffusion through the scale and scale viscosity play an important role in understanding the oxidation behaviour of the system. In the present work, diffusion coefficient and activation energies of the diffusing species have been calculated using Molecular Dynamics (MD) as these govern the scale growth and surface coverage. Diffusion was modelled in SiO<sub>2</sub> glass in the temperature range of 1200-1700 °C with elemental additions. To predict oxidation kinetics and to simulate oxide growth in Mo-Si-B alloys, a mathematical model based on Cellular Automata (CA) was developed. This model simulates the transient oxidation phenomenon both visually (microstructure evolution at each time step) as well as numerically (mass change at each time step). The microscopic nature of the model allows us to explore the roles of material chemistry and the microstructure on the oxidation behaviour quantitatively. Using the model as a guide, oxide evolution of Mo-Si-B alloys with addition of W, Ta and Al was studied at 1100 and 1350 °C experimentally and the results were comparable with those predicted by the developed model. For example, the model predicted higher mass loss on adding tungsten and lower mass loss on adding Ta to the alloy 711 at 1100 °C. The oxidation behaviour of ZrB<sub>2</sub>-SiC based ceramics was studied at 1600 with AlN, TaC and CeO2 additions. Poor oxidation resistance was observed in 70ZrB<sub>2</sub>-20SiC-10AlN composite which was attributed to the lower oxide scale viscosity resulting in faster diffusion through the scale and increased oxidation. This agreed with the diffusion modelling results obtained using MD where increased self-diffusion of species was observed with Al addition to SiO<sub>2</sub> glass. This work involves the use of a combination of computational and experimental approaches for better design of ultra-high temperature materials that form silica and borosilica scales.

#### List of Publications out of Thesis

#### Journal publications

- 1. **Jhalak**, Ganesh Balasubramanian, Pratik K Ray, Effect of Hf and Al addition on self-diffusion on amorphous silica using Molecular Dynamics, **JOM**, 76 (2), 941 (2024).
- 2. **Jhalak**, Dishant Beniwal, Pratik K Ray *Molecular Dynamics simulations of diffusivity in an atomic scale diffusion multiple"*, International Conference on Fundamental and Industrial Research in Materials (iConFIRM 2023), **Springer Proceedings in Physics**, vol 308. Springer, Singapore (2024).
- 3. **Jhalak**, Pratik K Ray, Effect of metal content and Si/B ratio on oxidation behaviour of refractory metal silicides, **Under preparation**
- 4. **Jhalak**, Arpan Arora, S. Mula, PK Ray, Oxidation behaviour of ZrB<sub>2</sub>-SiC based UHTCs with AlN, CeO<sub>2</sub> and TaC additions, **Under preparation**
- 5. **Jhalak**, Dishant Beniwal, Pratik K Ray, Modelling transient oxidation in Mo-Si-B alloys for predicting oxidation kinetics, **Under preparation**
- 6. **Jhalak**, Pratik K Ray, Exploring Tantalum silicates as oxidation barriers, **Under preparation**

#### **Conference presentations**

- 1. **Jhalak**, Pratik K. Ray, "Microstructural evolution and transient oxidation behaviour of Mo-Si-B alloys", EMSI 2024, IIT Bombay, Mumbai, India, 16-18th May 2024.
- 2. **Jhalak**, Pratik K. Ray, "*Microstructure and oxidation studies on Mo-Si-B alloys*", IIM ATM 2023, KIIT Bhubaneswar, Orissa, India, 22-24<sup>th</sup> November 2023.
- 3. **Jhalak**, Ganesh Balasubramanian, Pratik K. Ray, "Oxygen and silicon self-diffusion in pure and Al containing SiO<sub>2</sub> glasses", ASATM 2023, NTU, Singapore, 10-13<sup>th</sup> January 2023.
- 4. **Jhalak**, Ganesh Balasubramanian, Pratik K. Ray, "Self-diffusion studies in SiO<sub>2</sub> glasses formed on UHTCs using Molecular Dynamics", IIM ATM 2022, Hyderabad, India, 13-16<sup>th</sup> November 2022.
- 5. **Jhalak**, Indranil Roy, Pratik K. Ray, Ganesh Balasubramanian, "Self-diffusion in SiO<sub>2</sub> and ZrO<sub>2</sub> using Molecular Dynamics", (PM 22), International conference on Powder Metallurgy, Virtual mode, 18-20<sup>th</sup> April 2022.



## **Table of contents**

Acknowledgement	vii
Lay Summary	ix
Abstract	xi
List of Publications out of Thesis	xiii
Table of contents	xv
List of Tables	xix
List of Figures	xxi
List of Abbreviations	. xxix
List of Symbols	. xxxi
Chapter 1 Introduction	1
1.1 Application of high temperature materials	1
1.2 Key material challenges	2
1.3 Materials beyond Ni-based alloys	2
1.4 Scope of thesis	5
1.5 Thesis organization	5
Chapter 2 Literature Review	7
2.1 Refractory metal silicides	7
2.1.1 The Mo-Si-B alloy system: phase stability and general propertie	s7
2.1.2 Oxidation mechanism of Mo-Si-B alloys	12
2.1.3 The effect of alloying additions on oxidation	16
2.1.4 Oxidation behavior of other refractory metal silicides	19
2.2 Ultra-High Temperature Ceramics	21

2.2.1 Synthesis and physical properties of Ultra-high	Temperature
Ceramics	21
2.2.2 Oxidation mechanism of ZrB <sub>2</sub> -SiC ceramics	23
2.2.3 Effect of additives on oxidation resistance	28
2.3 Computational modeling of oxidation	29
2.3.1 Modeling diffusion in the oxide scale	29
2.3.2 Thermodynamics and volatility diagrams	34
2.3.3 Analytical models for Mo-Si-B and diboride systems	38
2.4 Problem definition and approach	41
2.4.1 Key research gaps and problem formulation	41
2.4.2 Conceptual approach and structure of thesis	42
Chapter 3 Dynamics of silica scale	45
3.1 Introduction	45
3.2 Computational methods	48
3.2.1 Generating amorphous silica structure	48
3.2.2 Interatomic potentials	49
3.2.3 Self-diffusion studies in SiO <sub>2</sub> glasses	51
3.3 Results and discussion	52
3.3.1 Structural analysis of SiO <sub>2</sub> glasses	52
3.3.2 Self-diffusion in amorphous SiO <sub>2</sub>	54
3.3.3 Self-diffusion in amorphous SiO <sub>2</sub> containing Hf	56
3.3.4 Self-diffusion in amorphous SiO2 containing Al	59
3.3.5 Shear viscosity calculations in SiO <sub>2</sub>	61
3.4 Conclusions	62
Chapter 4 Oxidation Modelling	65
4.1 Introduction	65

4.2 Experimental details67
4.3 Simulation details68
4.3.1 Preparing the initial microstructure68
4.3.2 Representing the state of the system70
4.4 Reactions and phase consumptions70
4.4.1 Oxidation events and their occurrence70
4.4.2 Modelling phase consumption using experimental data73
4.4.3 Phase consumption due to oxygen flux through the scale75
4.5 Temporal evolution of microstructure
4.5.1 Calculating the state of system after each time-step78
4.5.2 Volatilization of MoO <sub>3</sub> 81
4.5.3 Modeling the lateral flow of glass
4.6 Results & Discussion85
4.6.1 Simulating microstructure evolution during oxidation85
4.6.2 Effect of alloy chemistry on oxidation87
4.6.3 Oxidation kinetics
4.6.4 The effect of microstructure length scale on oxidation kinetics90
4.7 Summary92
Chapter 5 Oxidation behavior of refractory metal silicides with boron additives
93
5.1 Introduction93
5.2 Materials and Methods96
5.2.1 Experimental methods96
5.3 Microstructures of Mo-Si-B alloys98
5.4 Transient oxidation behaviour104
5.4.1 Temporal evolution of the oxide scale

5.4.2 Understanding oxidation pathways1	115
5.5 Long-term oxidation behaviour1	117
5.5.1 Effect of temperature1	117
5.5.2 Effect of refractory metals: W and Ta1	120
5.5.3 Effect of Si:B ratio1	126
5.5.4 Effect of Al additions	127
5.6 Summary	129
Chapter 6 Oxidation behaviour of Ultra-High Temperature Ceramics1	131
6.1 Introduction1	131
6.2 Experimental Methods	134
6.3 Thermodynamic stability and volatility diagrams1	135
6.4 Oxidation behaviour of Ultra-High Temperature Ceramics1	138
6.4.1 Oxide scale microstructures	138
6.4.2 Oxide scale cross sectional microstructures1	143
6.4.3 Oxidation kinetics	150
6.4.4 Phenomenological model and oxidation pathways1	153
6.5 Summary1	155
Chapter 7 Conclusion	157
7.1 General conclusions from the thesis	157
7.2 Scope for future work1	158
References	161

## **List of Tables**

Table 2.1 Crystal structures of some important phases of metal-silicon systems
[42]
Table 2.2. Mathematical forms of different interatomic potentials [126]31
Table 3.1 Buckingham potential (BP) parameters used [187]50
Table 3.2. Activation energy $(E_a)$ and diffusion pre-factor $(D_o)$ values for self-diffusion of Si and O in $SiO_2$
Table 3.3. Activation energies $(E_a)$ and diffusion pre-factor $(D_o)$ for self-diffusion of Si, O and Hf as a function of Hf concentration
Table 3.4. Activation energies $(E_a)$ and diffusion pre-factor $(D_o)$ for self-diffusion of Si, O and Al as a function of Al concentration61
Table 4.1. Compositions of the alloys fabricated for oxidation studies68
Table 5.1 Composition of fabricated alloys for oxidation studies97
Table 5.2. Weight percent of phases present in Mo-Si-B based alloys and the lattice parameters
Table 5.3. Lattice parameter of each phase in various alloy compositions102
Table 6.1. Composition of UHTCs in vol% for oxidation studies135
Table 6.2. Mass gain and average oxide layer thickness after 10 h of exposure at $1600~^{\circ}\text{C}$ .

## **List of Figures**

Figure 1.1 Comparison of stress-rupture temperature for various materials [15,16]
Figure 2.1 Phases in Mo-Si-B alloys at 1600 °C
Figure 2.2. Liquidus projections in Mo-Si-B alloy system [9]9
Figure 2.3 Schematic showing the transient oxidation mechanism in Mo-Si-B alloys at 1500 $^{\circ}$ C [13,28].
Figure 2.4. (a) The structure of molten silica and (b) shows the effect of Ca addition on silica network
Figure 2.5 Oxide scale composition for oxidation of ZrB <sub>2</sub> at different temperatures.
Figure 2.6 Convection cells formation on ZrB <sub>2</sub> -SiC UHTC [104]26
Figure 2.7. Length and time scales of various simulations approaches [121]30
Figure 2.8 Volatility diagram of ZrB <sub>2</sub> at (a) 1000, 1800 and 2500 K [98] (b) 1773K (1500 °C) [97]
Figure 2.9 Volatility diagram of (a) SiC and (b) ZrB <sub>2</sub> -SiC system at 1500 °C36
Figure 3.1 Methodology49
Figure 3.2 Structure of SiO <sub>2</sub> glass generated using Tersoff potential. (a) MD simulation cell showing initial configuration of SiO <sub>2</sub> glass structure at 300K. (b) XRD of the SiO <sub>2</sub> glass structure at 300K.
Figure 3.3 Radial distribution function of $SiO_2$ glass structures prepared using different potentials. Partial radial distribution function $g(r)$ corresponding to (a) Si-Si, (b) Si-O, and (c) O-O pairs. (d) Overall radial distribution function for
SiO <sub>2</sub> glass. The <i>ab initio</i> and experimental radial distribution function have been obtained from literature

Figure 3.4 Self-diffusion in SiO <sub>2</sub> glass. Self-diffusion coefficients of oxygen (O <sub>2</sub>
and silicon (Si) in $SiO_2$ glass as a function of temperature obtained using COMB
Tersoff and BP potentials. Linear fit (represented by dotted lines) has been
performed to extract the activation energy ( $E_a$ ) and diffusion pre-factor ( $D_o$ )
values54
Figure 3.5. Self-diffusion in SiO <sub>2</sub> glass containing hafnium. Self-diffusion
coefficients of (a) silicon (Si), (b) oxygen (O) and (c) hafnium (Hf), as a function
of temperature, in $SiO_2$ glass containing 1, 2, and 5 at. % Hf. Linear fit
(represented by dotted lines) for different glasses to extract the activation
energy (E <sub>a</sub> ) and D <sub>o</sub> values
Figure 3.6. Ellingham diagram for SiO <sub>2</sub> , HfO <sub>2</sub> and Al <sub>2</sub> O <sub>3</sub> [195]59
Figure 3.7. Self-diffusion in SiO <sub>2</sub> glass containing Aluminium. Self-diffusion coefficients of (a) silicon (Si), (b) oxygen (O) and (c) Aluminium (Al), as a function of temperature, in SiO <sub>2</sub> glass containing 1, 2, 3 and 5 at. % Al. Linear fit (represented by dotted lines) for different glasses to extract the activation energy (Ea) and D <sub>0</sub> values
basic oxides such as Na <sub>2</sub> O, CaO, MgO62
Figure 4.1 (a) Phase segmentation of actual alloy microstructure using ImageJ- Fiji (Labkit plugin [203]) followed by measurement of pixel size based on the number of pixels spanned by the scale bar. (b) 3-D array for storing volume fractions of all the phases at each (i,j) cell corresponding to 2-D microstructure
Figure 4.2. Determining access to oxygen through neighboring cells. The black
regions here represent solid oxidizing phases (T2, A15, Mo, T1) whereas the
light blue regions represent air/glass. The solid oxidizing phases are assumed
to be impervious to oxygen and thus, this figure highlights three key aspects

(a) Oxygen flux from above cell will be available only if the above cell has no

solid oxidizing phase present, (b) oxygen flux from side cell will be available if
the side cell has some air/glass present, and (c) oxygen flux from side cell will
be proportional to the amount of air/glass in side cells
Figure 4.3. Calculating the oxygen flux through glass layer above a cell77
Figure 4.4. Calculating phase consumption based on effective oxygen flux at cell $(i, j)$ taking into account oxygen from both the top as well as left & right
cells
Figure 4.5. Modelling lateral flow of glass85
Figure 4.6. Oxidation simulation for alloy 711 (70% Mo-15% Si-15%B). The first row shows the microstructure evolution as oxidation time increases (t=0 s, 10
s, 50 s, 300 s). Here, the phase label at each pixel was decided based on which
phase has the highest volume fraction at the pixel. Rows 2-7 show the volume
fraction phase maps of each individual phase as a function of time. The color
bar on right (spanning from 0 to 1) is mapped to the volume fractions86
Figure 4.7. Oxidation simulation for seven Mo-Si-B based alloys wherein small
slices were extracted from the actual microstructures to model the evolution.
(a) 711: 70%Mo-15%Si-15%B, (b) 721: 70%Mo-20%Si-10%B, (c) 811: 80%Mo-
10%Si-10%B, (d) 821: 80%Mo-13.33%Si-6.66%B, (e) 711-15W: 55%Mo-15%W-
15%Si-15%B, (f) 711-5Ta: 65%Mo-5%Ta-15%Si-15%B, (g) 721-5Ta: 65%Mo-
5%Ta-20%Si-10%B88
Figure 4.8. Oxidation kinetics for Mo-Si-B based alloys based on (a) oxidation
simulations and (b) experimental measurements
Figure 4.9. Oxidation kinetics calculated for three different microstructural size
scales of same alloy composition [Mo-14.2 at.% Si-9.6 at.% B]. The SEM
micrographs and experimental mass change results were obtained from Rioult
et al. [13]90
Figure 4.10. Visualization of microstructure evolution during oxidation of Size 1 and Size 3 samples shown in Fig 9
Figure 5.1 Selected compositions marked on phase diagram of Mo-Si-B alloys
at 1600 °C

Figure 5.2 X-ray diffraction showing phases present in each alloy. Mo <sub>3</sub> Si (A15)
phase eliminated after the addition of 20 at% W in alloy 811 and 821 with 15
at% W in alloy 711 and with 10 at% W in alloy 721100
Figure 5.3 SEM (SE mode) images of as-cast (a) 811 (b) 811-W20 (c) 821 and (d)
821-W20 alloys
Figure 5.4 SEM (SE mode) images of as-cast (a) 711 (b) 711-W15 (c) 721 and (d)
721-W10 alloys
Figure 5.5 Microstructure (BSE mode) of as-cast (a) 711-5Ta alloy, (b) 721-5Ta
alloy and (c) XRD results (d) liquidus projection of Mo-Si-B phase diagram [9]
Figure 5.6 Temporal oxide evolution in 811 and 821 Mo-Si-B alloys (SEI mode)
at 1100 °C and 1350 °C. Here, 8, 11 and 21 represent 80 at% Mo, Si/B ratio as 1/1
and 2/1 respectively
Figure 5.7 Temporal oxide evolution in 711 and 721 Mo-Si-B alloys (SEI mode)
at 1100 °C and 1350 °C. Here, 7, 11 and 21 represent 70 at % Mo, Si/B ratio as $1/1$
and 2/1 respectively109
Figure 5.8 Temporal evolution of oxide in alloys (SEI mode) containing 20 at%
W. Here, 8, 11 and 21 represent 80 at% Mo+W, Si/B ratio as 1/1 and 2/1
respectively111
Figure 5.9 Temporal evolution of oxide in alloys (SEI mode) containing 20 at%
W. Here, 7, 11 and 21 represent 70 at% Mo+W, Si/B ratio as 1/1 and 2/1
respectively112
Figure 5.10 Oxide evolution in Mo-Ta-Si-B alloys (SEI mode) at 1100 °C and 1350
°C. Here, 7, 11 and 21 represent 70 at% Mo, Si/B ratio as 1/1 and 2/1
respectively
Figure 5.11 Temporal oxide evolution of Mo-Al-Si-B alloys at 1100 and 1350 °C
5 at% Al was added to the alloys keeping the Mo/Si/B ratio as 8/1/1 and
8/2/1114

of Mo-Si-B alloys
Figure 5.13 Effect of Ta addition on oxidation mechanism in Mo-Si-B alloys
Figure 5.14 Mass change per unit area for (a) 811, 821 alloys and (b) 711, 721 alloys at 1100 and 1350 $^{\circ}$ C
Figure 5.15 Oxide scale thickness in 811 and 821 alloys at 1100 and 1350 °C.119
Figure 5.16 Oxide scale thickness in 711 and 721 alloys at 1100 °C and 1350 °C
Figure 5.17 Mass change plots with W addition to 811, 821, 711 and 721 alloys at 1100 and 1350 °C. 20 at% Mo was substituted with W in 811 and 821 alloys; 15 at% Mo was substituted with W in 711 and with 10 at% W in the alloy 721.
Figure 5.18 Mass change per unit area as function of time during oxidation of (a) alloys 711 and 721 without and with Ta addition at 1100 °C (b) alloys 711 and 721 without and with Ta addition at 1350 °C (c) alloys 711-5Ta and 721-5Ta showing comparison at 1100 °C and 1350 °C.
Figure 5.19 Mo-Si-B alloys with 5 at% Ta in non-oxidized condition and oxidized at 1100 °C and 1350 °C
Figure 5.20 Cross-sectional view of samples oxidized at 1100 °C and 1350 °C.
Figure 5.21 Effect of Si/B ratio on glassy scale flow
Figure 5.22 Mass change in (a) Mo-Si-B base alloys (b) alloys with Al at 1100 °C and 1350 °C.
Figure 5.23. Viscosity variation of SiO <sub>2</sub> glass with Al <sub>2</sub> O <sub>3</sub> content128
Figure 6.1 Volatility diagram of ZrB <sub>2</sub> -SiC-AlN system at 1600 °C136
Figure 6.2. Volatility diagram of ZrB <sub>2</sub> -SiC-AlN-TaC system at 1600 °C137
Figure 6.3. Volatility diagram of ZrB <sub>2</sub> -SiC-AlN-CeO <sub>2</sub> system at 1600 °C137

Figure 6.4 Microstructures and EDS maps of as-fabricated ZSA721, ZSAC72-5-5 and ZSAT72-5-5 UHTCs using back scattered imaging. All images are at same magnification.
Figure 6.5 Surface microstructures of UHTCs using BSE imaging prior to oxidation and post oxidation for 5 min, 15 min and 10 h. (a)-(d) ZSA 721, (e)-(h) ZSAT72-5-5, (i)-(l) ZST631
Figure 6.6. Surface microstructures of UHTCs using BSE imaging prior to oxidation and post oxidation for 5 min, 15 min and 10 h. (a)-(d) ZSAC72-5-5, (e)-(h) ZSC721, (i)-(l) ZSC631
Figure 6.7. a) Cross section of sample ZSA721 after oxidation for 10h, b), c) magnified view of the cross section, d) electron image of upper region of the cross section for elemental mapping, e) layered image, f)-O) elemental mapping.
Figure 6.8. a) Cross section of ZSAT72-5-5 sample after oxidation at 1600 °C for 10 h, b), c) magnified view the cross section obtained by stitching the images together from top to bottom, d)-i) EDS elemental mapping of the upper region.  145
Figure 6.9. a) Cross section of ZST631 sample after oxidation at 1600 for 10 h, b),c) magnified view the cross section obtained by stitching the images together from top to bottom, c)-h) EDS elemental mapping of the upper region146
Figure 6.10 a) Cross section of ZSAC72-5-5 sample after oxidation at 1600 °C for 10 h, b) magnified view the cross section obtained by stitching the images together from top to bottom, c)-h) EDS elemental mapping of the upper region.
Figure 6.11 a) Cross section of ZSC721 sample after oxidation at 1600 for 10 h, b) magnified view the cross section obtained by stitching the images together from top to bottom, c)-g) EDS elemental mapping of the upper region148
Figure 6.12. a) Cross section of ZSC631 sample after oxidation at 1600 for 10h, b) magnified view the cross section obtained by stitching the images together from top to bottom, c)-g) EDS elemental mapping of the upper region149

Figure 6.13. XRD analysis of samples ZSA721, ZSAT72-5-5 and ZST631 after
oxidation for 10 h at 1600 °C151
Figure 6.14 (a) Mass change per unit area during oxidation at 1600 °C after 10 h $$
of oxidation151
Figure 6.15. XRD analysis of samples containing $CeO_2$ after oxidation for 10 h
at 1600 °C. (a) shows the results with background and (b) shows the results after
background removal from ZSC721 and ZSC631 for better visibility of peaks.
Figure 6.16. Masks showing regions where the composition matches the ZrSiO <sub>4</sub>
stoichiometry. Maske were generated through quantitative analysis of EDS
maps using EDS-PhaSe software [241]155
Figure 6.17. Schematic showing effect of elemental addition on oxidation156



#### List of Abbreviations

**AC- Alternating Current** 

BM-Born-Mayer

CMCs- Carbon Matrix Composites

CA- Cellular Automata

COMB- Charge Optimized Many Body

DC- Direct Current

DFT- Density Functional Theory

EAM - Embedded-Atom Model

EDS- Energy Dispersive Spectroscopy

FS- Flash Sintering

LAMMPS- Large-scale Atomistic Molecular Massively Parallelized Simulator

LJ- Lennard-Jones

MD- Molecular Dynamics

MEAM- Modified Embedded-Atom Method

NBO- Non-Bridging Oxygen

RDF- Radial Distribution Function

**REBO-** Reactive Empirical Bond Order Potential

PBR- Pilling Bedworth Ratio

SEM-Scanning Electron Microscopy

SPS- Spark Plasma Sintering

SW-Stillinger-Weber

**UHTCs- Ultra-High Temperature Ceramics** 

XRD- X-Ray Diffraction



## **List of Symbols**

A-Area

$\rm \mathring{A}-Angstrom$
at % - Atomic percent
°C - Degree Celsius
D – Diffusion coefficient
$\Delta$ - Change
J - Flux
L <sub>px</sub> - Length of a pixel
mol % - Mole percent
μ - micro
η - Viscosity
p – partial pressure
$\Pi$ - Permeability
T – Temperature
t – Time
ρ - Density
T <sub>px</sub> - Thickness of a pixel
E <sub>a</sub> - Activation energy
R – Universal gas constant
s - Second
Vf - Volume fraction
vol % - Volume percent
F – Factor term
X - Fraction



#### **Chapter 1 Introduction**

#### 1.1 Application of high temperature materials

High temperature materials find applications in various areas including power generation systems (400-1300 °C [1]), aeroengines (1300-1980 °C [2]) and hypersonic vehicles (>1600 °C [3]). The material property requirements for components such as turbines, rockets, heat exchangers and modern aeroengines depends strongly on the operating conditions. For instance, higher operating temperature of turbines leads to higher efficiency and lower fuel consumption [4], thereby also resulting in lower emissions. The high temperature materials that are desired to withstand loading, must possess resistance to mechanical degradation and must tolerate severe operating environments and high loads for extended time periods, with creep resistance becoming an important criterion. Potential candidates for turbine blades or the thermal protection system for re-entry vehicles are often subjected to extreme temperatures (~1650 °C [5]) in an oxidative environment. Traditionally, Nibased alloys have been used for high temperature applications (up to 1100 °C). However, the need for higher temperature has necessitated an exploration of novel material systems, with the rapid growth rates of the alumina scale above 1100 °C resulting in high thermal stress and scale spallation. Silica forming materials are considered as potential candidates for high temperature applications. The glassy nature of the silica scale allows easy lateral scale growth imparting self-healing properties to the oxide scale at high temperatures.[6].

#### 1.2 Key material challenges

The major challenge associated with high temperature materials is their ability to maintain structural integrity when subjected to very high temperatures, loading conditions and aggressive environments. Components of turbines used for power generation and jet propulsion systems, leading edges and nose tips of hypersonic vehicles are subjected to such conditions and are prone to degradation due to oxidation. Hypersonic vehicles are fast moving vehicles that operate at speeds greater than Mach 5 and their applications include ballistic and interceptor missiles, re-entry vehicles, space access vehicles, hypersonic cruise missiles and aircraft [3]. These vehicles have air-breathing engines based on the concept of ramjet and scramjet propulsion systems and the thrust is generated using aerodynamics forces [7]. They have sharp leading edges where "sharp" refers to edges with nearly-zero radius of curvature. Such designs reduce the drag resulting in better maneuverability, performance, and safety [8]. As the design of hypersonic vehicles consists of sharp features, their leading edges and wings may experience extremely high temperatures, high heat flux and thermal shocks. Thermal shocks can raise the temperatures above 2000 °C and heat flux of the order of 100 W/cm<sup>2</sup> [3]. During re-entry at an altitude of 120 km with an initial speed of ~ 7800 m/s, the exposure duration will be around 15 s [9]. Several engine components such as inlet, combustor and nozzle undergo excessive heating as compared to other components due to burning of fuels [7]. Leading edges and nose tips of these vehicles are exposed to harsh environments where reactive dissociated gases are present, surfaces may undergo oxidation. Therefore, high melting points and oxidation resistance are key properties required for the materials that are used at these critical components.

#### 1.3 Materials beyond Ni-based alloys

Ni-based superalloys had emerged as materials of choice for components of gas turbines where temperatures may reach around 800 °C such as in coal fired power plants and chemical processing plants. These superalloys can be used

under static loading, fatigue and creep conditions [10,11]. The application of superalloys is limited as the operating temperature required to increase energy efficiency is higher than the melting temperature of Ni-based superalloys. While Ni-based superalloys have been the workhorse materials for gas turbines, very little increase in operating temperatures with these materials has progressed in the last quarter of a century, with an average of 1-2 °C increase per year [4]. A key challenge is to replace traditional superalloys, used in hot sections, with new materials that are lightweight, have high-strength and high thermal shock and are oxidation resistant. Refractory metal silicides may lead to an improvement of 10-20% in operating temperatures. Research on refractory metal silicides such as Mo-Si and Nb-Si based alloys have gained attention due to their high temperature stability and high creep resistance. However, Nb-Si alloys undergo catastrophic oxidation due to formation of non-protective Nb<sub>2</sub>O<sub>5</sub> oxide layer above 500 °C [12] and Mo-Si forms volatile MoO<sub>3</sub> around 700 °C [6]. The alloys which form multiphase structures are also known for their ultra-high temperature properties [13]. Systems that form stable oxide scales such as SiO<sub>2</sub> during oxidation at elevated temperatures enhance oxidation resistance. MoSi2 is known to have high oxidation resistance for applications up to 1700 °C as it forms stable SiO<sub>2</sub> layer, but it shows poor creep resistance [14,15]. Formation of multi-phase structures in an alloy can provide an optimal blend of properties. In Mo-Si-B alloys, Mo stays as solid solution which provides toughness. It co-exists with Mo<sub>5</sub>SiB<sub>2</sub> (T2) phase which has melting point of above 2100 °C and provides excellent oxidation resistance due to formation of protective borosilica scale [13,16,17]. Mo<sub>5</sub>Si<sub>3</sub> (T1) phase provides creep resistance and oxidation resistance. To achieve required oxidation resistance and other high temperature properties, it is crucial to control the size and distribution of each phase in the system. The size of Mo (ss) features and whether these features form continuously or not is important. Due to their melting points of above 3000 °C, these materials are considered promising candidates for next generation ultra-high temperature materials [18].

The requirements of materials for use in aerospace industries have been changing for decades due to the introduction of new propulsion systems and hypersonic designs. Light weight to reduce fuel consumption and high operating temperatures to improve thermal efficiency of engines has led to the development of composite materials. Carbon Matrix Composites (CMCs) are suitable for use in hot sections as they are capable to replace superalloys with significant weight reduction [19]. The CMCs find their application hot sections of turbine engine such as turbine vanes, blades and exhaust nozzles up to 1482 °C temperature [19,20]. Figure 1.1 provides an overview of the temperature capability of various CMCs compared to superalloys. Due to their capability of withstanding high temperatures, cooled CMCs are favorable for use in hypersonic engine components [21]. However, there are several limitations of using CMCs for hypersonic applications. Design of CMC components require textile architectures for better cooling and a high cost associated with their manufacturing becomes challenging [19]. There is another emerging category of materials known as Ultra-high temperature ceramics (UHTCs) considered to have superior properties and oxidation resistance compared to CMCs [22,23]. UHTCs which are favorable candidates for hypersonic and aerospace applications are discussed in detail in later sections.

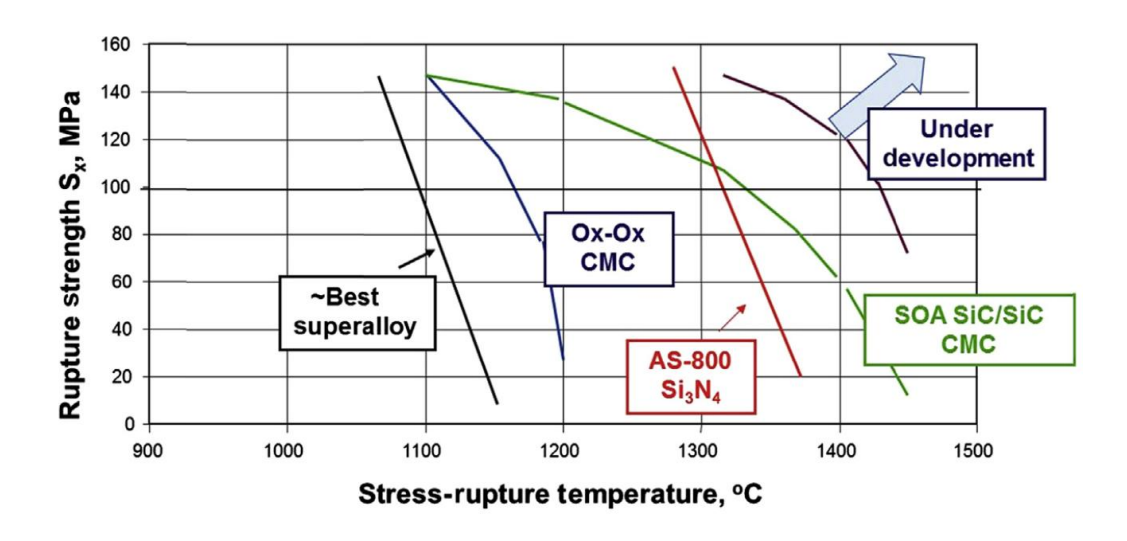


Figure 1.1 Comparison of stress-rupture temperature for various materials [19,20]

## 1.4 Scope of thesis

Mo-Si-B alloys and UHTCs undergo oxidation resulting in scale formation on the surface. This oxide scale can be protective or non-protective under certain temperature regimes. This depends on several factors such as temperature, partial pressure of oxygen, flow rate and material composition. Mo-Si-B alloys and boride based UHTCs with SiC form a silica-rich glassy scale during oxidation which protects the substrate from oxidation. The aim of this work is to understand and control the borosilica scale formation on these materials for better oxidation resistance by changing the substrate composition.

## 1.5 Thesis organization

The thesis consists of seven chapters starting with a brief introduction of the topic in chapter 1. Chapter 2 is a literature review that covers the general properties and oxidation behaviour of Mo-Si-B alloys and UHTCs. In chapter 3, Molecular Dynamics was used to simulate diffusion in SiO<sub>2</sub> glass and an oxidation model using Cellular Automata was developed in chapter 4. Chapter 5 consists of the experimental studies that were conducted to study the oxidation behavior of Mo-Si-B alloys. The oxidation behaviour of UHTCs studied using experimental techniques is presented in chapter 6. The conclusion and the scope of future work is discussed in chapter 7.

## **Chapter 2 Literature Review**

## 2.1 Refractory metal silicides

## 2.1.1 The Mo-Si-B alloy system: phase stability and general properties

Refractory metal silicides such as Mo-Si based alloys form protective oxide scales that provide oxidation resistance. These materials can be used as oxidation resistant coatings on high strength materials for high temperature applications [6,13]. Therefore, it is important to explore their compatibility with the alloy substrate, mechanical properties and oxidation behaviour in a range of operating temperatures and actual environmental conditions. An understanding of compositional effect and kinetic factors on oxidation behaviour is a key step for coatings design [6]. Mo in its pure form has high melting point of above 2600 °C, but it has poor oxidation resistance. Addition of Si results in formation of protective silicate glass and B addition together with Si leads to borosilica formation as studied by Meyer and Akinc [24]. This improves the oxidation resistance of the material. Boron doped Mo-Si alloys form multiple phases (including α-Mo, Mo<sub>3</sub>Si, Mo<sub>5</sub>Si<sub>3</sub>) which can provide good oxidation resistance and mechanical properties. The Mo<sub>5</sub>Si<sub>3</sub> phase provides oxidation resistance and when doped with boron, it forms protective borosilicate scale during oxidation [24-26]. The Mo<sub>3</sub>Si phase results in poor oxidation resistance [17]. The overall properties depend on the composition of the alloy and the phases formed. The phase diagram for Mo-Si-B alloys was

initially published by Nowotny et al. [27] and was updated later by Nunes et al. [28]. Figure 2.1 shows the stability of different phases in Mo-Si-B alloys at 1600 °C [28] and Figure 2.2 [13] shows the liquidus projections of Mo-Si-B alloys system. The region shaded with orange represents Berczik triangle comprises of Mo(ss), T1 and A15 phases. Berczik added Si and B to Mo to enhance its oxidation resistance with compositions lying in this triangle [29]. Later various compositions in Berczik region were studied by many researchers [6,17,30,31]. The compositions lying in the area shaded with green were studied by Akinc et al [30] and Meyer et al. [26].

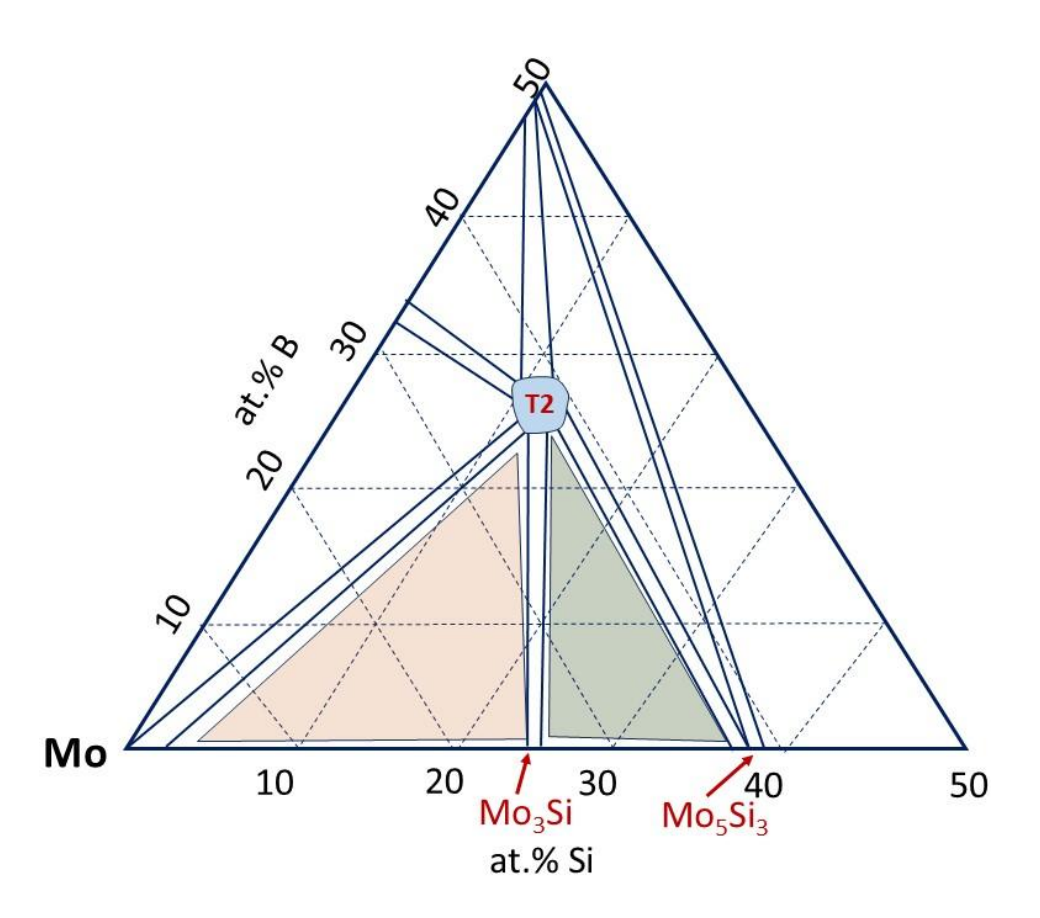


Figure 2.1 Phases in Mo-Si-B alloys at 1600 °C

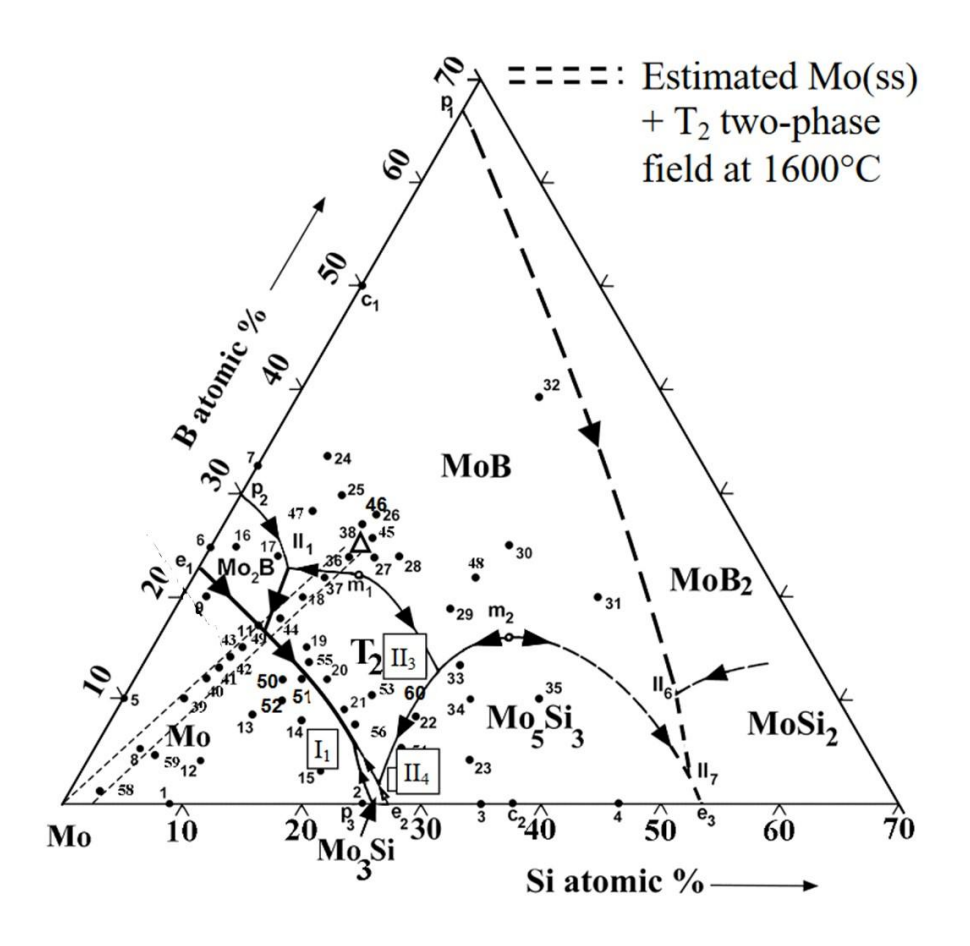


Figure 2.2. Liquidus projections in Mo-Si-B alloy system [13]

In these alloys,  $\alpha$ -Mo phase provides ductility, toughness and inhibits crack propagation. However, above 500 °C, pure Mo has tendency to oxidize rapidly to MoO<sub>3</sub> and volatilize. Therefore, it is important to limit its presence in the alloys [32]. Other phases that can co-exist with  $\alpha$ -Mo phase include Mo<sub>3</sub>Si, Mo<sub>3</sub>Si<sub>3</sub> and Mo<sub>5</sub>SiB<sub>2</sub>. Mo<sub>3</sub>Si forms A15 cubic structure and is often referred to as A15 phase, Mo<sub>5</sub>Si<sub>3</sub> with tetragonal structure is referred as T1 and Mo<sub>5</sub>SiB<sub>2</sub> with body-centered tetragonal structure as T2. Mo<sub>3</sub>Si phase is brittle as it has very few active slip systems [17] with a reported fracture toughness of up to 3 MPa $\sqrt{m}$  [33]. The A15 Mo<sub>3</sub>Si belongs to Pm-3n space group and m3m Laue class where the Mo atoms form three orthogonal chains [34,35]. It was reported that its cubic structure is due to increased overlap of d states of metal with its surrounding [36]. The Mo<sub>5</sub>Si<sub>3</sub> phase has D8<sub>m</sub> structure and I4/mcm space group (D8<sub>8</sub> structure with space group P6<sub>3</sub>/mcm is also found often) [37]. The D8<sub>m</sub> structure has strong bonds as it has high enthalpy of formation (-3.8 eV/formula unit) [37]. According to Fu et al. [37] the D8<sub>8</sub> structure can only be

stabilized in presence of interstitial elements such as carbon. The Mo<sub>5</sub>SiB<sub>2</sub> (T2) phase has D8<sub>1</sub> structure with I4/mcm space group [38]. Table 2.1 lists the Pearson symbols and space groups of some important phases of metal silicides.

The T2 phase has a range of homogeneity around its stoichiometric composition and it is a key component in Mo-Si-B system [28,39]. It has a melting point of above 2200 °C, excellent high-temperature strength and resistance against stress deformation [40]. The elemental addition to Mo-Si-B alloys affects the phase stability. For example, the effect of Nb substitution on Mo-Si-B phase stability was reported by Perepezko et al. [13] which shows that Nb forms solid solution in bcc (Mo,Nb) and T2 phases in two-phase Mo-10Si-20B alloy. The lattice parameters c and a in T2 phase lattice increased with an increase in Nb content. Sakidja et al. [38] reported that substituting small amounts of Mo with Nb inhibited the formation of Mo(ss) precipitates in T2 phase in two-phase Mo-Si-B alloys and suggested that its stability depends on constitutional defects. In as cast three-phase Mo-10Si-20B alloy (Mo(ss), Mo<sub>3</sub>Si and Mo<sub>5</sub>SiB<sub>2</sub>), there were very few dislocations present whereas after annealing at 1600 for 150 h, Mo(ss) particles precipitated in T2 matrix with increased dislocation density in primary T2 phase [38].

Table 2.1 Crystal structures of some important phases of metal-silicon systems [41]. The crystal structure images were taken from Materials Project [42]

Phase	Pearson symbol	Space group	Atomic representation
Mo <sub>3</sub> Si (A15)	cP8	Pm-3n	SI Mo

Mo <sub>5</sub> Si <sub>3</sub> (T1)	tI38	I4/mcm	Si Mo
Mo <sub>5</sub> SiB <sub>2</sub> (T2)	tI32	I4/mcm	SI MO B
Nb <sub>3</sub> Si	tP32	P4 <sub>2</sub> n	Nb2+ Si4
Nb <sub>5</sub> Si <sub>3</sub>	tI32	I4/mcm	
W <sub>5</sub> Si <sub>3</sub>	tI32	I4/mcm	

The creep strength of alloys changes with the composition and microstructure. Schneibel et al. [31] reported an increase in the creep strengthening with low  $\alpha$ -Mo content i.e. with high Mo<sub>3</sub>Si-Mo<sub>5</sub>SiB<sub>2</sub> volume fraction. The presence of continuous  $\alpha$ -Mo matrix reduced the creep strength. However,  $\alpha$ -Mo phase is ductile and increase in its volume fraction increases room temperature fracture toughness of the system [31]. Schneibel et al. [43] compared the creep behaviour of the two alloys with 21 vol %  $\alpha$ -Mo with its different grain sizes. For the sample with coarser grains, the stress component was higher (2.8 for coarse and 2.1 for fine) and the activation was lower (327 kJ/mol) than the sample with

finer microstructure (376 kJ/mol). The creep strength of alloys with fine microstructure was low because fine grains provide easy diffusion pathways for Mo [31,43]. The grain size also affects the fracture toughness of the material and it was reported that fine grained alloys have lower fracture toughness due to intergranular slip mechanism as compared to coarse grained alloys where intragranular slip mechanism is favorable [32,40]. However, the fine grain size increases the grain boundaries which hinders the dislocation movement and increases alloys strength [40]. The creep strength of Mo-X-Si-B alloy (where X = Nb, W) was reported at 2 % plastic deformation in terms of compressive engineering flow stress in the temperature range of 1200-1400 °C [43]. The activation energy for Mo-Si-B alloy was 295 kJ/mol and after 19.5 at% W addition it changed to 319 kJ/mol with slightly increased the creep strength [43]. The 19.5 at% Nb addition increased the activation energy to 489 kJ/mol and improved creep strength more than W addition [43]. The larger radius of Nb (1.44 Å) atom as compared to W (1.38 Å) and Mo (1.37 Å) inhibits dislocation movement and improves creep strength [32,44].

### 2.1.2 Oxidation mechanism of Mo-Si-B alloys

In a research work by Parthasarathy et al. [45] on Mo-Si-B alloy with Mo, Mo<sub>3</sub>Si and Mo<sub>5</sub>SiB<sub>2</sub> phases, oxidation studies were carried out in the temperature range of 500 to 1300 °C. In the temperature range of 500-600 °C, the overall oxidation rate was lower than that of pure Mo with parabolic weight gain. Here, Mo forms MoO<sub>3</sub> and the other two phases form borosilica scales which cover the surface gradually and prevents MoO<sub>3</sub> evaporation. The oxidation behaviour depends on the partial pressure of oxygen and when the oxygen partial pressure is high in initial stages, following reactions occur [46]:

$$2Mo + 3O_2 = 2MoO_3$$

Equation 2.1

$$2Mo_3Si + 11O_2 = 6MoO_3 + 2SiO_2$$

Equation 2.2

$$Mo_5SiB_2 + 10O_2 = 5MoO_3 + SiO_2 + B_2O_3$$

Equation 2.3

Once the oxide layers form and starts to thicken, partial pressure of oxygen decreases resulting in the following reactions [47,48]:

$$Mo + O_2 = MoO_2$$

Equation 2.4

$$Mo_3Si + 4O_2 = 3MoO_2 + SiO_2$$

Equation 2.5

$$2Mo_5SiB_2 + 15O_2 = 10MoO_2 + 2SiO_2 + 2B_2O_3$$

Equation 2.6

On further reduction of oxygen partial pressure, the reactions that occur are as follows [47,48]:

$$Mo_3Si + O_2 = 3Mo + SiO_2$$

Equation 2.7

$$2Mo_5SiB_2 + 5O_2 = 10Mo + 2SiO_2 + 2B_2O_3$$

Equation 2.8

The change in kinetics in the temperature range of 650-750 °C, resulting in pesting with parabolic weight loss with a thick borosilica scale was reported [17,45]. Mo forms MoO<sub>3</sub> and the borosilica scale that forms in this temperature range is porous through which gaseous MoO<sub>3</sub> is lost. Above 800 °C up to 1300 °C, a thinner borosilica scale is formed with lower oxidation rates. The thin scale was due to evaporation of boria from the scale and oxidation was lowered due to less oxygen diffusion through the scale. It was suggested that the continuous evaporation of boria does not allow oxygen to diffuse through the scale. As the borosilica scale covers the entire surface, oxidation reaches a steady state. The oxidation kinetics of these alloys is influenced by mass loss due to MoO<sub>3</sub>

evaporation and mass gain due to borosilica scale formation. Therefore, to understand oxidation behaviour more precisely, looking into the temporal microstructural evolution is crucial.

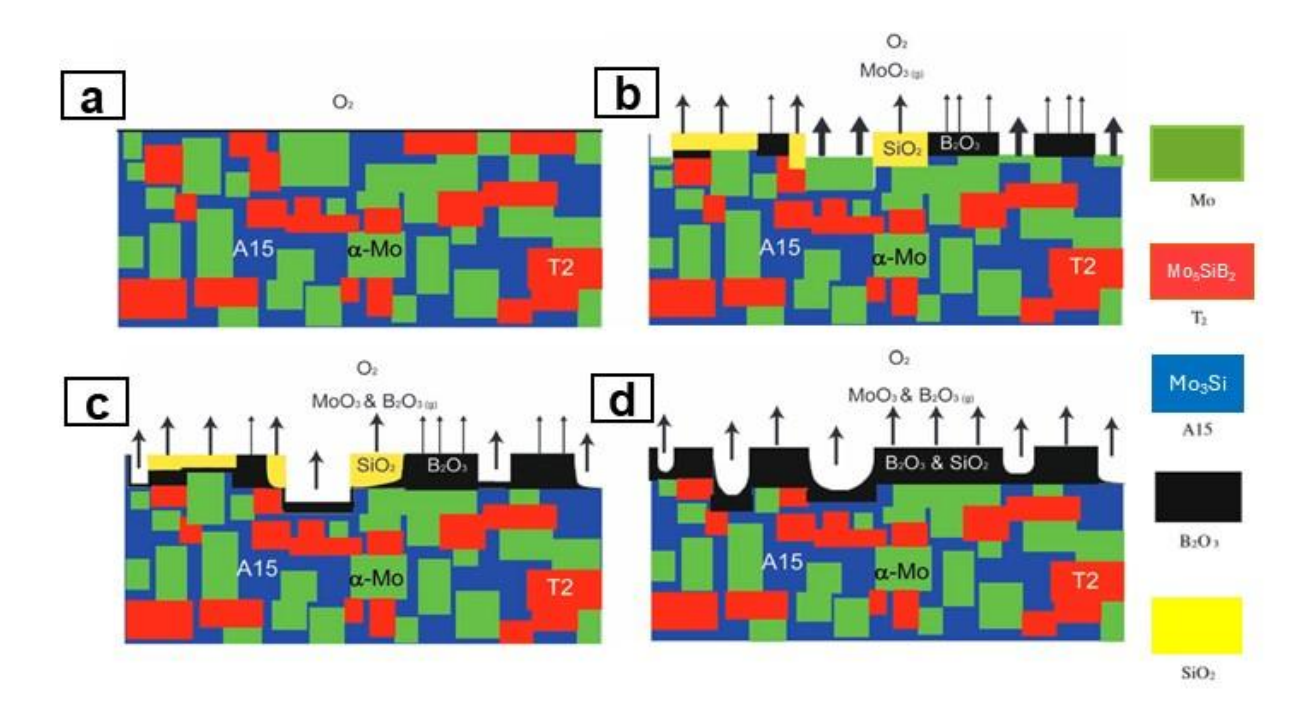


Figure 2.3 Schematic showing the transient oxidation mechanism in Mo-Si-B alloys at 1500  $^{\circ}$ C [17,32]. (a) Unoxidized sample (b) oxidation initiates where Mo forms volatile MoO<sub>3</sub>, Si forms SiO<sub>2</sub>, B forms B<sub>2</sub>O<sub>3</sub> (c) oxidation continues and B<sub>2</sub>O<sub>3</sub> starts to flow due to its low viscosity and mixes with SiO<sub>2</sub> (d) the borosilica scale formed due to mixture of SiO<sub>2</sub> and B<sub>2</sub>O<sub>3</sub> starts to form a protective scale on the surface.

Rioult et al. [17] studied oxidation of pure Mo, Mo<sub>3</sub>Si and Mo<sub>5</sub>SiB<sub>2</sub> phases at 1100 °C. The schematic in Figure 2.3 shows the transient oxidation mechanism of Mo-Si-B alloys. A linear mass loss rate for oxidation of Mo (-16.4 mg cm<sup>-2</sup> min<sup>-1</sup>) and Mo<sub>3</sub>Si (-4.2 mg cm<sup>-2</sup> min<sup>-1</sup>) due to the formation and volatilization of MoO<sub>3</sub> was reported [17]. However, the mass loss in Mo<sub>3</sub>Si was less than that in pure Mo. Mo<sub>3</sub>Si oxidized to form MoO<sub>3</sub> due to presence of Mo and glassy silica scale from Si. This silica scale was found to be discontinuous due to its high viscosity, which reduces the glass flow and results in poor surface coverage or discontinuous scale. This porous scale makes volatilization of MoO<sub>3</sub> easier resulting in mass loss. Additionally, the porous structure enables oxygen diffusion to the substrate resulting in increased oxidation. The oxidation of Mo<sub>5</sub>SiB<sub>2</sub> phase showed initial mass loss followed by steady state. The steady state was achieved due to formation of borosilica scale on the sample surface.

The presence of Boron leads to boria formation which resulted in reduced viscosity of the scale enabling its better flow and better surface coverage. The plot in Figure 2.4 shows a reduction in viscosity of borosilica scale with increasing B<sub>2</sub>O<sub>3</sub> content. This borosilica scale protects the surface from oxidation. Each phase has different oxidation resistance as well as different mechanical properties. The overall properties of these alloys depend on the amount and distribution of phases. Rioult et al. [17] observed faster borosilicate formation with fine and homogeneously distributed intermetallic phases. An optimum composition of borosilica scale may enhance the oxidation resistance which can be obtained either by changing the alloy microstructure or by changing the alloy composition [49]. Both factors are important to control the borosilica scale chemistry, its protective nature, and mechanical properties of the alloy. To modify the oxidation and mechanical properties of silicides, researchers have studied the effects of element and second-phase particles additions such as Zr [50], Ti [51,52], Y[48], Al [53,54], W [16,55] and ZrB<sub>2</sub> [56].

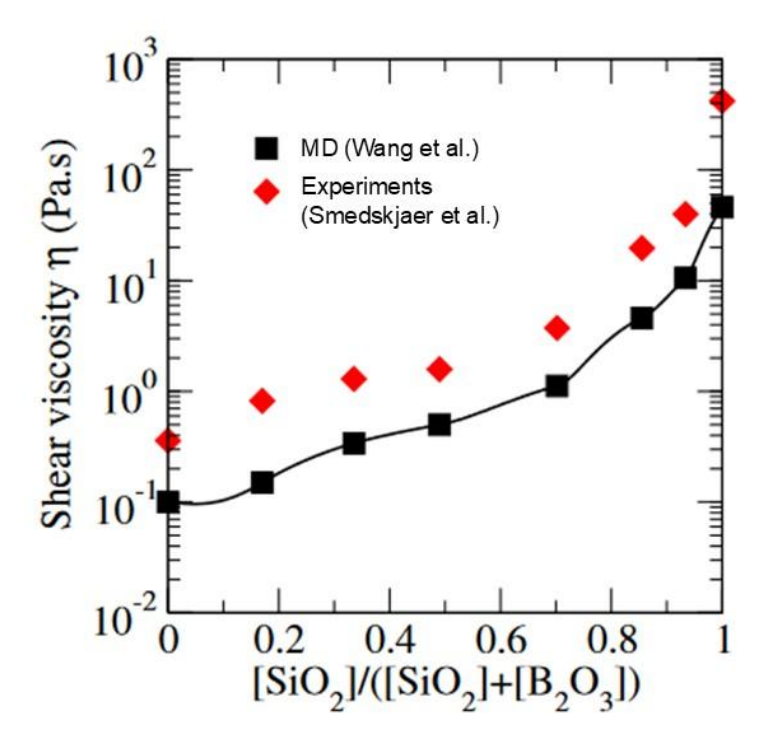


Figure 2.4. Viscosity variation in borosilica glass with varying  $SiO_2$  and  $B_2O_3$  content at 1150 °C [57,58]

## 2.1.3 The effect of alloying additions on oxidation

The grain boundaries act as primary paths for oxygen diffusion in alloys and addition of reactive elements such as Hf, Zr or Al has shown significant effect on oxidation properties of Mo-Si-B alloys [46]. The reactive elements migrate to the oxide grain boundaries when crystalline oxides such as Al<sub>2</sub>O<sub>3</sub> and Cr<sub>2</sub>O<sub>3</sub> are formed [59]. In case of amorphous SiO<sub>2</sub>-rich scale, the reactive elements diffuse outward through alloy grain boundaries and through silica scale. These elements react preferentially due to their electropositive nature with oxygen at the substrate grain boundaries or at oxide-substrate interface and suppress the inward oxygen diffusion. As reactive elements migrate to the silica scale these affect silica scale network and viscosity. The network modifiers disrupt the network and reduce viscosity whereas, the network formers make the bonds stronger and increase viscosity and perhaps densify the scale [60]. Figure 2.6 shows the effect of Ca ions as network modifier in silica. Alloying also aids in microstructural changes and increased oxide scale adhesion resulting in better oxidation resistance [47,61].

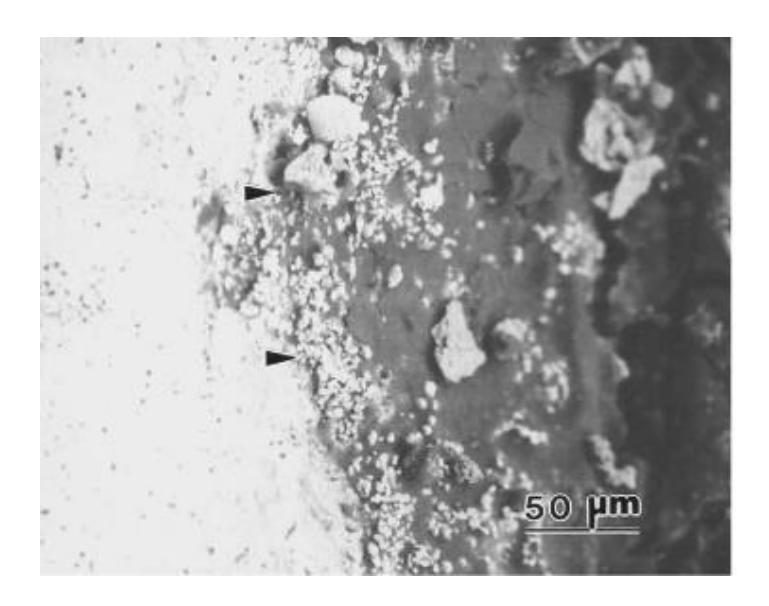


Figure 2.5. Cracks appeared on Mo-Si-B alloy with 7.3 at% Al on oxidation at 600 for 300 h [53]

Paswan et al. [53,54,62] studied Al addition to Mo-Si-B alloys in isothermal and non-isothermal conditions in different temperature ranges. Isothermal oxidation of Al added Mo-Si-B alloys at 400-800 °C resulted in formation of mullite and showed reduced oxidation resistance [53]. For 76Mo-14Si-10B

alloy, mass loss of 50 mg/cm² was found whereas after adding 7.3 at% Al (73.4Mo-11.2Si-8.1B7.3Al), the mass loss increased by about seven times at 700 °C after 20 h of exposure [53]. The oxide scale showed cracks at 500 and 600 °C. Figure 2.5 shows cracks in scale in alloy with 7.3 at% Al after oxidation at 600 °C for 300 h. It was suggested that the mass loss could be due to oxide scale spallation and volatilization of MoO<sub>3</sub>. Additionally, the high vapor pressure of MoO<sub>3</sub> can lead to internal stress generation and cracking of the scale [53]. The cyclic oxidation of Mo-Si-B alloys with Al resulted in the formation of low density mullite through which oxygen permeation increased [62]. Exposure of alloys with Al at 1150 °C and 1300 °C showed initial mass loss followed by steady state. However, the overall mass loss was lower in alloys without Al. Al addition showed degradation in oxidation properties and it was suggested that higher initial mass loss was due to delay in the formation of protective oxide scale in Al containing alloys.

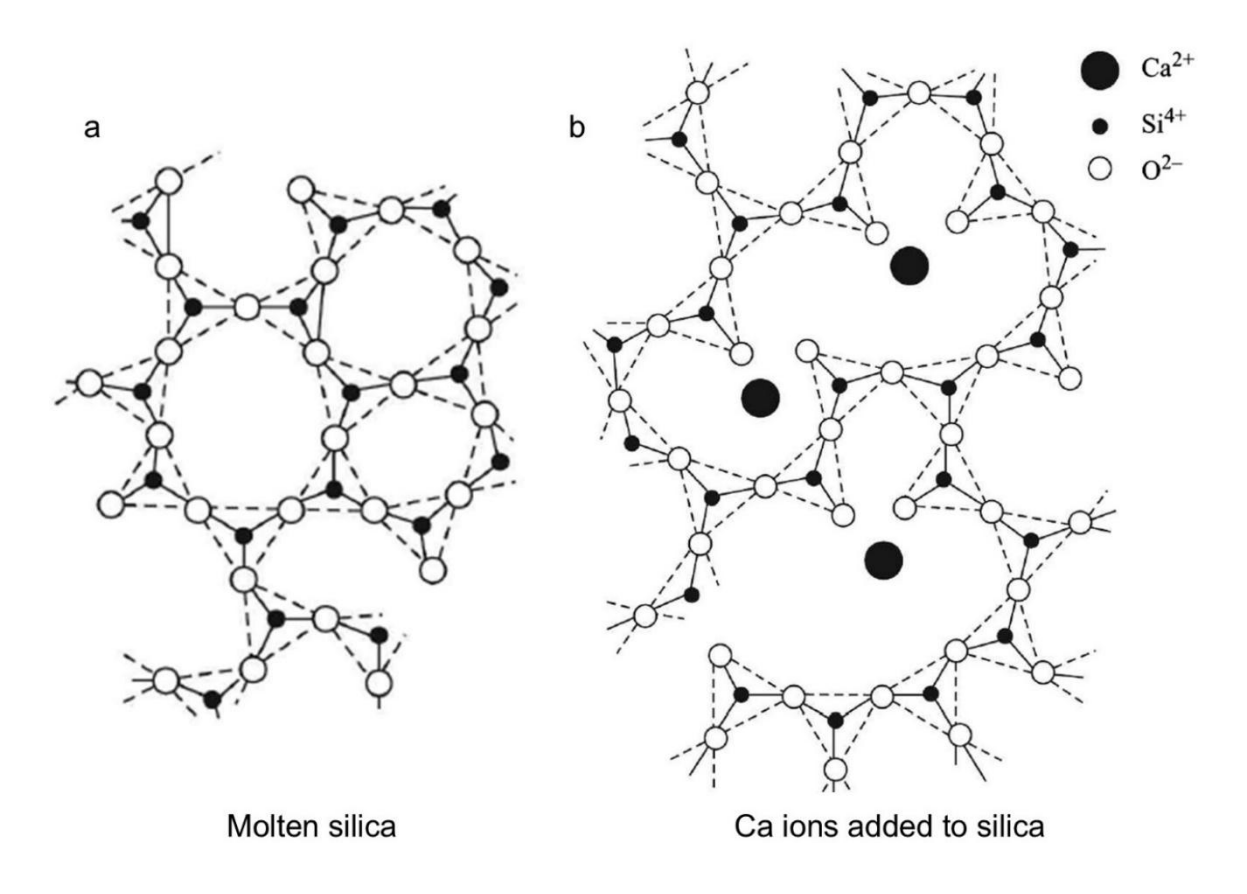


Figure 2.6. (a) The structure of molten silica and (b) shows the effect of Ca addition on silica network

In Mo-Si-B alloys, the presence of Mo<sub>3</sub>Si phase is detrimental to mechanical properties and does not significantly contribute to oxidation resistance. Ray et al. [63] reported that tungsten and niobium addition to Mo-Si alloys can eliminate the brittle Mo<sub>3</sub>Si (A15) phase. Karahan et al. [55] extended this to Mo-Si-B alloys and showed Mo<sub>3</sub>Si removal using tungsten and discussed their oxidation behaviour. It was reported that Mo-15Si-15B (at%) alloy constituted of Mo(ss), A15 and T2, and tungsten addition resulted in Mo(ss), T1 and T2 phases. However, tungsten addition showed detrimental effect on oxidation properties at 1200 °C due to formation of WO<sub>3</sub> which is non-volatile at this temperature. Non-volatile WO<sub>3</sub> that stays on the surface hinders SiO<sub>2</sub>-rich scale flow leading to poor surface coverage and discontinuous oxide scale formation. At 1400 °C, volatilization of WO<sub>3</sub> was reported resulting in densification of protective oxide scale [55]. Thus, this indicates that tungsten addition may lead to reduced oxidation resistance, but at higher temperatures (>1300 °C) or in pretreated samples, it may not deteriorate oxidation properties significantly [64].

Ti addition to Mo-Si-B alloys reduce density and provides better oxidation resistance [64]. Schliephake et al. [52] and Azim et al. [65] studied isothermal oxidation of Mo-9Si-8B-29Ti (at%) at 1100 °C, 1200 °C and 1300 °C and reported increased mass loss as compared to the alloy without Ti when oxidized till 100 h. The mass loss increased with the increase in temperature. The alloy with 29 at% Ti constituted of Mo(ss), T1 and T2 phases. The oxide layer composed of non-protective rutile outer layer, below which TiO<sub>2</sub> layer embedded with little borosilica was present. This oxide layer was thick and porous resulting in easy inward oxygen diffusion. It was suggested that cracks appeared due to mismatch in coefficients of thermal expansion of TiO<sub>2</sub> and SiO<sub>2</sub> [52]. Azim et al. [65] reported similar results for Mo-9Si-8B-29Ti alloy.

Burk et al. [50] observed improvement in oxidation resistance when 1 at% Zr is added to Mo-9Si-8B (at%) alloy below 1200 °C. However, above 1200 °C, the oxidation resistance decreased due to phase transformation of ZrO<sub>2</sub> particles in SiO<sub>2</sub>-rich scale resulting in volume change. This led to the formation of holes in the scale providing easy pathways for oxygen diffusion and MoO<sub>3</sub>

volatilization. The addition of zirconium to the alloys refines grain size, improves mechanical properties and results in quick formation of borosilicate layer [64]. Wang et al. [56] fabrication Mo-12Si-8.5B (at%) alloy with and without addition of 1 at%  $ZrB_2$  at 900 °C and found significant improvement in oxidation properties with  $ZrB_2$  addition. The mass loss changed to  $10 \text{ mg/cm}^2$  which was  $180 \text{ mg/cm}^2$  without  $ZrB_2$  addition when exposed for 30 h. Small amounts of dissolved Zr in  $SiO_2$ -rich scale and  $ZrSiO_4/ZrO_2$  particles were observed in the scale [56]. Presence of Zr in the scale affects the  $SiO_2$  network, increases scale viscosity and makes it more stable [64].

### 2.1.4 Oxidation behavior of other refractory metal silicides

Nb-Si based alloys have higher melting points (>1700 °C) and lower densities (6.6-7.2 g/cm³) than Ni-based superalloys, but, their high-temperature oxidation resistance make them unsuitable for ultra-high temperature applications [66]. Nb(ss) phase in Nb-Si alloys provides ductility. Other phases include Nb₃Si and Nb₅Si₃ [66]. Similar to Mo-silicides, Nb-Si-based alloys form SiO₂-rich glassy scale, but, during oxidation above 500 °C, porous and non-protective Nb₂O₅ forms as shown in Figure 2.7 [32]. Nb₂O₅ is non-volatile and impedes the surface coverage by the silica-rich scale. Additionally, its formation results in volume expansion and stress generation in the oxide scale leading to its cracking and spallation [67,68]. The Pilling-Bedworth Ratio (PBR) for Nb oxidation to Nb₂O₅ is 2.68. The volume expansion correlates with PBR and results in crack formation in the scale [69].

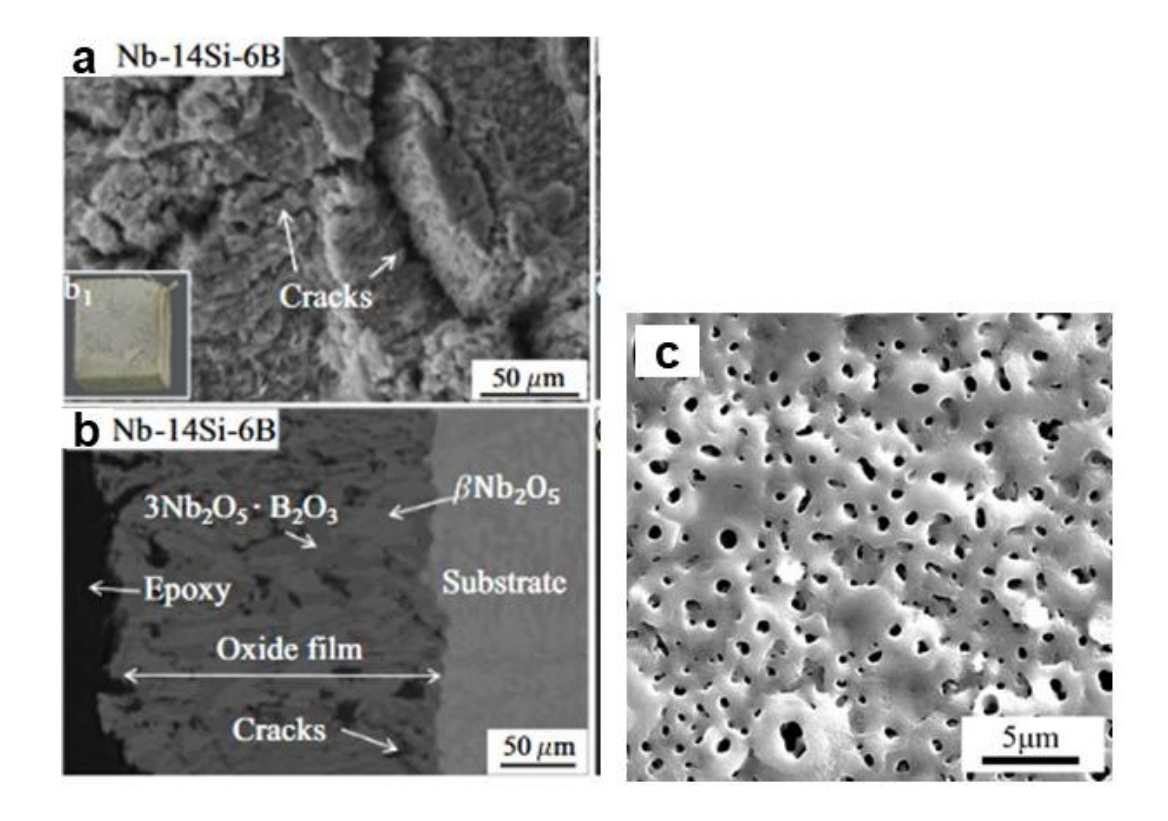


Figure 2.7. (a) Surface cracks (b) cracks on cross section on Nb<sub>2</sub>O<sub>5</sub> scale formed on Nb-Si-B alloy after 10 min of oxidation at 1100 °C [32] (c) Porous Nb<sub>2</sub>O<sub>5</sub> formed on Nb<sub>2</sub>O<sub>5</sub>-SiO<sub>2</sub>-Al<sub>2</sub>O<sub>3</sub>/NbSi<sub>2</sub>/Nb<sub>5</sub>Si<sub>3</sub> multilayer coating at 1300 °C for 8 h [69].

The addition of boron to Nb-Si based alloys improves oxidation resistance. Zhang et al [70] studied the effect of 2 and 5 at% boron addition to Nb-22Ti-16Si-5Cr-4Hf-3Al alloy on oxidation properties. The mass gain of 127.1, 90.5 and 67.6 mg/cm² was reported for 0, 2 and 5 at% boron respectively for 50 h oxidation at 1250 °C and oxide layer thickness also reduced to 441 μm for 5 at% boron addition from 882 μm without boron. Thomas et al. [71] studied the effect of Si and B content in Nb-silicides and concluded that high Si and B content are beneficial for oxidation resistance. Zhang et al. [72] studied the effect of B, Hf and Cr, and concluded that Cr together with B improves oxidation resistance. Su et al. [73] reported that Ge forms GeO<sub>2</sub> and boron forms B<sub>2</sub>O<sub>3</sub> and their presence synergistically improves oxidation resistance. The presence of these oxides together improves the coefficient of thermal expansion and improves scale integrity, inhibits crack formation and enhances oxidation resistance. In Mo-Nb-Si-B alloys, (Mo, Nb)<sub>5</sub>Si<sub>3</sub>(B) with hexagonal structure and poor oxidation resistance, and (Mo, Nb<sub>5</sub>Si<sub>8</sub>2 form in addition to (Mo, Nb)(ss) [74].

Reduction in oxidation resistance of these alloys as compared to Mo-Si-B alloys was observed due to presence of Nb that forms porous Nb<sub>2</sub>O<sub>5</sub> [74].

## 2.2 Ultra-High Temperature Ceramics

# 2.2.1 Synthesis and physical properties of Ultra-high Temperature Ceramics

UHTCs are borides, carbides or nitrides of early transition metals such as Zr, Hf, Ti, Nb and Ta [75] and are also defined as materials which can be used beyond 1650 °C for long durations [76]. Strong covalent bonds are formed between these metals and ceramics imparting a combination of metals and ceramic-like properties. Due to strong bonding, UHTCs exhibit high hardness, strength, chemical stability, high thermal and electrical conductivities that make them capable of surviving in extreme environments for extended durations. For hypersonic vehicles, high thermal conductivities are required so that the heat generated at the edges can be transferred to the atmosphere. Typical examples of UHTCs are ZrB<sub>2</sub>, HfB<sub>2</sub>, TaC, HfC, TaN, HfN, ZrB<sub>2</sub>-SiC and HfB<sub>2</sub>-SiC composites. The unique combination of properties such as better thermal conductivity, high temperature strength and oxidation resistance make them suitable for use at leading edges and nose tips of hypersonic vehicles and propulsion systems [77]. Carbides based UHTCs can be utilized for components such as nozzles and thrusters which require high resistance to thermal and mechanical shocks [78].

Zirconium and Hafnium diborides (ZrB<sub>2</sub> and HfB<sub>2</sub>) have been studied extensively and identified as prominent candidates for use in ultra-high temperatures due to their favorable mechanical and thermal properties. These diborides have extremely high melting points (>3000 °C), exceptionally high thermal conductivities (ZrB<sub>2</sub>- 60 [9], HfB<sub>2</sub>- 104 [10] W/m.K) and relatively low densities (ZrB<sub>2</sub>- 6.12 g/cm<sup>3</sup>, 11.212 g/cm<sup>3</sup>) as compared to other refractory metals [79]. As ZrB<sub>2</sub> has covalent bonding and high melting point, the diffusion rates at grain boundaries are extremely low during sintering and therefore, it

is extremely difficult to densify it completely [79–81]. Sintering of diborides using conventional sintering routes (e.g. pressureless sintering) require very high temperatures (>2000 °C) to achieve theoretical density >95% [81]. At low sintering temperatures, low theoretical densities are achieved, and with increase in temperature, increased theoretical densities are achieved. However, high temperature sintering results in grain growth and deteriorates mechanical properties [82]. The average grain size for monolithic materials is related to sintering time according to the relation  $G = G_0 + Kt^n$ , where, G is the average grain size,  $G_0$  is the initial grain size,  $G_0$  is grain growth coefficient and G is sintering time [83]. The theoretical density of G grain size G grain size

Table 2.2. Mechanical properties of hot pressed ZrB<sub>2</sub> with different sintering conditions [81]

Material	Conditions	Sintered density (%)	Grain size (µm)	Hardness (GPa)	Fracture toughness (MPa.m <sup>1/2</sup> )	Flexural strength (MPa)
ZrB <sub>2</sub>	2100 °C, 60 min, 32 MPa	97	25	13.7	3.1	392
ZrB <sub>2</sub>	2150 °C, 30 min, 32 MPa	96.7	27.7	13	3.2	398
ZrB <sub>2</sub>	2150 °C, 60 min, 32 MPa	97.3	33.4	14.1	3.0	394

ZrB <sub>2</sub>	2100 °C, 120	97.8	52.1	14.4	2.7	337
	min, 32 MPa					
ZrB <sub>2</sub>	2200 °C, 60	97	35.5	13.6	2.9	345
	min, 32 MPa					

Spark plasma sintering (SPS) is an advanced technique where in pulsed direct electric current is applied to the graphite dies containing powder along with uniaxial pressure [81,87,88]. This results in increased densification in lesser holding times at required sintering temperatures. As SPS involves use of current and pressure, it is possible to achieve heating rates of up to ~1000 °C/min in short durations resulting in highly dense samples [87,88]. The sintering density depends on various factors including sintering time, temperature and particle size of raw powders. For ZrB<sub>2</sub>, small particles size of ≤ 25 nm achieved a theoretical density of ~98% below 1700 °C within 16 min or lesser whereas, particle size of 70 nm resulted in maximum densification of ~95% at 1850 °C in 30 min [89]. Flash sintering (FS) is another efficient technique which uses Joule heating and samples can be sintered even faster than SPS. In this process, the current is passed directly through the sample when AC or DC voltage is applied resulting in sample densification within few seconds [90–92]. Although the sintering time in FS is very little, a large timespan is required for preheating. Additionally, it needs costly electrodes and can densify only small samples of less than 100 mm<sup>3</sup> [81]. There are other sintering techniques such as flash spark plasma sintering (FSPS), microwave sintering and laser sintering which can also be used [81].

## 2.2.2 Oxidation mechanism of ZrB<sub>2</sub>-SiC ceramics

Exposure of UHTCs to high temperatures in the air results in the formation of two-phase oxide scales over their surface. A dense and adherent scale of metal oxide (MO<sub>2</sub>) such as ZrO<sub>2</sub> on ZrB<sub>2</sub> and HfO<sub>2</sub> on HfB<sub>2</sub> forms[93]. In addition to that liquid boria (B<sub>2</sub>O<sub>3</sub>) also forms according to the reaction in Equation 2.9 [79,94]. The phases are distributed in scale depending on the temperature. The

zirconia scale is porous in nature and remains present at all temperatures. At lower temperatures of less than 1100 °C, a continuous layer of glassy  $B_2O_3$  stays at the top of  $ZrO_2 + B_2O_3$  scale and also fills the pores in zirconia present underneath as shown in Figure 2.8 [94]. This prevents oxygen diffusion towards the substrate and passive oxidation of diboride resulting in parabolic kinetics. The oxygen diffusion through  $B_2O_3$  controls the oxidation rate [95–98]. The activation energy for oxygen diffusion in  $B_2O_3$  lies in the range of 80-120 kJ/mole [95,99].

$$ZrB_{2}(cr) + \frac{5}{2}O_{2}(g) \rightarrow ZrO_{2}(cr) + B_{2}O_{3}(l)$$

### Equation 2.9

The B<sub>2</sub>O<sub>3</sub> layer protects the underneath oxides and substrate well from further oxidation only up to ~1100 °C. Oxidation kinetics changes to para-linear showing increased oxidation between ~1100 and ~1400 °C because in this temperature regime, overall mass change is the result of formation of large amount of ZrO<sub>2</sub> resulting in mass gain as well as due to evaporation of B<sub>2</sub>O<sub>3</sub> resulting in mass loss [97,100]. The increased formation rate and mass loss due to volatilization of B<sub>2</sub>O<sub>3</sub> is responsible for the change in kinetics. At 1500 °C, the equilibrium partial pressure for evaporation of B<sub>2</sub>O<sub>3</sub> was reported to be 1.8 x 10-11 Pa and its evaporation rate increases [101]. Evaporation loss of B<sub>2</sub>O<sub>3</sub> is more as compared to its formation and its complete volatilization occurs as the temperature approaches 1800 °C that leaves a porous zirconia skeleton. Linear oxidation kinetics is observed since the amount of formation of ZrO2 is more than the mass of ZrB<sub>2</sub> consumed [102,103] and the faster mass loss of B<sub>2</sub>O<sub>3</sub> due to its evaporation. Thermodynamic models and volatility diagrams support this theory of B<sub>2</sub>O<sub>3</sub> volatilization and change in kinetics [94] as discussed in section 2.3.2.

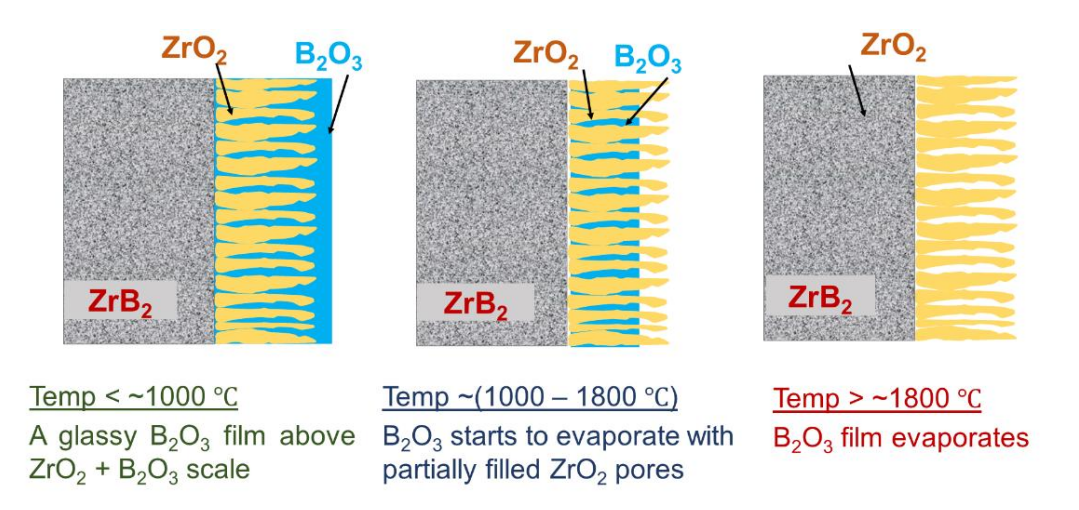


Figure 2.8 Oxide scale composition for oxidation of ZrB<sub>2</sub> at different temperatures.

To improve oxidation resistance above 1100 °C, silicon carbide is added to diborides to facilitate the formation of protective SiO<sub>2</sub> scale at the top. SiC reacts with oxygen to form a glassy SiO<sub>2</sub> film at the top of ZrO<sub>2</sub> (or HfO<sub>2</sub>) scale which remains protective up to 1500 °C (Equation 2.10 [101]) as it has low oxygen diffusivities at moderate temperatures [75,77,104]. SiO<sub>2</sub> has lower volatility at higher temperatures which leads to more stability of silica rich scale than B<sub>2</sub>O<sub>3</sub>. The formation of SiO<sub>2</sub> layer also prevents evaporation of gaseous B<sub>2</sub>O<sub>3</sub> present in pores. But at temperatures above 1600 °C active oxidation of SiC occurs after reacting with SiO<sub>2</sub> to form SiO (Equation 2.11) [75,77,104]. Many researchers [103,105-108] have noticed a SiC depleted zone beneath silica rich scale. The cross-section microstructures and EDS maps of 70ZrB<sub>2</sub>-30SiC UHTC oxidized at 1600 °C for 5 h is presented in Figure 2.9 from the work by Ouyang et al. [108]. A thickness of  $50 \pm 5 \mu m$  was reported for top SiO<sub>2</sub> scale and 160  $\mu m$  for total oxide layer [108]. The formation of SiC depleted zone can be justified using volatility diagram for SiC as explained in the later section 2.3.2 [101].

$$SiC\left(cr\right)+\frac{3}{2}O_{2}\left(g\right)\rightarrow SiO_{2}\left(l\right)+CO\left(g\right)$$

Equation 2.10

$$SiC(cr) + 2SiO_2(l) \rightarrow 3SiO(g) + CO(g)$$

Equation 2.11

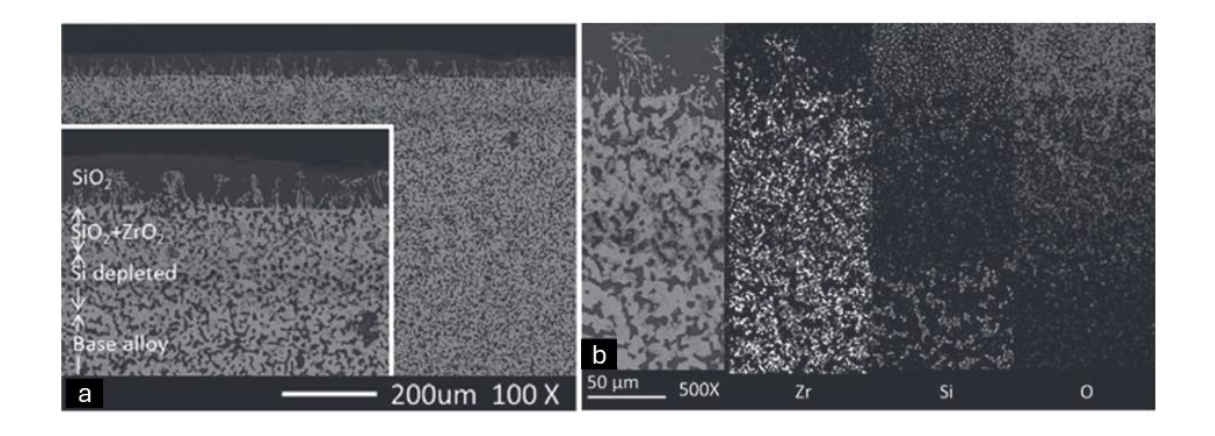


Figure 2.9. (a) Cross-section of ZrB<sub>2</sub>-SiC oxidized at 1600 °C for 5 h (b) EDS mapping of elements

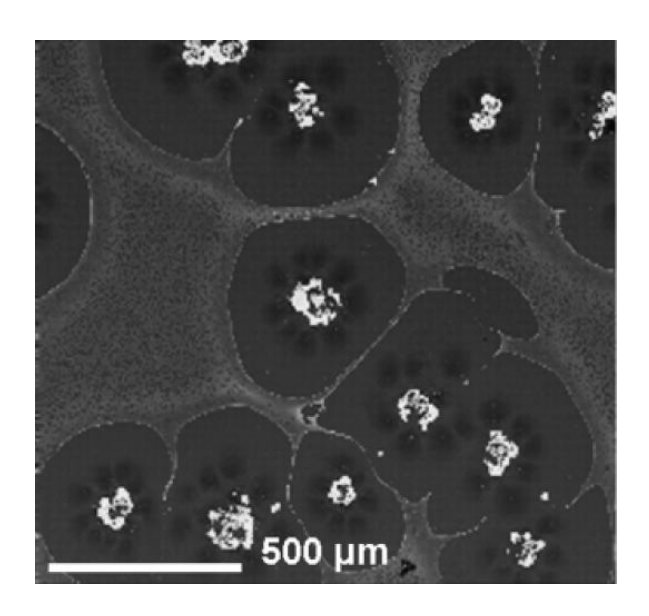


Figure 2.10 Convection cells formation on ZrB<sub>2</sub>-SiC UHTC [109]

Fahrenholtz [101] explained that when ZrB<sub>2</sub>-SiC is heated to higher temperatures, a sequence of reactions occurs with change in temperature. Around 1200 °C, ZrB<sub>2</sub> starts oxidizing resulting in formation of ZrO<sub>2</sub> and B<sub>2</sub>O<sub>3</sub> (l) layer where SiC particles remain present in unoxidized condition. As the temperature increases and approaches 1500 °C, protective B<sub>2</sub>O<sub>3</sub> scale starts evaporating due to its higher vapor pressure leading to ZrO<sub>2</sub> exposure which is a non-protective oxide. Significant oxidation of SiC particles occurs which form protective SiO<sub>2</sub>-rich scale with some B<sub>2</sub>O<sub>3</sub> as it does not evaporate completely. The continuous scale formation at this temperature shows parabolic mass gain kinetics. The scale at this stage is double layered consisting ZrO<sub>2</sub>+SiO<sub>2</sub> layer with SiO<sub>2</sub>-rich (l) layer at the top. It was suggested that the parabolic mass gain occurs due to oxygen diffusion through the oxide layer

that reacts with the underlying substrate to form more SiO<sub>2</sub>. When oxide layer grows, there are two possibilities, first, oxygen diffuses through the oxide layer and reacts with the substrate and second, ZrO<sub>2</sub> or SiO<sub>2</sub> reacts with underlying SiC. In the second case, a non-protective scale with linear mass gain or mass loss kinetics forms and at 1500 °C, these kinds of reactions have positive Gibb's free energies making them unfavorable. However, the local oxide structure does not allow the oxidation products to move out rapidly, therefore, the forward reaction as per the Equation 2.11 may take place resulting in non-protective oxide behaviour.

The presence of B<sub>2</sub>O<sub>3</sub> helps in reducing viscosity of SiO<sub>2</sub> scale that allows it to flow to the pores of ZrO<sub>2</sub> scale [25]. This fills the pores and reduces oxygen diffusion through them resulting in increased oxidation resistance. However, as mentioned earlier, B<sub>2</sub>O<sub>3</sub> evaporates after 1100 °C [94,102]. Some researchers [110,111] have reported the presence of retained B<sub>2</sub>O<sub>3</sub> in oxide scale at 1500 °C and its concentration decreases rapidly with increase in exposure time. Its vapor pressure increases from 200 Pa at 1500 °C to 1000 Pa at 1600 °C resulting in faster volatilization. This rapid increase in volatilization rate reduces the effectiveness of the borosilicate scale. Karlsdottir and Halloran [112] noticed complete absence of boron in oxide scale of ZrB<sub>2</sub>-SiC samples oxidized above 1600 °C. At 1550 °C, authors [109,113] reported the formation of convection patterns on the scale surface with very small amount of B<sub>2</sub>O<sub>3</sub>. It was proposed that when oxygen diffuses through oxide scale and oxidation occurs at substrate-scale interface, borosilicate oxide liquid forms. This mixture also dissolves some ZrO<sub>2</sub> in it. Formation of this fresh oxide leads to a large change in oxide volume at the interface which results in upward flow of this liquid. As this fresh liquid reaches the surface it starts to move in lateral direction due to huge difference in viscosity of SiO<sub>2</sub> which was already present and the fresh  $B_2O_3 + SiO_2$  mixture. The viscosity of  $SiO_2$  at this temperature was reported to be around 100 GPa.s whereas that of B<sub>2</sub>O<sub>3</sub> is only 40 Pa.s [109,114]. Viscosity of fresh liquid depends on the mole fraction of B<sub>2</sub>O<sub>3</sub> which is around 1000 Pa.s [109,114]. This fresh oxide displaces more viscous SiO<sub>2</sub> which is known as viscous fingering. At the surface, the vapor pressure of B<sub>2</sub>O<sub>3</sub> (233 Pa) is comparatively high that SiO<sub>2</sub> (3x10<sup>-4</sup> Pa) resulting in its easy volatilization. This leads to the formation of petal-like structures rich in B<sub>2</sub>O<sub>3</sub> surrounded by SiO<sub>2</sub> lagoons as shown in Figure 2.10. Fresh liquid oxide contains solid zirconia particles which are carried away by the moving liquid and are decorated around the convection cells [115]. Here, evaporation of B<sub>2</sub>O<sub>3</sub> and change in scale viscosity is clearly visible, therefore, it becomes important to understand the oxidation mechanism and to explore the effect of other additives on scale chemistry and overall oxidation behaviour.

### 2.2.3 Effect of additives on oxidation resistance

The addition of additives to UHTCs affects their microstructure and the oxide scale properties. For example, AlN addition improves densification and controls grain growth in ZrB<sub>2</sub>-SiC composites [116,117]. Ouyang et al. [118] studied its effect on isothermal oxidation properties of ZrB<sub>2</sub>-30SiC (vol%) UHTCs with 5, 10 and 15 vol% AlN in the temperature range of 1400-1600 °C. During oxidation, Al<sub>2</sub>O<sub>3</sub> was formed in the SiO<sub>2</sub>-rich oxide scale and reduced scale viscosity. It was reported addition in optimum amount which was 10 vol%, enhanced oxidation resistance while increasing AlN to 15 vol% decreased oxidation resistance. Excessive amount of ZrO<sub>2</sub> was observed in outer SiO<sub>2</sub>-rich oxide scale which moved there due to lower scale viscosity which aided in easy ZrO<sub>2</sub> mobility [108,118]. The flow and spread of scale with lower viscosity is high, but, at the same time oxygen diffusion increases through it resulting in poor oxidation properties.

Researchers have studied Ta addition in different forms such as TaC [119], Ta<sub>5</sub>Si<sub>3</sub> [120], TaB<sub>2</sub> [121] and TaSi<sub>2</sub> [120–122]. Improvement in oxidation properties at 1100-1400 °C was observed on adding Ta<sub>5</sub>Si<sub>3</sub> with the oxide layer thickness of 115  $\mu$ m for 15 vol% addition and 300  $\mu$ m for pure ZrB<sub>2</sub> in 2 h [120]. Improved oxidation resistance was attributed to the immiscibility produced in borosilica glass due to the presence of Ta-O units. This results in increased scale viscosity and reduced oxygen diffusion through the scale. Above 1300 °C, a

discontinuous SiO<sub>2</sub>-rich scale appeared on ZrB<sub>2</sub>-Ta<sub>5</sub>Si<sub>3</sub> samples resulting in poor oxidation properties as compared to ZrB<sub>2</sub>-SiC samples [120]. The discontinuous scale could be due to increased viscosity leading to reduced scale spread and poor surface coverage. Similar results were reported for TaSi<sub>2</sub> addition [120]. Opila et al. [122] observed improved oxidation resistance with addition of 20 vol% TaSi<sub>2</sub> to ZrB<sub>2</sub>-SiC at 1627 °C and degradation at 1927 °C. On the other hand, it was found that TaC addition is not effective for improving oxidation properties [122]. Poor oxidation at 1927 °C was due to formation of liquid phase resulting from melting of Ta<sub>2</sub>O<sub>5</sub> or Ta<sub>2</sub>O<sub>5</sub>.6ZrO<sub>2</sub>. Wang et al. [119] reported reduced oxidation resistance with 10 vol % TaC addition and improvement with 30 vol% TaC addition to ZrB<sub>2</sub>-20SiC (vol%) composite. ZrSiO<sub>4</sub> peaks were found in samples with 30 vol% TaC and it was suggested that ZrSiO<sub>4</sub> improves thermal stability of silica-rich scale providing good oxidation resistance [119]. Zhang et al. [123] reported improved oxidation resistance of ZrB<sub>2</sub> on adding WC at 1500 °C and 1600 °C. Sengupta and Manna [124] recently studied the effect of WC and TiC and reported improvement in oxidation resistance of ZrB<sub>2</sub>-SiC composites due to formation of dense ZrO<sub>2</sub> layer and increased viscosity of outermost SiO<sub>2</sub>-rich scale.

## 2.3 Computational modeling of oxidation

## 2.3.1 Modeling diffusion in the oxide scale

There are many materials modelling approaches that are based on quantum mechanical methods such as density functional theory (DFT) and approaches based on semi-empirical analytical interatomic potentials. Figure 2.11 [125] shows the key simulation approaches with length and time scales. DFT calculations are based on electronic structure methods that provide force and energy calculations with high accuracy [126,127]. These can be employed for a wide range of materials including single and multicomponent systems. Inspite of their high accuracy, these cannot be used for large systems with more than a few hundred atoms as they demand high computational power [126]. Instead of DFT, the use of classical molecular dynamics can accelerate the development

of materials as it can capture interatomic interactions in a simpler manner and can easily be used for larger length and time scales. However, it may also require high computational power depending on the system size and the type of potential that is being used.

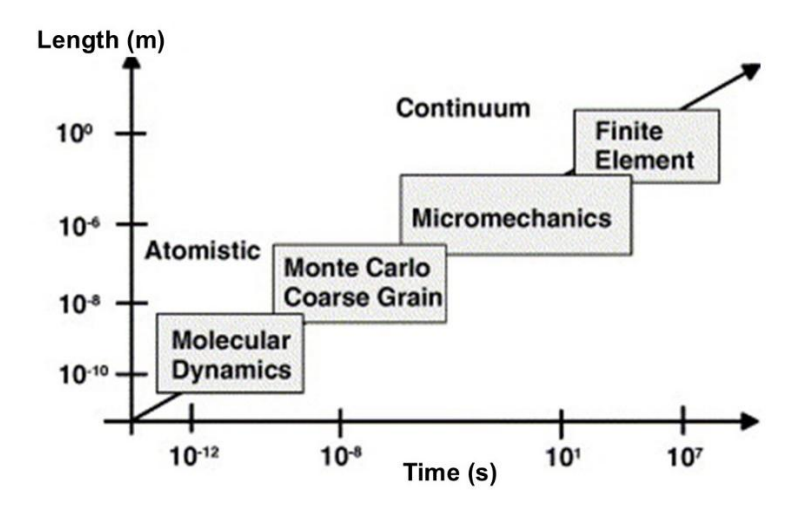


Figure 2.11. Length and time scales of various simulations approaches [125]

Diffusion is an important parameter to understand the microstructural changes that materials encounter during processing and in operating conditions. Diffusion can be studied using both experimental and computational techniques. Some common processes which are related to diffusion include nucleation and growth of phases, recrystallization, thermal creep, thermal oxidation etc. [128]. Mo-Si-B systems and ZrB2 with SiC addition form a protective SiO<sub>2</sub>-rich scale through which diffusion of species can occur. Diffusion can be modelled using computational techniques such as Molecular Dynamics to cut down the number of experiments. As discussed in earlier sections, UHTCs undergo oxidation and form different oxidation products depending on environmental and temperature conditions. Diffusion of one or more species occurs in such conditions. The diffusion coefficient is a key parameter that influences material behaviour in diffusion-related processes. It has a significant effect on microstructural changes in metals and its proper analysis promotes improvement in material properties and their development. However, it is not available for all metal systems and in different temperature conditions. There are several experimental methods used to determine the

diffusion coefficient values for self-diffusion and impurity diffusion in metals. In many metastable metallic systems, it is difficult to obtain the value of diffusivity experimentally because it is difficult to synthesize metastable alloys. In addition, the experimental methods to find out diffusivity involve high cost [129]. Another method to calculate diffusion coefficients is use of first-principles calculations, but these calculations are time consuming and are often difficult to converge.

Predictive materials modelling using atomistic simulations is revolutionizing diverse fields of materials including tribology, nano-particles self-assembly, catalysis and sensing. Atomistic simulations use interatomic potentials such as pair potentials, Embedded-atom model (EAM) potentials, bond-order potentials and reactive force potentials [126]. Table 2.3 shows the various forms of interatomic potential.

Table 2.3. Mathematical forms of different interatomic potentials [130]

Interatomic Potential	Mathematical Form
Lennard-Jones	$\emptyset(r) = \frac{B}{r^{12}} - \frac{A}{r^6}$
	r- interatomic separation; A, B- constants that depend on
	interacting species
Born-Mayer	$\emptyset(r) = Ae^{-\alpha r} - \frac{C}{r^6}$
	A, C, $\alpha$ are constants that depend on interacting species
EAM	$U = \sum_{i} F_{i} \left[ \sum_{j \neq i} f_{ij}(r_{ij}) \right] + \frac{1}{2} \sum_{i=1}^{N} \sum_{j=1}^{N} \emptyset_{ij}(r_{ij})$
	f- function of interatomic distance; Ø- pair potential

Bond-order	$E_{i} = \frac{1}{2} \sum_{j=1}^{Z_{i}} [qV_{R}(r) + bV_{A}(r)]$		
	q- parameter that depends on local electron density; b- bond order; $V_R$ and $V_A$ are repulsive and attractive terms respectively; Z- no. of nearest neighbors		
Reactive force (COMB and ReaxFF)	$E = \frac{1}{2} \sum_{i} \sum_{j=1}^{Z_i} [V_R(r_{ij}, q_i, q_j) + b^{eff} V_A(r_{ij}, q_i, q_j)]$		
	q- charge on each atom; beff- sum of bond-order terms		

Interatomic potentials are mathematical formulations that deal with two-body, three-body and many body interaction energy terms or use bond-order concepts. Lennard-Jones (LJ) potential [131] is a pair potential consisting of long-range interaction term as -A/r<sup>6</sup> that captures attraction and a short-range repulsive term of the form  $B/r^{12}$ . This potential lacks accuracy as it depends only on two terms [130]. Born-Mayer potential has an exponential repulsive term which makes it more accurate than LJ potential. The attractive term which shows long-range interaction is the van der Waals term. This potential is generally used for ionic systems as it involves electrostatic interactions between ions [130]. Stillinger-Weber [132] (SW) potential for covalent bonded systems and Vashishta [133] potentials use two-body or three body interaction terms. Finnis-Sinclair [134] (FW), embedded-atom method [135] (EAM), and modified embedded-atom method [136] (MEAM) potentials for metallic systems are based on many body interactions treated as a function of atomic density. Interatomic potentials such as Abell [137], Tersoff [138,139] and reactive empirical bond order potential [140] (REBO) are based on the concept of bondorder. The bond order potential was developed for covalently bonded systems under the assumption that the system's total binding energy may be represented as a sum over its individual bonds [141]. Although these potentials

are widely used, they have some limitations. They do not allow charge transfer and emphasize on equilibrium configurations too much that may lead to errors in predicting energies for non-equilibrium systems [126]. Recently developed ReaxFF potentials and charged optimized many body potentials (COMB) have gained popularity. These potentials integrate the concepts of bond-order with charge equalization schemes.

For a few decades, MD simulations have been used to study diffusion in materials. A few examples include studying the effect of grain boundaries for self-diffusion of metal [142], oxygen self-diffusion in metal oxides [143] which are used as electrolytes in fuel cells, hydrogen diffusion in metals [144] etc. The first MD simulation study for silica was carried out by Woodcock et al. [145] in 1976 where they used a two-body potential model that involved Coulombic and Born-Mayer short-range interaction terms. After that several authors [146– 150] used various two-body potential models for MD simulations of silica glass and some [145,148,149] observed discrepancy in O-Si-O bond angle results when compared with the experimental data. It was suggested that lower degree of short-range order may result in inaccurate results [151]. In the late 80s, threebody interaction terms were introduced by Feuston et al. [152] and Vessal et al. [153] to get better bond angle distribution of O-Si-O bonds. Tsuneyuki et al. [154] developed interatomic potential for SiO<sub>2</sub> which employed two-body interaction terms fitted to ab initio calculations on SiO<sub>4</sub> clusters. This model also considered many-body interactions. Using this potential, Della Valle et al. [151] calculated heat capacity, glass transition temperature and self-diffusion coefficients for liquid silica and silica glass. They found heat capacity and glass transition temperature values in agreement with the experimental values. But there was a discrepancy in self-diffusion coefficients of Si and O atoms. It was suggested that viscosity and diffusivity should have the same temperature dependence, and the viscosity is very sensitive to volume changes. The simulations were carried out at constant volume and their results were compared to the experimental results which were carried out at constant pressure. This comparison may result in discrepancy in simulation or

experimental values. Another reason could be improper capturing of interatomic interactions by the selected potential model [151]. It is important to select the suitable potential for an effective study of materials using molecular dynamics.

Guillot and Sator [155] used MD to evaluate diffusivities in various silica glasses in the temperature range of 1473-2273 K. They developed Buckingham potential to calculate self-diffusion coefficients of species present in silica glasses using Einsteins equation [156] given by the following relation.

$$D_{s} = \lim_{t \to \infty} \frac{1}{N} \sum_{i=1}^{N} \frac{\langle \left(\vec{r}_{i}(t) - \vec{r}_{i}(0)\right)^{2} \rangle}{6t}$$

Where N is no. of ions of any specie and  $r_i$  is the position of i<sup>th</sup> ion which on averaging over time gives the mean square displacement. They found similar trends as experimental values with one to few orders of magnitude difference in the values depending on the composition and temperature. In some works self-diffusion of ions was modelled in oxides such as  $CrO_3$  and  $Al_2O_3$  using Molecular Dynamics [157,158]. Cao et al [157] investigated the diffusion pathways for vacancy and interstitial mediated ion diffusion using Buckingham potential and found their results in agreement with experiments. Roy et al. [158] modelled tracer diffusion through  $Al_2O_3$  and  $Cr_2O_3$  oxides to study the effect of impurity additions to these oxides. This model helped in estimation of diffusion kinetics of individual species which indicated their influence on oxide growth. Such models can provide useful insights on scale growth kinetics and can help with better alloy design. Similar approaches can be used for modelling diffusion in oxides that are formed during oxidation of borosilica forming materials.

### 2.3.2 Thermodynamics and volatility diagrams

The thermodynamic driving force for any reaction to occur which is Gibb's free energy change can be plotted as a function of temperature. These graphical representations known as Ellingham diagrams can provide relative thermodynamic stabilities of the elements/compounds [159]. These plots are commonly used for determining stability in oxidation and sulfidation reactions in metals. As this work involves the formation of multiple oxides at high temperatures, Ellingham diagrams can be beneficial in determining their stability at different temperatures.

Volatility diagrams are graphical representations showing volatility of gaseous species plotted in terms of vapor pressure as a function of  $p_{o_2}$ . Opeka et al. [77] studied stability of oxides such as SiO<sub>2</sub>, ZrO<sub>2</sub> and B<sub>2</sub>O<sub>3</sub> that are formed on UHTCs using volatility diagrams. Later on, volatility diagram of ZrB<sub>2</sub> [102] and ZrB<sub>2</sub>-SiC [101] systems were developed and used to study stability of different phases. During oxidation of ZrB<sub>2</sub>-SiC, Zr-rich oxide layer, a passive Si-rich oxide layer and a SiC depleted zone underneath is formed due to its active oxidation. Fahrenholtz [101] developed a thermodynamic model to explain the stability of these layers using volatility diagrams at 1500 °C. Pure ZrB<sub>2</sub> forms ZrO<sub>2</sub> and B<sub>2</sub>O<sub>3</sub> while ZrB<sub>2</sub>-SiC forms ZrO<sub>2</sub>, B<sub>2</sub>O<sub>3</sub> and SiO<sub>2</sub>. Volatility diagram of pure ZrB<sub>2</sub> as shown in Figure 2.12 a shows stability of different oxides at 727°C (1000 K), 1527 °C (1800 K) and 2227 °C (2500 K). The construction of the volatility diagrams was based on the calculations of equilibrium partial pressure of oxygen for possible oxidation reactions [102]. The vapor pressure for predominant species (BO<sub>2</sub>) at 727 °C (1000 K) was predicted to be 10-6 Pa consistent with the experimental results showing B<sub>2</sub>O<sub>3</sub> (l) layer on the surface for ZrB<sub>2</sub> to ZrO<sub>2</sub> and B<sub>2</sub>O<sub>3</sub> (l) transformation. On increasing temperature to 1527 °C (1800 K), B<sub>2</sub>O<sub>3</sub> was the predominant species with increased vapor pressure of 344 Pa resulting in its volatilization and active oxidation. Volatility diagram in Figure 2.12 b shows formation of ZrO<sub>2</sub> and liquid B<sub>2</sub>O<sub>3</sub> when in air at 1500 °C, with a partial pressure for B<sub>2</sub>O<sub>3</sub> (g) evaporation as 209 Pa. Here, B<sub>2</sub>O<sub>3</sub> (g) is the predominant vapor species that leaves ZrO<sub>2</sub> (cr). This shows consistency with the experimental data of ZrB<sub>2</sub> oxidation at 1500 °C that indicates rapid linear oxidation kinetics [95–97,99,160]. The absence of protective B<sub>2</sub>O<sub>3</sub> layer leads to easy diffusion of oxygen and faster oxidation. Figure 2.14 shows the weight change in ZrB<sub>2</sub> and ZrB<sub>2</sub>-SiC UHTCs.

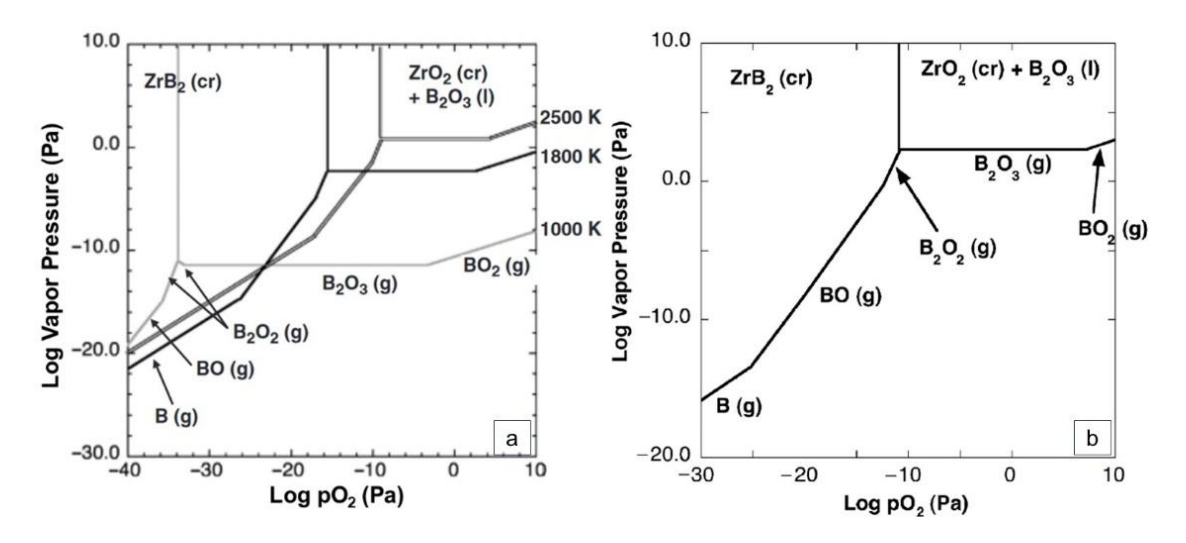


Figure 2.12 Volatility diagram of  $ZrB_2$  at (a) 1000, 1800 and 2500 K [102] (b) 1773K (1500 °C) [101]

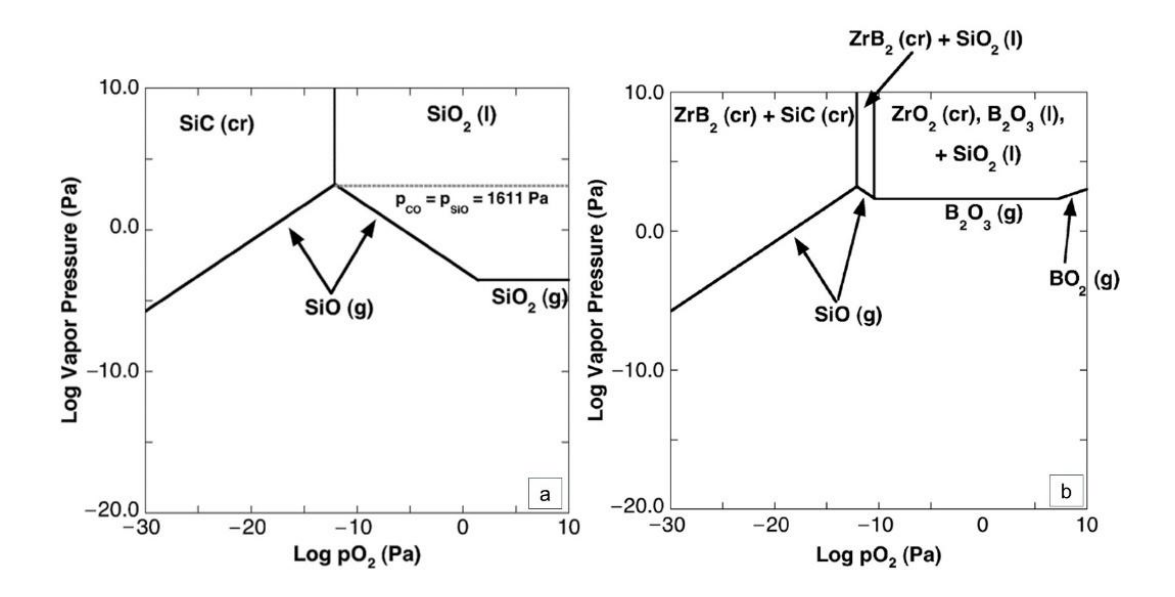


Figure 2.13 Volatility diagram of (a) SiC and (b) ZrB<sub>2</sub>-SiC system at 1500 °C

Volatilitity diagram of SiC as shown in Figure 2.13a indicates the formation of SiO<sub>2</sub> (l) at 1500 °C in air. The predicted equilibrium partial pressure of oxygen for  $\alpha$ -SiC oxidation to SiO<sub>2</sub> is  $10^{-12}$  Pa. The partial pressure of predominant gas species SiO<sub>2</sub> (g) is ~ $10^{-4}$  Pa and that of SiO (g) is even lower which is ~ $10^{-5}$  Pa. These values are lower than the partial pressure for SiC to SiO<sub>2</sub> (l) conversion which is 1611 Pa. It is indication of stable and protective scale formation of SiO<sub>2</sub> (l) [101]. Experimental results on SiC oxidation have shown formation of passive SiO<sub>2</sub> oxide formation at 1500 °C [161,162]. Unlike ZrB<sub>2</sub>, where active oxidation occurs because of volatilization of B<sub>2</sub>O<sub>3</sub> layer, the transition

mechanism of protective  $SiO_2$  layer to active oxidation is different. Above 1600 °C,  $SiO_2$  (l) reacts with underlying SiC forming SiO (g) and CO (g) according to the following reaction:

$$SiC(cr) + 2SiO_2(l) \rightarrow 3SiO(g) + CO(g)$$

#### Equation 2.12

Fahrenholtz [101] combined the volatility diagrams of SiC and ZrB<sub>2</sub> and concluded that SiC oxidizes to SiO<sub>2</sub> at lower oxygen partial pressures (10<sup>-12</sup> Pa) than ZrB<sub>2</sub> (10-11 Pa) to ZrO<sub>2</sub>-B<sub>2</sub>O<sub>3</sub> mixture as shown in Figure 2.13 b. According to the diagram, ZrB<sub>2</sub>-SiC on oxidation at 1500 °C in air would form ZrO<sub>2</sub>, B<sub>2</sub>O<sub>3</sub> and SiO<sub>2</sub>. It was claimed that the resulting stable oxide on ZrB<sub>2</sub>-SiC consists of  $ZrO_2$  (cr) and  $SiO_2$  (l) as the  $B_2O_3$  (l) should evaporate due to its higher vapor presssure than SiO<sub>2</sub> (l) and parabolic kinetics is expected in case of stable oxide scale and the analysis was found to be consistent with the experimental studies conducted on oxidation of ZrB<sub>2</sub>-SiC ceramics [75,100,103,106,107,163–165]. Parabolic kinetics is observed when oxidation occurs due to diffusion of oxygen through oxide scale. If stable SiO<sub>2</sub> oxide forms then oxidation will occur through diffusion resulting in parabolic kinetics. The formation of SiC depleted zone was attributed to the high vapor pressure of SiO (g). The calculated  $p_{0_2}$  in this zone was reported to be in between 4.1 x  $10^{-14}$  to 1.8 x  $10^{-11}$  Pa. Due to its high vapor pressure and  $p_{\mathcal{O}_2}$  gradeint , SiO is transported outwards and the outer scale grows.

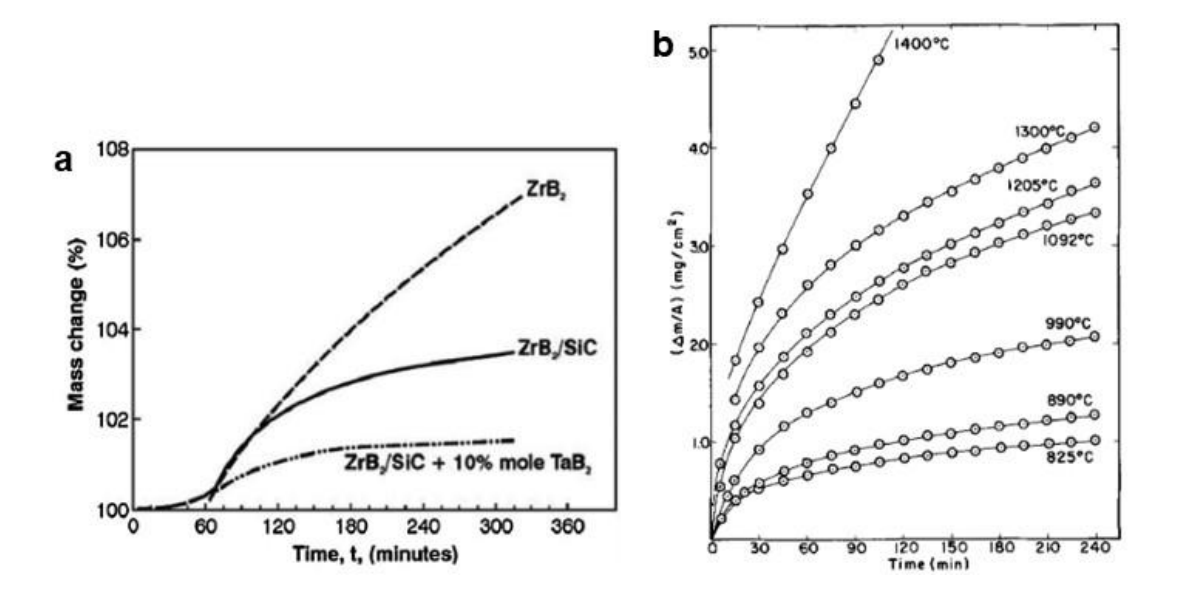


Figure 2.14.. Oxidation of (a)  $ZrB_2$  and  $ZrB_2$ -SiC ceramics at 1500 °C (b)  $ZrB_2$  at different temperatures [81,166,167]. At 1400 °C, linear oxidation kinetics was observed [97].

### 2.3.3 Analytical models for Mo-Si-B and diboride systems

The Mo-Si-B and diboride systems containing SiC form borosilica scale on the surface during their oxidation. To study the effect of substrate composition and microstructure on the oxidation behaviour in transient and steady-state stages of Mo-Si-B alloys, experimental and analytical approaches were used in previous studies [6,16,17]. Rioult et al. [17] modelled oxidation kinetics for Mo-Si-B alloys and calculated mass change with time as shown in Figure 2.15. As these alloys have multiple phases (Mo, A15 and T2), the individual phases were assumed as cylinders. The size of these phases was calculated based on their phase distributions found from the experimental analysis. To model oxidation, these cylinders were assumed to be distributed randomly such that their amount in the original microstructure can be replicated. The oxidation rates of individual phases were obtained from their oxidation in air. These rates were then used to estimate the mass change in the assumed microstructure at 1100 °C [17].

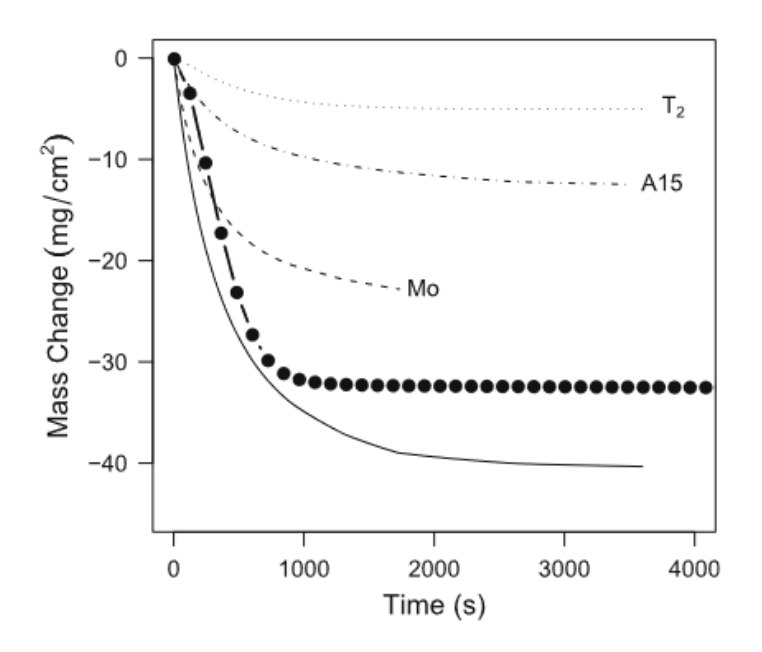


Figure 2.15. Mass change in Mo-14.2Si-9.6B alloy. The solid line shows the curve predicted from the model; round dots show the experimental curves. The contribution of individual phase is shown as marked [17].

Parthasarathy et al. [94,168] developed a mathematical models to predict oxidation kinetics for diboride UHTCs. In one of their models a diboride substrate consisting of UHTC as substrate with a multi-layer oxide was considered [94]. The oxide layer consisted of crystalline ZrO<sub>2</sub> with columnar grains filled with liquid B<sub>2</sub>O<sub>3</sub> and liquid B<sub>2</sub>O<sub>3</sub> film at the top. An equation for parabolic growth of oxide scale for this system was derived. Oxidation reactions at different interfaces were utilized to obtain the diffusion flux of oxygen and B<sub>2</sub>O<sub>3</sub> flux evaporating to the surroundings. The formation and presence of oxide scales depends on the operating temperature. For this work, the authors focused on intermediate temperature range between 1000-1800 °C with oxide on ZrB<sub>2</sub> substrate as crystalline ZrO<sub>2</sub> filled with B<sub>2</sub>O<sub>3</sub> up to a certain thickness. The presence of B<sub>2</sub>O<sub>3</sub> gas and its evaporation was assumed in rest of the thickness of ZrO<sub>2</sub>. The interfaces for oxidation reaction and species diffusion were considered as (i) ZrB<sub>2</sub>-ZrO<sub>2</sub> interface (ii) B<sub>2</sub>O<sub>3</sub>(l) -B<sub>2</sub>O<sub>3</sub>(g) interface and (iii) oxide-atmosphere interface. Authors [94] first considered the oxidation reactions occurring at these interfaces, then calculated diffusion fluxes using thermodynamic database across the interfaces. The equation obtained for oxide thickness is:

$$L^{2} = 2 \left[ \frac{2}{5} \left( \frac{M_{ZrO_{2}}}{\rho_{ZrO_{2}}} \right) \left( \frac{f}{1 - f} \right) D_{O_{2}} \left( \frac{C_{O_{2}}^{a} - C_{O_{2}}^{i}}{(1 - (h/L))} \right) \right] t$$

Equation 2.13

Here, L is oxide scale thickness, M is molar volume,  $\rho$  is density, D is diffusivity, f is scale fraction which is porous and h is thickness to which B<sub>2</sub>O<sub>3</sub> is filled. The effective diffusivity for oxygen diffusion was calculated using using Knudsen diffusivity and the gas diffusivity. The Kundsen diffusivity is the diffusion though the narrow pores between the ZrO<sub>2</sub> columns and is taken into account when the system scale size is smaller than the mean free path of the particles. The Knudsen effect was determined by the pore radius and was assumed to be 0.5 µm. Later, Parthasarthy et al. [168] developed a model for SiC contanind diborides for temperature range of 1200-2000°C to predict weight gain and oxide scale thickness. This model was more complex where SiC was present as an additional component in the ZrB2 or HfB2 substrate. The oxide layer was composed of columns of ZrO<sub>2</sub> (or HfO<sub>2</sub> for HfB<sub>2</sub> substrate) partially filled with SiO<sub>2</sub> and B<sub>2</sub>O<sub>3</sub> mixture. An approach similar to their previous model [94] was used with an additional modelling of SiC depletion. It was mentioned that the predicted results for weight gain, oxide scale thickness, scale ressession, and SiC layer depletion thickness agreed with the experimental results carried out using furnace. The weight gain and oxide scale thickness predicted from the model were compared with experimental results as shown in Figure 2.16 [168]. However, there was a disagreement with the experimental values obtained using arc-jet testing [168]. One possible reason for this could be that their model did not consider the effect of high velocity, high enthalpy and erosion that is encountered during arc-jet testing and in actual operating conditions.

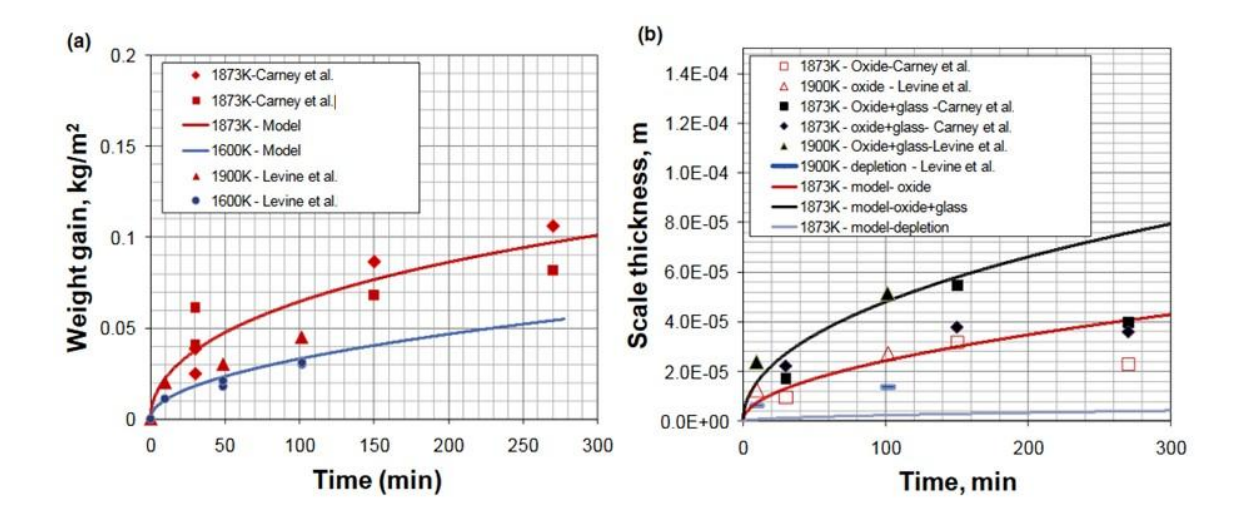


Figure 2.16. (a) Weight gain (b) scale thickness in ZrB<sub>2</sub>-20 vol% SiC. The solid lines represent values predicted by Parthasarathy's model [168] compared by experimental results from different works [169,170].

# 2.4 Problem definition and approach

#### 2.4.1 Key research gaps and problem formulation

Mo-Si-B alloys and UHTCs are potential candidates for high-temperature applications because of protective silica scale formation during their oxidation. The oxidation resistance of silica scale is affected by many factors such as elemental additions and operating temperature. To understand this protective effect, we need to know how the scale behaves at different temperatures as well as the effect of material composition on the formation of the scale. Since oxidation kinetics is strongly related to diffusion through the scale, it is important to measure or calculate the diffusivity values. But this is challenging, because the experimental measurement of accurate diffusivity values is difficult, and the use of different experimental techniques results in huge variation in the values. This becomes even more crucial for complex systems. The diffusivity and viscosity data to understand the oxidation in silica glasses at temperatures above 1200 °C is not available in the existing literature.

Elemental addition to the oxide scale significantly affects the scale properties and oxidation resistance of the system. In earlier works [16,55], W addition to Mo-Si and Mo-Si-B systems destabilized the detrimental A15 phase, therefore it becomes important to explore its effect om various compositions. Since, W is

a refractory metal, the effect of addition of other refractory metals such as Ta (melting temperature  $\sim 3017$  °C) to the system should also be studied. It was reported Ta which forms Ta<sub>2</sub>O<sub>5</sub> during oxidation improved oxidation behaviour of Si based hard coatings [171]. Al addition is known to reduce SiO<sub>2</sub> scale viscosity which is important parameter that affects the protective nature of oxide scale [172]. It also reduces MoO<sub>3</sub> pesting during oxidation [173]. Additionally, most of the research on Mo-Si-B alloys was done using experimental techniques and a small amount of work was done to predict oxidation kinetics computationally. The available mathematical model for predicting oxidation kinetics for these alloys does not consider the effect of microstructural changes and oxide evolution with time.

ZrB<sub>2</sub> has a melting point of ~3100 °C and it shows good oxidation resistance at elevated temperatures [81]. ZrB<sub>2</sub>-20 vol% SiC ceramic has thermal conductivity (Wm- $^{1}$ K- $^{1}$ ) of 89.53 at room temperature and 74.79 at 1000 °C and coefficient of thermal expansion of 6.74 x 10- $^{6}$ /°C at 200-1000 °C [174]. In ZrB<sub>2</sub> based UHTCs containing SiC, which also form protective silica rich scale (or borosilica scale), the effect of Ta addition to in the form of TaSi<sub>2</sub> and Ta<sub>5</sub>Si<sub>3</sub> on oxidation properties was investigated earlier [120]. It improved the oxidation properties below 1400 °C. AlN addition to ZrB<sub>2</sub>-SiC in limited quantities improved the oxidation resistance [108,118] of UHTCs at 1600 °C. The effect of these third particles when added all together, on oxidation behaviour of ZrB<sub>2</sub>-SiC system has not been investigated. Another oxide CeO<sub>2</sub> which is known to change the structural properties of SiO<sub>2</sub> may change the oxidation behaviour of the system. Its effect has also not been explored yet.

The key problem for this work is to explore the effect of scale chemistry on oxidation behaviour and tune the composition of oxide scales by changing the base material composition.

# 2.4.2 Conceptual approach and structure of thesis

Firstly, to address the key literature gaps discussed above, we have used different approaches. To understand diffusion through this scale, we have used

MD and calculated diffusivities for silica glasses in the temperature range of 1200-1700 °C. Secondly, to study the effect of elemental addition on Mo-Si-B alloys, W, Ta and Al containing alloys were fabricated and oxidized at 1100 and 1350 °C. Additionally, a model was developed to predict oxidation kinetics which considers the effect of microstructural changes and oxide scale evolution with time. Finally, ZrB<sub>2</sub>-SiC UHTCs with AlN, TaC and CeO<sub>2</sub> additions with various compositions were fabricated and oxidized at 1600 °C.

#### The outline of the thesis is as follows:

Chapter 1 provides introduction to high temperature materials for modern technologies such as energy and power generation systems and hypersonic applications along with the challenges associated with these materials. It discusses the existing work done using experimental and computational techniques for investigating oxidation behaviour of borosilica forming materials that include refractory metal silicides and UHTCs.

Chapter 2 presents the computational framework for modelling diffusion in silica scale, structural analysis of the simulation cell generated for the studies and viscosity and self-diffusion measurements in silica at required temperatures.

Chapter 3 presents a mathematical modelling framework to simulate the growth of oxide scale over Mo-Si-B alloys considering the actual microstructure of the alloy. It models and visualizes the oxide growth during a transient oxidation stage. The model can help in tailoring the alloy chemistry and optimize the oxidation resistance. Experimental studies to validate the model were conducted as mentioned in the next chapter.

Chapter 4 provides experimental details on transient and long-term oxidation behaviour of Mo silicides. Temporal evolution of oxide at different temperatures was characterized using SEM analysis followed by understanding kinetics with long term exposure to high temperatures. The effect of temperature, refractory metal additions, Al addition and Si/B ratio to

these alloys was studied. To observe how protective silica scale affects the oxidation in UHTCs, experimental studies on ZrB<sub>2</sub>-SiC ceramics were carried out and are presented in chapter 5.

Chapter 5 presents experimental results on oxidation kinetics and oxide scale microstructural growth in ZrB<sub>2</sub>-SiC based UHTCs. The oxide scale microstructures were characterized using XRD, SEM and EDS analysis. The chapter provides useful insights on the effect of third particles additions on oxide scale structure and overall oxidation behaviour.

Chapter 6 summarizes the thesis and presents the future scope for the research work done for this thesis.

# Chapter 3 Dynamics of silica scale

#### 3.1 Introduction

Silica forming Ultra-High Temperature Ceramics (UHTCs) are candidate materials for thermal protection systems for hypersonic re-entry. These materials are subject to harsh oxidative conditions, which results in the formation of a silica scale [108,118,168,175,176]. Similarly, a number of refractory metal silicide systems considered as candidates for high temperature applications also form a silica scale upon oxidation [6,16,55,177]. The silica scale forming during the oxidation process is inherently glassy in nature. Thermodynamically, glasses are treated as supercooled liquids and exhibit a range of viscosity as a function of temperature and chemistry. The efficiency of silica in covering the surface through a viscous flow mechanism and providing a hermetic scale is strongly influenced by the oxide scale viscosity, which is intimately connected with the diffusivity of ionic species through the scale [118]. A key challenge, however, is to accurately determine the viscosity of the scales as a function of other cations present within the scale. This becomes especially critical in light of several attempts to modify Mo-Si-B alloys and the traditional ZrB<sub>2</sub>-SiC composites through chemical modifications such as addition of Al<sub>2</sub>O<sub>3</sub>, AlN, BN, HfB<sub>2</sub>, etc. [108,118,122,176,178].

The role of diffusivity and viscosity in the development of the oxide scale can be understood when we consider the oxidation mechanisms of the different components of high temperature materials. For example, Zirconium and Hafnium diborides (ZrB<sub>2</sub> and HfB<sub>2</sub>) have been studied extensively and identified as prominent candidates for use in ultra-high temperatures due to their high oxidation resistance at elevated temperatures, favourable thermal and mechanical properties [179]. Oxidation of these materials leads to formation of multi-layered oxide scales whose top layer is silica rich [122]. Oxygen can easily diffuse through the oxide scale resulting in further oxidation of base material. Oxide-scale features called convection cells are formed from liquid and solid oxide reaction products upon oxidation of the ZrB2-SiC composites. These convection cells form in the outermost borosilicate oxide film of the oxide scale formed on the ZrB<sub>2</sub>-SiC during oxidation at high temperatures (≥1500°C) [180–183]. It is important to study the effect of additives on the properties of protective scale and tune the chemistry for improved stability and oxidation resistance. Ouyang et al. [108,118] studied oxidation of ZrB<sub>2</sub>-SiC composites after addition of AlN since it forms Al<sub>2</sub>O<sub>3</sub> which can stay at elevated temperatures and helps in reducing the viscosity of silica scale. The addition of AlN results in formation of Al<sub>2</sub>O<sub>3</sub> which is known to reduce viscosity of silica melts allowing easy flow of zirconia through the scale [184]. Cheng et al. [185] studied the effect of nine different transition elements oxides on evaporation of SiO<sub>2</sub> glass. It was observed that addition of 8.5 mol % HfO<sub>2</sub> to SiO<sub>2</sub> matrix provided least mass loss of 0.56 ± 0.19 wt.% and reduced SiO<sub>2</sub> evaporation at 1700 °C. SiO<sub>2</sub> samples doped with HfO<sub>2</sub> on oxidation resulted in formation of non-volatile phase that improves SiO<sub>2</sub> stability. They also studied the effect of doping transition metal atom including Hf in cristobalite SiO<sub>2</sub> using first-principles calculations. It is reported that HfO<sub>2</sub> is a trivalent oxide similar to SiO<sub>2</sub> and when added to SiO<sub>2</sub>, Hf atoms can substitute Si atoms [186]. Calculation of solution energies (-10.41 eV for Hf addition [185]) indicated high stability of Hf doped SiO<sub>2</sub>. Its addition was found to result in shorter bond length than pure Si-O bonds and enhanced bond strength that can lead to improved high temperature stability up to 1700 °C [185].

Oxygen diffusivity plays an important role in studying the oxidation behaviour of UHTCs at various temperatures. It is crucial to understand the defect chemistry of the oxides to model various processes as it affects diffusivity and viscosity of the scale. Structural unit of SiO<sub>2</sub> glassy scale consists of tetrahedra where Si and O form strong bonds. If there is any missing atom or other dopant substitutes Si, it results in defect. Oxygen ion that forms bond with other element is known as non-bridging oxygen (NBO) that may diffuse easily [172]. This concept is discussed in section 3.3.2. Diffusion coefficient is a key parameter that influences material behaviour in diffusion-related processes. It is a challenging task to determine the self-diffusivities experimentally for many metals and oxides. In fact, available experimental results for self-diffusion of oxygen in silica glasses show a large scatter in activation energy and preexponential factor values, often arising due to different impurity content for different glasses and use of different experimental techniques for same glasses [172]. Norton [187], Haul & Dumbgen [188] and Williams [189] studied diffusion parameters using rate uptake method in vitreous SiO<sub>2</sub> and there was several orders of magnitude difference in the obtained D<sub>0</sub> values which are 2.8  $\times 10^{-8}$ , 4.3  $\times 10^{-10}$  and 2  $\times 10^{-13}$  respectively. In work by Mikkelson [190] and Cawley & Boyce [191], there was five orders of magnitude difference in D<sub>0</sub> and 174 kJ/mol difference in activation energy values obtained using SIMS technique in vitreous SiO<sub>2</sub>.

According to Stokes-Einstein [192] diffusion coefficient is related to viscosity as:

$$D = \frac{kT}{6\pi rn}$$

Where, D is diffusion coefficient,  $\eta$  is viscosity, r is radius of diffusing particle. Any change in diffusivity is related to modification in viscosity. Elemental addition often seen to modify the impurities, with cation substitutions (while maintaining charge neutrality) often resulting in enhanced diffusivities. As seen in the work done by Roy et al. [158]. Maintaining electrical neutrality, computationally, while adding cations with a different valance necessitates the

formation of additional ionic vacancies, which could be a contributing factor in the observed enhanced diffusivities [158,193]. In case of SiO<sub>2</sub> scale formation on UHTCs, viscosity (and hence, the diffusivity) is an important parameter as any change in viscosity affects the surface coverage and oxidation resistance.

In the present work, we have used Molecular Dynamics (MD) simulations for estimation of diffusivities which govern the kinetics of oxidation processes [194]. Diffusivities and activation energies for self-diffusion of O<sup>2-</sup> and Si<sup>4+</sup> in SiO<sub>2</sub> were investigated. Activation energies dictate the diffusion dynamics. The effect of adding Hf and Al to SiO<sub>2</sub> was also studied as it is expected to improve high temperature stability and oxidation resistance of SiO<sub>2</sub> scale. The self-diffusion of individual species was studied within the oxide scale considering it as bulk because the oxidation which occurs at the oxide-substrate interface is controlled by diffusion through the oxide scale.

## 3.2 Computational methods

# 3.2.1 Generating amorphous silica structure

A silica (SiO<sub>2</sub>) polycrystal with 32,328 atoms was created using Atomsk [195] which is an open-source code for generating datafiles for atomic-scale simulations. The crystalline SiO<sub>2</sub> structure was then converted to an amorphous structure with melt-quench process implemented using Large-scale Atomistic Molecular Massively Parallelized Simulator (LAMMPS) [196]. A time step of 1 fs was fixed for MD simulation. Periodic boundary conditions in all the three directions were employed. The SiO<sub>2</sub> polycrystal was melted at 3000 K (well above the melting point of SiO<sub>2</sub>  $\sim$  1983 K) using NVT ensemble for 250 ps followed by NPT ensemble for 100 ps to ensure complete loss of the initial configuration. The system was then quenched to 300 K at a cooling rate of 1 K/ps to allow formation of glassy structure, followed by relaxation at 300 K for 100 ps using NPT ensemble. Anionic (O<sup>2-</sup>) and cationic (Si<sup>4+</sup>) vacancies, together, corresponding to a vacancy concentration of 0.25% were incorporated in the amorphous structure in such a way that the charge neutrality was

maintained in the simulation cell. Here, the term vacancy represents missing Si or O ion from the structural SiO<sub>2</sub> unit. This initial structure was used for the simulation of vacancy mediated self-diffusion in SiO<sub>2</sub> glass. SiO<sub>2</sub> glasses containing hafnium (Hf) were created by adding Hf<sup>4+</sup> ions to the amorphous SiO<sub>2</sub> structure. X-ray diffraction (XRD) was done using "compute xrd" command in LAMMPS to confirm the amorphous structure of SiO<sub>2</sub> glass. Radial distribution function (RDF) of the amorphous SiO<sub>2</sub> was calculated using "compute rdf" command in LAMMPS to observe the density of pair-wise distances for different atomic pairs.

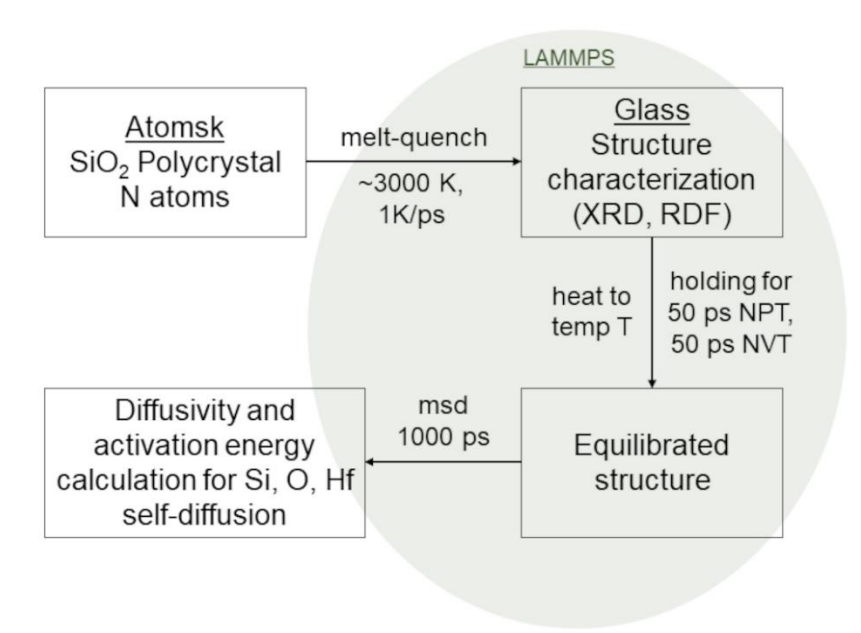


Figure 3.1 Methodology

#### 3.2.2 Interatomic potentials

Self-diffusion in  $SiO_2$  was simulated using three different interatomic potentials previously reported in literature. The first is a Tersoff potential (referred to as "Tersoff" in current paper) developed by Munetoh et al. [197] wherein the potential parametrization was done based on *ab initio* calculations of small molecules and experimental data of  $\alpha$ -quartz. It was validated by the authors [197] for structural properties of various silica polymorphs. Moreover, the RDF and phonon density of states of  $SiO_2$  glass prepared using MD simulations (melt-quench process) were shown to have a good match with the

experimental values. The second is a Buckingham potential (referred to as "BP" in current paper) developed by Guillot and Sator [155] and later modified by Wang et al. for [57] for borosilicate glasses. This potential was shown to satisfactorily predict the glass density, shear viscosity, short-range and medium-range order structure for a wide range of borosilicate glasses and liquids developed using MD simulations. Wang et al. [57] showed that the glass density measured using MD was matching experimental values for SiO<sub>2</sub>\(B<sub>2</sub>O<sub>3</sub>+SiO<sub>2</sub>\) ratio up to 0.7. For higher SiO<sub>2</sub> content and for pure SiO<sub>2</sub> there was a slight discrepancy. The experimental value for pure SiO<sub>2</sub> glass was 2.475 g/cm<sup>3</sup> [58] and 2.375 g/cm<sup>3</sup> [57] using MD. The shear viscosity for various SiO<sub>2</sub>/B<sub>2</sub>O<sub>3</sub> ratios at 1150 °C was calculated using MD. The values were underestimated but the trend was like experimental values [58] with difference around 1 order [57].

Table 3.1 Buckingham potential (BP) parameters used [57]

Bond	Bond A <sub>ij</sub> (eV)		C <sub>ij</sub> (eV.Å <sup>6</sup> )	
O-O	208071.224	0.265	1962.27772	
<b>Si-O</b> 1160089.75		0.161	1067.65535	
Si-Si	<b>Si-Si</b> 0.0		0.0	
Al-O	658113.08	0.172	797.38	

Partial distribution function (PDF) plots from MD simulations were compared with the experimental results for a type of silicate glass [57]. The pattern matched with the experimental results, and it showed the Rx factor value equals to 6.1 %. In general, a value up to 10 %, is considered good [198]. The current work focuses on amorphous silica and thus the relevant parameters of the BP potential used here have been listed in Table 3.1. A cut-off distance of 11 Å was used for both short-range and long-range interactions. The third is a charge-optimized many-body (COMB) potential (referred to as "COMB" in current paper) developed by Shan et al [199,200] for SiO<sub>2</sub>/Hf/HfO<sub>2</sub> systems. It

is based on the extended Tersoff potential for semiconductors and COMB potential for SiO<sub>2</sub>. Shan et al. [199] validated the potential by comparing the structural properties, mechanical properties, defect energies and phase stability obtained from MD simulations with first principles calculations and experimental results.

### 3.2.3 Self-diffusion studies in SiO<sub>2</sub> glasses

The initial structure was first equilibrated using NPT ensemble followed by NVT ensemble for 50 ps at each. The mean squared displacement (MSD) was calculated after 1000 ps runs. The time step for diffusion simulations was fixed as 0.001 ps. Diffusion coefficient (D) can be related to MSD with Einstein's Smoluchowski relation as:

$$D = \lim_{t \to \infty} \frac{1}{N} \sum_{i=1}^{N} \frac{\langle R^2(t) \rangle}{6t}$$

Equation 3.1

Where, R is mean squared displacement and can be written as:

$$\langle R^2(t) \rangle = \langle |\vec{r}_i(t) - \vec{r}_i(0)|^2 \rangle$$

Equation 3.2

Diffusion coefficient was calculated at each temperature in the range of 1200-1700 °C using the plot of MSD versus time. Slope of the curve provides the value of diffusion coefficient. Diffusion coefficient as function of temperature was plotted to calculate the values of activation energy and pre-exponential factor (D<sub>0</sub>) using the Arrhenius relation which is written as:

$$D = D_0 exp\left(-\frac{E_a}{RT}\right)$$

Equation 3.3

Where,  $E_a$  is the activation energy, R is universal gas constant and T is temperature. The diffusivity at each temperature was computed from the MD run.

## 3.3 Results and discussion

## 3.3.1 Structural analysis of SiO<sub>2</sub> glasses

The initial configuration of  $SiO_2$  glass formed using melt-quench process has been visualized in Figure 3.2 a. The structure of  $SiO_2$  glass was characterized using simulated XRD in LAMMPS, as shown in Figure 3.2 b, to confirm the amorphous nature. The broadening of peaks into a wide band spanning  $2\theta$ =18-40° indicates the formation of amorphous  $SiO_2$  structure.

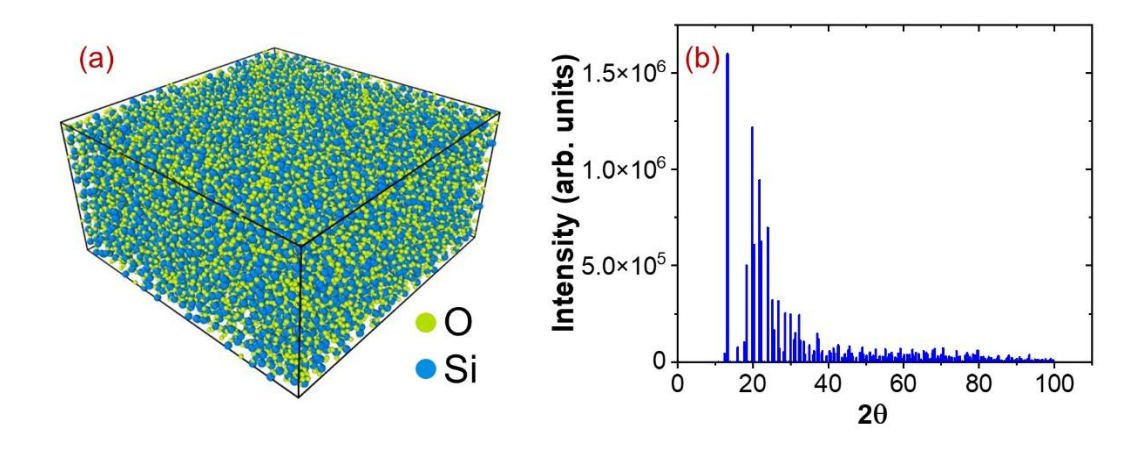


Figure 3.2 Structure of  $SiO_2$  glass generated using Tersoff potential. (a) MD simulation cell showing initial configuration of  $SiO_2$  glass structure at 300K. (b) XRD of the  $SiO_2$  glass structure at 300K.

Three different glass structures were created using the three potentials (Tersoff, BP and COMB) detailed in section 3.2.2. The RDF of these glass structures at 300 K was compared with experimental measurements [197,201], as seen in Figure 3.3, whereas the partial RDF of each atomic pair (Si-Si, Si-O and O-O) was compared with the ab initio measurements [197,202], as seen in Figure 3.3 (a-c). The absence of well-defined peaks in RDF of these glasses beyond the first coordination shell provides additional confirmation of the amorphous structure. The comparison in Figure 3.3 suggests that the glass formed using Tersoff potential shows the best match with the experimental RDF and *ab initio* partial RDF measurements from literature [197,201,202]. Therefore, for all self-diffusion studies in this work, the initial glass structure was generated using Tersoff potential. However, there is a slight shift in the peak for Si-Si system obtained in glass generated by Tersoff potential as compared to existing ab-

initio results. The fitted parameters that were used by Munetoh et al. [197] includes a parameter h that strongly affects the Si-O-Si bond angles. Any change in bond angle affect the spatial arrangement of atoms in the SiO2 network resulting in peak shift in radial distribution function. Munetoh et al. [197] reported high Si-O-Si bond angle (146.2°) obtained after simulations. For tetrahedral bond angle the angle must be close to tetrahedral bond angle which is 108° [197]. The difference in intensity could be due to running MD simulations on larger (~30000 atoms) structures as compared to small structures in ab-initio (few hundreds or less). As ab-initio methods calculate electronic interactions, these can capture even small changes in bond strength and coordination number. Interatomic potentials work on fitted parameters due to which there is a possibility of predicting slightly different coordination environments which affect peak intensities.

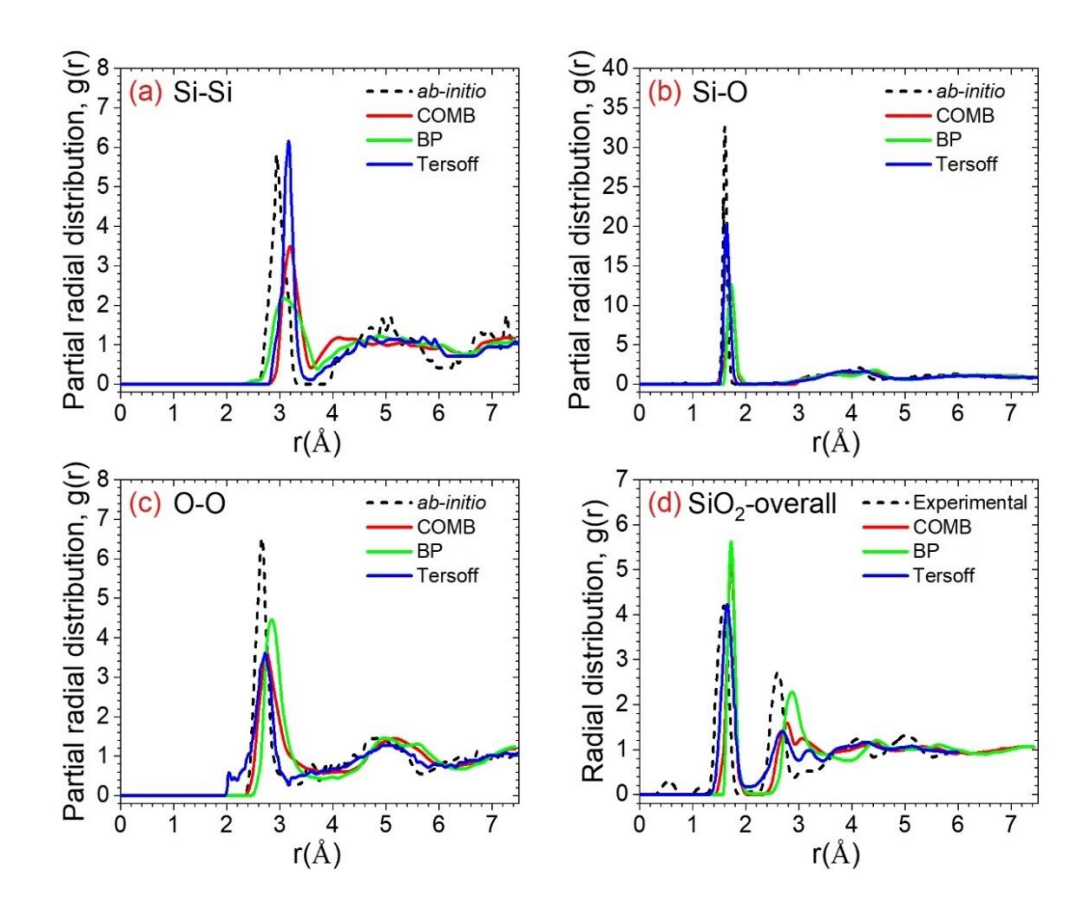


Figure 3.3 Radial distribution function of SiO<sub>2</sub> glass structures prepared using different potentials. Partial radial distribution function g(r) corresponding to (a) Si-Si, (b) Si-O, and (c) O-O pairs. (d) Overall radial distribution function for SiO<sub>2</sub> glass. The *ab initio* and experimental radial distribution function have been obtained from literature.

## 3.3.2 Self-diffusion in amorphous SiO<sub>2</sub>

The self-diffusion of Si and O in amorphous SiO<sub>2</sub> was simulated in the temperature range of 1200 to 1700 °C using all three potentials - Tersoff, BP and COMB. Out of the three configurations that were generated using Tersoff, BP and COMB, the glass created using Tersoff potential showed best consistency with the experimental and ab initio measurements of SiO<sub>2</sub> glass (Figure 3.3). As forcefields depend on system, these are developed by fitting the parameters to reproduce the required properties [203]. Tersoff potential for the large Si-O system was developed by Munetoh et al. [197] by fitting twelve adjustable parameters which include bond angle, bond length, charge transfer between Si and O, weaking and strengthening of heteropolar bonds and was found to well reproduce the structural properties of SiO<sub>2</sub>. Therefore, in our work we used the initial configuration of amorphous SiO2 that was generated using Tersoff potential. Further, to calculate diffusivities three potentials were used and the values were compared. The diffusion coefficients (D) of Si<sup>4+</sup> and O<sup>2-</sup>, obtained from MD runs using different potentials, have been plotted as a function of temperature in Figure 3.4. The activation energies (E<sub>a</sub>) and diffusion pre-factor (D<sub>0</sub>) for self-diffusion of Si and O in SiO<sub>2</sub> glass (obtained from the linear fitting of lnD values with respect to 1/T) have also been listed in Table 3.1.

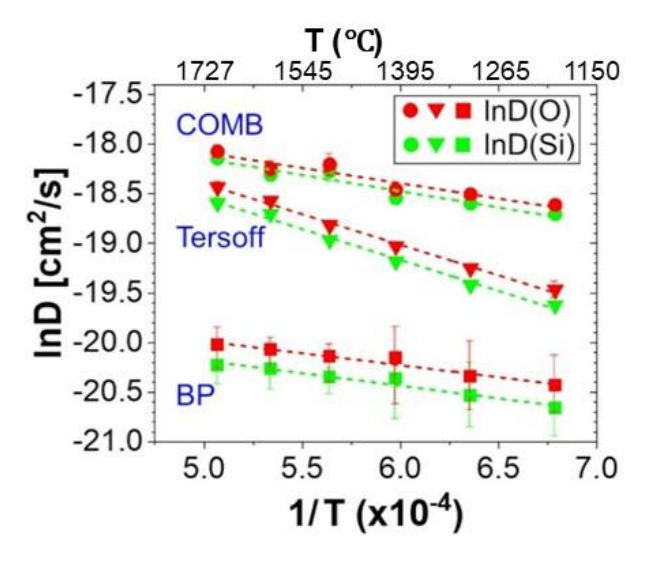


Figure 3.4 Self-diffusion in  $SiO_2$  glass. Self-diffusion coefficients of oxygen (O) and silicon (Si) in  $SiO_2$  glass as a function of temperature obtained using COMB, Tersoff and BP potentials. Linear fit (represented by dotted lines) has been performed to extract the activation energy ( $E_a$ ) and diffusion pre-factor ( $D_o$ ) values.

Table 3.2. Activation energy ( $E_a$ ) and diffusion pre-factor ( $D_o$ ) values for self-diffusion of Si and O in SiO<sub>2</sub>

Potential	Silicon [Si]		Oxygen [O]		
	Ea	D <sub>o</sub>	Ea	D <sub>o</sub>	
	[kJ/mol]	[cm <sup>2</sup> /s]	[kJ/mol]	[cm <sup>2</sup> /s]	
COMB	27	7x10 <sup>-8</sup>	26	7 x10 <sup>-8</sup>	
BP	21	6 x10 <sup>-9</sup>	20	7 x10 <sup>-9</sup>	
Tersoff	52	2 x10 <sup>-7</sup>	51	2 x10 <sup>-7</sup>	

The diffusivity of both Si and O increases with temperature following the Arrhenius relationship. MD runs with all potentials show a higher diffusivity values and lower activation energy of O diffusion as compared to Si (Figure 3.4 and Table 3.2), indicating that the O anions diffuse faster than Si cations in SiO<sub>2</sub> glass. As the activation energy is low, it facilitates easy movement of O anions suggesting that, in UHTCs containing SiC, the growth of glassy SiO<sub>2</sub> scale might be driven by the inward diffusion of O to a larger extent.

In SiO<sub>2</sub> glass structure, Si-O-Si bonds are present and the linked oxygen that connects two Si atoms is termed as the bridging oxygen (BO). The diffusion of BO is considerably more difficult than the non-bridging oxygen (NBO) and thus, during diffusion, it is mostly the NBO that diffuses [172]. Nascimento and Zanatto [172] suggested that in SiO<sub>2</sub>, tight links are formed between Si and O, therefore, in case of pure SiO<sub>2</sub>, diffusivities of both the ions are identical. However, the oxygen ions which are not so tightly bounded (NBO) with Si can move much faster. On the contrary, in pure SiO<sub>2</sub> glass, similar diffusivity values have been observed for Si and O ions [172]. Similar theory was proposed by Kalen et al. [204] for oxygen ions diffusion in SiO<sub>2</sub>. In our work, both anionic and cationic vacancies were incorporated in the amorphous SiO<sub>2</sub> which may result in the presence of open bonds and NBO in the structure; thereby making the diffusion easier. Higher values of diffusion prefactor and lower activation

energy indicating smaller temperature dependence for oxygen diffusion as compared to Si diffusion is consistent with the experimental results [204,205].

## 3.3.3 Self-diffusion in amorphous SiO2 containing Hf

Cheng et al. [185] studied the effect of Ti and Hf addition on thermal stability of SiO<sub>2</sub> and found that their addition enhances the strength of Si-O bonds. This was analysed by calculating Mulliken bond population. A larger value was obtained for Hf doped SiO<sub>2</sub> as compared to pure SiO<sub>2</sub>. Higher value of overlap population indicates formation of strong covalent bond and higher high temperature stability.

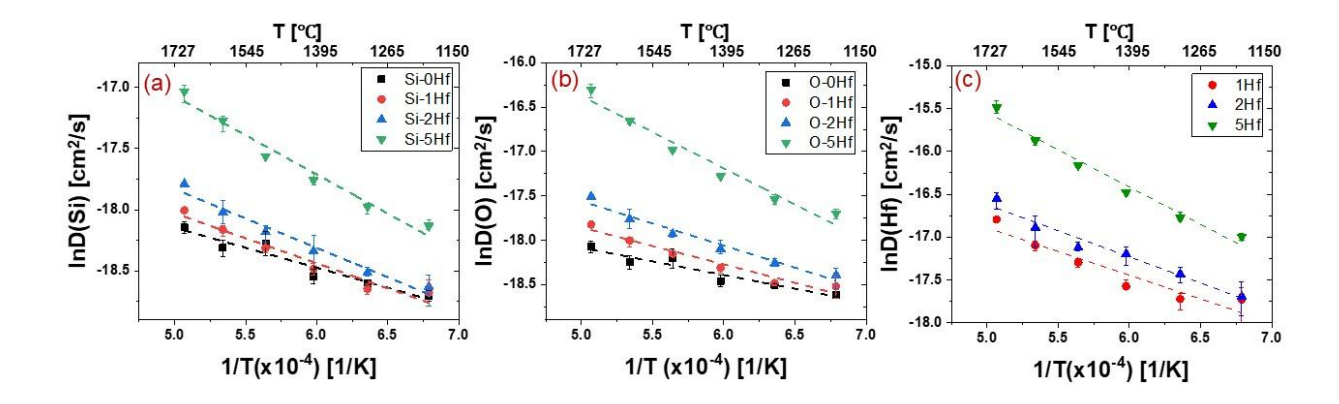


Figure 3.5. Self-diffusion in  $SiO_2$  glass containing hafnium. Self-diffusion coefficients of (a) silicon (Si), (b) oxygen (O) and (c) hafnium (Hf), as a function of temperature, in  $SiO_2$  glass containing 1, 2, and 5 at. % Hf. Linear fit (represented by dotted lines) for different glasses to extract the activation energy ( $E_a$ ) and  $D_o$  values.

Experimental observations by Cheng et al on effect of adding HfO<sub>2</sub> to SiO<sub>2</sub> has shown reduced its evaporation due to the formation of a non-volatile phase. This non-volatile phase covers SiO<sub>2</sub> surface and improves its stability at temperatures up to 1700 °C. Moreover, the addition of HfO<sub>2</sub> to cristobalite SiO<sub>2</sub> has been found to increase the Si-O bond strength up to 1700 °C due to the inward diffusion of Hf atoms in the SiO<sub>2</sub> lattice [185]. As Hf or HfO<sub>2</sub> addition to SiO<sub>2</sub> was found to improve thermal stability and bonding characteristics, it may lead to changes in self-diffusivity values. In this section, we have reported the effect of Hf addition on self-diffusivities of Si, O and Hf in amorphous SiO<sub>2</sub>. Three different Hf containing SiO<sub>2</sub> glass structures, denoted as 1Hf, 2Hf and 5Hf corresponding to 1, 2 and 5 at % Hf respectively, were studied using COMB

potential. Figure 3.5 shows the diffusivity values obtained as a function of temperature and Table 3.3 shows the activation energies ( $E_a$ ) and diffusion prefactor ( $D_o$ ) for self-diffusion of Si, O and Hf as a function of Hf concentration.

Table 3.3. Activation energies ( $E_a$ ) and diffusion pre-factor ( $D_o$ ) for self-diffusion of Si, O and Hf as a function of Hf concentration.

	Silicon [Si]		Oxygen [O]		Hafnium [Hf]	
Material	Ea	Do	Ea	Do	Ea	Do
	[kJ/mol]	[cm <sup>2</sup> /s]	[kJ/mol]	[cm <sup>2</sup> /s]	[kJ/mol]	[cm <sup>2</sup> /s]
SiO <sub>2</sub>	27.15	6.72x10 <sup>-8</sup>	25.639	6.53 x10 <sup>-8</sup>	-	-
SiO <sub>2</sub> -1 Hf	33.96	1.15 x10 <sup>-7</sup>	34.6	6.56 x10 <sup>-7</sup>	46.15	7.45 x10 <sup>-7</sup>
SiO <sub>2</sub> -2 Hf	39.87	1.99 x10 <sup>-7</sup>	41.54	1.41 x10 <sup>-7</sup>	50.72	1.28 x10 <sup>-6</sup>
SiO <sub>2</sub> -5 Hf	53.16	9.47 x10 <sup>-7</sup>	67.73	4.55 x10 <sup>-6</sup>	72.15	1.35 x10 <sup>-5</sup>

As seen in Figure 3.5, the addition of Hf to SiO<sub>2</sub> glass results in: (a) increase in both the diffusivity values as well as the activation energies for self-diffusion of Si and O ions; although the increase for O is more than that for Si, and (b) higher activation energy for self-diffusion of O than Si, which is contrary to the observation in pure SiO<sub>2</sub>, and (c) considerably higher diffusivity and activation energy of Hf as compared to both Si and O. If we look at the Ellingham diagram [206] for oxide formation in Figure 3.6, free energy change for HfO<sub>2</sub> formation is lower than that of SiO<sub>2</sub> indicating HfO<sub>2</sub> is thermodynamically more stable at all temperatures. It shows more energy is required to break HfO<sub>2</sub> bonds and same (higher activation energy than SiO<sub>2</sub>) is evident from our MD simulation results. Additionally, with increase in both diffusivity and activation energy, increase in  $D_0$  was observed. High value of  $D_0$  denotes longer jump distance. Addition of Hf is increasing the activation energy for O diffusion more than Si making its movement difficult to initiate. This may lead to lesser O penetration in the scale and can reduce the overall oxidation of the substrate. If we compare electronegativity values of Si and Hf, Hf has a lower value of 1.3 than Si which

is 1.9, which means Hf has higher affinity for oxygen, and it can move out of the scale. This may explain the higher diffusivity values of Hf. Pint [59] observed similar behaviour of outward diffusion of Hf through α-Al<sub>2</sub>O<sub>3</sub> and α-Cr<sub>2</sub>O<sub>3</sub> oxides. Existence of the oxygen potential gradient between oxide-gas interface and the substrate is the driving force for the outward movement of the Hf or any element present in the small amount (reactive element). Whenever oxide forms, some perturbations always remain present at the metal-oxide interface due to defects and when a reactive element moves to those positions, it results in lowering the free energy of the system. Later, the element moves towards the oxide-gas interface [59]. However, as the activation energy for Hf diffusion is higher, it is difficult to initiate its movement. Change in activation energy shows thermodynamics and increase in D<sub>0</sub> shows kinetics indicating high diffusivity when D<sub>0</sub> is higher. In addition to that, the phase diagram of HfO2-SiO2 system provides useful insight according to which addition of small amount of HfO<sub>2</sub> (~2 mol %) to SiO<sub>2</sub> results in formation of a relatively low melting point eutectic [207] which is a mixture of HfSiO<sub>4</sub> and α-SiO<sub>2</sub> at ~1680 °C. Due to its low melting point, and hence higher homologous temperatures, species can diffuse faster. Diffusion data shows higher diffusivities with an increase in Hf addition up to 5 at %. The MD results indicate that Hf may diffuse easily through the amorphous SiO<sub>2</sub>. Work by Cheng et al. [185] shows that the presence of Hf may cause formation of HfSiO<sub>4</sub> phase in the SiO<sub>2</sub> scale, resulting in reduced mass loss and evaporation of SiO<sub>2</sub> up to temperatures as high as 1700 °C. Reduced mass loss can be attributed to increased bond strength as discussed above. HfSiO4 has tetragonal crystal structure with a density of 7.02 g/cm<sup>3</sup> and a packing fraction of ~0.68. The packing fraction of SiO<sub>2</sub> doped with Hf is even higher (close to 0.74) as calculated using the c/a and packing fraction relation derived by Dunlap [208]. High density of the phase and high packing fraction indicates formation of a dense protective oxide. This indicates that the Hf can make the SiO<sub>2</sub> layer more protective.

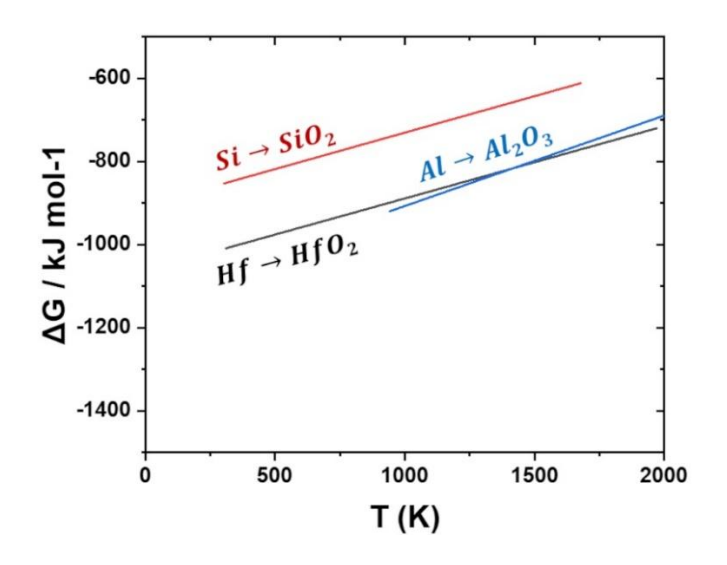


Figure 3.6. Ellingham diagram for SiO<sub>2</sub>, HfO<sub>2</sub> and Al<sub>2</sub>O<sub>3</sub> [206]

### 3.3.4 Self-diffusion in amorphous SiO2 containing Al

In SiO<sub>2</sub>-Al<sub>2</sub>O<sub>3</sub> system, phase diagram shows formation of a eutectic at ~3.02 mol% Al<sub>2</sub>O<sub>3</sub> and 1600 °C. According to this, when the amount of Al<sub>2</sub>O<sub>3</sub> increases to this composition, the melting point of the system decreases, and it again increases beyond this amount of Al<sub>2</sub>O<sub>3</sub>. Low melting point facilitates easy mobility of species due to higher homologous temperature and lower resistance to viscous flow. To validate whether the use of MD for diffusivity calculations captures this trend, the amount of Al addition to SiO<sub>2</sub> was selected as 1, 2, 3 and 5 at% and the systems are named as 1Al, 2Al, 3Al and 5Al respectively. On increasing the Al content, the diffusivity of both Si and O was found to increase up to 3 at % Al as can be seen in Figure 3.7. Activation energies and D<sub>0</sub> values are reported in Table 3.4. At 5 at % Al addition, reversal in the trend was observed as expected. Increased diffusivity could be attributed to the network breakdown of strong SiO<sub>4</sub> tetrahedra leading to less resistance to viscous flow and higher mobility of ions. In addition to that, lower bond dissociation energy of Al-O (512 kJ/mol) than Si-O (798 kJ/mol) has been reported in the existing literature [209,210]. Low bond dissociation energy means it can easily detach, and higher bond dissociation energy shows stronger bond and a more stable structure. Once Al detaches, NBO can easily move through the oxide scale. At all compositions, the diffusivity of Al ions is highest and that of Si ions is lowest. At 3 at % Al addition, diffusivity of both Si and O increased with temperature with a maximum at 1600 °C. Urbain et al. [184] observed increased diffusivity with addition of 5 vol % Al<sub>2</sub>O<sub>3</sub> to SiO<sub>2</sub> melts which show viscosity reduction and enhanced diffusivity. However, increased Al<sub>2</sub>O<sub>3</sub> content resulted in a small reduction in viscosity.

As compared to SiO<sub>2</sub>-Al systems, addition of Hf affects the diffusivity more. Diffusivity values are much higher when the same amount (1 and 2 at %) of Hf and Al is added to SiO<sub>2</sub>. Hf has an electronegativity value of 1.3, which for Al is 1.5. This may indicate that Hf has higher tendency to form oxide than Al and it can move outwards faster. However, this trend changes at high dopant content. Pint [45] demonstrated the effect of Al and Hf ions to  $\alpha$ -Cr<sub>2</sub>O<sub>3</sub> scale and it was found that Hf can diffuse faster than Al ions and was more effective in inhibiting diffusion of Cr ions. It was due to the larger size of Hf ions than Al (which is smaller than Cr ions in  $\alpha$ -Cr<sub>2</sub>O<sub>3</sub>). In SiO<sub>2</sub>-Al<sub>2</sub>O<sub>3</sub> system low melting point eutectic forms at 3.02 mol % Al<sub>2</sub>O<sub>3</sub> at 1600 °C whereas in SiO<sub>2</sub>-HfO<sub>2</sub> it forms at 2 mol % HfO<sub>2</sub> at ~1680 °C. As the melting temperature of this eutectic is higher, we do not expect the effect of melting on ions mobility and any reversal for the temperature range of our study even at compositions higher than 2 at % Hf.

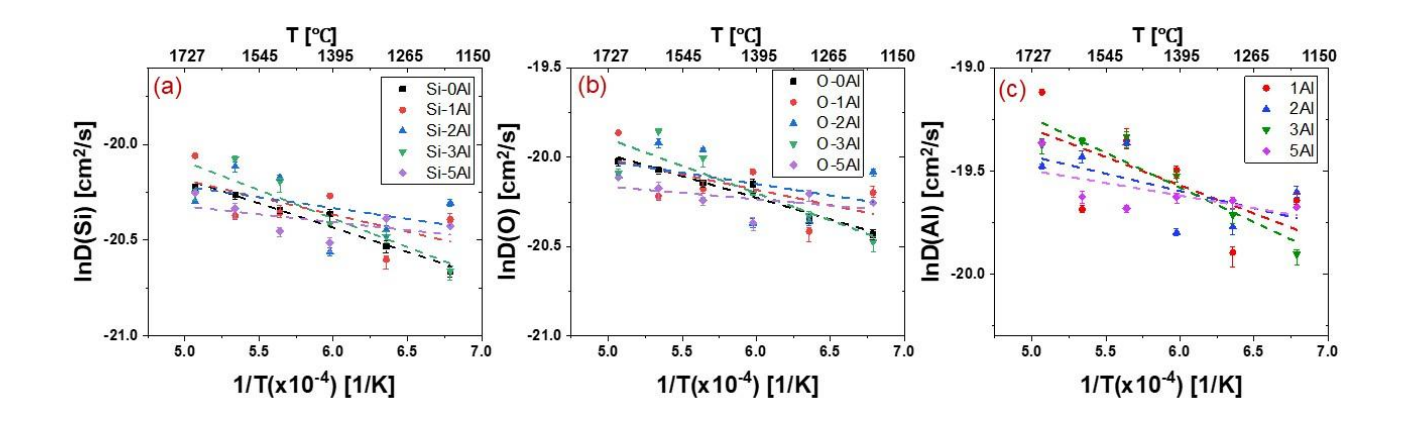


Figure 3.7. Self-diffusion in  $SiO_2$  glass containing Aluminium. Self-diffusion coefficients of (a) silicon (Si), (b) oxygen (O) and (c) Aluminium (Al), as a function of temperature, in  $SiO_2$  glass containing 1, 2, 3 and 5 at. % Al. Linear fit (represented by dotted lines) for different glasses to extract the activation energy (Ea) and  $D_0$  values

Table 3.4. Activation energies ( $E_a$ ) and diffusion pre-factor ( $D_o$ ) for self-diffusion of Si, O and Al as a function of Al concentration.

Material	Silicon [Si]		Oxygen [O]		Aluminium [Al]	
	Ea	Do	Ea	Do	Ea	Do
	[kJ/mol]	[cm <sup>2</sup> /s]	[kJ/mol]	[cm <sup>2</sup> /s]	[kJ/mol]	[cm <sup>2</sup> /s]
SiO <sub>2</sub>	21.089	6.12x10 <sup>-9</sup>	20.11	7.01x10 <sup>-9</sup>	-	-
SiO <sub>2</sub> -1 Al	14.924	4.23x10 <sup>-9</sup>	14.21	4.79x10 <sup>-9</sup>	22.69	1.63 x10 <sup>-9</sup>
SiO <sub>2</sub> -2 Al	9.395	2.92x10 <sup>-9</sup>	10.62	3.83x10 <sup>-9</sup>	10.61	8.45 x10 <sup>-9</sup>
SiO <sub>2</sub> -3 Al	24.709	8.36x10 <sup>-9</sup>	25.27	1.04x10 <sup>-8</sup>	27.92	2.35 x10 <sup>-8</sup>
SiO <sub>2</sub> -5 Al	6.874	2.27x10 <sup>-9</sup>	5.83	2.52x10 <sup>-9</sup>	10.09	6.25 x10 <sup>-9</sup>

#### 3.3.5 Shear viscosity calculations in SiO<sub>2</sub>

Shear viscosity values of SiO<sub>2</sub> were calculated in the temperature range 600-1700 °C using Green-Kubo (GK) formalism with Buckingham potential modified by Wang et al. [57]. An inverse relation of shear viscosity with temperature was observed. Shear viscosity value of ~ 30 Pa.s was obtained at 1150 °C, which is close to the value reported by Wang et al. [57] for borosilica glass with SiO<sub>2</sub>/SiO<sub>2</sub>+B<sub>2</sub>O<sub>3</sub> ratio equal to 1. Wang et al. [57] calculated shear viscosity at 1150 °C for borosilica glass as function of change in SiO<sub>2</sub> and B<sub>2</sub>O<sub>3</sub> composition and reported lower viscosities from MD as compared to the experimental values. It was suggested that use of interatomic potential overestimates the fluidity of supercooled liquids. In addition to that Bauchy et al. [211] concluded that even after using high performance computer simulations to calculate viscosity in a reasonable time, only low viscosity regimes with value of less than 10<sup>4</sup> Pa.s can be investigated for a longest run of 1  $\mu s$  or  $10^9$  steps. Running simulations for 10 ns would result in low values of ~ 10 Pa.s. In our work, the simulations were run for 9900 steps for which the variation of viscosity as function of temperature is shown in Figure 3.8. The results for shear viscosity of pure SiO<sub>2</sub> were compared with the MD results by

Bauchy et al. [211] for silicate melts namely MORB (50.59 wt % SiO<sub>2</sub> with significant amount of CaO, MgO, Na<sub>2</sub>O, Al<sub>2</sub>O<sub>3</sub> etc.) and Na<sub>2</sub>O-2SiO<sub>2</sub>. It was found that the viscosity values of pure SiO<sub>2</sub> in our work are one and two order higher than that of Na<sub>2</sub>O-2SiO<sub>2</sub> and MORB respectively in the same temperature range. Addition of any basic oxide such as CaO, MgO, Na<sub>2</sub>O to SiO<sub>2</sub> melt causes O<sup>2</sup>- to enter the SiO<sub>2</sub> network leading to its breakdown and viscosity reduction [212]. Hence, higher viscosity of pure silica agrees with the work done by Bauchy et al. [211].

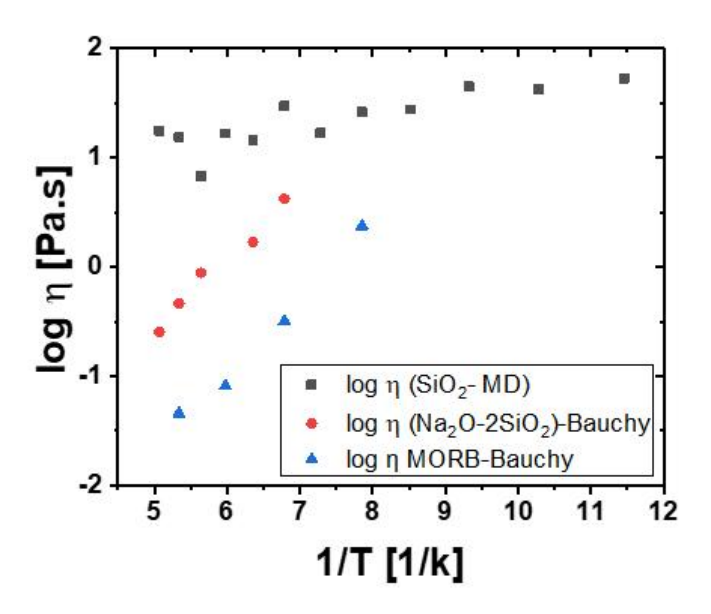


Figure 3.8. Shear viscosity of  $SiO_2$  as function of temperature compared with viscosities for silicate melts obtained from the work by Bauchy et al. [50]. Lower viscosities for MORB and  $Na_2O-2SiO_2$  melts can be attributed to the addition of basic oxides such as  $Na_2O$ , CaO, MgO.

### 3.4 Conclusions

In this work, we calculated the self-diffusivity of Si and O in amorphous SiO<sub>2</sub> using molecular dynamics simulations. Amongst the three different interatomic potentials used, we found that the Tersoff potential results in the best glass structure; based on comparison with experimental and *ab initio* structural characterization. The diffusion of O is faster as compared to Si indicating that the growth of SiO<sub>2</sub> is driven by the inward diffusion of O. The addition of Hf to amorphous SiO<sub>2</sub> increases both the diffusivity values as well as the activation energies for Si and O diffusion. The diffusion of Hf in amorphous SiO<sub>2</sub> is faster as compared to both Si and O which indicates that, if

Hf is added to ZrB<sub>2</sub>-SiC, it can diffuse through the SiO<sub>2</sub> to form a HfSiO<sub>4</sub> phase in the SiO<sub>2</sub> scale resulting in reduced mass loss and evaporation of SiO<sub>2</sub> up to temperatures as high as 1700 °C. Addition of Al to SiO<sub>2</sub> was found to increase diffusivity values up to 3 at %. Diffusivities were found to reduce on adding 5 at % Al to the system probably due to formation of high melting mixture as evident from the phase diagram of SiO<sub>2</sub>-Al<sub>2</sub>O<sub>3</sub> system. Viscosity values as function of temperature for pure silica were calculated using MD and the results agreed with the MD results by Bauchy et al. [211] for silicate melts. Even if the values using MD differs with the existing experimental results, the estimates of self-diffusion activation energies and diffusivity values for amorphous SiO<sub>2</sub> calculated in this work will be useful for building mathematical and computational models for oxidation studies wherever SiO<sub>2</sub> scales are encountered, including but not limited to ZrB<sub>2</sub>-SiC ceramic composites for ultra-high temperature applications.

# **Chapter 4 Oxidation Modelling**

#### 4.1 Introduction

Refractory metal silicides such as Mo-Si and Mo-Si-B alloys are candidate materials for high temperature applications where oxidation presents a major challenge [6]. Therefore, understanding and predicting the oxidative degradation pathways is a key challenge that needs to be addressed. We have developed a predictive framework through a combination of mathematical modelling and numerical implementation through a modified Cellular Automata (CA) scheme that allows us to investigate the growth of protective borosilica scale on the underlying alloy substrate. Unlike traditional CA models that assign a single state to a cell, we use fractional states (phase volume fractions) that can map the existence of multiple phases in varying amounts within a single cell. The model takes the actual microstructure as input and simulates the transient oxidation of Mo-Si-B alloys based on the experimentally measured oxidation rates of individual phases and the thermodynamics of the oxidation reactions.

The oxidation of Mo-Si-B alloys presents significant complexity owing to the presence of multiple oxidizing phases (Mo, A15, T2 & T1) that form a variety of oxides (MoO<sub>3</sub>, SiO<sub>2</sub>, B<sub>2</sub>O<sub>3</sub> etc.), each of which behaves uniquely [6,17]. While MoO<sub>3</sub> volatilizes as a trimer at temperatures above 475 °C, SiO<sub>2</sub> & B<sub>2</sub>O<sub>3</sub> form a glassy layer whose viscosity (and the resultant flow behavior) is strongly governed by the B<sub>2</sub>O<sub>3</sub> content [183,213]. These phenomena, viz. (a) the

formation of pits upon MoO<sub>3</sub> volatilization and (b) the flow behavior of borosilica scale, are strongly dictated by the quantity, size and distribution of phases within the alloy microstructure [17]. For example, a smaller size of Mo phase will result in smaller pits after volatilization that can be filled much more easily by the flow of the glassy layer as compared to large sized pits. Similarly, the distribution of T2 phase (which acts as the source of boria upon oxidation) dictates the local flow behavior of glassy scale since boria reduces the viscosity [16,63]. Thus, the alloy microstructure plays a critical role in controlling the oxidation behavior of Mo-Si-B alloys. In view of this, Rioult et al. [17] developed a microstructure-based kinetic model for oxidation of Mo-Si-B alloys that incorporated the size distribution of individual phases (extracted from actual microstructures) along with the individual phase consumption rates (calculated from experimental oxidation mass change curves) to model the transient oxidation stage. Despite the simplistic nature of the model, it can estimate the effect of changes in size distribution of phases on the oxidation kinetics. But it suffers from three major drawbacks: (a) the diffusion through the glassy scale is not considered, (b) microstructural evolution during oxidation cannot be visualized, and (c) the lateral spread of the glassy layer is ignored. Parthasarathy et al. [93] also developed an oxidation model for SiCcontaining refractory diborides wherein they incorporate the microstructural characteristics as well as the oxygen diffusion through glassy scale to estimate oxidation kinetics. But this even model does not enable visualization of microstructure evolution and ignores the flow of the glassy scale. Building upon these approaches, we have developed here an oxidation model for Mo-Si-B alloys that takes the actual microstructure as an input and models the temporal evolution of microstructure during oxidation while taking cognizance of both diffusion-limited oxidation as well as the lateral spread of viscous glassy scale.

First, we carry out phase segmentation to create a labelled microstructure image with unit thickness and then discretize it spatially. Initially, each voxel is encoded as a separate phase, but each voxel is also linked to an array that

tracks the volume fraction of all possible phases at that voxel as the system evolves over time. At the beginning, the rate of change of each phase is computed based on the experimentally measured mass loss rates of individual phases and the stoichiometry of oxidation reactions. But as the system evolves and the thickness of silica/borosilica glass layer increases, the rate of change becomes limited by the oxygen diffusion through the glassy scale that is dictated by the thermodynamics of oxidation, oxygen permeability and scale composition. We also simulate the spread of the glassy layer based on its viscosity that is in turn a function of glass composition. Thus, the model simulates the transient oxidation phenomenon both visually (simulated microstructure at each time step) as well as numerically (mass change at each time step). Since the model takes the alloy microstructure as input, it can simulate the effect of size, shape, volume and distribution of phases on oxidation behavior. Moreover, the methodology can be extended to new systems with some changes in code and system specific thermodynamic and physical data.

# 4.2 Experimental details

The alloys with compositions mentioned in Table 4.1 were fabricated using arc melting technique. The microstructures of as-fabricated alloys were obtained using Scanning Electron Microscopy (SEM). We identify the phases present in the alloy through the indexing of powder X-ray Diffraction (XRD) pattern. The obtained XRD patterns and phase quantification of the alloys are mentioned in Chapter 5. Then, we correlate the elemental distribution maps obtained from Energy Dispersive Spectroscopy (EDS) with the microstructural images and XRD identified phases to establish regions corresponding to each phase. The amount of each phase in the fabricated alloys was quantified with Rietveld refinement using GSAS II [214]. This matching is also informed by microstructural characterization reported in previously published literature for similar alloys [16,17,55]. For oxidation studies the samples were introduced inside a pre-heated furnace at 1100 °C and mass change was measured after different time intervals.

Table 4.1. Compositions of the alloys fabricated for oxidation studies

Alloy	Mo (at %)	W (at %)	Ta (at %)	Si (at %)	B (at %)
Nomenclature					
711	70	-	-	15	15
711-W10	60	10	-	15	15
711-W15	55	15	-	15	15
721	70	-	-	20	10
721-W10	60	10	-	20	10
721-W15	55	15	-	20	10
811	80	-	-	10	10
821	80	-	-	13.33	6.67
711-5Ta	65	-	5	10	10
721-5Ta	65	-	5	13.33	6.67

#### 4.3 Simulation details

The oxidation modeling framework developed in this work takes an actual phase-segmented microstructural image as input and performs a modified cellular automata simulation to model the temporal evolution of alloy microstructure during transient oxidation. This involves: (a) generating a phase segmented image and quantifying spatial discretization, (b) defining a scheme for storing system information at any given time, (c) defining oxidation events and their occurrence, (d) calculating phase consumptions based on experimental measurements and oxygen diffusion-based calculations, (e) calculating formation of product phases, (f) modeling outward diffusion of volatile phases, and (f) modeling lateral flow of viscous silica/borosilica glass. Each of these steps has been elaborated here.

#### 4.3.1 Preparing the initial microstructure

We start out with an actual alloy microstructure obtained through SEM and perform phase segmentation using a series of tasks., We phase-segment the microstructure using an automated segmentation routine within the Labkit plugin in ImageJ-Fiji [215]. This requires manual labelling of some regions within the microstructure as a guidance for the automated segmentation algorithm. Figure 4.1 a shows an actual SEM image alongside its phase-segmented counterpart.

The microstructure is inherently spatially discretized by the virtue of how it is stored as a 2-D array of pixels. It is assumed that the 2D microstructure has a thickness ( $T_{px}$ ) of 1 unit length that is sufficiently small to neglect perturbations in the oxidation process across the thickness. The choice of thickness will not affect the specific oxidation rates calculated during modeling since both volume and surface area scale linearly with the thickness ( $T_{px}$ ) and thus, the per unit area mass change becomes independent of the thickness. But it is important to calculate the microstructural length of each pixel. Each image has a size (width x height) associated with it which is measured as the number of pixels along the width and height of the image. The image shown in Figure 4.1 has a size of 1280 pixels x 952 pixels. The microstructural length of each pixel is calculated by dividing the actual length of the scale bar by the number of pixels spanned by it. For example, in Figure 4.1, the scale bar (10  $\mu$ m) in the image spans 161 pixels; thus, each pixel represents a microstructural length of (10/161 = 0.0621  $\mu$ m).

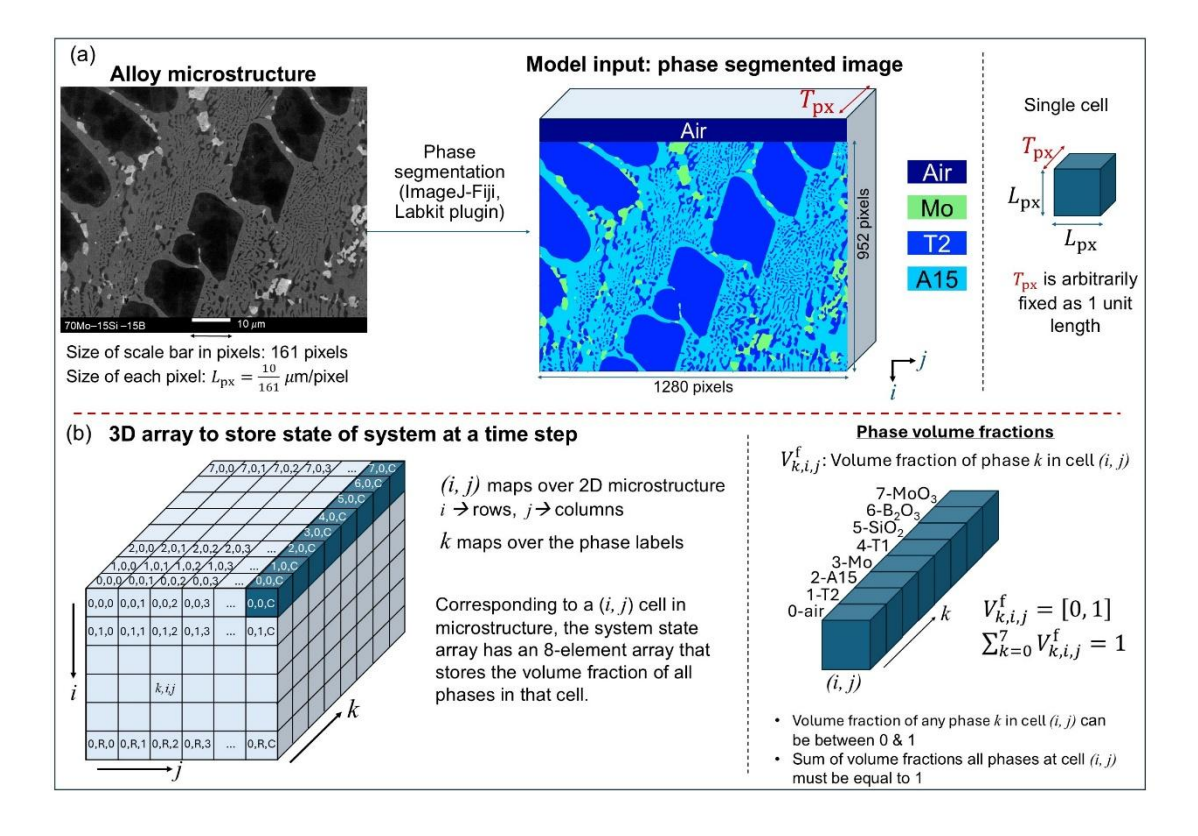


Figure 4.1 (a) Phase segmentation of actual alloy microstructure using ImageJ-Fiji (Labkit plugin [215]) followed by measurement of pixel size based on the number of pixels spanned by the scale bar. (b) 3-D array for storing volume fractions of all the phases at each (i,j) cell corresponding to 2-D microstructure.

# 4.3.2 Representing the state of the system

Initially, at time zero, each cell in the system contains only one type of phase and can thus be described fully using a single cell state value. But as oxidation progresses with time, a cell can contain multiple phases simultaneously. Thus, a single cell state is not sufficient to describe the system. To account for this, we use a modified approach wherein, at any given time during oxidation, the state of the system is stored as a 3-D array that comprises of eight 2-D arrays stacked on top of each other, as shown in Figure 1b. Each layer stores the volume fraction of a particular phase at all cells. Thus, (k, i, j) cell in the system state array represents the volume fraction of phase k in (i, j) cell of the microstructure  $(V_{k,i,j}^f)$ . For Mo-Si-B alloys, there are 8 possible phases that can exist within a cell, and these are encoded as integer labels: {0: Air, 1: T2 (Mo<sub>5</sub>SiB<sub>2</sub>), 2: A15 (Mo<sub>3</sub>Si), 3: Mo, 4: T1 (Mo<sub>5</sub>Si<sub>3</sub>), 5: SiO<sub>2</sub>, 6: B<sub>2</sub>O<sub>3</sub>, 7: MoO<sub>3</sub>}. The formation of MoO<sub>2</sub> phase has not been considered here since the kinetics data for that phase is not available. These labels are identical to the *k* index of layers that represent these phases in the 3D array. The constraints here are: (a) volume fraction of a phase k at any cell  $(V_{k,i,j}^f)$  can be between 0 and 1, and (b) the summation of volume fraction of all phases at any cell  $(\sum_{k=0}^{7} V_{k,i,j}^{f})$  must be equal to 1. At time zero, the state of the system array is initiated by putting all values as zero and then for each (i, j), putting  $V_{k,i,j}^f\Big|_{k=I_{i,i}} = 1$  where  $I_{i,j}$  is the phase label at (i, j) pixel in phase segmented microstructure image *I*.

# 4.4 Reactions and phase consumptions

#### 4.4.1 Oxidation events and their occurrence

The possible oxidation reactions [46] and free energy change (kJ/mol) calculated using NIST-JANAF tables [216] for Mo-Si-B alloys are:

$$Mo + \frac{3}{2}O_2 \rightarrow \frac{1}{3}(MoO_3)_3; \ \Delta G = -203.683$$

Equation 4.1

$$Mo_3Si + \frac{11}{2}O_2 \rightarrow (MoO_3)_3 + SiO_2; \ \Delta G = -1221.12$$

Equation 4.2

$$Mo_5SiB_2 + 10O_2 \rightarrow \frac{5}{3}(MoO_3)_3 + SiO_2 + B_2O_3$$

Equation 4.3

$$Mo_5Si_3 + 10.5O_2 \rightarrow \frac{5}{3}(MoO_3)_3 + 3SiO_2; \Delta G = -2776.84$$

Equation 4.4

$$Mo + O_2 \rightarrow MoO_2$$
;  $\Delta G = 0.347$ 

#### Equation 4.5

Reaction in Equation 4.5 occurs at low oxygen partial pressures [47,48], leading to the presence of MoO<sub>2</sub> primarily in the subscale region. The kinetics of formation of MoO<sub>2</sub> is not well-known and not considered in the present simulations. Given its location in the oxide layer, this is not likely to influence the initial oxidation stages; however, we anticipate that not including the formation of MoO<sub>2</sub> in the simulations may somewhat affect (potentially delay) the onset of the steady-state region our simulations. At any cell (i, j), the oxidation events follow two rules: (a) oxidation can happen only if the cell has access to oxygen (air) through its neighboring cells, and (b) the amount of oxidation will increase if the access to oxygen increases. As shown in Figure 4.2, a cell (i, j) can have access to  $O_2$  through its above (i-1, j), left (i, j-1) and right (i, j+1) neighboring cells. Whether these cells can provide  $O_2$  depends on two factors: (a) these cells must themselves have access to O2 i.e., they must contain some air or glass (SiO<sub>2</sub>/B<sub>2</sub>O<sub>3</sub>) phase, and (b) there must be an interaction area between these cells and the oxidation cell through which O2 can interact. The interaction area will be measured as a value between 0 to 1 wherein 0 implies no access to O<sub>2</sub> and 1 implies the entire contact area is available for  $O_2$  interaction. For the above cell (i-1, j), either the entire contact area is available for O2 interaction if there is no solid phase present, or no

interaction is possible if even a small amount of solid phase is present. Thus, the interaction area with oxygen from above cell  $(A_{i,j}^{A,O_2})$  is modelled as a delta function:

$$A_{i,j}^{A,O_2} = \delta_{\sum_{k \in \{1,2,3,4\}} V_{k,i-1,j}^f = 0}$$

Equation 4.6

The interaction area with  $O_2(A_{i,j}^{L,O_2})$  and  $A_{i,j}^{R,O_2}$  for left cell (i, j-1) and right cell (i, j+1), can be modelled as the sum of volume fraction of air and glass phases in these cells i.e.,

$$A_{i,j}^{L,O_2} = \sum_{k=\{0,5,6\}} V_{k,i,j-1}^f$$

Equation 4.7

$$A_{i,j}^{R,O_2} = \sum_{k=\{0,5,6\}} V_{k,i,j+1}^f$$

Equation 4.8

Thus, the total interaction area of cell (i, j) with  $O_2$  from neighboring cells is:

$$A_{i,j}^{O_2} = A_{i,j}^{A,O_2} + A_{i,j}^{L,O_2} + A_{i,j}^{R,O_2}$$

Equation 4.9

Oxidation events can happen at cell (i, j) only if  $A_{i,j}^{O_2} > 0$ . These interaction areas will be further used for scaling the amount of oxidation that happens as a result of oxidation events.

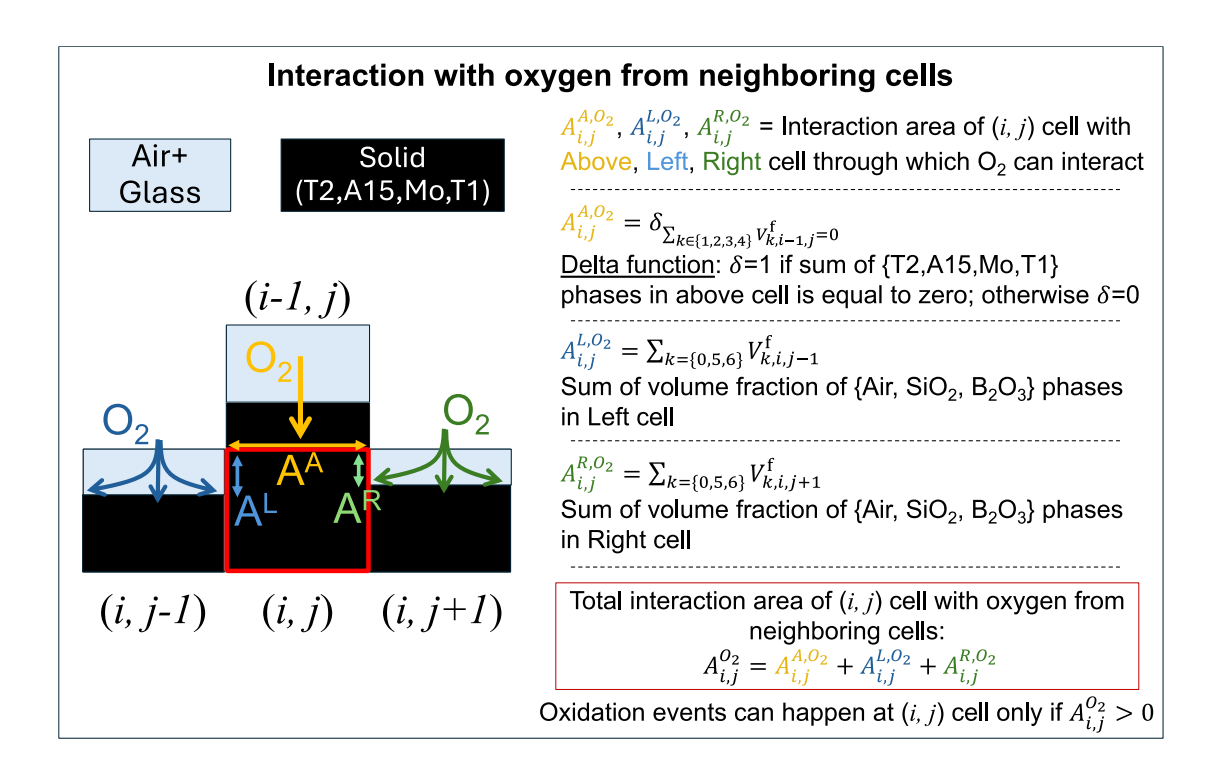


Figure 4.2. Determining access to oxygen through neighboring cells. The black regions here represent solid oxidizing phases (T2, A15, Mo, T1) whereas the light blue regions represent air/glass. The solid oxidizing phases are assumed to be impervious to oxygen and thus, this figure highlights three key aspects: (a) Oxygen flux from above cell will be available only if the above cell has no solid oxidizing phase present, (b) oxygen flux from side cell will be available if the side cell has some air/glass present, and (c) oxygen flux from side cell will be proportional to the amount of air/glass in side cells.

#### 4.4.2 Modelling phase consumption using experimental data

Oxidation events (Equation 4.1 to Equation 4.4) can occur at a cell (i, j) if that cell interacts with oxygen from neighboring cells i.e.,  $A_{i,j}^{O_2} > 0$ . If oxidation happens, the phase consumption of the oxidizing phase is calculated in two ways: (a) based on experimentally measured oxidation kinetics of the pure phase, and (b) based on the flux of  $O_2$  through glass scale that is present above the cell. In this section we elaborate on how the former is calculated.

The experimental mass change rate of a pure phase k ( $k \in \{1 \text{ (T2)}, 2 \text{ (A15)}, 3 \text{ (Mo)}, 4 \text{ (T1)}\}$ ) is obtained from literature. But this value represents the overall mass change which is a combination of mass loss due to (MoO<sub>3</sub>)<sub>3</sub> volatilization and mass gain due to formation of SiO<sub>2</sub> and B<sub>2</sub>O<sub>3</sub>. Thus, the mass change rate of any given phase k can be expressed as:

$$\left(\frac{dm}{dt}\right)_k = \left(\frac{dm}{dt}\right)_{\text{exp}} \left(\frac{M_k}{M_k - N_{SiO_2} M_{SiO_2} - N_{B_2O_3} M_{B_2O_3}}\right)$$

Equation 4.10

where  $\left(\frac{dm}{dt}\right)_{\text{exp}}$  is the experimentally observed overall mass change rate,  $M_k$  is the molar mass of phase k,  $M_{SiO_2}$  and  $M_{B_2O_3}$  are the molar mass of SiO<sub>2</sub> and B<sub>2</sub>O<sub>3</sub> respectively,  $N_{SiO_2}$  and  $N_{B_2O_3}$  represent the stoichiometric coefficients of SiO<sub>2</sub> and B<sub>2</sub>O<sub>3</sub> respectively in oxidation reaction of phase k. For example,  $N_{SiO_2} = 0$  and  $N_{B_2O_3} = 0$  for Mo phase (k=3), whereas  $N_{SiO_2} = 1$  and  $N_{B_2O_3} = 1$  for T2 phase (k=1). Equation 4.10 gives the phase consumption rate for a single phase (k) and has to be implemented separately for each phase with its associated parameters.

Based on experimental kinetics, when a cell (i, j) containing phase k oxidizes, the change in volume fraction of phase k in that cell over one time step  $(\Delta t)$  is calculated as:

$$\Delta V_{k,i,j}^{f,\text{exp}} = \frac{\Delta V_{k,i,j}^{\text{exp}}}{V_{DX}} = \left(\frac{1}{\rho_k}\right) \left[\left(\frac{dm}{dt}\right)_k * \Delta t\right] \left(\frac{1}{L_{DX}}\right)$$

Equation 4.11

where  $\Delta V_{k,i,j}^{\rm exp}$  is the volume change (cm<sup>3</sup>) of phase k in one time step and is equal to  $\left(\frac{1}{\rho_k}\right)\left[\left(\frac{dm}{dt}\right)_k*A_{px}*\Delta t\right]$ . Here,  $\rho_k$  is the density of phase k (g/cm<sup>-3</sup>),  $\left(\frac{dm}{dt}\right)_k$  is the experimental specific mass change rate (g.cm<sup>-2</sup>.s<sup>-1</sup>) of phase k (obtained from Equation 4.10),  $A_{px}$  is the exposed surface area of a pixel (cm<sup>2</sup>), and  $\Delta t$  is the time step (s).  $V_{px}$  is the volume of a pixel (cm<sup>3</sup>) and is equal to  $A_{px}*L_{px}$ ; where  $L_{px}$  is the pixel height (cm). The density (in g/cm<sup>3</sup>) values for different phases here are: Mo (10.02), A15 (8.97), T2 (8.6), T1 (8.21), SiO<sub>2</sub> (2.65) and B<sub>2</sub>O<sub>3</sub> (2.46).

As noted in section 4.4.1, the amount of oxidation should change based on how exposed a cell is to oxygen which is captured by the interaction areas of cell (i, j) with O<sub>2</sub> from neighboring cells (section 4.4.1). At cell (i, j), an oxidation factor term ( $F_{i,j}^{O_2}$ ) is calculated as:

$$F_{i,j}^{O_2} = A_{i,j}^{A,O_2} + \frac{1}{3}A_{i,j}^{L,O_2} + \frac{1}{3}A_{i,j}^{R,O_2}$$

Equation 4.12

The factor of 1/3 here signifies that the oxygen available in the side cells has three possible sinks (same/below cell, left cell and right cell) and thus only one-third of the oxygen is effectively available for the oxidation of cell (i, j).

Consequently, the phase consumption calculated in Equation 4.11 is then rescaled as:

$$\Delta V_{k,i,j}^{f,\exp} = F_{i,j}^{O_2} \, \Delta V_{k,i,j}^{f,\exp}$$

Equation 4.13

## 4.4.3 Phase consumption due to oxygen flux through the scale

As oxidation progresses, a borosilica glass layer can form and the oxidation cells may no longer have direct access to air through neighboring cells but instead, there is a flux of oxygen through the glassy scale that drives the oxidation. The oxygen flux  $(J_{i,j}^{O_2})$  through the glass layer above a cell (i, j) can be calculated based on the oxygen concentration gradient across the scale and the kinetics of oxygen diffusion through the glass layer. Mathematically [93]:

$$J_{i,j}^{O_2} = \frac{\Pi_{i,j}^{O_2-glass}}{h_{i,j}^{glass}} (p_{O_2}^{air} - p_{O_2}^k) \text{ [moles/(cm^2.s)]}$$

Equation 4.14

where,  $p_{02}^{air}$  is the partial pressure of  $O_2$  in air (=0.21 atm),  $p_{02}^i$  is the partial pressure of  $O_2$  in thermodynamic equilibrium with the phase k present in cell (i, j),  $\Pi_{i, j}^{O_2 - glass}$  is the permeability of  $O_2$  gas in [moles/(cm.s.atm)] through the glass layer above cell (i, j), and  $h_{i, j}^{glass}$  is the height of glass layer above cell (i, j) in [cm].

Since  $p_{02}^{air} \gg p_{02}^k$ , we neglect  $p_{02}^k$  in Equation 4.12. The value of  $h_{i,j}^{glass}$  is calculated as the sum of volume fraction of glass phases in all cells above cell (i, j) multiplied by the length of each pixel i.e.,

$$h_{i,j}^{glass} = L_{px} \sum_{i=0}^{i} (V_{5,i,j}^f + V_{6,i,j}^f)$$

#### Equation 4.15

where  $L_{px}$  is the length of a pixel and  $V_{5,i,j}^f \& V_{6,i,j}^f$  are the volume fraction of silica (k=5) and boria (k=6) at cell (i, j).

Since the glass comprises of both silica and boria which have different oxygen permeabilities, the effective permeability ( $\Pi_{i,j}^{O_2-glass}$ ) through glass layer above cell (i, j) is assumed as the composition-weighted function of individual permeabilities of silica and boria.

$$\Pi_{i,j}^{O_2-glass} = X_{i,j}^{SiO_2,Above} \, \Pi_{SiO_2}^{O_2} + X_{i,j}^{B_2O_3,Above} \, \Pi_{B_2O_3}^{O_2}$$

#### Equation 4.16

where,  $X_{i,j}^{SiO_2,Above}$  &  $X_{i,j}^{B_2O_3,Above}$  are the fractions of silica and boria in glass above cell (i,j), and  $\Pi_{SiO_2}^{O_2}$  &  $\Pi_{B_2O_3}^{O_2}$  are the oxygen permeabilities through pure silica and boria glass.

$$X_{i,j}^{SiO_{2},Above} = \frac{\sum_{i=0}^{i} V_{5,i,j}^{f}}{\sum_{i=0}^{i} \left(V_{5,i,j}^{f} + V_{6,i,j}^{f}\right)} \ \& \ X_{i,j}^{B_{2}O_{3},Above} = \frac{\sum_{i=0}^{i} V_{6,i,j}^{f}}{\sum_{i=0}^{i} \left(V_{5,i,j}^{f} + V_{6,i,j}^{f}\right)}$$

Equation 4.17

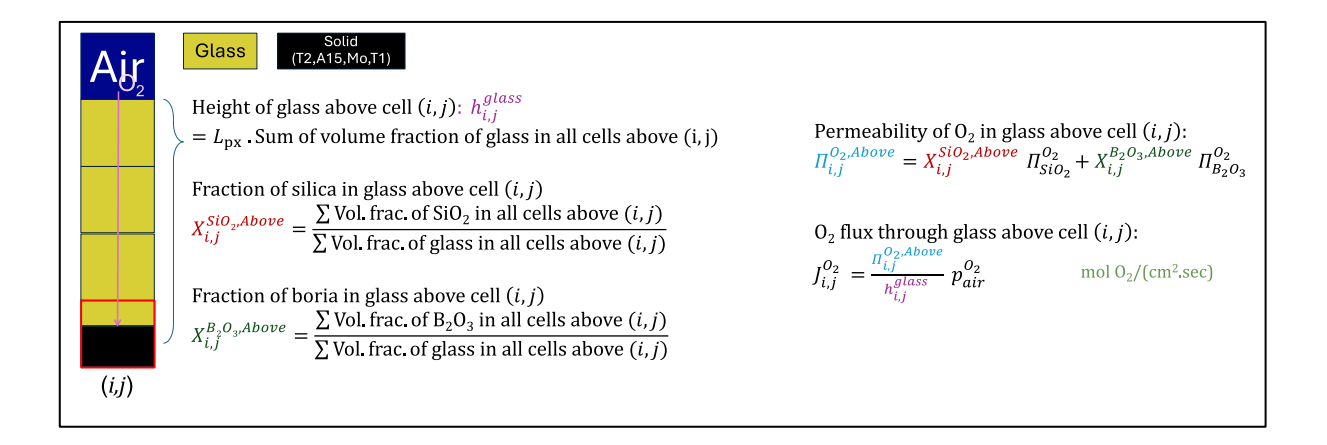


Figure 4.3. Calculating the oxygen flux through glass layer above a cell.

For any cell (i, j), Figure 4.3 shows how the downward flux of oxygen through the glass layer above it can be calculated. But, as shown in Figure 4.4,  $O_2$  can also flow from left and right cells provided these cells have a finite  $O_2$  flux through the glass layer above them. Also, the amount of this flux available to cell (i, j) will depend on the interaction areas  $(A_{i,j}^{L,O_2})$  and  $A_{i,j}^{R,O_2}$  shown in Figure 4.2. Taking this into account, the effective  $O_2$  flux at cell (i, j) is calculated as:

$$J_{i,j}^{O_2,\text{eff}} = A_{i,j}^{A,O_2} J_{i,j}^{O_2} + A_{i,j}^{L,O_2} J_{i,j-1}^{O_2} + A_{i,j}^{R,O_2} J_{i,j+1}^{O_2}$$

Equation 4.18

Based on the flux calculated in equation 17, when a cell (i, j) containing phase k oxidizes, the change in volume fraction of phase k in that cell over one timestep  $(\Delta t)$  is calculated as:

$$\Delta V_{k,i,j}^{\text{f,flux}} = \frac{1}{N_k} J_{i,j}^{O_2,\text{eff}} \, \Delta t \, \frac{M_k}{\rho_k} \left( \frac{1}{L_{\text{px}}} \right)$$

Equation 4.19

where,  $N_k$  is the stoichiometric coefficient of  $O_2$  in oxidation reaction of phase k (i.e., moles of  $O_2$  consumed per mole of phase k),  $M_k$  &  $\rho_k$  are the molar mass and the density of the phase.

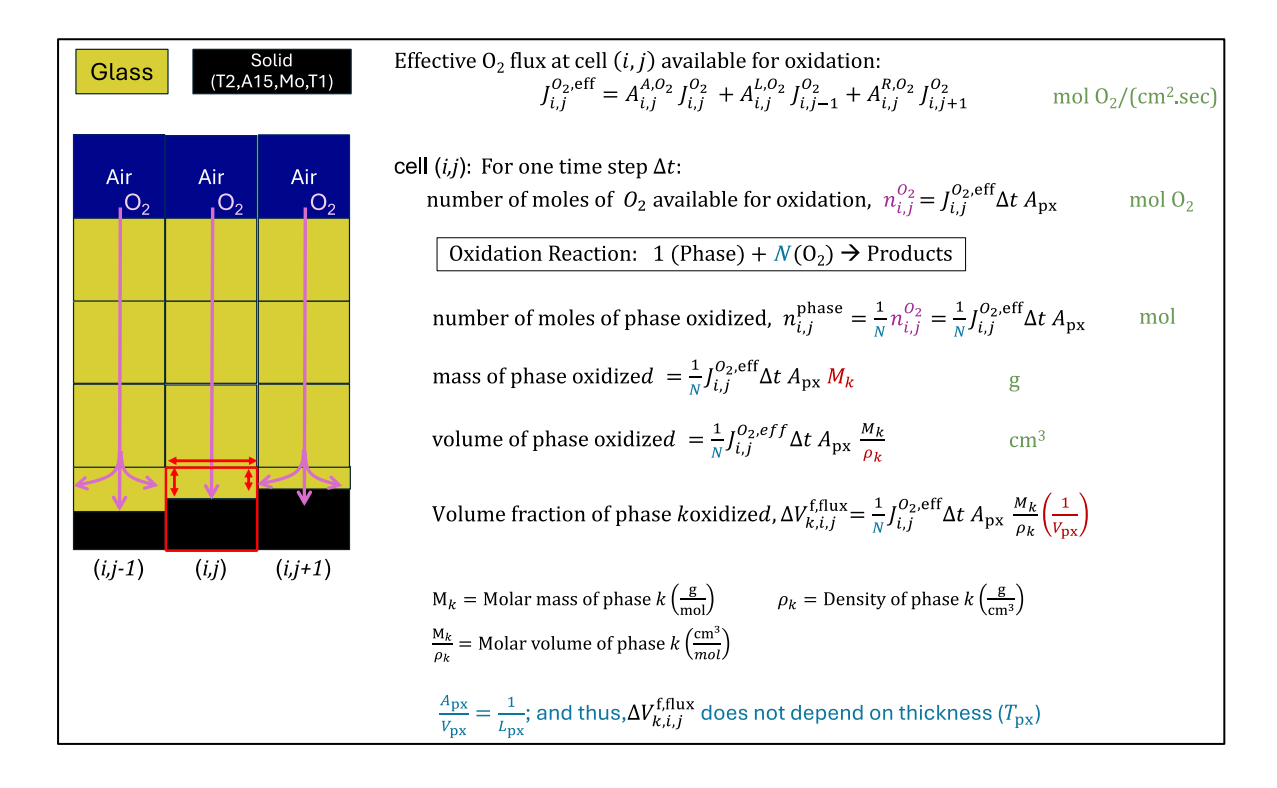


Figure 4.4. Calculating phase consumption based on effective oxygen flux at cell (i, j) taking into account oxygen from both the top as well as left & right cells.

## 4.5 Temporal evolution of microstructure

## 4.5.1 Calculating the state of system after each time-step

At time t, if a phase k ( $k \in \{1 \text{ (T2)}, 2 \text{ (A15)}, 3 \text{ (Mo)}, 4 \text{ (T1)}\}$ ) is present in cell (i, j), then the change in volume fraction of that phase over next time step ( $\Delta t$ ) is calculated as:

$$\Delta V_{k,i,j}^f = -\min(\left|\Delta V_{k,i,j}^{f,\mathrm{exp}}\right|,\left|\Delta V_{k,i,j}^{\mathrm{f,flux}}\right|)$$

Equation 4.20

Initially, when glass layer thickness is very small, magnitude of  $\Delta V_{k,i,j}^{\rm f,flux}$  is very large and outweighs the magnitude of  $\Delta V_{k,i,j}^{f,\rm exp}$ . But, as the glass layer thickness increases, the magnitude of  $\Delta V_{k,i,j}^{\rm f,flux}$  will eventually become smaller than that of  $\Delta V_{k,i,j}^{f,\rm exp}$ . Thus, Equation 4.20 effectively implies that as the oxidation progresses and borosilica scale forms, the oxidation will eventually be limited by the diffusion of  $O_2$  through the glassy scale. Based on the phase consumption calculation in Equation 4.20, the changes in volume fractions of product phases

( $k \in \{5 \text{ (SiO}_2), 6 \text{ (B}_2\text{O}_3), 7 \text{ (MoO}_3)\}$ ) are subsequently calculated using the oxidation reaction stoichiometries.

The following calculations are carried out at each cell (*i*, *j*):

(a) If  $V_{2,i,j}^f > 0$ , i.e. the oxidizing phase is Mo, then:

Mo consumption: 
$$\Delta V_{2,i,j}^f = -\min(|\Delta V_{2,i,j}^{f,\text{exp}}|, |\Delta V_{2,i,j}^{f,\text{flux}}|)$$

Equation 4.21

MoO<sub>3</sub> formation:  $\Delta V_{7,i,j}^f = -\Delta V_{2,i,j}^f$ 

Equation 4.22

Updating the new state of the system after time step ( $\Delta t$ ):

$$V_{k,i,j}^f \Big|_{t+\Lambda t} = V_{k,i,j}^f \Big|_t + \Delta V_{k,i,j}^f$$
 for  $k \in \{2, 7\}$ 

Equation 4.23

(b) If  $V_{3,i,j}^f > 0$ , i.e. the oxidizing phase is A15, then:

A15 consumption:  $\Delta V_{3,i,j}^f = -\min(|\Delta V_{3,i,j}^{f,\text{exp}}|, |\Delta V_{3,i,j}^{f,\text{flux}}|)$ 

Equation 4.24

SiO<sub>2</sub> formation: 
$$\Delta V_{5,i,j}^f = -\Delta V_{3,i,j}^f \left(\frac{\rho_{A15}}{M_{A15}}\right) \cdot 1 \cdot \left(\frac{M_{SiO_2}}{\rho_{SiO_2}}\right)$$

Equation 4.25

MoO<sub>3</sub> formation: 
$$\Delta V_{7,i,j}^f = -\Delta V_{3,i,j}^f - \Delta V_{5,i,j}^f$$

Equation 4.26

Updating the new state of the system after time step ( $\Delta t$ ):

$$V_{k,i,j}^f \Big|_{t+\Delta t} = V_{k,i,j}^f \Big|_t + \Delta V_{k,i,j}^f$$
 for  $k \in \{3, 5, 7\}$ 

Equation 4.27

(c) If  $V_{4,i,j}^f > 0$ , i.e. the oxidizing phase is T1, then:

T1 consumption:  $\Delta V_{4,i,j}^f = -\min(\left|\Delta V_{4,i,j}^{f,\mathrm{exp}}\right|,\left|\Delta V_{4,i,j}^{\mathrm{f,flux}}\right|)$ 

Equation 4.28

SiO<sub>2</sub> formation: 
$$\Delta V_{5,i,j}^f = -\Delta V_{4,i,j}^f \left(\frac{\rho_{T_1}}{M_{T_1}}\right) \cdot 3 \cdot \left(\frac{M_{SiO_2}}{\rho_{SiO_2}}\right)$$

Equation 4.29

MoO<sub>3</sub> formation:  $\Delta V_{7,i,j}^f = -\Delta V_{4,i,j}^f - \Delta V_{5,i,j}^f$ 

Equation 4.30

Updating the new state of the system after time step ( $\Delta t$ ):

$$V_{k,i,j}^f \Big|_{t+\Lambda t} = V_{k,i,j}^f \Big|_t + \Delta V_{k,i,j}^f$$
 for  $k \in \{4, 5, 7\}$ 

Equation 4.31

(d) If  $V_{1,i,j}^f > 0$ , i.e. the oxidizing phase is T2, then:

T2 consumption:  $\Delta V_{1,i,j}^f = -\min(\left|\Delta V_{1,i,j}^{f,\mathrm{exp}}\right|,\left|\Delta V_{1,i,j}^{\mathrm{f,flux}}\right|)$ 

Equation 4.32

SiO<sub>2</sub> formation: 
$$\Delta V_{5,i,j}^f = -\Delta V_{1,i,j}^f \left(\frac{\rho_{T2}}{M_{T2}}\right) \cdot 1 \cdot \left(\frac{M_{SiO_2}}{\rho_{SiO_2}}\right)$$

Equation 4.33

B<sub>2</sub>O<sub>3</sub> formation: 
$$\Delta V_{6,i,j}^f = -\Delta V_{1,i,j}^f \left(\frac{\rho_{T2}}{M_{T2}}\right) \cdot 1 \cdot \left(\frac{M_{B_2O_3}}{\rho_{B_2O_3}}\right)$$

Equation 4.34

MoO<sub>3</sub> formation: 
$$\Delta V_{7,i,j}^f = -\Delta V_{1,i,j}^f - \Delta V_{5,i,j}^f - \Delta V_{6,i,j}^f$$

Equation 4.35

Updating new state of the system after time step ( $\Delta t$ ):

$$V_{k,i,j}^f \Big|_{t+\Lambda t} = V_{k,i,j}^f \Big|_t + \Delta V_{k,i,j}^f$$
 for  $k \in \{1, 5, 6, 7\}$ 

Equation 4.36

It should be noted that at any given cell, only one of the above four calculations (a-d) will occur since these phases (T2, A15, Mo, T1) cannot coexist in a cell. Since the simulations are carried out over sections of the microstructure, boundary conditions were implemented. The bottom row is considered as rigid, and the oxidation model runtime stops when the oxidation front reaches the bottom most row. For the left and right boundaries, we apply a timedependent Dirichlet boundary condition wherein, at the beginning of each time step, the left and right boundary values are assumed to be same as the left and right edge values computed at the end of previous time step. In doing this, the microstructure follows spatial continuity and thus the left and right columns are treated in a way that maintains this continuity. In terms of implementation, this is achieved by attaching two boundary columns (one to the left and one to the right) to the simulation cell such that these columns are not a part of the actual simulation domain and are meant only to provide environment to the left and right most columns in the microstructure. At the beginning of each time step, the left boundary column is changed to match the current state of the left most simulation column and the right boundary column is changed to match the current state of the right most simulation column.

# 4.5.2 Volatilization of MoO<sub>3</sub>

MoO<sub>3</sub>, formed as an oxidation product, volatilizes as (MoO<sub>3</sub>)<sub>3</sub> trimer [217] and can thus easily escape to the environment provided a path is available. In other words, MoO<sub>3</sub> formed in a cell can be replaced by air that may be present in neighboring cells. At the end of a time step, if a cell (i, j) has MoO<sub>3</sub> (i.e.,  $V_{7,i,j}^f > 0$ ), then displacement of MoO<sub>3</sub> by air can occur if:

$$A_{i,j}^{A,O_2} V_{0,i,j}^f + V_{0,i,j-1}^f + V_{0,i,j+1}^f > 0$$

Equation 4.37

If this condition is satisfied, then the state of the system is updated as:

$$\left.V_{0,i,j}^f\right|_{new}=V_{7,i,j}^f$$
 and  $\left.V_{7,i,j}^f\right|_{new}=0$ 

## 4.5.3 Modeling the lateral flow of glass

The borosilica glass formed after oxidation behaves as a highly viscous fluid at high temperatures. At the end of a time step, flow steps are carried in the simulation wherein no oxidation events happen, but if cell (i, j) contains glass, then it can flow outwards to adjacent left (i, j-1) and right (i, j+1) cells provided the elevation of glass in adjacent cells is lower than that in cell (i, j). This flow can continue until the height of glass in all three cells is the same. Mathematically, the outflow required from cell (i, j) to reach the same glass level in all three cells is calculated as:

Outflow to left cell: 
$$\Delta V_{i,j-1}^{f,glass} = \max\left\{\frac{1}{3}\left(2h_{i,j-1}^{air} - h_{i,j+1}^{air} - h_{i,j}^{air}\right),0\right\}$$

Equation 4.39

Outflow to right cell: 
$$\Delta V_{i,j+1}^{f,glass} = \max\left\{\frac{1}{3}\left(2h_{i,j+1}^{air} - h_{i,j-1}^{air} - h_{i,j}^{air}\right),0\right\}$$

Equation 4.40

where,  $\Delta V_{i,j}^{f,glass}$  represents change in volume fraction of glass in cell (i, j),  $h_{i,j}^{air}$  represents height of air in cell (i, j) and is the same as  $V_{0,i,j}^f$  i.e., the volume fraction of air in cell (i, j).

When operating on a cell (i, j) during a flow step, only the outflow is calculated from that cell to adjacent cells and the new volume fraction of glass in adjacent cells will be adjusted accordingly. This is enforced in Equation 4.39 and Equation 4.40 by taking a flow value of zero in instances where a negative (i.e. inward) flow may be calculated. The inward flow in a cell gets compensated for when that cell becomes an adjacent cell to another cell with higher elevation. For example, if elevation of glass in cell (i, j+1) is higher than that in cell (i, j), then when operating on cell (i, j), zero outflow to (i, j+1) will be calculated but when operating on (i, j+1), a positive outflow to (i, j) will be calculated.

There can also be instances where the amount of glass present in (i, j) cell is not sufficient to reach the same elevation in all cells (as shown in Figure 4.5) i.e.,  $V_{i,j}^{f,glass} < (\Delta V_{i,j-1}^{f,glass} + \Delta V_{i,j+1}^{f,glass})$ . In such a case, all the glass present in (i, j) cell will flow out to adjacent cells in the proportion of outflows calculated in Equation 4.39 and Equation 4.40.

Outflow to left cell: 
$$\Delta V_{i,j-1}^{f,glass} = \max \left\{ V_{i,j}^{f,glass} \frac{\Delta V_{i,j-1}^{f,glass}}{\Delta V_{i,j-1}^{f,glass} + \Delta V_{i,j+1}^{f,glass}}, 0 \right\}$$

Equation 4.41

Outflow to right cell: 
$$\Delta V_{i,j+1}^{f,glass} = \max \left\{ V_{i,j}^{f,glass} \frac{\Delta V_{i,j+1}^{f,glass}}{\Delta V_{i,j-1}^{f,glass} + \Delta V_{i,j+1}^{f,glass}}, 0 \right\}$$

Equation 4.42

where,  $\Delta V_{i,j-1}^{f,glass}$  and  $\Delta V_{i,j-1}^{f,glass}$  values on the right hand side of equations are the outflow values calculated from Equation 4.39 and Equation 4.40,  $V_{i,j}^{f,glass}$  is the total amount of glass (silica + boria) volume fraction present in cell (i, j) and is equal to  $V_{5,i,j}^f + V_{6,i,j}^f$ 

Furthermore, at any cell (i, j) the amount of outflow that occurs is also dependent on the viscosity of glass in that cell  $(\eta_{i,j}^{glass})$  which is in turn a function of the glass composition. Thus, while simulating the lateral flow, we scale the outflows calculated above using a viscosity-dependent factor. The experiment results in literature show that the viscosity of pure boria is almost 1000 times lower than that of pure silica. Taking pure boria as a reference, we define a viscosity-based factor  $\eta_{i,j}^o = \frac{1}{(\eta_{i,j}^{glass}/\eta_{B_2O_3})}$  that is calculated at each cell to scale the glass outflow. This means that if the glass comprises of pure boria, then all the flow calculated in above equations will occur whereas if it is a mixture of boria and silica, then the flow will be less depending on the viscosity of glass in that cell. At any cell (i, j), glass viscosity is calculated as:

$$\eta_{i,j}^{glass} = A + B \exp(C.f_{i,j}^{SiO_2})$$

Equation 4.43

where, 
$$A = 4.04, B = 1.46 \times 10^{-14}, C = 38.054, \ f_{i,j}^{SiO_2} = \frac{V_{5,i,j}^f \left(\frac{\rho_{SiO_2}}{M_{SiO_2}}\right)}{V_{5,i,j}^f \left(\frac{\rho_{SiO_2}}{M_{SiO_2}}\right) + V_{6,i,j}^f \left(\frac{\rho_{B_2O_3}}{M_{B_2O_3}}\right)}$$
 is

the mole fraction of  $SiO_2$  in the glass present in cell (i, j)

At the beginning of a flow step, the new state of system array is created as a copy of the existing state of the system array and is then updated based on these outflow calculations at each cell (i, j):

• Updating SiO<sub>2</sub> & B<sub>2</sub>O<sub>3</sub> volume fraction in left cell:

$$\left. V_{5,i,j-1}^{f} \right|_{new} = \left. V_{5,i,j-1}^{f} \right|_{prev} + f_{i,j}^{SiO_2} \, \Delta V_{i,j-1}^{f,glass}$$

Equation 4.44

$$V_{6,i,j-1}^f \big|_{new} = V_{6,i,j-1}^f \big|_{nrev} + \left(1 - f_{i,j}^{SiO_2}\right) \Delta V_{i,j-1}^{f,glass}$$

Equation 4.45

• Updating SiO<sub>2</sub> & B<sub>2</sub>O<sub>3</sub> volume fraction in right cell:

$$V_{5,i,j+1}^f\Big|_{new} = V_{5,i,j+1}^f\Big|_{nrev} + f_{i,j}^{SiO_2} \Delta V_{i,j+1}^{f,glass}$$

Equation 4.46

$$\left. V_{6,i,j+1}^{f} \right|_{new} = \left. V_{6,i,j+1}^{f} \right|_{prev} + \left( 1 - f_{i,j}^{SiO_2} \right) \Delta V_{i,j+1}^{f,glass}$$

Equation 4.47

• Updating SiO<sub>2</sub> & B<sub>2</sub>O<sub>3</sub> volume fraction in (i, j) cell:

$$V_{5,i,j}^{f}\big|_{new} = V_{5,i,j}^{f}\big|_{nrev} + f_{i,j}^{SiO_2} \left(\Delta V_{i,j-1}^{f,glass} + \Delta V_{i,j+1}^{f,glass}\right)$$

Equation 4.48

$$V_{6,i,j}^{f}\big|_{new} = V_{6,i,j}^{f}\big|_{nrev} + (1 - f_{i,j}^{SiO_2}) (\Delta V_{i,j-1}^{f,glass} + \Delta V_{i,j+1}^{f,glass})$$

Equation 4.49

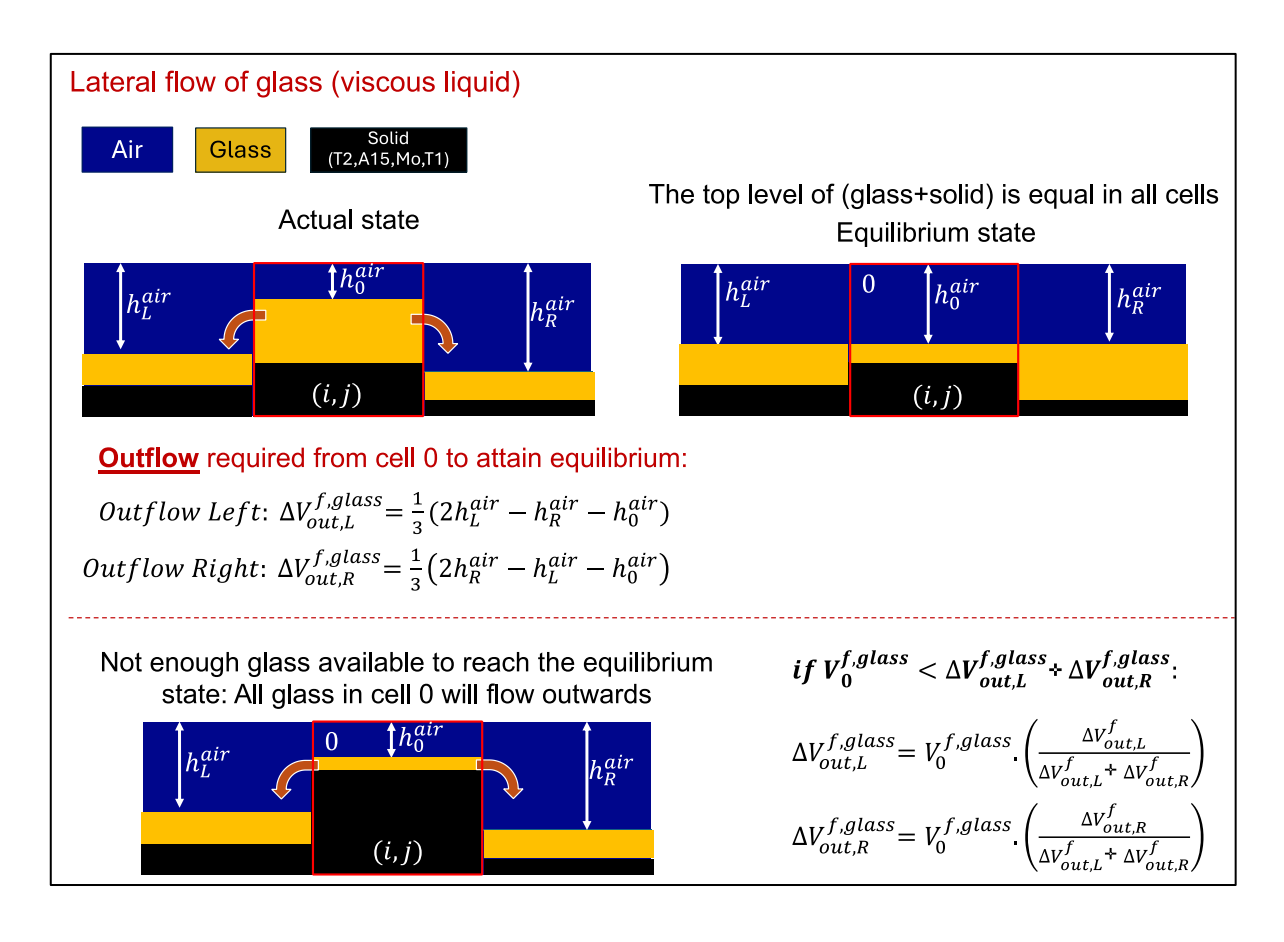


Figure 4.5. Modelling lateral flow of glass

#### 4.6 Results & Discussion

# 4.6.1 Simulating microstructure evolution during oxidation

The oxidation modeling framework detailed in section 4.2- 4.5 was used to simulate the temporal evolution of microstructure during oxidation of Mo-Si-B alloys. Figure 4.6 shows the simulation results for alloy 711 which contains 70% Mo, 15% Si and 15% B. The alloy compositions are mentioned in Table 4.1. The as-cast microstructure contains three phases: Mo-solid solution, A15 (Mo<sub>3</sub>Si) and T2 (Mo<sub>5</sub>SiB<sub>2</sub>). The oxidation simulation was done at 1100 °C using a time-step of 0.1 seconds on a segmented microstructure with a pixel size of 0.0621  $\mu$ m. The state of the system array calculated at each time step captures the volume fraction of all phases at each cell. The first row in Figure 6 shows how the overall microstructure evolves as a function of oxidation time, whereas the subsequent rows show the evolution of volume fraction phase maps for individual phases. The Mo (ss) phase has the highest oxidation rate and does not form any glass as it oxidizes. The simulation also shows that, as we go from

t=0 s to t=10 s, the Mo (ss) phase that is exposed to air gets rapidly consumed causing the formation of a pit due to (MoO<sub>3</sub>)<sub>3</sub> volatilization. On the contrary, A15 forms silica and T2 forms borosilica glass upon oxidation and we observe the formation of a glass layer on top of these phases. As seen at t=10 s and t=50 s, this glass also flows into the cavity created by Mo (ss) oxidation. As time increases, the glass layer coverage over the surface becomes much more uniform.

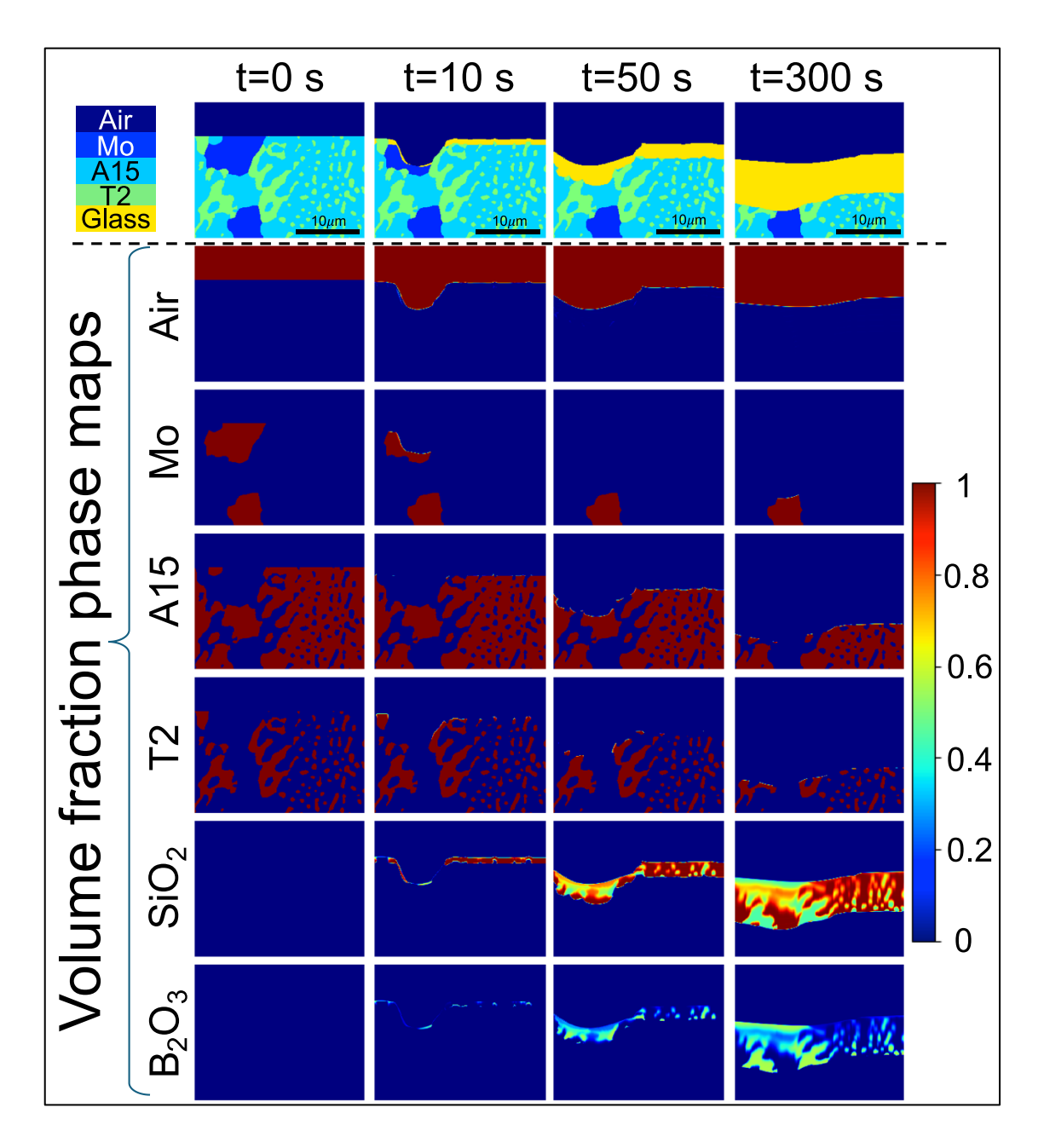


Figure 4.6. Oxidation simulation for alloy 711 (70% Mo-15% Si-15%B). The first row shows the microstructure evolution as oxidation time increases (t=0 s, 10 s, 50 s, 300 s). Here, the phase label at each pixel was decided based on which phase has the highest volume fraction at the pixel. Rows 2-7 show the volume fraction phase maps of each individual phase as a function of time. The color bar on right (spanning from 0 to 1) is mapped to the volume fractions.

The individual phase maps of boria and silica at t=50 s and t=300 s show that the glass that flowed into the Mo (ss) pits have a higher boria content confirming that the boria containing glass undergoes larger flow during the simulation due to its lower viscosity.

## 4.6.2 Effect of alloy chemistry on oxidation

The chemical composition of an alloy strongly affects its microstructure which in turn affects the oxidation phenomenon and how the microstructure will evolve during oxidation. The model developed in this work is a microstructurebased model and while we can't take the chemical composition directly as an input, we can take the microstructures corresponding to different alloy compositions as the input and then simulate their evolution during oxidation. Figure 4.7 shows the oxidation simulation results over small microstructural regions for seven different alloy compositions (a) 711: 70%Mo-15%Si-15%B, (b) **721**: 70%Mo-20%Si-10%B, (c) **811**: 80%Mo-10%Si-10%B, (d) **821**: 80%Mo-13.33%Si-6.66%B, (e) **711-15W**: 55%Mo-15%W-15%Si-15%B, (f) **711-5Ta**: 65%Mo-5%Ta-15%Si-15%B, (g) **721-5Ta**: 65%Mo-5%Ta-20%Si-10%B. These alloys have unique microstructures with different type, amount and morphology of phases that are present. For example, alloy 811 and 821 have large Mo (ss) phases whereas 711-5Ta & 721-5Ta do not contain Mo (ss) phase. Figure 4.7 shows that microstructural evolution during oxidation occurs quite differently for different alloys. 811, 821 and 711-15W alloys contain significant amounts of Mo (ss) phases which when exposed to air quickly oxidizes to form (MoO<sub>3</sub>)<sub>3</sub> trimer which is volatile and leaves behind cavities. Moreover, the oxidation of Mo (ss) phase does not form any glass layer and thus the simulations a significantly lower thickness glass scale on these alloys as compared to other alloys that contain less amount of Mo (ss) phases. The Tacontaining alloys do not have any Mo (ss) phases and thus form a uniform and thick glass layer quite early during the oxidation process.

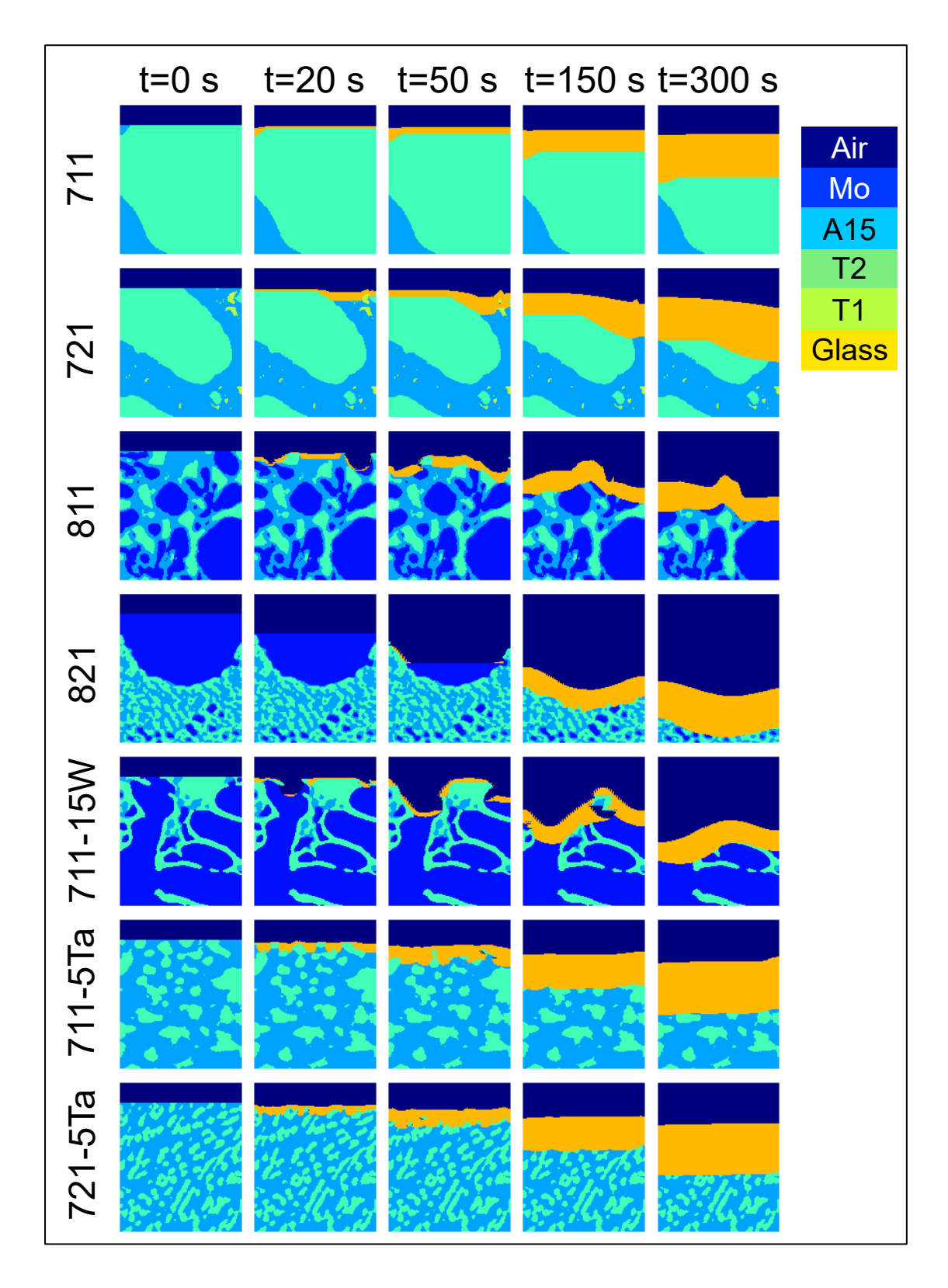


Figure 4.7. Oxidation simulation for seven Mo-Si-B based alloys wherein small slices were extracted from the actual microstructures to model the evolution. (a) 711: 70%Mo-15%Si-15%B, (b) 721: 70%Mo-20%Si-10%B, (c) 811: 80%Mo-10%Si-10%B, (d) 821: 80%Mo-13.33%Si-6.66%B, (e) 711-15W: 55%Mo-15%W-15%Si-15%B, (f) 711-5Ta: 65%Mo-5%Ta-15%Si-15%B, (g) 721-5Ta: 65%Mo-5%Ta-20%Si-10%B

#### 4.6.3 Oxidation kinetics

As the modeling framework here calculates the state of the system array (containing volume fraction of all phases in each cell) at every time step, we can calculate the specific mass change for each time step based on the changes in volume fraction of phases. Figure 4.8 a shows the oxidation kinetics (mass change as a function of time) for the seven alloys simulated in section 4.6.2, and Figure 4.8 b shows the experimentally measured oxidation kinetics for the same alloys. The model predicts that alloys 711 and 721 have similar oxidation kinetics, which are in agreement with the experimental measurements also wherein very similar mass change curves were obtained experimentally for these alloys. The model predicts that the addition of Ta to 711 and 721 will not have any adverse effect on the oxidation kinetics, whereas the addition of W will significantly increase the oxidation kinetics. The experimental results also show similar trends wherein the addition of 5% Ta to 711 and 721 actually improves the oxidation resistance whereas the addition of W increases the oxidation kinetics drastically. This shows that the oxidation model can capture the effect of alloy chemistry on oxidation provided we have the alloy microstructure that can be used as input for oxidation simulations.

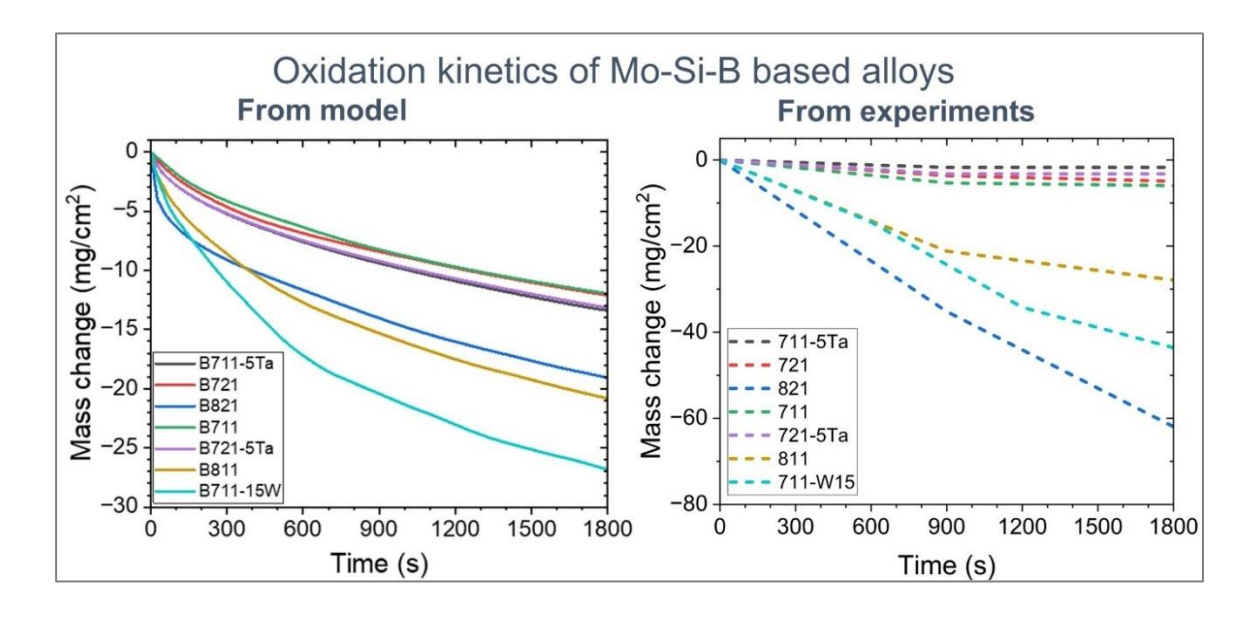


Figure 4.8. Oxidation kinetics for Mo-Si-B based alloys based on (a) oxidation simulations and (b) experimental measurements.

#### 4.6.4 The effect of microstructure length scale on oxidation kinetics

To observe the effect of microstructural size scale on oxidation kinetics, we performed the oxidation simulation on three micrographs that correspond to the same alloy composition (Mo-14.2 at.% Si-9.6 at.% B) but differ in the size of phases present in them. These micrographs (shown in Figure 4.9) were obtained from Rioult et al [17] who had extracted these three samples from different positions within the same ingot. Size 1 sample was extracted from the ingot surface and has a finer microstructure since it experienced higher cooling rate as compared to Size 2 and Size 3 samples that were extracted from regions away from the surface. The model predicts a lower mass change for Size 1 than Size 2 & 3, and predicts almost similar mass changes for Size 2 & 3 samples. The experimental results from Rioult et al. [17] also show similar trends, albeit the experimentally observed increase in oxidation kinetics is larger than that predicted by the model.

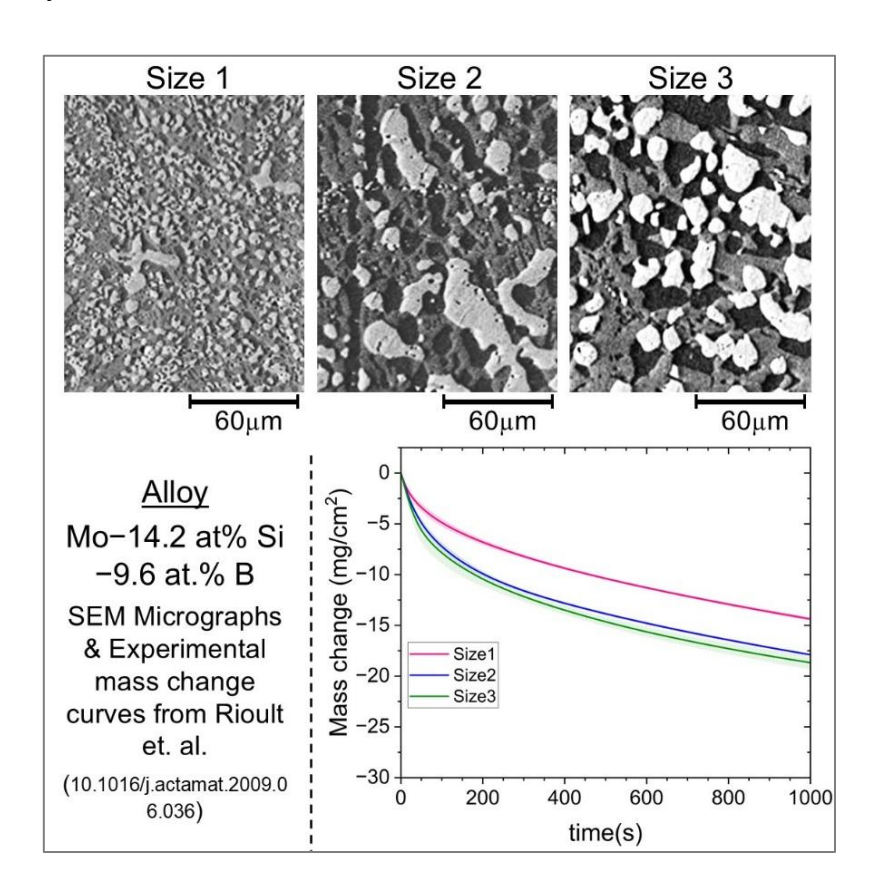


Figure 4.9. Oxidation kinetics calculated for three different microstructural size scales of same alloy composition [Mo-14.2 at.% Si-9.6 at.% B]. The SEM micrographs and experimental mass change results were obtained from Rioult et al. [17]

The smaller size of Mo-phase in Size 1 sample results in formation of smaller pits after MoO<sub>3</sub> volatilization that can be filled relatively easily by the flow of glassy scale as compared to the larger pits that form in Size 2 & 3 samples owing to larger size of Mo-phase in them. This can also be seen in the microstructure evolution in Figure 4.10 as predicted by the model, wherein a uniform glassy scale starts appearing in Size 1 sample after around 50 s whereas it does not appear in Size 3 sample even after 200 s. The microstructural evolution shows that the flow of glassy scale is not able to keep up with the large MoO3 volatilization that happens in Size 3 sample due to the presence of large continuous Mo phase regions.

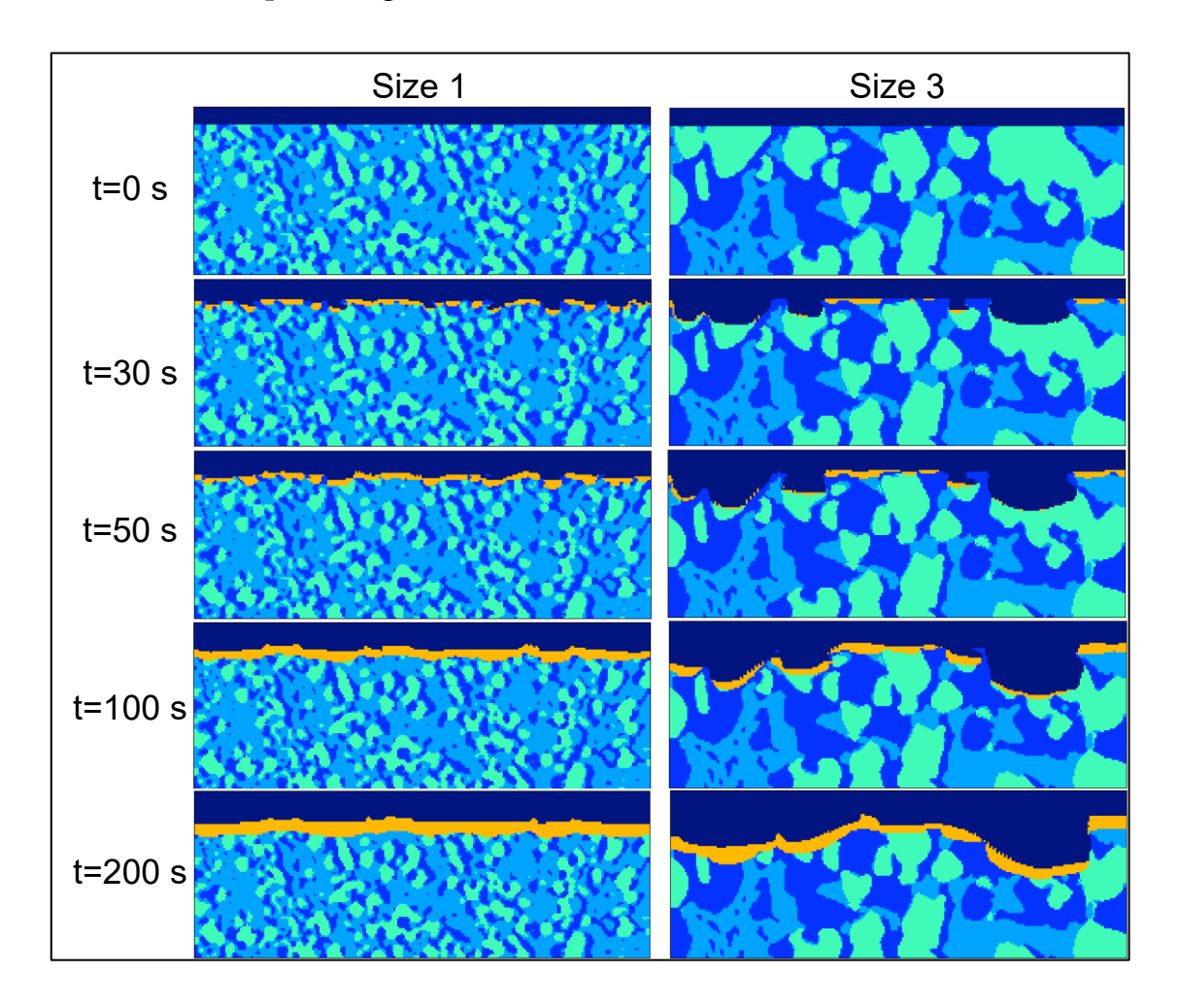


Figure 4.10. Visualization of microstructure evolution during oxidation of Size 1 and Size 3 samples shown in Fig 9.

## 4.7 Summary

We developed a CA model for modeling the oxidation behavior of silica forming materials (specifically, Mo-Si-B based alloys). The CA model developed over here differs from the traditional CA model in that a single cell is assigned different fractions of multiple states. This allows us to ensure that we capture the effects at a finer length scale than would have been normally possible. This also allows us to factor in the differential reaction rates for the different phases present. The model is based on phase consumption rates obtained experimental inputs from the pure phases, which are already reported in the literature, as well as from diffusivity values and oxygen permeability through the glass. The rules for updating the state of the cell are based on the phase fractions of each phase present in the cell as well as the conditions of the neighboring cells (considered in a Von Neuman neighborhood). The model thus developed could simulate the evolution of the oxide scale and the crosssection microstructure as a function of time. The microscopic changes are reflected in the states of the cell, which was then used to compute oxidation kinetics where a good match was seen with the experimental data. We used this model to assess the effect of alloy chemistry, where the effects of changing the refractory metal content as well as Ta and W substitutions (which modifies the microstructure and phase assemblages) were studied. Finally, we also assessed the effect of the alloy microstructure length scale and demonstrated the effect of microstructure on oxidation behavior of the material. The oxidation behavior of Mo-Si-B alloys show a significant microstructural length scale dependence with finer microstructures resulting in lower volatilization and quicker scale coverage of the volatilized regions which in turn improved the oxidation resistance. The model developed here, therefore, has the potential to help tailor the alloy chemistry and microstructures to optimize the oxidation resistance.

# Chapter 5 Oxidation behavior of refractory metal silicides with boron additives

#### 5.1 Introduction

Molybdenum silicides doped with boron have emerged as favorable candidates for high temperature applications [17,177,218,219]. These alloys form a glassy borosilica scale which can provide excellent oxidation resistance at high temperatures in dry air [30,177]. The applicability of these alloys are limited primarily by three factors - (i) presence of a brittle A15 phase which neither affords ductility nor oxidation resistance [17,220,221] (ii) efficient hermetic surface coverage by the glassy borosilica scale [17,63,220,221] and (iii) moisture content in the environment [43,220]. In this work, we address the first two aspects through controlled alloying of Mo-Si-B compositions. The choice of W in destabilizing the A15 phase has been influenced by earlier works [16,55,63] while the choice of alloying additions for improved scale coverage has been motivated by the possibility of tuning the scale viscosity [171]. We examine the efficacy of various alloying additions on oxidation resistance at 1100 and 1350 °C and demonstrate that the formation of a protective glassy scale and subsequent hermetic surface coverage can be obtained by tuning the scale chemistry through a control over the base alloy compositions.

Boron doped Mo-Si alloys form multiple phases as shown in Figure 5.1 that are considered capable of providing oxidation resistance and mechanical properties that depend on their composition. Metal rich solid solution phase in

Mo-Si-B alloys provides toughness and Mo<sub>5</sub>SiB<sub>2</sub> (T2) provides excellent oxidation resistance as it forms a protective borosilica scale upon oxidation [17,32,177]. This scale stays protective up to around 1300 °C [30,222]. Another phase Mo<sub>3</sub>Si (A15) is brittle, imparts poor fracture toughness and does not provide significant oxidation resistance [17]. Therefore, W and Nb addition to Mo-Si-B alloys was done earlier to destabilize the detrimental A15 phase in Mo-Si and Mo-Si-B alloys [16,55,63,223]. Akinc et al. [30] and Meyer et al. [26] studied these alloys with compositions lying in region containing Mo<sub>5</sub>Si<sub>3</sub> (T1), T2 and A15 (shaded in green). The alloys in this region exhibit impressive oxidation resistance but lack fracture toughness (2-4 MPa√m) [224]. Another region that many researchers [6,17,30,31] have studied comprises of Mo(ss), T1 and A15 phases also known as Berczik triangle (shaded in orange) [40]. The alloys in this region have good toughness due to presence of Mo(ss) [225,226]. Therefore, a three-phase microstructure with T1 phase, T2 and metal-rich solid solution phase is desirable. The type and quantity of phases dictates the alloy mechanical and oxidation properties and decides the scale composition under certain environmental conditions. Therefore, it is important to carefully control the substrate composition to get a protective and stable oxide scale.

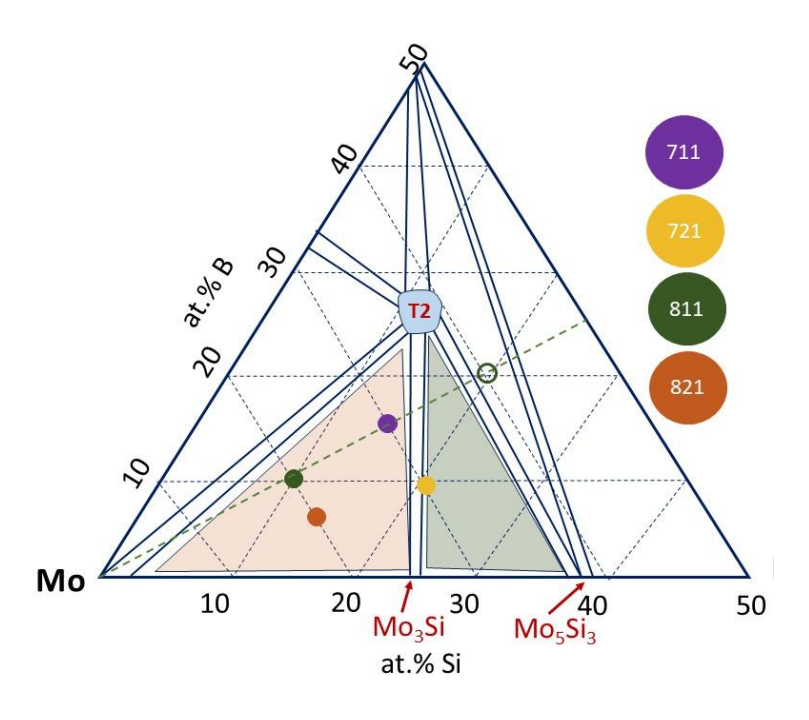


Figure 5.1 Selected compositions marked on phase diagram of Mo-Si-B alloys at 1600 °C

Karahan et al. [55] found that A15 phase in alloy with 70 at % Mo, 15 at % Si and 15 at% B destabilized by substituting 15 at% of Mo with W. But they observed degradation in oxidation properties of the alloy at 1100 °C and some improvement at 1400 °C. The properties degraded at lower temperature because WO<sub>3</sub> that forms during oxidation does not show pesting below 1300 °C unlike MoO<sub>3</sub> and stays on the substrate hindering the borosilica scale flow. Complete volatilization of WO<sub>3</sub> at 1400 °C imparting better flow and improved oxidation resistance was reported [55]. Therefore, exploring the oxidation behavior within 1300-1400 °C since a transition in the oxidation mechanism is expected to occur in this range. Another important consideration is the amount of metal content in the alloy. As enrichment in metal phase improves fracture toughness (albeit with a concomitant loss of oxidation resistance), it is crucial to investigate the region with high Mo content. Additionally, the right balance of Si/B ratio impacts the scale properties, so, in this work, oxidation properties of alloys rich in Mo with varying Si/B were studied [6,30]. SiO<sub>2</sub>-rich oxide passivates and protects the substrate at higher temperatures. Due to its high viscosity at lower temperatures, the flow of glassy scale becomes difficult. Boron addition reduces the scale viscosity and increases flowability and surface coverage. The scale viscosity above 1200 °C is influenced by two competing factors: (i) evaporation of boria [213] which would make the scale *more* viscous and (ii) accelerated diffusivity and mobility at elevated temperatures which would make the scale <u>less</u> viscous.

Zeman et al. [171] reported that Ta which forms  $Ta_2O_5$  during oxidation improved oxidation behaviour of Si based hard coatings. Additionally, it is reported that the presence of  $Ta_2O_5$  in borosilica glasses increases their viscosity [227]. Ta is an electropositive element (significantly more electropositive than Mo or Si). Hence, Ta present in Mo-Si-B alloys can migrate to the oxide scale resulting in the formation  $Ta_2O_5$  during oxidation leading to a change in oxide scale chemistry and viscosity. Any change in viscosity will affect surface coverage and oxidation properties of the alloys. To the best of our knowledge,

reports on the effect of Ta addition on oxidation behaviour of Mo-Si-B are not available. Therefore, we have studied the effect of Ta addition to these alloys.

In chapter 3, the effect of elemental additions on diffusion through SiO<sub>2</sub> and its viscosity was studied where Al addition reduced the scale viscosity. Viscosity is an important parameter that affects the protective nature of oxide scale. In oxidation studies of pure Mo<sub>3</sub>Si phase alloyed with Al, Ochiai [173,221] reported improvement in oxidation resistance as it reduced MoO<sub>3</sub> pesting. In another work, 1 mol % Al addition improved oxidation resistance of Mo-Si-B alloys by forming a dense and complex Si-Al-O oxide in the temperature range of 800 °C to 1300 °C [228]. In the selected compositions of alloys, Al addition can modify scale composition, structure or viscosity and may improve oxidation resistance. Therefore, the effect of Al addition was also studied.

In this work, different compositions of Mo-Si-B alloys were investigated to answer the following questions.

- a. It is known that with increase in Mo content, the ductility improves, but oxidation resistance becomes a challenge. If Mo is increased from 70 to 80 at%, how will tungsten addition affect the oxidation resistance and how much tungsten is needed to remove the A15 phase?
- b. Since tungsten differentially partitions into T1 and T2 phases [63], will the tungsten required also change with different Si to B ratio?
- c. How will Ta and Al addition affect the oxidation behavior of the Mo-Si-B alloys?

# 5.2 Materials and Methods

#### 5.2.1 Experimental methods

Mo-Si-B based alloys with compositions mentioned in Table 5.1 were fabricated using arc melting process. Material chunks with ≥99.5 % purity (procured from Sigma Aldrich and Alfa Aesar) was weighed in the required amount and kept on a water-cooled copper hearth inside the vacuum chamber. The materials

were arc-melted in the presence of argon gas using a tungsten electrode. To ensure homogeneity, each sample was remelted at least 10 times. Then the samples were drop-cast to obtain cylinders. Samples with 80 at% and 70 at% metal content were prepared with Si/B ratio as 1 and 2 for both series based on compositions marked in Figure 5.1. Alloys with 70 and 80 at% Mo were considered as baseline alloys. To observe the effect of W and Ta addition, 10, 15, 20 at% W and 5 at% Ta was added at the expense of Mo such that the total Mo+W or Mo+Ta content remains as 80 at% in 8 series alloys and 70 at% in 7 series baseline alloys. The naming of fabricated alloys was done such that the first digit represents the total metal content, and the last two digits represent Si/B ratio. For example, alloy 811 has 80 at% Mo, Si/B ratio equals to 1/1 and for alloy 811-W20, 8 represents a total of 80 at% metal out of which 20 at% is W, 60 at% is Mo. The effect of Al addition on oxidation was studied by adding 5 at% Al to alloy 811 and 821 and the alloys were named as 811-5Al (76Mo-9.5Si-9.5B-5Al) and 821-5Al (76Mo-12.67Si-6.33B-5Al) (Table 5.1).

Table 5.1 Composition of fabricated alloys for oxidation studies

Alloy	Mo (at %)	W (at %)	Ta (at %)	A1 (at%)	Si (at %)	B (at %)
Nomenclature						
711	70	-	-	-	15	15
711-W10	60	10	-	-	15	15
711-W15	55	15	-	-	15	15
721	70	-	-	-	20	10
721-W10	60	10	-	-	20	10
721-W15	55	15	-	-	20	10
811	80	-	-	-	10	10
811-W10	60	10	-	-	10	10
811-W15	65	15	-	-	10	10
811-W20	60	20	-	-	10	10
821	80	-	-	-	13.33	6.67
821-W10	60	10	-	-	13.33	6.67
821-W15	65	15	-	-	13.33	6.67
821-W20	60	20	-	-	13.33	6.67
711-5Ta	65	-	5	-	10	10
721-5Ta	65	-	5	-	13.33	6.67
811-5Al	76	-	-	5	9.5	9.5
821-5Al	76	-	-	5	12.67	6.33

The as-cast alloys were sectioned and polished using emery papers up to 2500 grit size followed by alumina polishing and ultrasonic cleaning in ethanol.

Phase analysis was done by X-ray diffraction (XRD, PANalytical XPERT-PRO, Cu-Kα radiation = 1.54 Å) using powdered samples to identify the phases formed. Rietveld refinement was done using GSAS II to quantify the phases [214]. Microstructural characterization was done using Scanning Electron Microscopy (SEM, JEOL-6610LV) and Energy Dispersive Spectroscopy (EDS).

The oxidation behavior of the alloys was studied at 1100 °C and 1350 °C in a preheated tube furnace that was calibrated using multiple thermocouples. Transient oxidation was done for short time intervals starting with 30 s of exposure. After this, SEM and EDS analyses were done and then samples were re-inserted in the furnace for the next 30 s making a total of 60 s of exposure. This was repeated up to 120 s to observe the oxide scale evolution in initial stages. At each step, the same region from the sample was carefully focused under SEM to capture the change in oxide formation more precisely. The oxidation kinetics were assessed over a period of 20 h. The change in mass was measured using a microbalance by taking samples out from the furnace after certain time intervals. The oxidized samples were further characterized using XRD and SEM (to obtain cross-section micrographs from where the oxide scale thicknesses could be measured).

# 5.3 Microstructures of Mo-Si-B alloys

The as-cast Mo-Si-B alloys 711, 811 and 821 constituted of Mo solid solution (ss), Mo<sub>3</sub>Si (A15) and Mo<sub>5</sub>SiB<sub>2</sub> (T2) phases in different proportions as mentioned in Table 5.2. The phases were identified from XRD analysis (Figure 5.2), and the phase quantification was done using Rietveld refinement with GSAS II [214]. The lattice parameters for each phase for all alloys is mentioned in Table 5.3. Mo(ss) was absent in alloy 721 and phases T1 (7.5 wt%), T2 (35.5 wt%) and A15 (57 wt%) were present. Addition of 10 at% tungsten eliminated A15 phase and resulted in the formation of a 36.5 wt% Mo,W (ss) phase along with 32.2 wt% T1 and 31.3 wt% T2. In alloy 711, the addition of 15 at% W eliminated the A15 phase which is same as the amount reported by Karahan et al. [55]. On increasing the amount of tungsten from zero to 10 at% and then to

15 at%, the amount of T2 phase decreased in 711 alloy. When A15 destabilized in alloy 721 at 10 at%, further tungsten addition minutely increased T2 phase. In alloys 811 and 821, 20 at% W removed the A15 phase. Addition of 5 at%, 10 at% and 15 at% tungsten could not eliminate A15 phase and the amount of T2 phase decreased on increasing amount of tungsten and at 20 at% W addition minute increment in T2 phase was observed similar to alloy 721. It clearly shows that once A15 destabilizes, tungsten addition does not affect T2 phase composition much. The increase in tungsten content also increases Mo-W solid solution phase in all the alloys. Referring to the ternary phase diagram in Figure 5.1, it shows that higher Mo/Si ratio promotes A15 formation. When tungsten is added Mo-W solid solution forms that reduces the effective Mo/Si ratio for intermetallic formation. This promotes the formation of T1 phase at higher tungsten content which is associated with significantly more Mo-W solid solution.

The compositions 811, 821 and 711 marked in phase diagram lie in the regions where A15 phase is stable. At fixed Si/B ratios, the Mo content must reduce so that the compositions shift to region the regions where A15 phase is not stable. In alloy 811, A15 is present and if Mo content is changed to 60 at % keeping Si/B ratio as 1/1, then the composition will shift to the region where A15 is not present (as shown using green circle in Figure 5.1). In this case the Mo content is reduced by substituting it with 20 at % tungsten. Similarly for alloy 711 with 70 at% Mo, addition of tungsten greater than 10 at% will shift the composition to that region. Table 5.2 shows that solid solution phase increases as W content is increased from 10 at% to 20 at% in alloys with 80 at% metal content. The partitioning of W into a phase can be explained based on the Meidema interaction parameters. The Miedema interaction parameter for W in Si is -110 kJ/mol, Si in W is -102 kJ/mol, Mo in Si is -126 kJ/mol and Si in Mo is -120 kJ/mol. This indicates that Mo-Si interactions are strongest [229]. Since W in Si has higher enthalpy than Mo in Si, formation of W-Si bonds in A15 will increase its formation enthalpy. According to Karahan et al. [55], when W is added, most of it partitions into Mo (ss) and T2 phases because Mo-Si interaction is stronger than W-Si interaction [230,231] and when W goes into solid solution and T2 phase, the number of Mo-Si bonds in T1 phase remains higher. The microstructures of as-cast alloys are shown in Figure 5.3 and Figure 5.4.

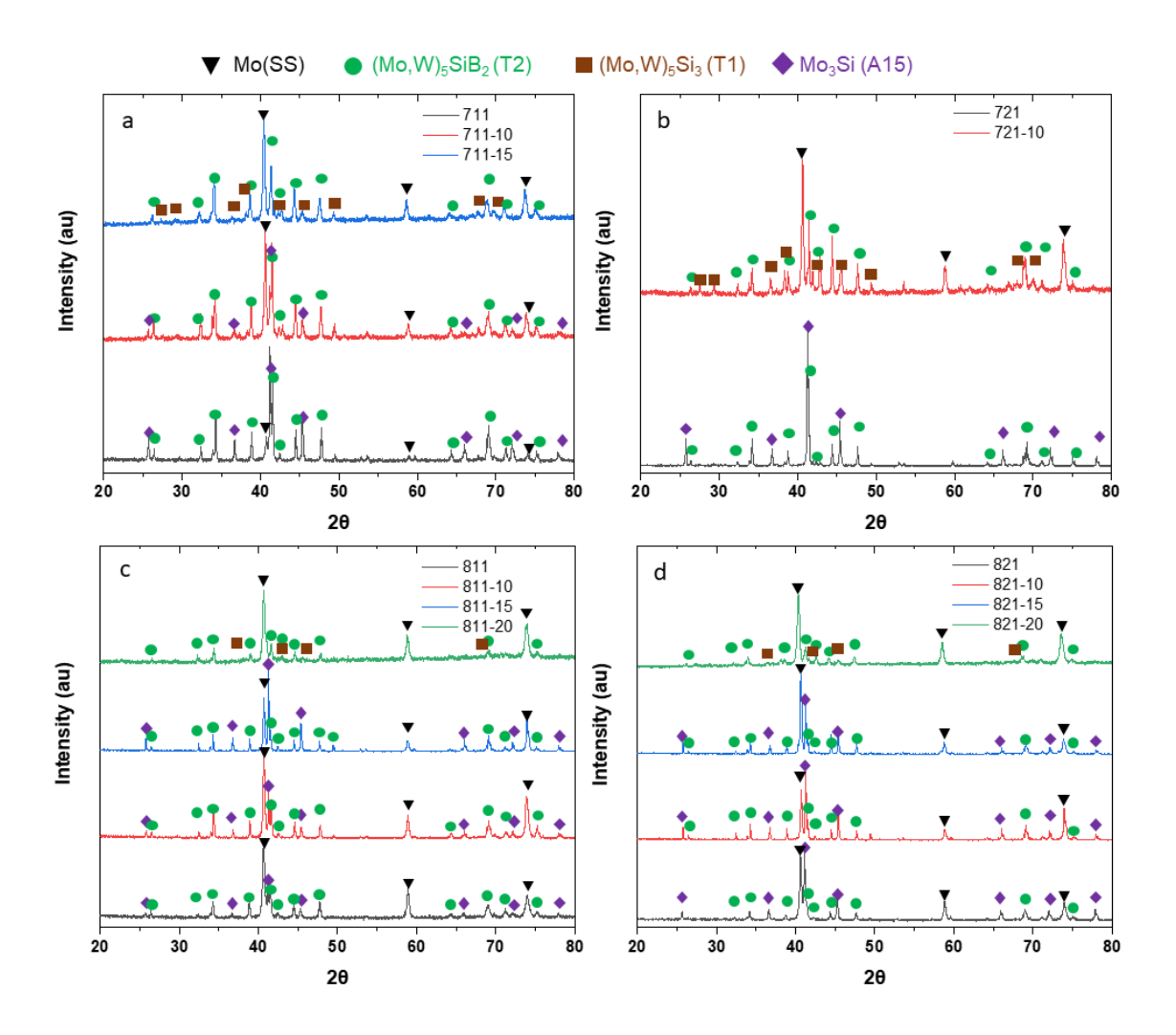


Figure 5.2 X-ray diffraction showing phases present in each alloy. Mo $_3$ Si (A15) phase eliminated after the addition of 20 at% W in alloy 811 and 821 with 15 at% W in alloy 711 and with 10 at% W in alloy 721.

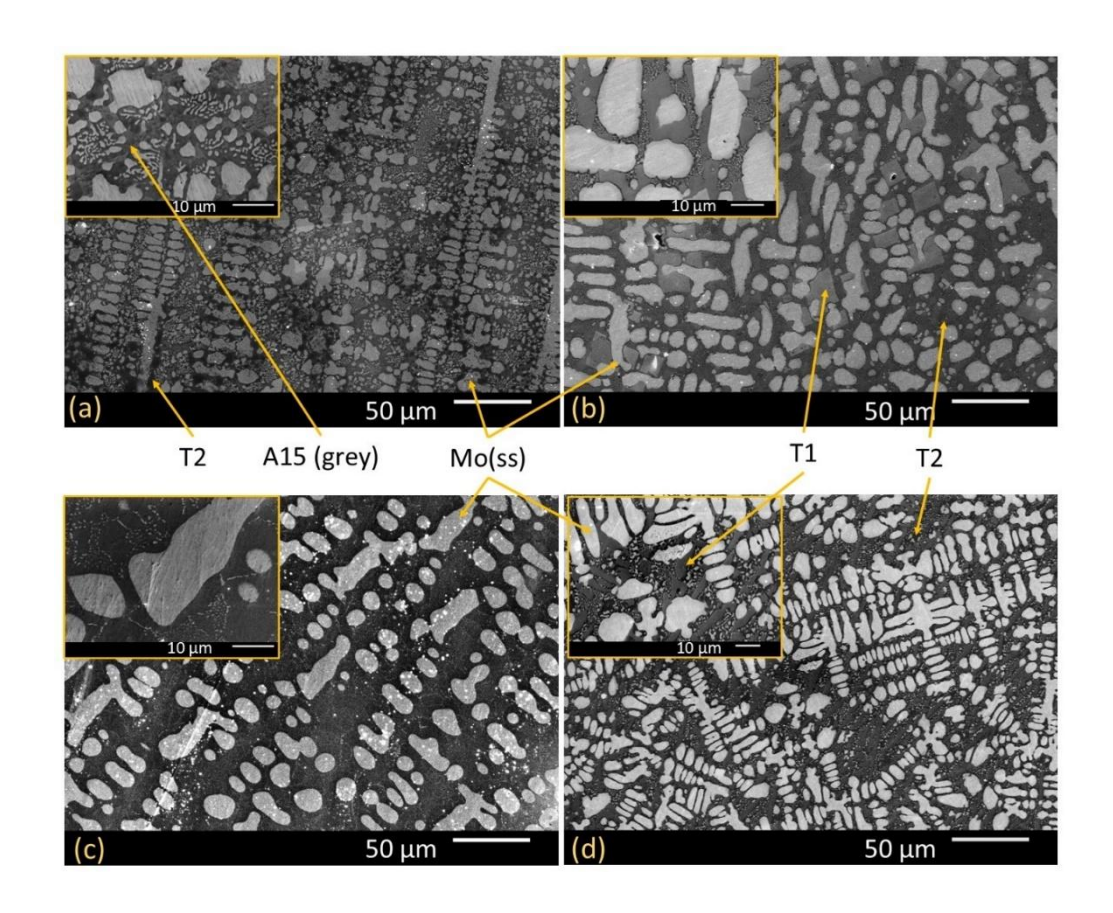


Figure 5.3 SEM (SE mode) images of as-cast (a) 811 (b) 811-W20 (c) 821 and (d) 821-W20 alloys.

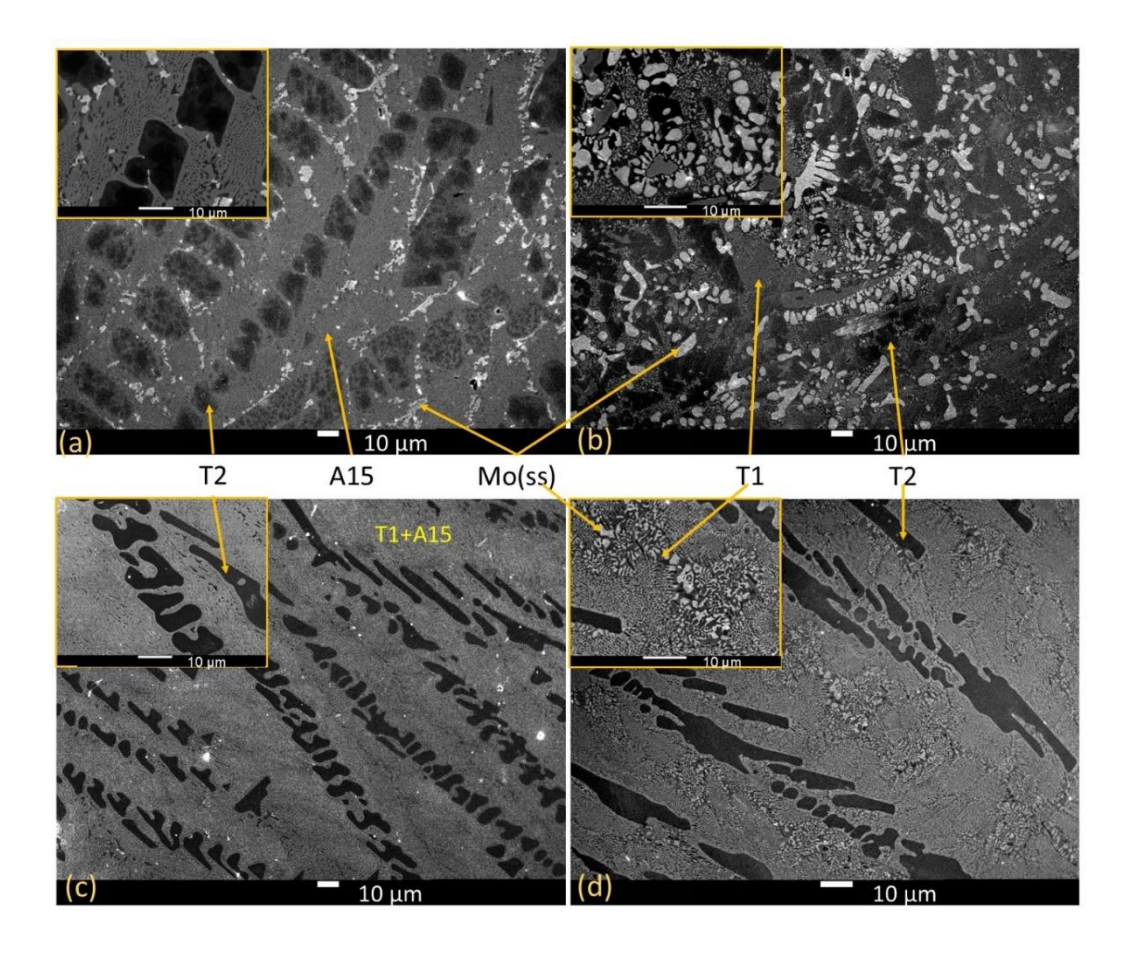


Figure 5.4 SEM (SE mode) images of as-cast (a) 711 (b) 711-W15 (c) 721 and (d) 721-W10 alloys.

Table 5.2. Weight percent of phases present in Mo-Si-B based alloys and the lattice parameters.

Alloy	a-Mo,W (SS)	Mo <sub>3</sub> Si (A15)	Mo <sub>5</sub> Si <sub>3</sub> (T1)	Mo <sub>5</sub> SiB <sub>2</sub> (T2)
711	$7.6 \pm 0.14$	$45.4 \pm 0.22$	-	$47 \pm 0.19$
711-W10	$27.6 \pm 0.21$	$16.4 \pm 0.28$	-	56 ± 0.29
711-W15	$34 \pm 0.29$	-	$13.5 \pm 0.46$	$52.5 \pm 0.41$
721	-	57 ± 0.25	$7.5 \pm 0.24$	$35.5 \pm 0.21$
721-W10	$36.5 \pm 0.26$	-	$32.2 \pm 0.34$	31.3
721-W15	$38 \pm 0.22$	-	$29.4 \pm 0.29$	$32.6 \pm 0.25$
811	$48.8 \pm 0.31$	$12.7 \pm 0.29$	-	$38.5 \pm 0.34$
811-W10	$50.3 \pm 0.36$	$16 \pm 0.37$		$33.7 \pm 0.43$
811-W15	$61.6 \pm 0.42$	$10.7 \pm 0.31$	-	$27.7 \pm 0.51$
811-W20	$61.3 \pm 0.61$	-	$10.3 \pm 0.7$	$28.4 \pm 0.63$
821	$46.3 \pm 0.24$	$37.6 \pm 0.23$	-	$16.1 \pm 0.22$
821-W10	$34.5 \pm 0.31$	41.7 ± .38	-	$23.8 \pm 0.4$
821-W15	$42.1 \pm 0.28$	$34.5 \pm 0.32$	-	$23.4 \pm 0.33$
821-W20	$56.3 \pm 0.01$	-	19 ± 0.01	$24.7 \pm 0.01$

Table 5.3. Lattice parameter of each phase in various alloy compositions

Alloy	a-Mo,W (SS)	Mo <sub>3</sub> Si (A15)	Mo <sub>5</sub> Si <sub>3</sub> (T1)	Mo <sub>5</sub> SiB <sub>2</sub> (T2)
711	a = 3.134	a = 4.8994	-	a = b = 6.0209
				c = 11.0564
711-W10	a = 3.142	a = 4.8998	-	a = b = 6.0333
				c = 11.0647
711-W15	a = 3.154	-	a = 9.6685	a = b = 6.0525
				c = 11.0954
721	-	a = 4.8918	a = 9.6299	a = b = 6.0348
				c = 11.0759
<b>721-W</b> 10	a = 3.142	-	a = 9.6394	a = b = 6.0367
				c = 11.0668
811	a = 3.137	a = 4.9001	-	a = b = 6.0235
				c = 11.0571
811 <b>-W</b> 10	a = 3.135	a = 4.8887	-	a = b = 6.0126
				c = 11.0341
811-W15	a = 3.157	a = 4.9203	-	a = b = 6.0539
				c = 11.1131

811-W20	a = 3.136	-	a = 9.6078	a = b = 6.0107
				c = 11.0303
821	a = 3.139	a = 4.9057	-	a = b = 6.0342
				c = 11.0840
821-W10	a = 3.141	a = 4.9012	-	a = b = 6.0329
				c = 11.0675
821-W15	a = 3.144	a = 4.8993	-	a = b = 6.0348
				c = 11.0624
821-W20	a = 3.158	-	a = 9.6956	a = b = 6.0644
				c = 11.1115

In alloy 711, 5 at% Ta addition (alloy 711-5Ta) resulted in a three-phase alloy with Mo (ss), A15 and T2 phases. The Miedema interaction parameter for Ta in Si was reported as -217 kJ/mol, -197 for Ta in Si, -20 kJ/mol for Ta in Mo, -19 kJ/mol for Mo in Ta, -126 kJ/mol, -322 for Ta in B, for Mo in Si and -120 kJ/mol for Si in Mo [229,231]. This indicates that Ta-Si interactions are strongest as compared to Ta-Mo or Mo-Si. The interaction parameter of Ta with B was even higher. As alloys 711-5Ta and 721-5Ta have A15 and T2 phases where equal number of metal-Si bonds are possible, Ta would prefer to partition into these phases Ta-Si bonds increase. Additionally, as the Ta-B interactions are very strong, it would prefer to segregate in T2 phase where B is present. EDS maps suggest the preferential segregation of Ta to T2 phase. Figure 5.5 shows SEM microstructures and XRD results of as-cast alloys showing the present phases. In alloy 711-5Ta, T2 phase was present as large grains while A15 and Mo(ss) are present as eutectic mixture.

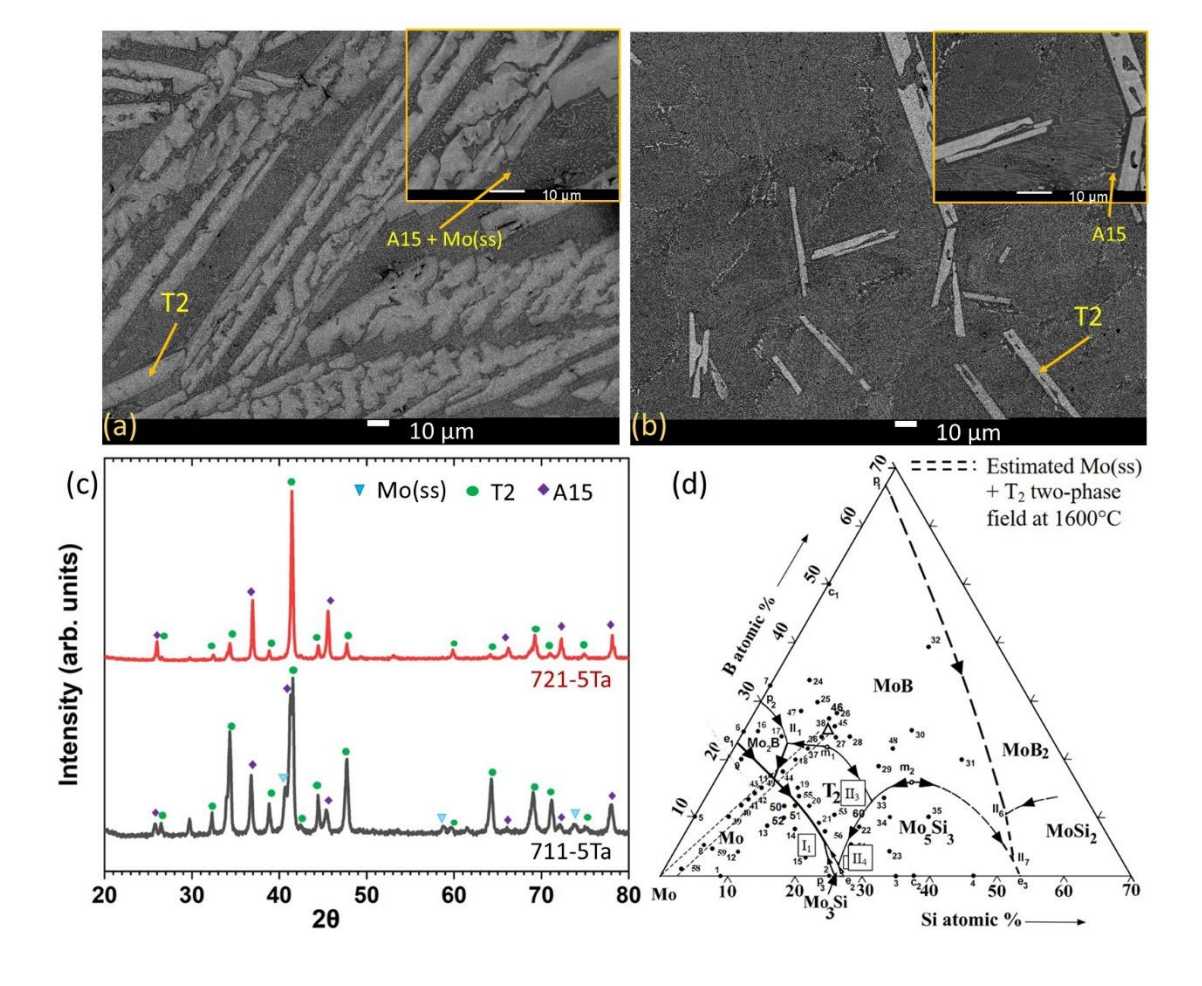


Figure 5.5 Microstructure (BSE mode) of as-cast (a) 711-5Ta alloy, (b) 721-5Ta alloy and (c) XRD results (d) liquidus projection of Mo-Si-B phase diagram [13]

#### 5.4 Transient oxidation behaviour

# 5.4.1 Temporal evolution of the oxide scale

Oxide evolution in Mo-Si-B alloys with addition of W, Ta and Al was observed using SEM and EDS analysis at 1100 °C and 1350 °C. The as-cast alloy 811 consisted of Mo(ss), Mo<sub>5</sub>SiB<sub>2</sub> (T2) and Mo<sub>3</sub>Si (A15) phases as shown in Figure 5.6. As these alloys consisted of multiple phases, the oxidation mechanism can be explained by considering the behaviour of individual oxides that are formed during oxidation at these temperatures. The oxidation reactions in initial stages when oxygen partial pressure is high are as mentioned below [46]. The free energy change values (in kJ/mol) were calculated using JANAF tables [216] only for those equations for which the data was available. The first value shows free energy change at 1100 °C and the second was calculated at 1350 °C for all equations.

$$2Mo + 3O_2 \rightarrow 2MoO_3$$
;  $\Delta G = -203.683$ ;  $-135.592$ 

Equation 5.1

$$2Mo_3Si + 11O_2 \rightarrow 6MoO_3 + 2SiO_2$$
;  $\Delta G = -1221$ ;  $-989.684$ 

Equation 5.2

$$Mo_5SiB_2 + 10O_2 \rightarrow 5MoO_3 + SiO_2 + B_2O_3$$

Equation 5.3

Once the oxide layers form and starts to thicken, partial pressure of oxygen decreases resulting in the following reactions [47,48]:

$$Mo + O_2 \rightarrow MoO_2$$
;  $\Delta G = 0.347$ ; 95.409

Equation 5.4

$$Mo_3Si + 4O_2 \rightarrow 3MoO_2 + SiO_2; \Delta G = -551.841; -433.185$$

Equation 5.5

$$2Mo_5SiB_2 + 15O_2 \rightarrow 10MoO_2 + 2SiO_2 + 2B_2O_3$$

Equation 5.6

When W is added to the system, following oxidation reactions in the temperature range of 800 to 1300 °C are possible as suggested by Karahan et al [55].

$$Mo_x W_{1-x} + \frac{3}{2}O_2 \to x MoO_3 + (1-x)WO_3$$

Equation 5.7

$$2(Mo_{\nu}W_{1-\nu})_{5}Si_{3} + 21O_{2} \rightarrow 10yMoO_{3} + 10(1-y)WO_{3} + 6SiO_{2}$$

Equation 5.8

$$(Mo_yW_{1-y})_5Si_3 + 3O_2 \rightarrow 5yMo + 5(1-y)W + 3SiO_2$$

$$2(Mo_zW_{1-z})_5SiB_2 + 5O_2 = 10zMo + 10(1-z)W + 2SiO_2 + B_2O_3$$

Equation 5.10

Based on the equations discussed above, the following equations are possible with Ta addition to the system.

$$Mo_x Ta_{1-x} + \frac{(x+5)}{2}O_2 \to xMoO_3 + \frac{(1-x)}{2}Ta_2O_5$$

Equation 5.11

$$(Mo_y Ta_{1-y})_3 Si + \frac{(3y+19)}{4} O_2 \rightarrow 3yMoO_3 + \frac{3(1-y)}{2} Ta_2 O_5 + SiO_2$$

Equation 5.12

When Al is added to the system, the additional possible reaction is [54]:

$$3Mo_3(Si_xAl_{1-x}) + (28.5 - 16.5x)O_2$$
  
 $\rightarrow xMo_5Si_3 + 1.5(1-x)Al_2O_3 + (9-5x)MoO_3$ 

Equation 5.13

Mo<sub>3</sub>Si and Mo<sub>5</sub>Si<sub>3</sub> phases form MoO<sub>3</sub> and SiO<sub>2</sub> oxides. Mo<sub>3</sub>Si forms porous SiO<sub>2</sub> scale with poor oxidation resistance. Additionally, higher Mo content in these phases [32] leads to the formation MoO<sub>3</sub> which volatilizes around 700 °C. Oxidation studies on Mo<sub>5</sub>SiB<sub>2</sub> by Yoshimi et al. [232] in the temperature range of 700-1400 °C showed formation and volatilization of MoO<sub>3</sub> below 800 °C with slight mass gain. In our work, when the alloy 811 was exposed to 1100 °C for 30 s, the region with Mo(ss) phase started appearing as depressed regions (Figure 5.6 where all images SE images). The surrounding regions with T2 and A15 phases showed the formation of oxides. The topographic profile of the oxidized surface indicates loss of Mo region which could be due to the formation and evaporation of its oxides similar to what was observed in the existing studies [17,55]. As the exposure time increased to 60 s, increased oxidation was observed. Exposure after 90 s and 120 s showed SiO<sub>2</sub> rich scale formation with

very little coverage of Mo rich regions. Exposure of the same alloy at 1350 °C for 20 s revealed brighter, uniform and smooth oxide formation on the T2 phase. After 60 s of exposure, the amount of oxidation increased, and the  $SiO_2$ -rich scale started covering the sample surface. The T2 phase contains boron which results in formation of  $B_2O_3$  and has tendency to reduce viscosity of the borosilica scale [6].

As viscosity decreases, the diffusivity increases, in accordance with Stokes-Einstein relation; hence the oxygen penetration through the scale increases leading to further subsurface oxidation. However, at high temperatures above 1200 °C, B<sub>2</sub>O<sub>3</sub> starts evaporating, which can affect the viscosity of scale [6]. The overall viscosity is balanced by the temperature and scale composition. On increasing exposure time to 90 s and 120 s, EDS maps showed the presence of Mo and oxygen on regions where T2 was present which indicates formation of oxides of Mo in the scale and incomplete surface coverage with protective SiO<sub>2</sub>rich scale. This suggests the formation of oxides of Mo possibly MoO<sub>2</sub> or MoO<sub>3</sub> in the scale. When the alloy 821 with higher Si/B ratio was exposed to 1100 °C, Mo(ss) regions showed depression like the alloy 811. The other regions formed oxides with fine pores which could not cover the depressed regions even after 120 s of exposure. This alloy has lower boron content as compared to the 811 alloy resulting in higher scale viscosity and reduced flow at this temperature. On increasing temperature, the glassy scale was able to flow and fill the depressed areas. The flow of the glassy scale is clearly visible in the SEM images shown in Figure 5.6 on comparing images at 30 and 60 s. In alloy 821, at 1100 °C, the lower temperature and less boron content in the substrate contributed to higher viscosity and reduced scale flow. Consequently, more oxidation and greater pesting of Mo can occur under such conditions.

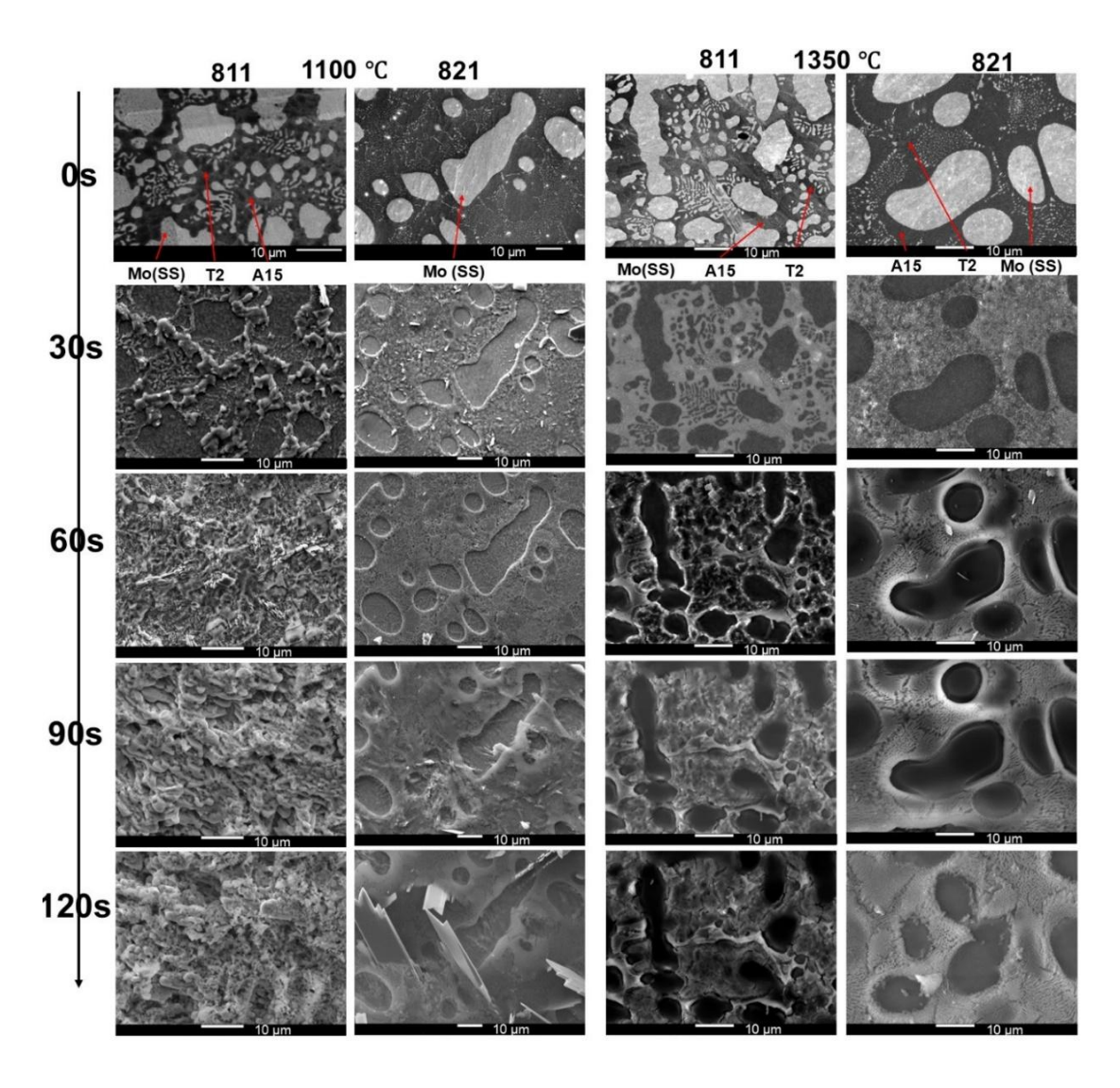


Figure 5.6 Temporal oxide evolution in 811 and 821 Mo-Si-B alloys (SEI mode) at 1100 °C and 1350 °C. Here, 8, 11 and 21 represent 80 at% Mo, Si/B ratio as 1/1 and 2/1 respectively.

Alloy 711 showed oxide formation on each phase like alloy 811. At 1100 °C, T2 phase which solidified as dendrites and also present as a eutectic mixture with A15 and Mo(ss) started to form brighter oxide scale (Figure 5.7). Mo(ss) initially showed depression due to volatilization of (MoO<sub>3</sub>)<sub>3</sub> oxide and then slowly got covered with SiO<sub>2</sub>-rich scale after 90s. The oxide scale formed on T2 present as eutectic mixture appeared smooth and the scale formed on A15 phase appeared porous. This was consistent with the studied reported by Karahan et al. [55] and Rioult et al [17]. The oxidation of 711 at 1350 °C occurred much faster and a dense oxide scale covered the surface within 90 s of exposure. The Mo(ss) phase was missing from alloy 721 and it consisted of T1, T2 and A15 phases. As the sample oxidized for 30 s at 1100 °C, smooth silica scale formed on T2 phase and globular oxides appeared at some regions. T2 is Mo<sub>5</sub>SiB<sub>2</sub> with boron in it

that results in the formation of borosilica glass. The presence of B<sub>2</sub>O<sub>3</sub> enables the scale to flow and form a smooth scale. Mo<sub>3</sub>Si (A15) and Mo<sub>5</sub>Si<sub>3</sub> phases form SiO<sub>2</sub> without any B<sub>2</sub>O<sub>3</sub> in it resulting in the formation of a viscous scale that doesn't flow quite as readily which could lead to a relatively granular scale appearance on these phases. On increasing exposure time, the oxide scale completely covered the sample surface. This oxide scale covers the substrate and protects against oxidation depending on its structure. SiO<sub>2</sub> scale that forms on Mo<sub>3</sub>Si (A15) phase is porous [17] and oxygen can permeate through them. To eliminate Mo<sub>3</sub>Si phase, effect of W addition was studied and is discussed below.

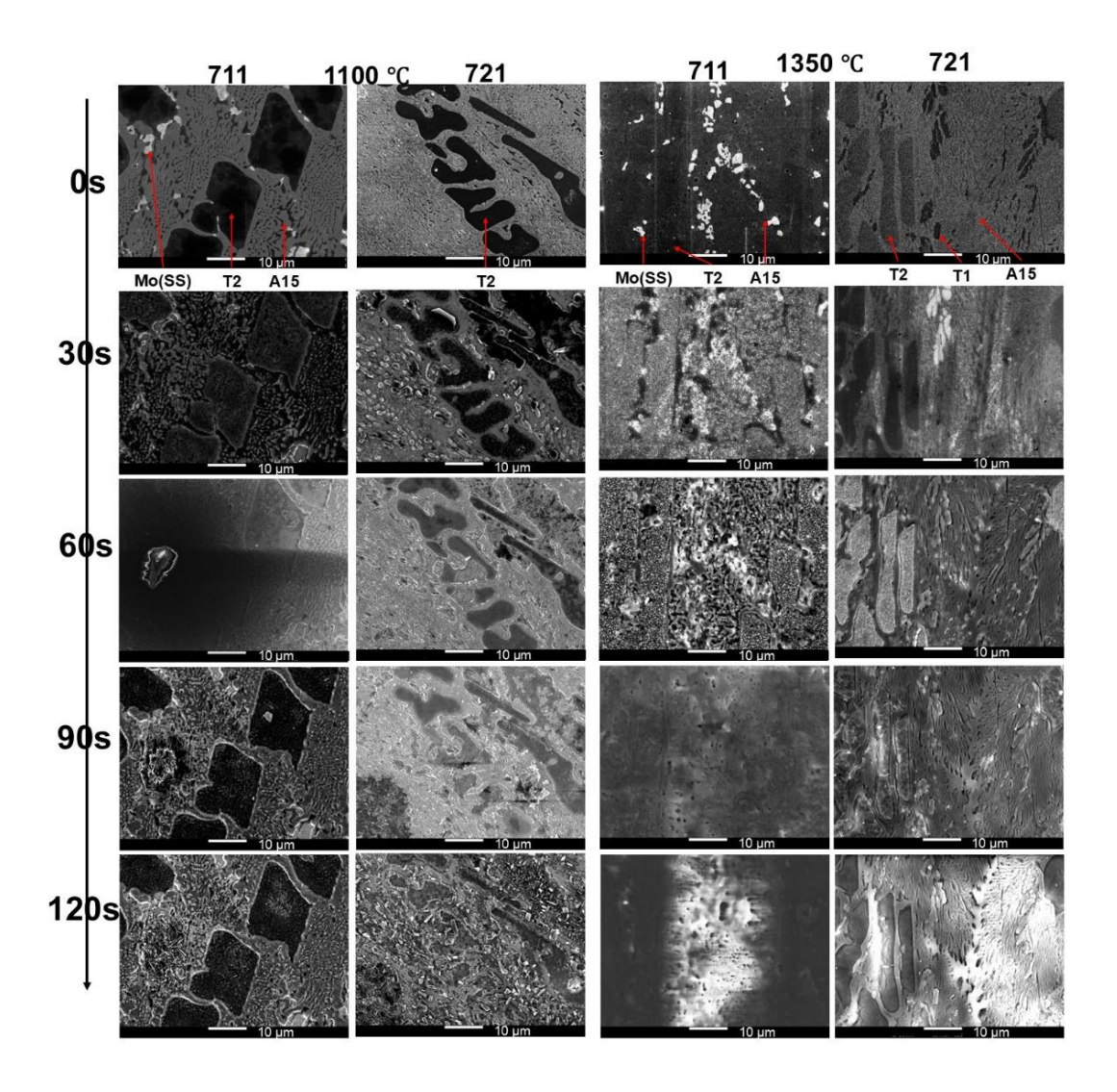


Figure 5.7 Temporal oxide evolution in 711 and 721 Mo-Si-B alloys (SEI mode) at 1100 °C and 1350 °C. Here, 7, 11 and 21 represent 70 at% Mo, Si/B ratio as 1/1 and 2/1 respectively.

On addition of W to these alloys, the observed temporal evolution of the oxide scale was similar to the results reported by Karahan et al [55] and Ouyang et al [16]. During casting of these alloys, W mostly forms solid solution with Mo and upon oxidation it forms WoO<sub>3</sub> which is non-volatile at temperatures below 1300 °C. In both 811-20 and 821-20 alloys in which 20 at % Mo was substituted with 20 at % W, the Mo(ss) phase showed oxidation and volatilization of Mo for 120 s in 811-20 and for 60 s in 821-20 at 1100 °C (Figure 5.8). After 90 s of exposure, alloy 821-20 showed protruded oxide formation on Mo(ss) region due to formation of non-volatile WoO<sub>3</sub> at this temperature [55]. SiO<sub>2</sub>-rich oxide scales formed on other phases but could not cover the entire surface as the SiO<sub>2</sub> scale has lower viscosity at this temperature and WO<sub>3</sub> hinders the scale flow that leads to a non-protective oxide scale formation [55]. At 1350 °C, similar behaviour was observed for both the alloys up to 30 s after which oxide scale formation occurred on the entire surface. These oxides were mixtures of Mo, W and Si oxides with a porous appearance. According to work by Karahan et al. [55] and Ouyang et al. [16], (WO<sub>3</sub>)<sub>3</sub> volatilizes like (MoO<sub>3</sub>)<sub>3</sub> trimer in 1300-1400 °C temperature regime[16,55].

In our work, rapid oxidation of all species occurs and since the oxide scale is porous, it provides an easy pathway for oxygen penetration. Hence, oxide formation and evaporation of volatile oxides can occur easily through these pores. This indicates continuous oxide formation and evaporation under such conditions. Alloy 711-W15 showed similar behaviour which was consistent with the studies by Karahan by et al. [55]. In alloy 721-W10, addition of only 10 at% W removed A15 phase and not much oxidation was seen in first 30 s of exposure at 1100 °C. Oxides formed on these phases after 60 s and covered the entire surface with the scale showing discontinuity as shown in Figure 5.9. Black regions started to appear, indicating depressions due to volatilization of (MoO<sub>3</sub>)<sub>3</sub>) oxide. At 1350 °C, finger-like oxides with gaps in between covered the sample surface. This indicates rapid oxide formation without much SiO<sub>2</sub> glassy scale flow during oxidation. Silica has high viscosity and the presence of boria along with increased helps it to flow. But boria has tendency to evaporate above

1200 °C which again reduces the scale viscosity making the flow difficult and reduced substrate coverage with protective scale.

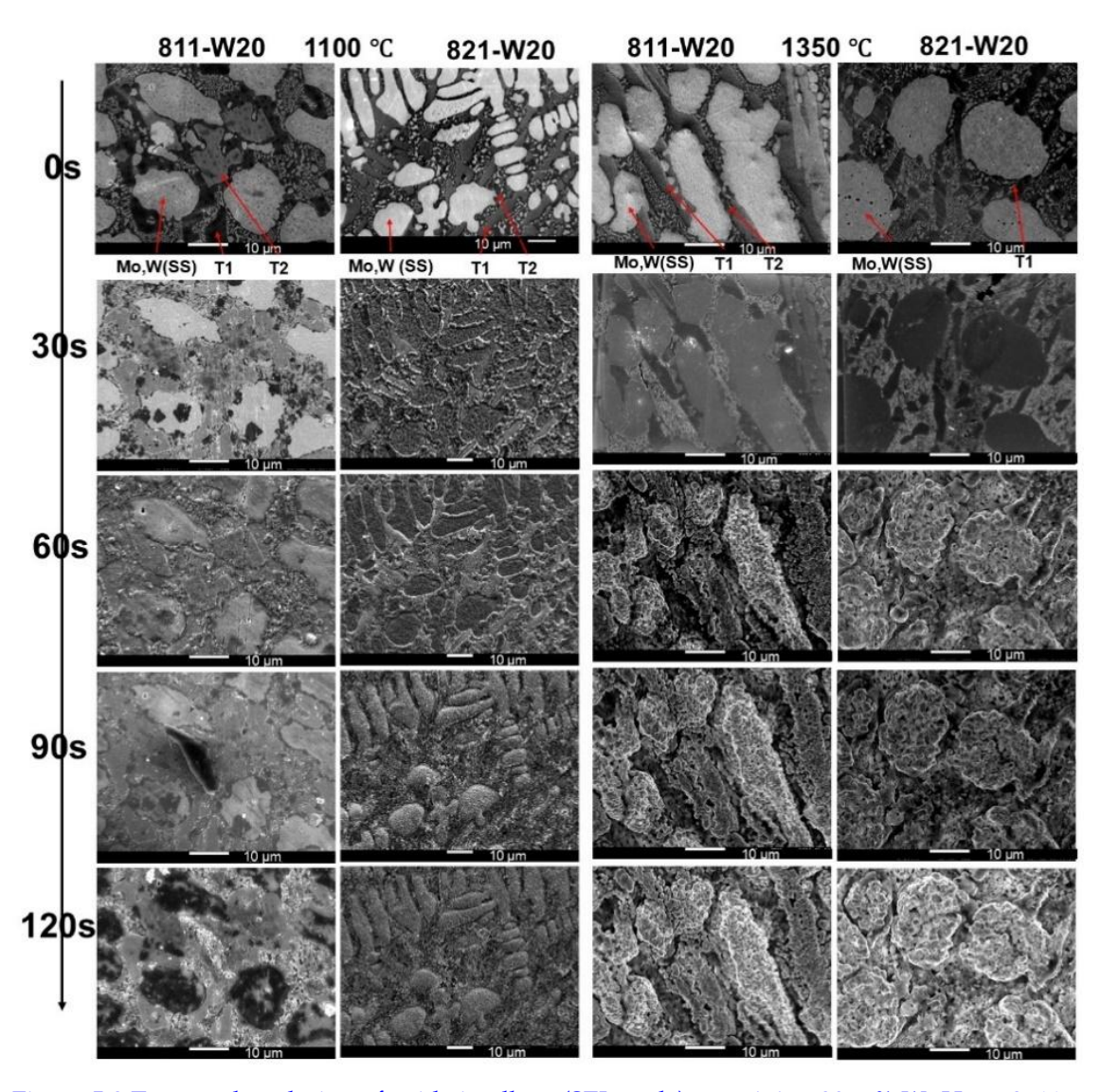


Figure 5.8 Temporal evolution of oxide in alloys (SEI mode) containing 20 at% W. Here, 8, 11 and 21 represent 80 at% Mo+W, Si/B ratio as 1/1 and 2/1 respectively.

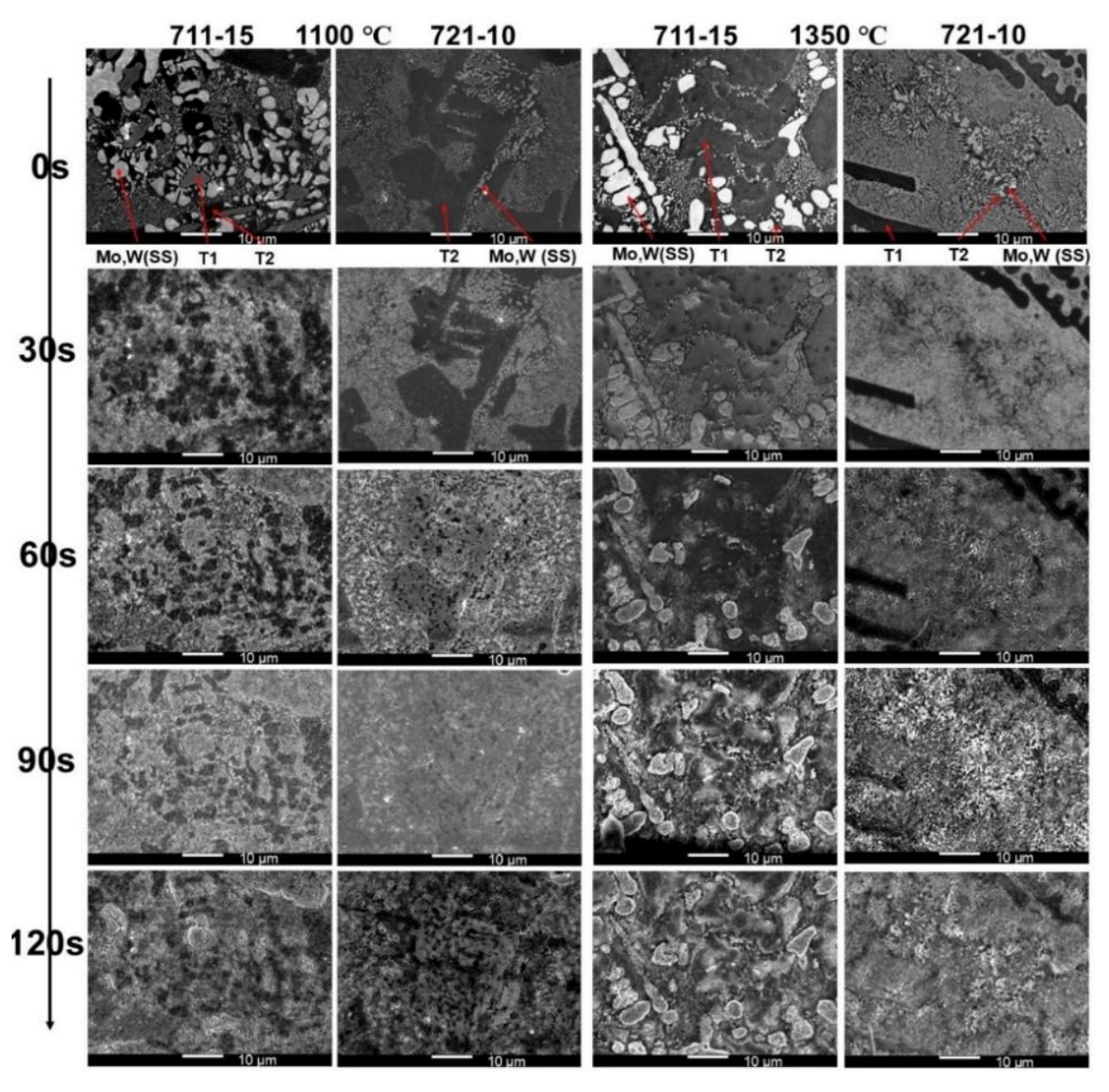


Figure 5.9 Temporal evolution of oxide in alloys (SEI mode) containing 20 at% W. Here, 7, 11 and 21 represent 70 at% Mo+W, Si/B ratio as 1/1 and 2/1 respectively.

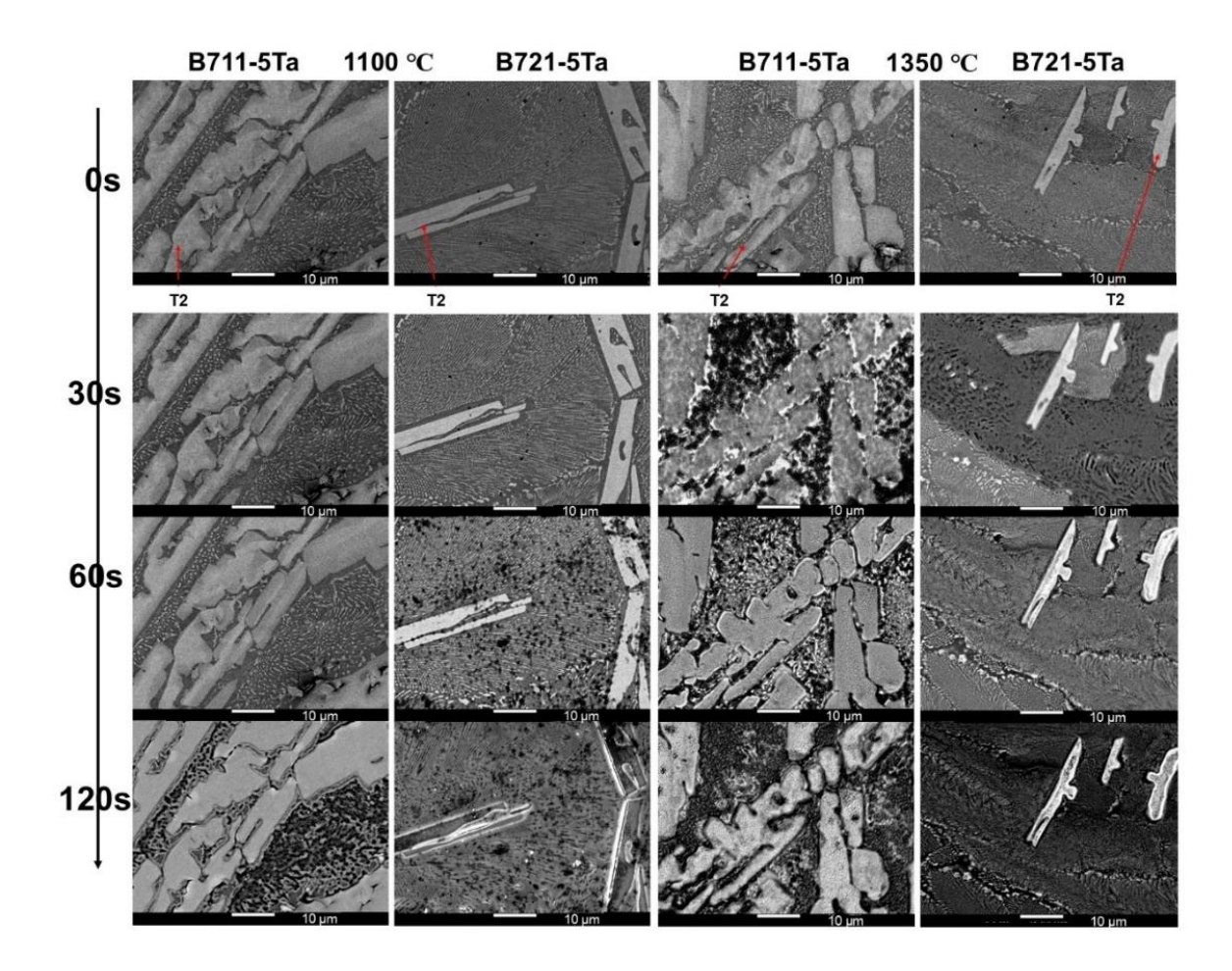


Figure 5.10 Oxide evolution in Mo-Ta-Si-B alloys (SEI mode) at 1100 °C and 1350 °C. Here, 7, 11 and 21 represent 70 at% Mo, Si/B ratio as 1/1 and 2/1 respectively.

In alloy 711-5Ta which had 5 at% Ta, no change in microstructure was seen up to 60 s of exposure at 1100 °C (Figure 5.10). After 120 s, SiO<sub>2</sub>-rich oxide started to cover the sample surface. At 1350 °C, silica rich oxide formed on T2 phase and the eutectic region with Mo(ss) and Mo<sub>3</sub>Si region started appearing darker indicating loss of Mo in form of oxide. SiO<sub>2</sub>-rich scale started to appear in the eutectic region after 60s of exposure. EDS maps indicated the presence of Ta in oxide scale which was due to the formation of Ta<sub>2</sub>O<sub>5</sub> as confirmed by XRD analysis later. Alloy 721-5Ta showed similar oxidation behavior as 711-5Ta. After 30 s of exposure at 1350 °C, a difference in contrast within oxide scale was observed which indicates oxide formation and start of glassy flow in some regions. Oxide evolution was also studied in alloys 811-5Al and 821-5Al at 1100 °C and 1350 °C as shown in Figure 5.11. The oxides evolved like the base alloys 811 and 821 where Mo (ss) phase formed MoO<sub>3</sub> and A15, T2 phases formed SiO<sub>2</sub>-rich oxides. Al present in the alloy causes formation of Al<sub>2</sub>O<sub>3</sub> oxide as

reported by Paswan et al. [54]. After exposure of alloy 821-5Al for 60 s at 1350 °C, needle like Al-rich flakes started to appear on the sample surface. After 120 s, Mo(ss) appeared as depressed region covered with α-Al<sub>2</sub>O<sub>3</sub> needles. Paswan et al. [54] observed similar structures of 3Al<sub>2</sub>O<sub>3</sub>.2SiO<sub>2</sub> during oxidation of Al containing Mo-Si-B alloy at 1150 °C. The borosilica scale covered only T1 and A15 regions of the sample as indicated by EDS maps. In alloy 811-5Al also, silica could not cover Mo(ss) regions leading to excessive oxidation and mass loss due to MoO<sub>3</sub> volatilization.

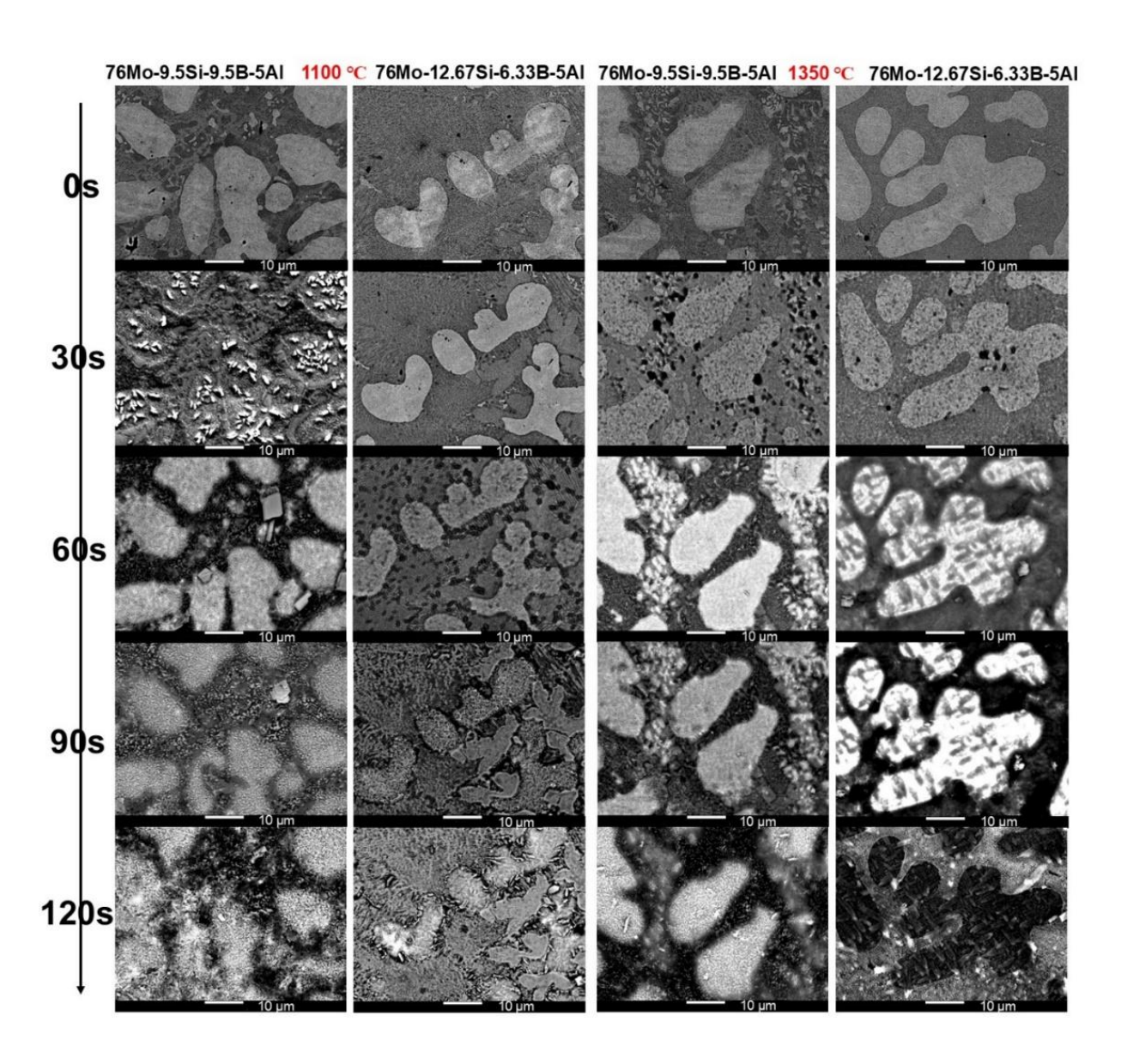


Figure 5.11 Temporal oxide evolution of Mo-Al-Si-B alloys at 1100 and 1350 °C. 5 at% Al was added to the alloys keeping the Mo/Si/B ratio as 8/1/1 and 8/2/1.

## 5.4.2 Understanding oxidation pathways

Mo-Si-B alloys undergo different oxidation stages, and during transient stage Mo oxidizes to form volatile MoO<sub>3</sub> with rapid linear mass loss. Later, Si containing phases Mo<sub>3</sub>Si, Mo<sub>5</sub>Si<sub>3</sub> and Mo<sub>5</sub>SiB<sub>2</sub> supply Si and B to form borosilica that covers the surface and reduces inward oxygen diffusion [6]. But at lower temperatures the oxide scale does not passivate. Helmick et al [233] observed catastrophic oxidation and bubbles in oxide scale due to MoO<sub>3</sub> volatilization at 800 °C.

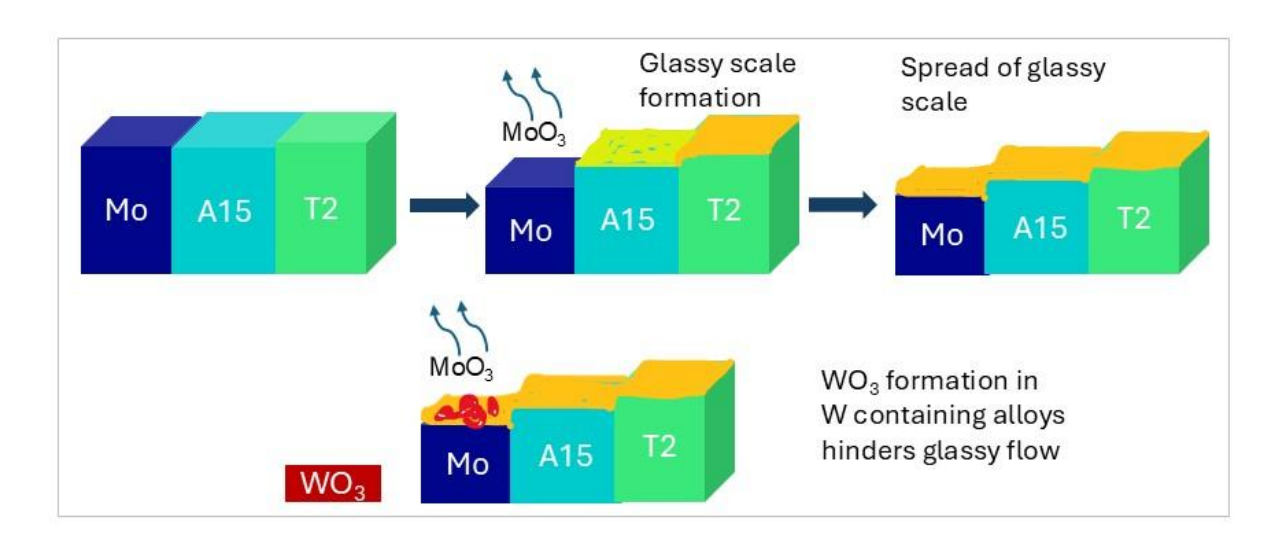


Figure 5.12 Effect of W addition on glassy oxide flow formed during oxidation of Mo-Si-B alloys

For alloys 811, 821, 711 and 721 the oxidation for 20 hours resulted in the formation of borosilica scale at the top as shown in the schematic in Figure 5.12. The glass formed on silicon and boron containing phases flows and covers the sample surface including the depressions formed on Mo phase due to its volatilization. However, the rates of oxides formation and glass flow were different for every alloy. For example, if we compare the mass change plots of alloys 711 and 721 in Figure 5.14, the mass loss is relatively lesser in 721 at both temperatures. In this alloy, Mo (ss) is absent, and it has three phases that can provide SiO<sub>2</sub> to the oxide scale. Additionally, the weight percent of T2 phase which is source of boron is lesser in alloy 721 (35.5 wt%) than in alloy 711 (47 wt%). When oxidation starts, 711 can provide large amounts of boria than alloy 721 and may result in faster enrichment of silica scale in boria. Figure 5.7 shows

the oxide evolution in two alloys at 1100 and 1350 °C. Alloy 711 shows a more uniform oxide formation than alloy 721 at the end of 120 s which indicates better initial spread of borosilica scale in alloy 711. This agrees with the observations in the existing literature [6,234]. SiO<sub>2</sub>-rich scale prevents oxygen diffusion, but overall oxidation depends on scale porosity, surface coverage and scale passivation which is explained in the next section 5.5. In W containing alloys, a discontinuous borosilica scale was observed. It was found in earlier studies that it forms WO<sub>3</sub> which hinders the glassy scale flow resulting in reduced surface coverage as can be seen in the schematic [16,55].

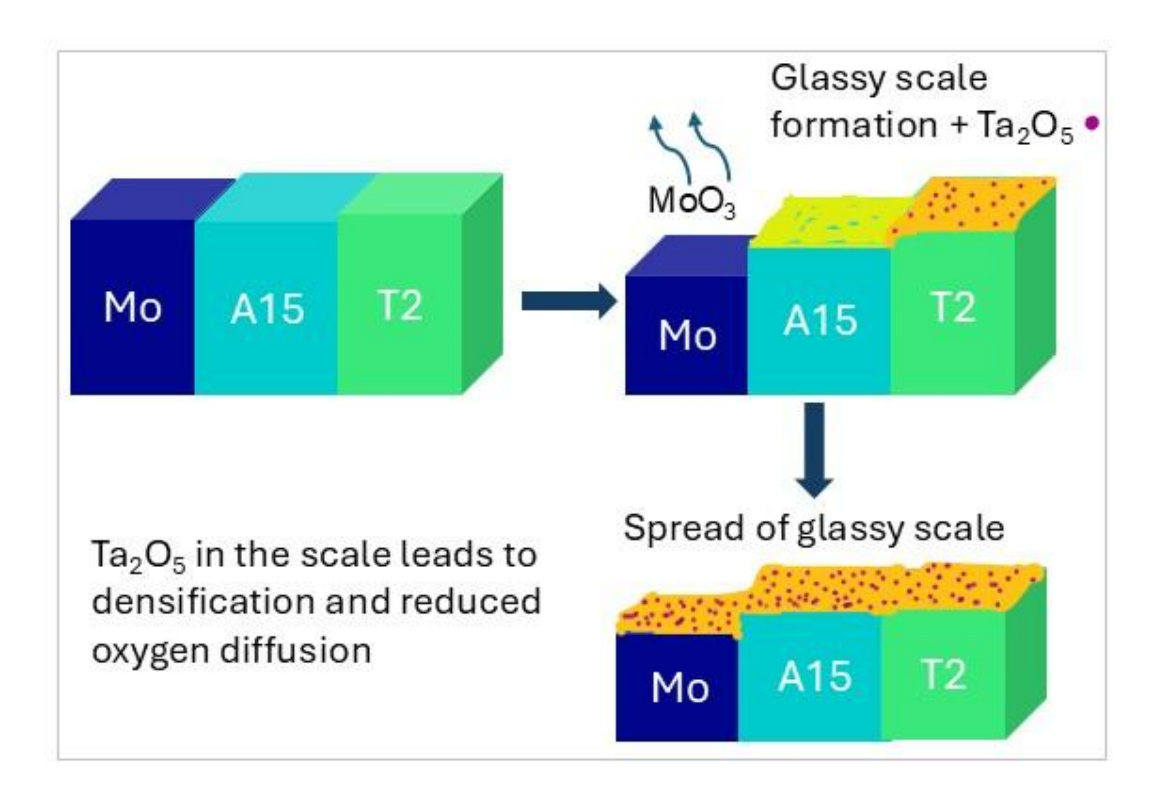


Figure 5.13 Effect of Ta addition on oxidation mechanism in Mo-Si-B alloys

When Ta is added, it forms Ta<sub>2</sub>O<sub>5</sub> which was confirmed from XRD analysis after oxidation. The proposed oxidation mechanism for Ta addition to Mo-Si-B alloys is shown in Figure 5.13. As Ta partitions into A15 phase, it forms Ta<sub>2</sub>O<sub>5</sub> in addition to borosilica scale. As oxidation proceeds, borosilica scale above A15 grains gets enriched in Ta<sub>2</sub>O<sub>5</sub> which increases scale viscosity and oxygen diffusion through the scale slows down. The borosilica scale formed on surrounding T2 grains starts to flow on A15 phases and then scales interact with each other resulting in formation of homogenous borosilica scale with

 $Ta_2O_5$  oxide. The scale spreads on the entire surface of the sample and mass change stabilizes. The effect of Ta addition on oxide structure and flow properties is discussed in detail in the next section.

# 5.5 Long-term oxidation behaviour

### 5.5.1 Effect of temperature

The fabricated alloys were exposed to  $1100\,^{\circ}\text{C}$  and  $1350\,^{\circ}\text{C}$  and mass change per unit area was recorded at different time intervals up to 20 h. Plots for base alloys 811, 821, 711 and 721 are shown in Figure 5.14. The effect of temperature on long term exposure of the alloys is clearly visible. Alloy 811 which constituted of Mo (ss), A15 and T2 phases showed lower mass loss per unit area at 1100 °C than that at 1350 °C. The formation of glassy SiO<sub>2</sub>-rich scale was observed at both temperatures with average oxide scale thickness of approximately 80  $\mu$ m. The alloy experienced initial mass loss due to the formation and volatilization of oxides of Mo followed by mass gain due to formation of SiO<sub>2</sub> oxide. The glassy SiO<sub>2</sub> is highly viscous which prevents oxygen inward diffusion helping in mass change stabilization and flattening of the curve.

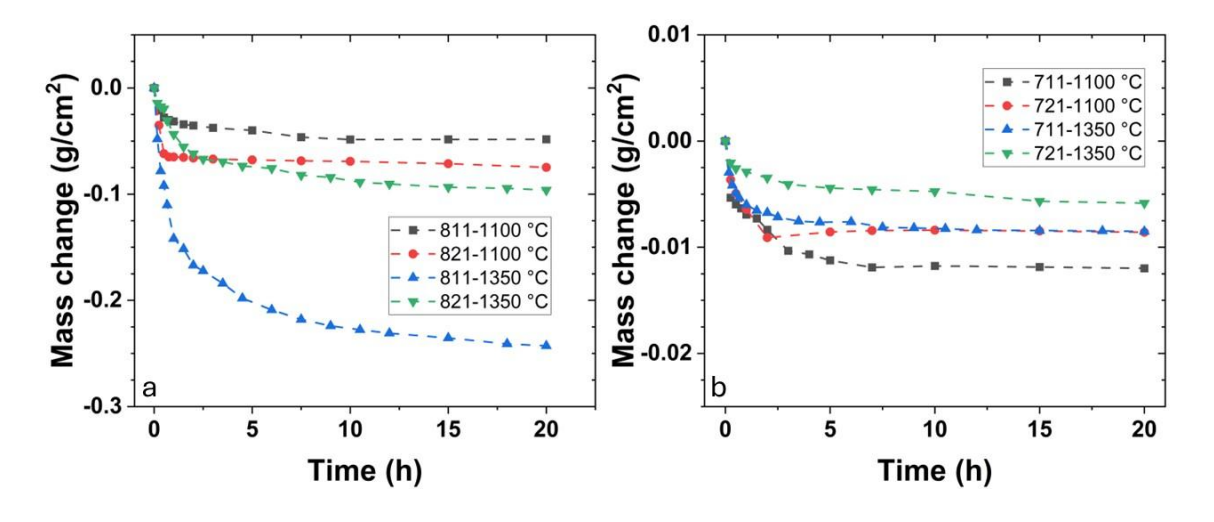


Figure 5.14 Mass change per unit area for (a) 811, 821 alloys and (b) 711, 721 alloys at 1100 and 1350  $^{\circ}\text{C}$ 

Increase in temperature from 1100 °C to 1350 °C resulted in rapid oxidation and evaporation of MoO<sub>3</sub> oxide till the stable glassy scale formed. Presence of Mo

oxide was observed beneath a thin top layer of SiO<sub>2</sub> scale indicating its evaporation during oxidation until the stable SiO<sub>2</sub> scale covers the surface at 1350 °C. The oxide layer stabilized faster at 1100 °C as observed from the mass change plot in Figure 5.14. These alloys contain B which is known to lower the viscosity of SiO<sub>2</sub> glass [235]. This helps in faster spreading of oxide scale and shorter transient period.

Alloy 821 where Si to B ratio is 2, showed higher mass loss at 1350 °C in comparison with exposure at 1100 °C. Lower B content in 821 than that in 811, may lead to more viscous scale formation during oxidation. Due to high scale viscosity, the flow becomes difficult which may lead to improper surface coverage and rapid oxidation. On the other hand, viscous scale can make oxygen penetration through the scale difficult which could be a possible reason for lower mass loss in alloys 811 at 1100 °C.

The oxide scale thickness formed on alloy 821 at 1100 °C and 1350 °C is 236  $\mu$ m and 93  $\mu$ m respectively as shown in Figure 5.15. Mo was detected in oxide scale formed at 1100 °C after 20 h of exposure. This indicated continuous evaporation of MoO<sub>3</sub> similar to what was observed in the existing work on Mo-Si-B alloys [16,55] resulting in mass loss. The initial mass loss at 1100 °C was faster and oxide layer was thicker than 1350 °C. Later, the mass loss was compensated by the formation of more oxides. At 1350 °C, Mo was not observed in the oxide scale after 20 h indicating the formation of stable SiO<sub>2</sub>-rich oxide layer. The top oxide scale appeared smooth and uniform without any Mo inclusions. The overall mass change in alloys during oxidation depends on losses due to evaporation of oxides and mass gain due to formation of oxides.

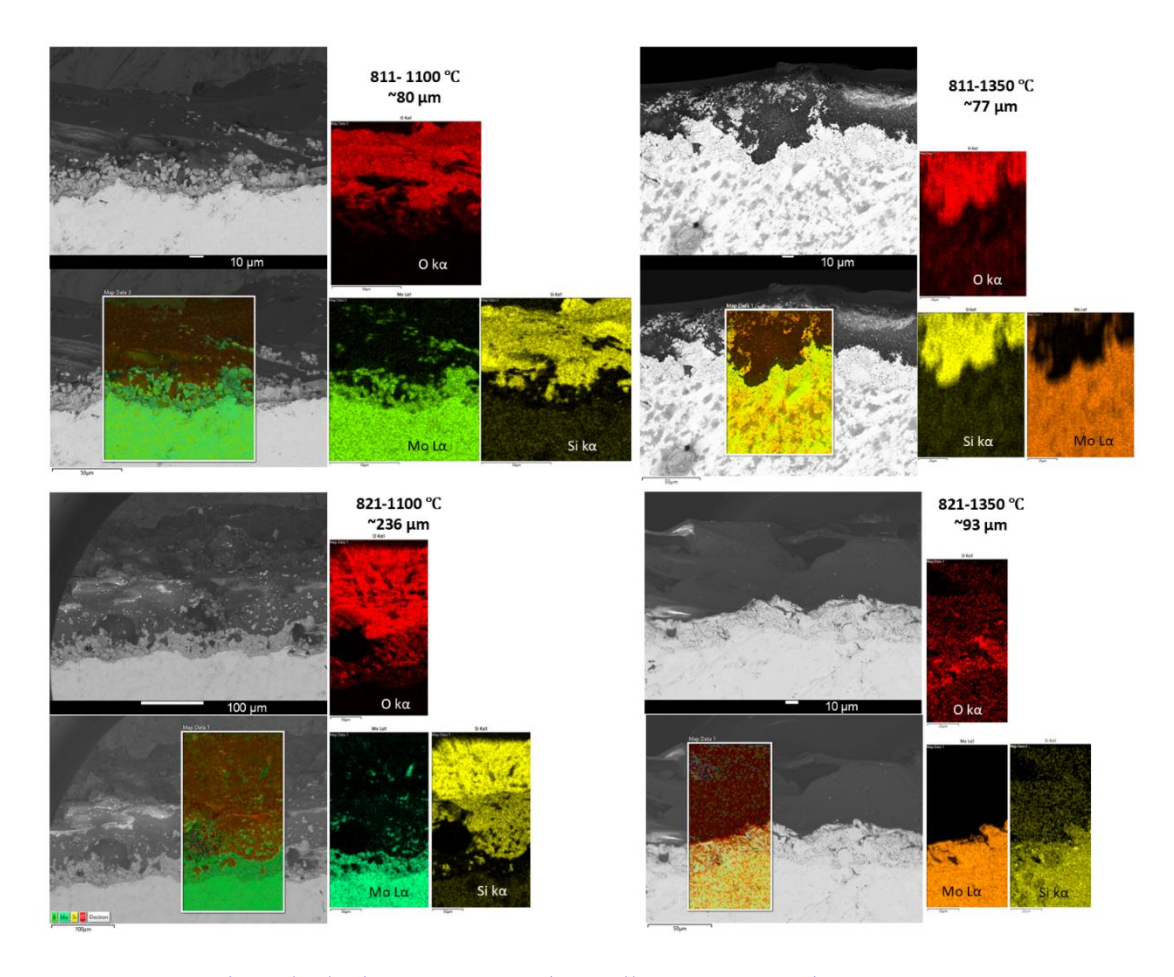


Figure 5.15 Oxide scale thickness in 811 and 821 alloys at 1100 and 1350 °C

Alloys 711 and 721 with Si to B ratio as 1 and 2 respectively consisted of different phases. Mo (ss), Mo<sub>3</sub>Si (A15) and Mo<sub>5</sub>Si<sub>3</sub> (T1) phases were present in 711 and Mo (ss) was completely absent from the alloys 721 with presence of Mo<sub>3</sub>Si (A15), Mo<sub>5</sub>Si<sub>3</sub> (T1) and Mo<sub>5</sub>SiB<sub>2</sub> (T2). At higher oxidation temperature, the alloys 711 showed lower mass loss as compared to 1100 °C. The SEM and EDS analysis of the cross section showed a smooth SiO<sub>2</sub>-rich oxide scale at 1350 °C while the oxide scale was rich in Mo at 1100 °C as shown in Figure 5.16. This indicates slow SiO<sub>2</sub> scale formation resulting in higher MoO<sub>3</sub> loss at 1100 °C. The alloy 721 showed lower mass loss and a thin stable SiO<sub>2</sub>-rich oxide scale indicating better oxidation properties at both temperatures than alloy 711. At 1350 °C, the mass loss after 20 h was minimum and the oxide scale stabilized faster than 1100 °C. The alloys 721 has absence of Mo(ss) phase and T1 phase was present unlike other alloys. Absence of Mo(ss) phase can make MoO<sub>3</sub> formation and evaporation difficult providing faster surface coverage. The

oxide layer as shown in Figure 5.16 shows glassy SiO<sub>2</sub>-rich scale without any inclusions with oxide scale thickness of 26 µm at both temperatures.

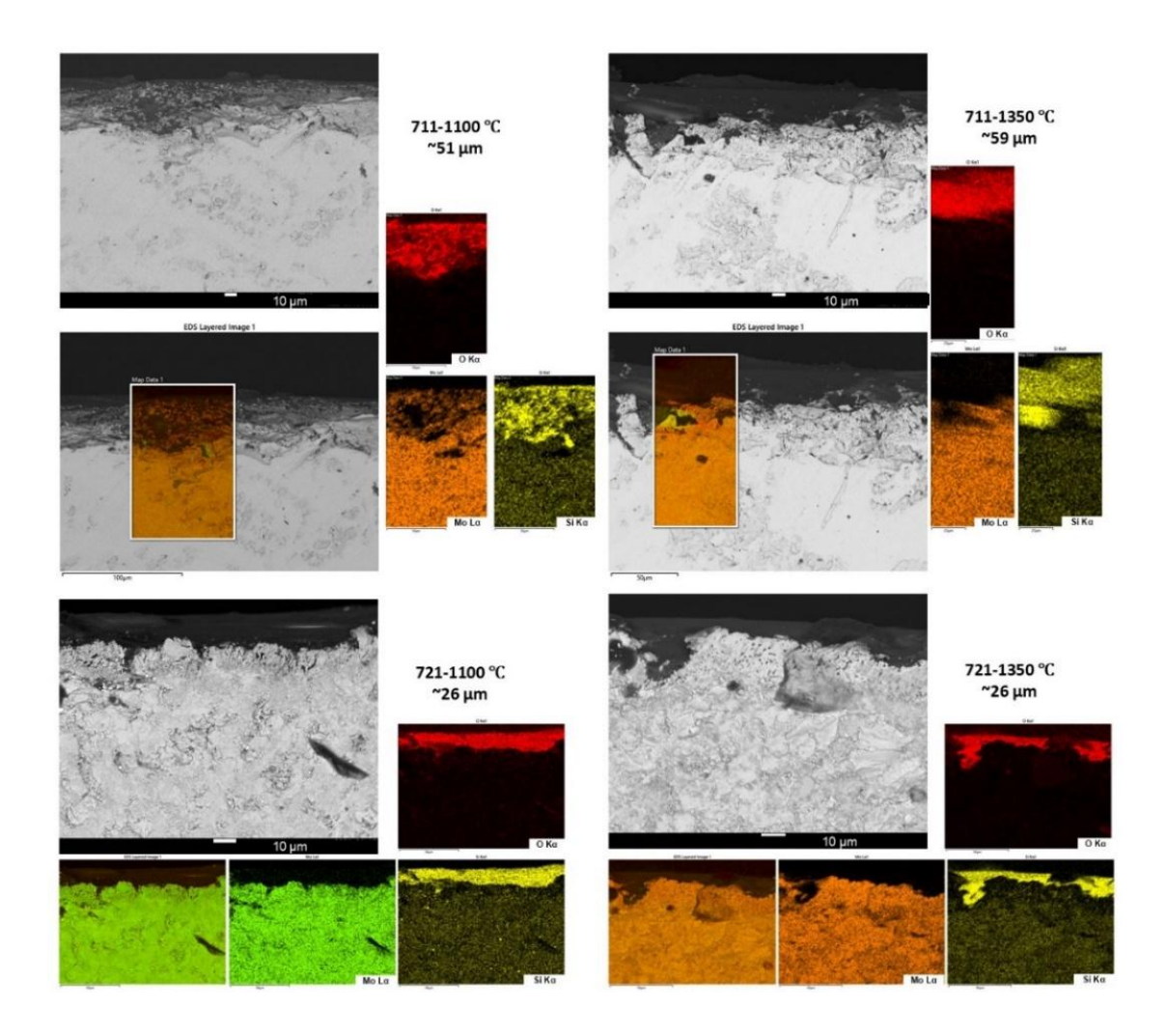


Figure 5.16 Oxide scale thickness in 711 and 721 alloys at 1100 °C and 1350 °C

## 5.5.2 Effect of refractory metals: W and Ta

Refractory metals W and Ta were added to Mo-Si-B alloys to observe their effect on oxidation behaviour. The alloy 811-W20, 821-W20, 711-W15 and 721-W10 containing W were selected as these alloys were free from A15 phase. During oxidation, rapid mass loss occurred at both temperatures as indicated by mass change curves in Figure 5.17. W forms WO<sub>3</sub> during oxidation which volatilizes as (WO<sub>3</sub>)<sub>3</sub> trimer like (MoO<sub>3</sub>)<sub>3</sub>, but only at temperature ranging between 1300-1400 °C [236]. Yoon et al [237] reported that WO<sub>3</sub> in borosilica scale hinders scale flow leading to poor surface coverage. Karahan et al. [55] reported similar observations for borosilica scale flow during oxidation of alloy

711 with 15 at% W. In this work, oxidation resistance reduced on addition of W as it forms WO<sub>3</sub> which impedes borosilica flow. Formation of protruded regions was clearly visible in SEM images of samples oxidized at 1100 °C as discussed in previous section. In alloy 811-W20, the initial mass loss at 1350 °C as can be seen in Figure 5.17 is slightly higher than that at 1100 °C. It was because of faster evaporation of MoO<sub>3</sub> and WO<sub>3</sub> trimers with increased temperature. Karahan et al. [55] plotted vapor pressure of these oxides to understand their volatilization behaviour. It was reported that the vapor pressure of MoO<sub>3</sub> is higher than WO<sub>3</sub> and B<sub>2</sub>O<sub>3</sub> at 1100 °C and thus it evaporates easily. As the temperature reaches above 1300 °C, the vapor pressure of WO<sub>3</sub> increases sufficiently allowing its easy volatilization from the surface.

For alloy 811-W20, as the oxidation time increased mass loss was much higher and rapid at 1100 °C than at 1350 °C. As the temperature increased above 1300 °C, volatilization of WO<sub>3</sub> and better surface coverage by borosilica scale occurred. XPS analysis after 120 s of oxidation during transient stage did not show presence of WO<sub>3</sub> in the scale. However, a stable SiO<sub>2</sub>-rich oxide scale could not form on any alloy system after long exposure and the overall mass loss increased drastically. The surface coverage depends on scale viscosity which again depends on temperature and composition of the scale. For example, the entrapped WO<sub>3</sub> hinders the flow of the glassy scale and Ta<sub>2</sub>O<sub>5</sub> increases scale viscosity. To study this effect, the alloys with different Si/B ratio with and without elemental additions were studied and discussed in section §5.5.3 to §1.5.5.

For alloys, 711-W15 and 721-W10, large degradation of samples occurred within 2 h of oxidation at 1100 °C. The mass change is the overall effect of mass loss due to evaporation and mass gain due to oxides formation showing an overall mass loss of 100 mg/cm<sup>2</sup> and 90 mg/cm<sup>2</sup> for 711-W15 and 721-W10 respectively at the end of 1.5 h.

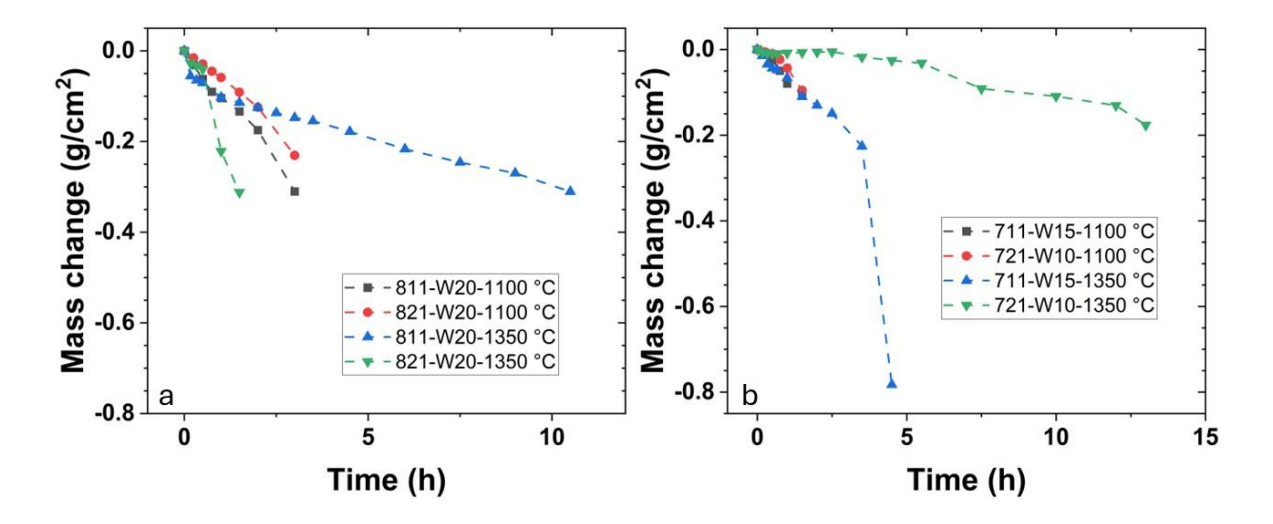


Figure 5.17 Mass change plots with W addition to 811, 821, 711 and 721 alloys at 1100 and 1350 °C. 20 at% Mo was substituted with W in 811 and 821 alloys; 15 at% Mo was substituted with W in 711 and with 10 at% W in the alloy 721.

The effect of Ta addition was studied by substituting 5 at% of Mo with Ta in

alloys 711 and 721. These alloys consisted of three phases Mo(ss), A15 and T2 with Ta preferentially going to T2 phase as indicated by EDS maps. As discussed in the previous sections, Ta-Si bonds are more favorable than Ta-Mo or Mo-Si bonds. Therefore, Ta prefers to go to T2 phase to form a greater number of Ta-Si bonds. Mass change plots of these alloys are shown in Figure 5.18. It is clearly visible that the addition of Ta results in lowering the mass loss at both temperatures. Alloys 711 and 721 with Ta addition exhibited slight initial mass loss for a short duration and then became constant. The stabilization of oxide scale was faster at 1100 °C than at 1350 °C. According to Talmy et al. [238], the oxidation resistance increases with increase in cation field strength which is given by  $Z/r^2$  (Z is valance electrons and r is the ionic radius). When a transition metal is present in borosilicate glass the liquid immiscibility increases with increase in cation field strength. As Ta has high ionic strength, it forms a strong bond with oxygen. This breaks Si-O bonds and modifies the glass structure resulting in the formation of independent Ta-O units [227]. Due to this, there are two liquid phases, one with Ta-O rich units with some Si and the other with Si-O units with some Ta co-exist in glass [227]. The phase separation due to immiscibility leads to increased viscosity of glass [239]. Now as viscosity increases it affects the surface coverage and diffusion through the scale. Higher viscosity leads to reduced flow and poor surface coverage which

promotes oxidation by providing exposed surface. On the other hand, high viscosity reduces oxygen penetration through the oxide scale and reduces oxidation. In case of alloy 711-5Ta in which Mo(ss), T1 and A15 phases were present, the SEM images showed very little oxidation in first 30 s of exposure at 1100 °C. As the time increased to 120 s, the amount of oxidation increased with Si-rich oxide mostly present on T2 and A15 phases. It is expected to cover other regions slowly with time.

The cross-section of the alloy after 20 h of oxidation in Figure 5.19 showed formation of silica rich film at the top with Ta dispersed in it. XRD results as shown in Figure 5.20 confirmed that Ta is present in the form of  $Ta_2O_5$ . Table 5.4 provides the phase fractions of each phase. However, these phase fractions do not include the amount of glassy phase as its peaks were not seen in XRD. Ta is more electropositive as compared to other elements in the system (Pauling's electronegativity [240]: Ta = 1.5, Ta =

SEM images indicated initial mass loss due to (MoO<sub>3</sub>)<sub>3</sub> evaporation followed by mass gain due to oxides formation. In alloy 711-5Ta at 1100 °C, the oxide scale is thickest (~72 μm) as compared to 71-5Ta at 1350 °C and 721-5Ta at both temperatures. Thick scale indicates greater metal recession due to Mo evaporation, however, the mass gain due to Si and Ta oxides formation compensates for the mass loss numerically resulting in slower mass loss before reaching to steady state (Figure 5.18). This shows the amount of Mo lost at 1100 °C was much more than that at 1350 °C. At 1100 °C, there are two factors that decrease the scale viscosity, lower temperature and the presence of Ta. At higher temperatures (1350 °C in this work), the temperature reduces scale

viscosity, so the role of Ta in scale densification becomes easier. This indicates that Ta improves oxidation resistance at higher temperatures. A thin oxide layer with thickness 20  $\mu$ m formed on alloy 711-5 Ta alloy at 1350 °C (as shown in Figure 5.19 Cross-sectional view of samples oxidized at 1100 °C and 1350 °C. Figure 5.19) quickly and the oxide scale became stable without any significant mass loss. The alloy 711-5Ta performed better than all other alloys without and with Ta.

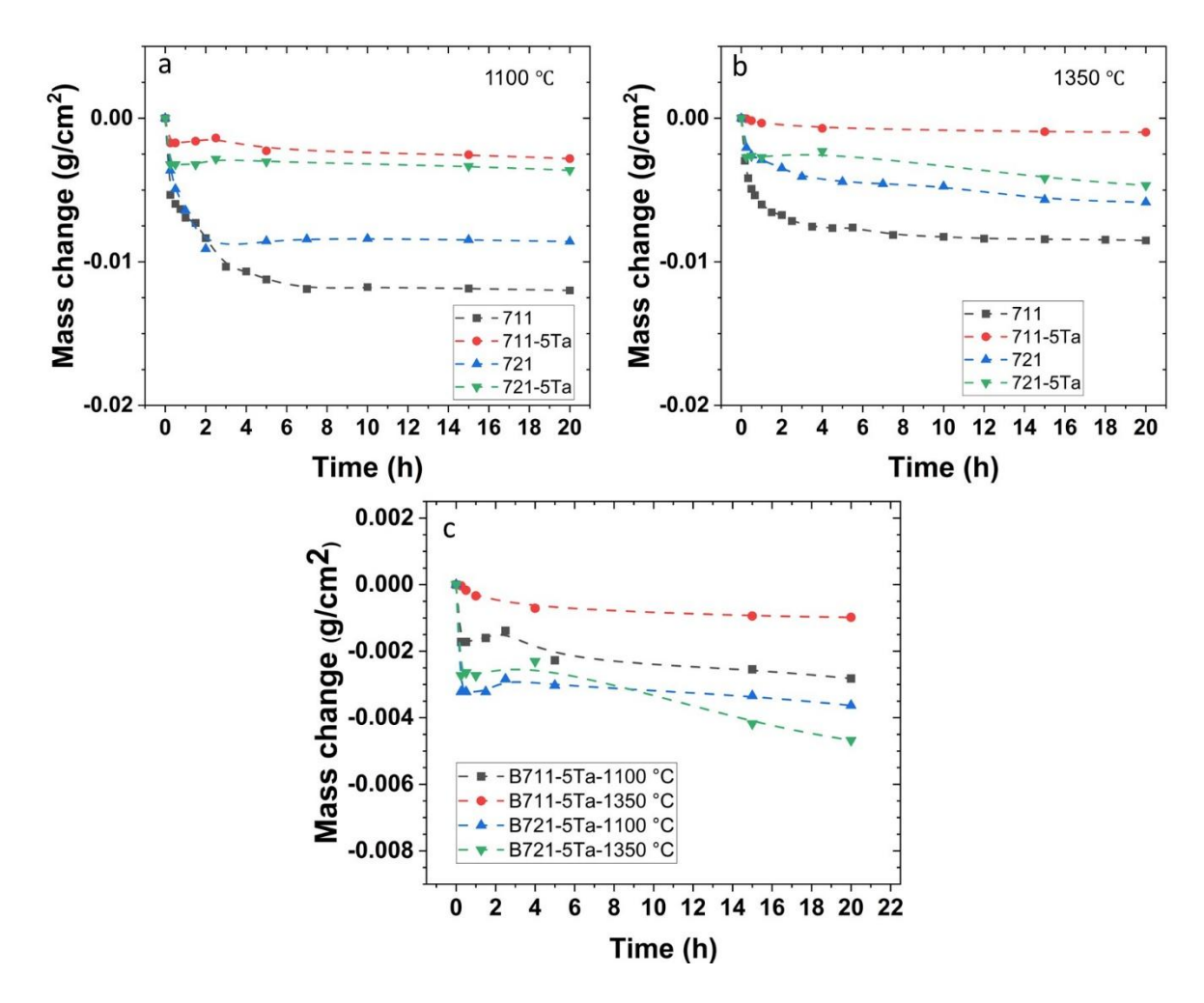


Figure 5.18 Mass change per unit area as function of time during oxidation of (a) alloys 711 and 721 without and with Ta addition at 1100 °C (b) alloys 711 and 721 without and with Ta addition at 1350 °C (c) alloys 711-5Ta and 721-5Ta showing comparison at 1100 °C and 1350 °C.

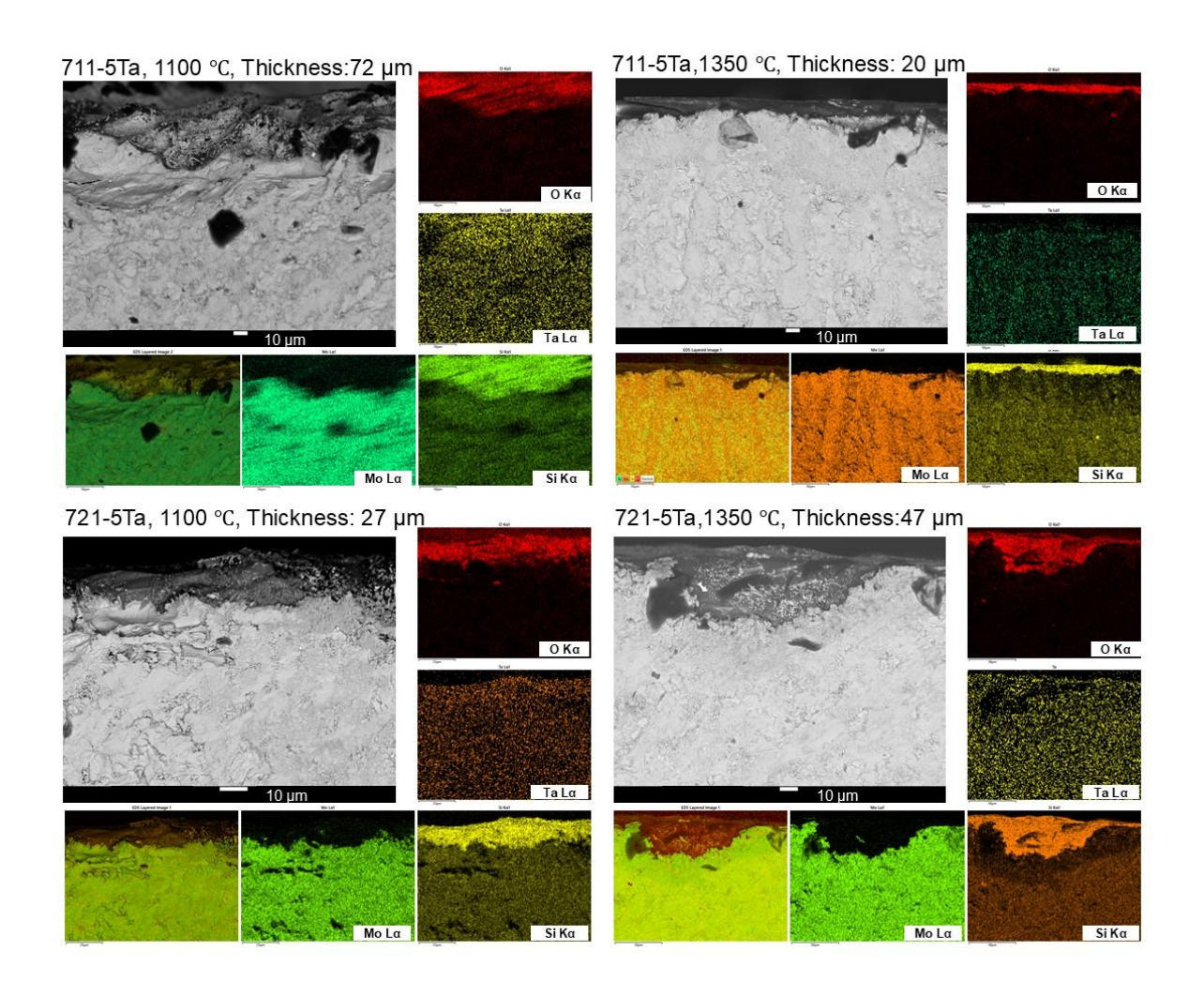


Figure 5.19 Cross-sectional view of samples oxidized at 1100 °C and 1350 °C.

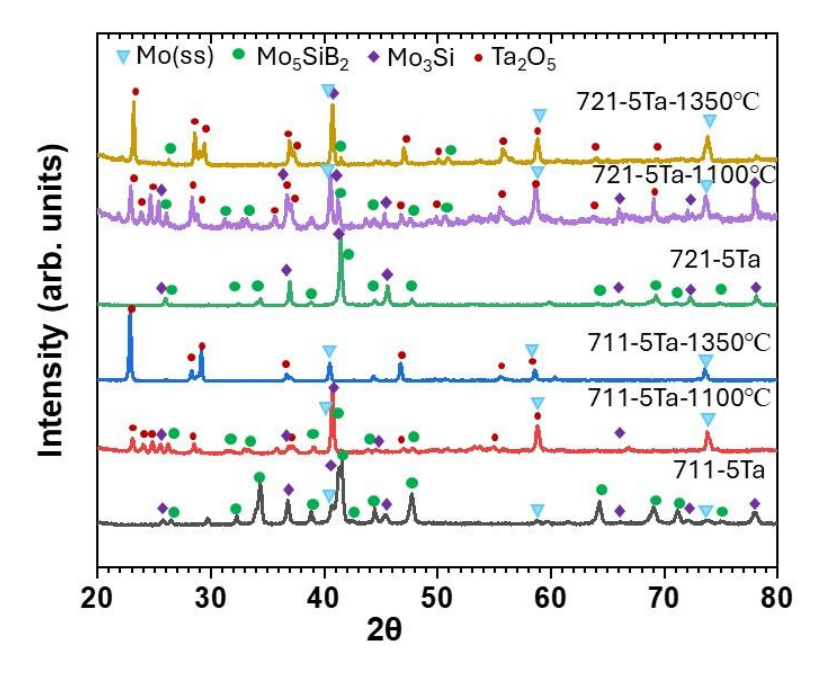


Figure 5.20 Mo-Si-B alloys with 5 at % Ta in non-oxidized condition and oxidized at 1100 °C and 1350 °C.

Table 5.4. Phase fraction sin Mo-Si-B alloys containing Ta after oxidation.

Alloy	Mo (ss)	Mo <sub>3</sub> Si (A15)	Mo <sub>5</sub> SiB <sub>2</sub> (T2)	Ta <sub>2</sub> O <sub>5</sub>
711-5Ta	9.1	29.2	61.6	-
711-5Ta-1100 ℃	71.2	1.8	1.4	25.6
711-5Ta-1350 ℃	65.7	-	-	34.3
721-5Ta	-	68.5	31.5	-
721-5Ta-1100 ℃	41.7	28.2	5.3	24.8
721-5Ta-1350 ℃	84.5	-	6.4	9.1

# 5.5.3 Effect of Si:B ratio

In this work, the alloys were made with Si/B ratio as 1 and 2. Presence of boron in the alloy affects the viscosity of the oxide scale that forms during oxidation. The effect of Si/B ratio on scale viscosity and its flow can be explained with the help of schematic shown in Figure 5.21. More Si will contribute to more SiO<sub>2</sub> formation and better protection of the substrate. But the formation of SiO<sub>2</sub> is not sufficient for improved oxidation. The SiO<sub>2</sub> that was formed must flow and cover the surface. At higher temperatures the viscosity reduces which improves flowability of glassy oxide.

When the amount of B<sub>2</sub>O<sub>3</sub> increases, the scale viscosity decreases [54,213]. Therefore, alloys with Si/B ratio as 1 will have lower scale viscosities as compared to the alloys with Si/B ratio as 2. If we compare initial mass loss of alloys 811 and 821 at 1350 °C, the loss is more in alloy 811 which is the alloy with lower viscosity. It can be inferred that the faster mass loss could be due to more diffusion through the oxide scale due to its less amount of SiO<sub>2</sub> present and lower scale viscosity under these conditions. Even if the scale can flow easily and provide better surface coverage, oxygen can penetrate easily to form

oxides and once MoO<sub>3</sub> forms it can vaporize. However, the oxide layer became stable after some time in both alloys. Similar effect of Si/B ratio was observed in 711 and 721 alloys at 1350 °C. Viscosity of alloys depends not only on the Si/B ratio, but also on temperature. At lower temperature i.e., 1100 °C, the behaviour of alloys 811 and 821 changed. The temperature increased the viscosity of the alloys but as the alloy 811 has lower viscosity than 821 due to more  $B_2O_3$  formation, it achieved sufficient viscosity for a better flow, surface coverage and reduced oxygen penetration.

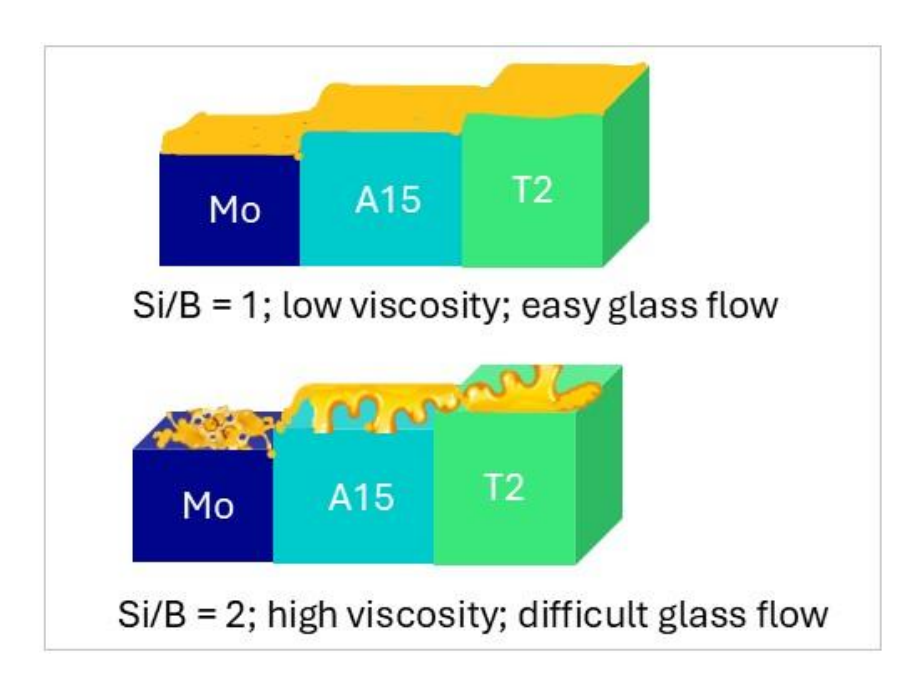


Figure 5.21 Effect of Si/B ratio on glassy scale flow

## 5.5.4 Effect of Al additions

Oxidation of alloy 811-5Al at 1100 °C initially showed mass loss which was higher than 821-5Al under same conditions and then mass change became constant (Figure 5.22). In alloy 821-5Al, after a smaller initial mass loss, the curve flattened after 13 hours of oxidation. In these alloys, the presence of Al is an additional factor that reduces viscosity. It forms Al<sub>2</sub>O<sub>3</sub> upon oxidation and when it mixes with SiO<sub>2</sub>, it tends to reduce its viscosity [211,241]. In the alloy with lower boron content, the lower viscosity helps borosilica scale to flow and cover the surface. It seems that Al addition to the alloy with high boron content reduces viscosity to a larger extent and allows easy oxygen permeation through

it resulting in faster initial mass loss. At 1350 °C, both alloys exhibited rapid mass loss, and the samples were destroyed with oxide formation within 5 hours. Above 1300 °C when most of the boria evaporated, two factors, first is temperature and second is Al<sub>2</sub>O<sub>3</sub> which stays in the scale, reduced scale viscosity. Looking at the mass change trend, it can be concluded that the viscosity was low enough for easy oxygen penetration through it. This resulted in mass loss due to oxide formation and volatilization. Viscosity of SiO<sub>2</sub> glass with varying Al<sub>2</sub>O<sub>3</sub> amount was calculated based on the data provided by Urbain et al. [184] and is plotted in Figure 5.23. It shows that as Al<sub>2</sub>O<sub>3</sub> content increases, the viscosity of scale reduces. This reduction was rapid at lower Al<sub>2</sub>O<sub>3</sub> contents and then becomes low as the Al<sub>2</sub>O<sub>3</sub> content increases.

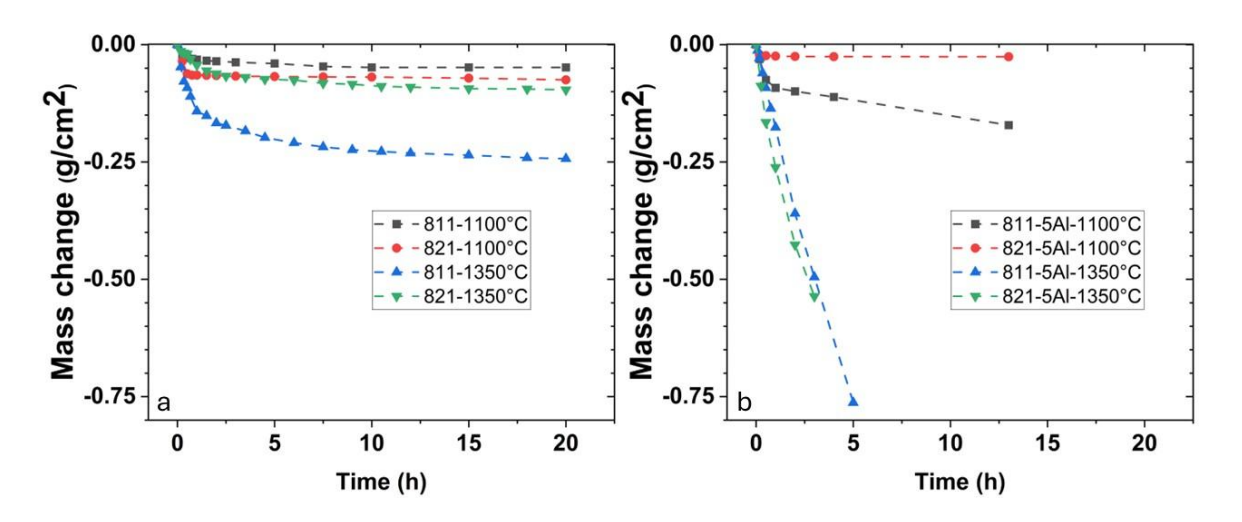


Figure 5.22 Mass change in (a) Mo-Si-B base alloys (b) alloys with Al at 1100 °C and 1350 °C.

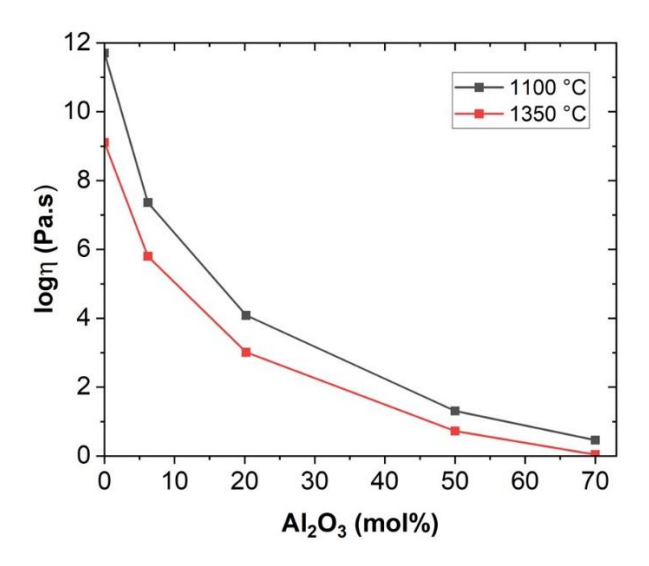


Figure 5.23. Viscosity variation of SiO<sub>2</sub> glass with Al<sub>2</sub>O<sub>3</sub> content

## 5.6 Summary

Oxidation behaviour of Mo-Si-B alloys and effect of refractory metals (W, Ta) and Al addition was studied. W was added to remove detrimental A15 phase, and it was found that addition of 10 at % W to alloy 721 resulted in A15 removal along with formation of metal rich solid solution which was absent from the base alloy. To remove A15 from alloys with 80 at% Mo, a relatively higher amount of W (20 at%) was required. However, W addition to the alloys degraded the oxidation properties. Addition of 5 at% Ta improved the oxidation properties by forming Ta<sub>2</sub>O<sub>5</sub> during oxidation. Alloy 711 with 5 at% Ta showed the maximum improvement in oxidation resistance and formed stable oxide layer faster without any significant mass loss at 1100 and 1350 °C. A thin SiO<sub>2</sub>-rich oxide layer (~20 µm) without any significant damage to the substrate was observed through the cross-sectional view of the sample oxidized at 1350 °C. Al addition to the alloy 811 showed some improvement at 1100 °C, but the properties degraded drastically at 1350 °C which possibly occurred due to reduction in viscosity of borosilica scale due to combined effect of temperature and Al<sub>2</sub>O<sub>3</sub> formation. Based on this work, it can be concluded that Al is not a good choice for addition to Mo-Si-B alloys for higher operating temperatures. Since Ta has shown better results, the effect of its addition to Mo-Si-B alloys should be explored in future studies.

# Chapter 6 Oxidation behaviour of Ultra-High Temperature Ceramics

### 6.1 Introduction

Materials such as borides and carbides of Zr and Hf are often considered as ultra-high temperature ceramics (UHTCs) [168,169,242]. The borides are often used in tandem with SiC to form UHTC composites for potential applications in thermal protection systems (exposure temperatures > 1500 °C [213,243]), e.g., in hypersonic re-entry vehicles. UHTCs for hypersonic vehicles (with speeds of Mach 5 or higher) may experience a wide temperature range from room temperature to over 2000 °C [244]. Broadly, the oxidation mechanisms can be divided into two distinct types at elevated temperatures. At temperatures above 1650 °C, active oxidation of SiC occurs and the structure of the oxide scale includes a ZrO<sub>2</sub> top-layer and a sub-surface SiO<sub>2</sub> rich layer [63,213]. At temperatures below the active oxidation temperature, the structure of the oxide scale is completely different, with SiO<sub>2</sub> forming as the external layer with ZrO<sub>2</sub> islands developing within the silica scale [108,213,245]. In the first case, Ouyang et al. [108] showed that ZrO<sub>2</sub> acts as a natively grown thermal barrier, with a relatively pliant SiO<sub>2</sub> being instrumental in anchoring the ZrO<sub>2</sub> grains. Following a temperature drop across the ZrO<sub>2</sub>, the temperature to which the underlying SiO<sub>2</sub> layer is exposed would be under the active oxidation temperature.

The temperature of interest for this work is 1600 °C up to which a SiO<sub>2</sub>-rich scale is formed at the top which is known to protect the underlying substrate during oxidation. Investigating the oxidation behavior at these temperatures allows us to explore the SiO<sub>2</sub> scale formation mechanism directly through a series of *ex-situ* studies that allows us to monitor the evolution of the surface oxide. The dynamics of the scale formation thus studied potentially provides information about tuning the SiO<sub>2</sub> scale chemistry, which in turn can translate to higher surface temperatures, where ZrO<sub>2</sub> forms externally, but SiO<sub>2</sub> nonetheless forms at the subscale and is exposed to approximately 1600-1650°C. At temperatures below the active oxidation temperature, beneath the protective SiO<sub>2</sub> layer, crystalline ZrO<sub>2</sub> in case of ZrB<sub>2</sub> and HfO<sub>2</sub> in case of HfB<sub>2</sub> is formed. The coarsening kinetics of these refractory oxides provide insights into the dynamics of the SiO<sub>2</sub> scale. Furthermore, these oxides are porous which are filled with SiO<sub>2</sub>-rich oxide.

The stability of oxide scale depends on many factors such as composition and operating temperature [93,168]. Therefore, to improve oxidation resistance, it becomes extremely important to control the composition and properties of oxide scale. This can be accomplished by modifying the composition of base ceramics. For example, in some studies nitrides, carbides and silicides of various metals such as AlN [108,118], TaC [119,122], M (Zr, Mo, Ta, W)Si2 [120,246] were added to ZrB2-SiC ceramics. These additions affect silica scale composition, viscosity, surface coverage, oxide scale structure and overall oxidation properties of the system [108,120,242], which is reflected in the coarsening of crystalline oxide features on the surface scale as well as in the development of the multilayered structure in the oxygen affected zones along the cross-section.

In studies by Ouyang et al. [108,118], the effect of AlN on oxidation properties of  $ZrB_2$ -SiC ceramics was studied. It was reported that at 1600 °C, an optimal amount of AlN (10 vol%) increased oxidation resistance. When the amount was too small or too high, it was harmful. AlN addition to the these ceramics results in the formation of  $Al_2O_3$  which reduces the  $SiO_2$  scale viscosity

[172,184,211,241]. The reduced viscosity facilitates faster spreading of SiO<sub>2</sub> scale and better surface coverage, at the same time it promotes oxygen permeation through the scale. The addition of other elements such as Ta in the scale along with AlN can alter oxidation properties. Ta oxidizes to form Ta<sub>2</sub>O<sub>5</sub> in the oxide scale. It is reported that Ta<sub>2</sub>O<sub>5</sub> increases scale viscosity of borosilicate glasses and also modifies other structural properties of the oxides such as SiO<sub>2</sub> network and phase separation within the oxide scale [120,122]. As Al<sub>2</sub>O<sub>3</sub> decreases viscosity and Ta<sub>2</sub>O<sub>5</sub> increases it, their combination will be helpful in tuning the scale viscosity. Wang et al. studied the effect of TaC addition on oxidation of ZrB<sub>2</sub>-20 vol% SiC ceramics in temperature range of 1200-1500 °C and showed that 10 vol% reduced oxidation resistance, whereas 30 vol% addition improved the oxidation resistance.

Opila et al. [122] added 20 vol% TaC and 20 vol% TaSi<sub>2</sub> to ZrB<sub>2</sub>-20 vol% SiC ceramics and found that TaSi2 addition improved oxidation resistance while TaC degraded oxidation resistance. This indicates that the form of Ta addition plays an important role in the oxidation behaviour. It was shown that improved oxidation resistance on TaSi2 addition is not due to presence of Si which may form more glass, but it is solely because of Ta which causes phase separation in glassy scale resulting in increased viscosity [122]. However, during oxidation, C from TaC may escape from the substrate resulting in increased porosity providing paths for easy oxygen permeation [122]. Another possible addition could be CeO<sub>2</sub> due the relatively large size of Ce atom (atomic radius [247] Ce: 1.85 Å, Ta: 1.45 Å, Si: 1.32 Å, Zr: 1.6 Å) and low electronegativity (Pauling electronegativities [247]- Ce: 1.12, Ta: 1.5, Si: 1.9, Zr: 1.33 ). Due to its highly electropositive nature, it is likely to preferentially diffuse outward to the surface and react with atmospheric oxygen to form an oxide. The electropositive nature of the Ce cation can also influence the SiO<sub>2</sub> network, thus affecting the scale viscosity and dynamics. The large size of Ce is known to result in a blocking effect in crystalline scales; elements with larger cationic sizes also tend to diffuse slowly, thereby slowing down the scale growth. To the best of our knowledge, the effect of CeO2 additions on the oxidation of UHTCs has not been reported in the literature; however, it was found that CeO<sub>2</sub> affects the structural properties of silicate glasses [248]. It promotes Al ions to stay in Al(6) coordination or as AlO<sub>6</sub> resulting in the formation of non-bridging oxygens (NBOs) in the glass structure which reduce glass viscosity [248]. A combined effect of reduced viscosity (i.e., faster surface coverage by the glassy SiO<sub>2</sub> rich scale) and preferential oxidation resulting in the formation of CeO<sub>2</sub> may improve the oxidation resistance of ceramics. Therefore, in this work, the effect of AlN, TaC and CeO2 addition to ZrB2-SiC UHTCs was studied. The effects of TaC and CeO2 addition, in isolation, as well as their effect when added in tandem with AlN were explored. The combined effect of these ceramics and CeO<sub>2</sub> addition on oxidation properties of UHTCs has not been studied yet and it is worth studying how Al and Ce ions would affect synergistically. Therefore, the alloys with varying compositions were prepared expecting that these combinations may tune the scale viscosity and improve oxidation resistance. The fabricated samples were then exposed to stagnant air at 1600 °C for oxidation.

# 6.2 Experimental Methods

The powders with purity  $\geq$  99.5 % were procured from Sigma Aldrich and Thermofisher Scientific and the compositions of the samples prepared for this work is mentioned in Table 6.1. The powders were mixed first using a mortar and pestle and then milled for 1 hour. The prepared powders were then sparkplasma sintered at 1750 °C applying 40 MPa pressure for 10 min in graphite mould of 10 mm diameter. The thickness of the prepared samples was approximately 4 mm. After this, the samples were ground to remove the graphite layer and then cleaned ultrasonically in ethanol and distilled water. Densification of the samples was measured using Archimedes method which was in the range of 96-99%. X-ray diffraction (XRD, PANalytical XPERT-PRO, Cu-K $\alpha$  radiation = 1.54 Å), Scanning electron microscopy (SEM, JEOL-6610LV) and Energy Dispersive Spectroscopy (EDS) analysis using 15 kV, was done prior to oxidation to confirm the phases formed after sintering.

The samples were inserted in a pre-heated muffle furnace (SMNANO TECH-CAMF-1700-8L model with MoSi<sub>2</sub> heating element) at 1600 °C for oxidation in stagnant air, heated for 5 min and were taken out for SEM and EDS analyses. This step was repeated after heating samples for 15 min and 10 h to study temporal evolution of the oxide scale. The mass of each sample was measured periodically throughout the oxidation experiments. After 10 h of oxidation, the samples were sectioned to observe the oxide growth through cross section. The cross-sections of the oxidized samples were studied systematically, starting from the top of the sample to the inner core, with a series of micrographs captured and stitched seamlessly to reveal the chemical gradients set-up within the oxidized samples as a function of depth.

Table 6.1. Composition of UHTCs in vol% for oxidation studies

Sample	ZrB <sub>2</sub>	SiC	AlN	CeO <sub>2</sub>	TaC
ZSA721	70	20	10		
ZSAT72-5-5	70	20	5	-	5
ZSAC72-5-5	70	20	5	5	-
ZSC721	70	20	-	10	-
ZSC631	60	30	-	10	-
ZST631	60	30	-	-	10

# 6.3 Thermodynamic stability and volatility diagrams

Volatility diagram for ZrB<sub>2</sub>-SiC-AlN, ZrB<sub>2</sub>-SiC-AlN-TaC and ZrB<sub>2</sub>-SiC-AlN-CeO<sub>2</sub> shown in Figure 6.1, Figure 6.2 and Figure 6.3 respectively. According to these diagrams, the stable (non-volatile) oxides that will form at 1600 °C should be SiO<sub>2</sub>, ZrO<sub>2</sub>, B<sub>2</sub>O<sub>3</sub>, and Al<sub>2</sub>O<sub>3</sub>, Ta<sub>2</sub>O<sub>5</sub> and CeO<sub>2</sub> and volatile species will be SiO, B<sub>2</sub>O<sub>3</sub>, BO<sub>2</sub> and Al<sub>2</sub>O. Lower pO<sub>2</sub> values for SiO<sub>2</sub>(l) formation from SiC indicates that it is more stable than ZrO<sub>2</sub> formation from ZrB<sub>2</sub> at all temperatures. AlN or Al<sub>2</sub>O<sub>3</sub> transforms into vapor species as Al<sub>2</sub>O at very low oxygen partial pressures. Therefore, Al<sub>2</sub>O<sub>3</sub> should remain stable at pO<sub>2</sub> in air. This suggests

that the possible stable oxides in the outer scale in sample containing  $Al_2O_3$  will be  $ZrO_2$  and  $Al_2O_3$ .  $B_2O_3$  has a tendency to evaporate as gas due to its high vapor pressure as compared to other species. Experimental results on UHTCs show formation of smooth Si-rich scale without any grains indicating amorphous silica or borosilica glass with  $ZrO_2$  agglomerates. The volatility diagram in Figure 6.3 shows  $CeO_2$  remains stable at wide range and forms  $CeO_2$  gas at very low oxygen partial pressure values.

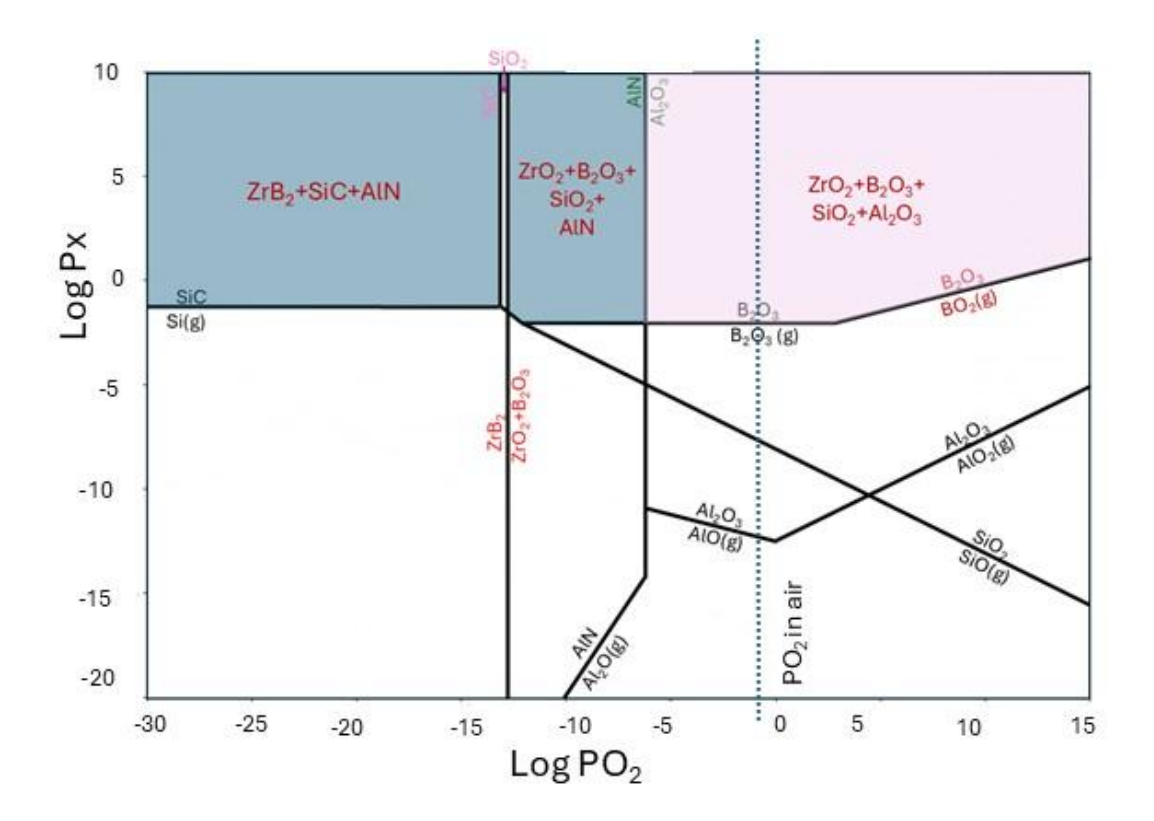


Figure 6.1 Volatility diagram of ZrB<sub>2</sub>-SiC-AlN system at 1600 °C

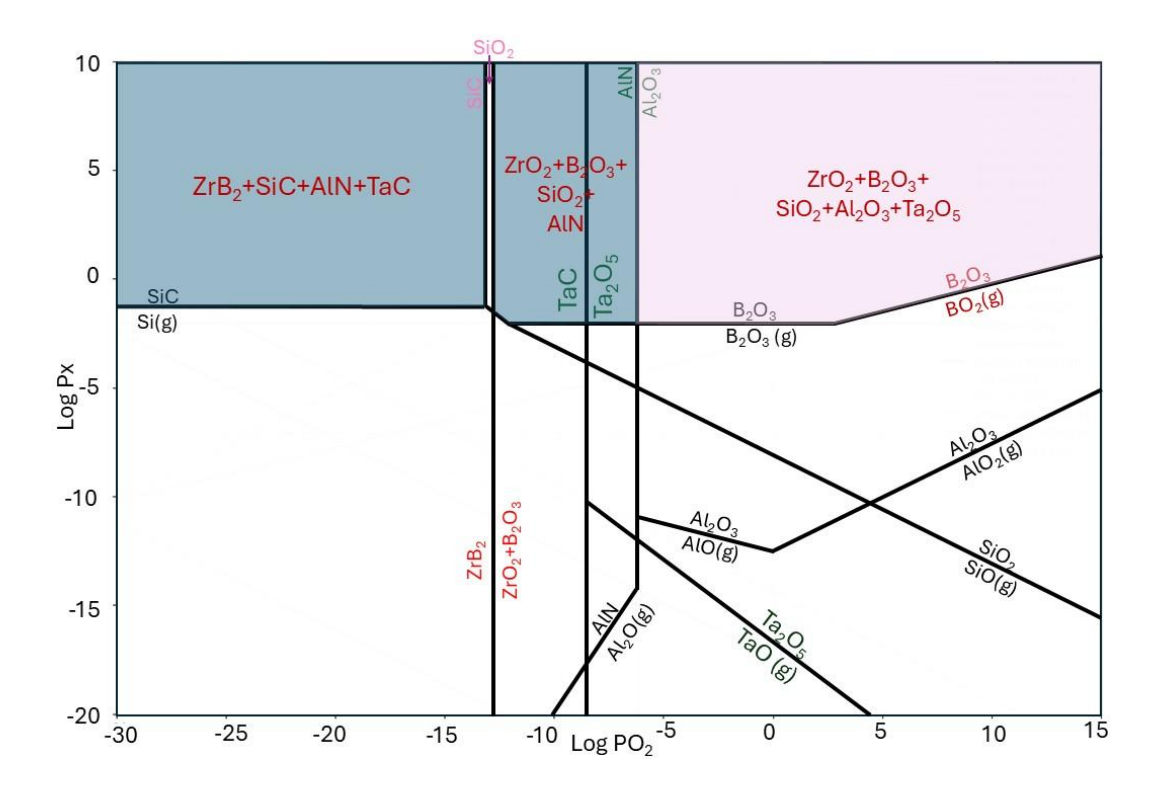


Figure 6.2. Volatility diagram of ZrB2-SiC-AlN-TaC system at 1600  $^{\circ}\text{C}$ 

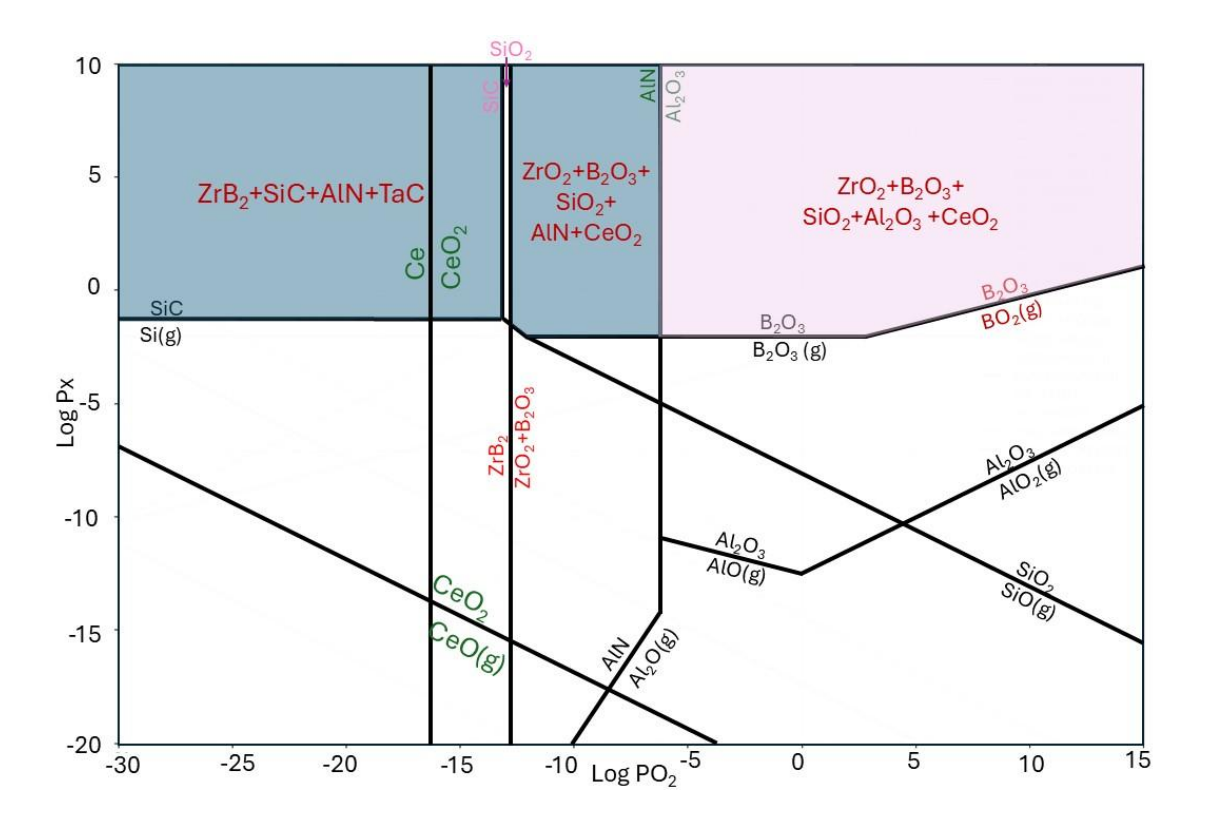


Figure 6.3. Volatility diagram of ZrB₂-SiC-AlN-CeO₂ system at 1600 °C

# 6.4 Oxidation behaviour of Ultra-High Temperature Ceramics

### 6.4.1 Oxide scale microstructures

Initial microstructures show ZrB<sub>2</sub> matrix as brighter phase while SiC and AlN as dark phases (Figure 6.4). Since SiC and AlN have similar Z contrasts, it was difficult to differentiate the two phases using SEM. In UHTC ZSA721, dark SiC and AlN phases are embedded in bright ZrB<sub>2</sub> matrix, where AlN particles are smaller than SiC as evident from EDS maps. CeO<sub>2</sub> and TaC appeared as small brighter particles in ZrB<sub>2</sub> matrix in alloy ZSAC72-5-5 and ZSAT72-5-5 respectively.

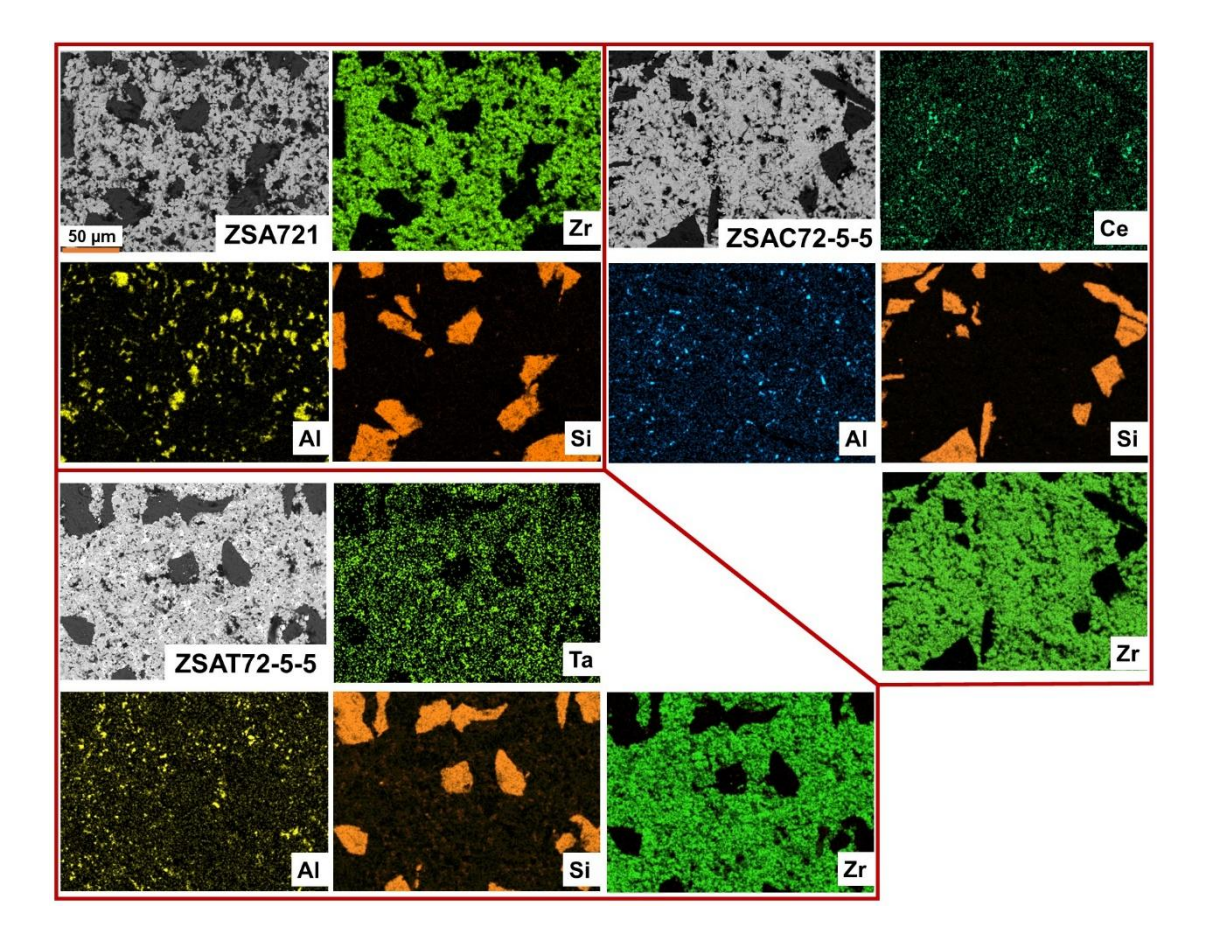


Figure 6.4 Microstructures and EDS maps of as-fabricated ZSA721, ZSAC72-5-5 and ZSAT72-5-5 UHTCs using back scattered imaging. All images are at same magnification.

The microstructures of as-fabricated ceramics and their surfaces after oxidation at different time intervals are shown in Figure 6.5. Oxidation of ZSA721 for 5 min at 1600 °C resulted in formation of smooth glassy surface embedded with

coarse bright particles. After 15 min, more SiO<sub>2</sub> scale formation was observed and at the end of 10 h, SiO<sub>2</sub> scale enriched with ZrO<sub>2</sub> agglomerates was found. The elemental maps clearly show Si and XRD results after oxidation (Figure 6.13) do not show Si peak indicating formation of amorphous oxide. This agrees with the observations by Ouyang et al. [118,176]. AlN results in formation of Al<sub>2</sub>O<sub>3</sub> during oxidation which results in glass viscosity reduction and increased diffusivity. In our previous work also, Al ions addition to SiO<sub>2</sub> glass resulted in increased diffusivity [241]. Coarse ZrO<sub>2</sub> formation occurs due to Ostwald ripening process which depends on the solubility of ZrO<sub>2</sub> particles in glassy melt [118]. According to Karlsdottir and Halloran [182,245], SiO<sub>2</sub>-B<sub>2</sub>O<sub>3</sub>-ZrO<sub>2</sub> ternary liquid forms during oxidation of ZrB<sub>2</sub>-SiC UHTCs in which ZrO<sub>2</sub> is soluble. As B<sub>2</sub>O<sub>3</sub> evaporates from this liquid, the composition shifts to SiO<sub>2</sub>-ZrO<sub>2</sub> composition where ZrO<sub>2</sub> does not remain soluble and precipitates out. The presence of Al<sub>2</sub>O<sub>3</sub> results in low viscosity of the melt can make ZrO<sub>2</sub> movement easier resulting in Ostwald ripening and formation of coarse agglomerates.

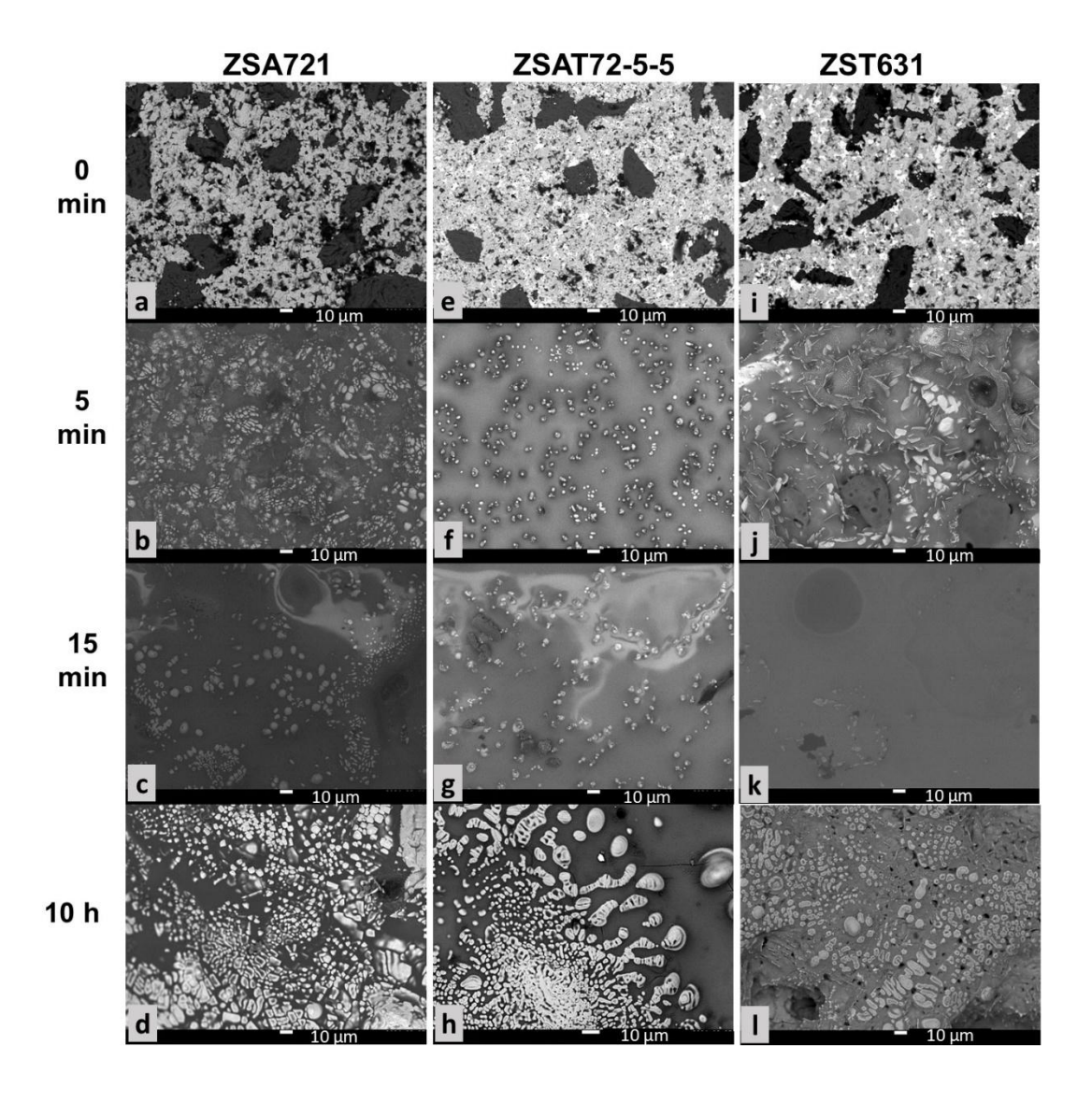


Figure 6.5 Surface microstructures of UHTCs using BSE imaging prior to oxidation and post oxidation for 5 min, 15 min and 10 h. (a)-(d) ZSA721, (e)-(h) ZSA772-5-5, (i)-(l) ZST631

When 5 at% TaC was added along with 5 at% AlN to make ZSAT72-5-5, its oxidation after 5 minutes resulted in SiO<sub>2</sub> scale embedded with ZrO<sub>2</sub> particles as can be seen in Figure 6.5 e-h. The scale morphology at this step was different from the sample containing only AlN. This could be due to the presence of Ta cation in the SiO<sub>2</sub>-rich scale in initial stage as it results in increased scale viscosity [120]. The presence of smaller ZrO<sub>2</sub> particles at the surface indicates less ZrO<sub>2</sub> mobility resulting in slightly lower coarsening. Coarsening of ZrO<sub>2</sub> agglomerates occurred all over the surface after 10 h of exposure. EDS analysis of cross section and XRD of exposed surface after oxidation confirmed the particles as ZrO<sub>2</sub>. This suggests that the presence of small amount of TaC does not affect scale structure much. In sample ZST631, oxide flakes and cavities

appeared after 5 min of oxidation. Upon oxidation for 15 min SiO<sub>2</sub> with ZrO<sub>2</sub> agglomerates at some places was seen. Later, after 10 h SiO<sub>2</sub> scale got enriched with ZrO<sub>2</sub> agglomerates on the entire surface. It appears that the amount of ZrO<sub>2</sub> is more in ZSAT72-55 as compared to ZST631 which could be due to the relatively lower amount of ZrB<sub>2</sub> (60 vol%) in the latter sample. In addition to this, deep cavities/pores also appeared on the surface. These cavities were clearly visible on the cross section of the sample as well and it seems that these were formed due to bubble formation. These were probably because of escaping of CO or CO<sub>2</sub> formed from carbon present in SiC and TaC. These results were consistent with the observations by Opila et al. [122]. Oxygen can easily penetrate through these cavities resulting in increased oxidation which inhibits formation of protective scale. Ta diffuses outwards like Si and as there is no protective layer, and in presence of pores it becomes easier for Ta to diffuse and oxidize [119]. It was reported that Ta forms Ta<sub>2</sub>O<sub>5</sub> and increases the scale viscosity [120]. High viscosity may reduce oxygen diffusion through the scale, but at the same time it may reduce the scale flow or spread over the surface.

During oxidation of samples when both AlN and CeO<sub>2</sub> were added to ZrB<sub>2</sub>-SiC (ZSAC721-5-5), small convection cells were observed at some regions after 15 min of exposure along with Al-rich rod-like structures which probably have formed due to oxidation of AlN to Al<sub>2</sub>O<sub>3</sub>. When fresh ZrO<sub>2</sub>+SiO<sub>2</sub>+B<sub>2</sub>O<sub>3</sub> oxides form beneath ZrO<sub>2</sub> layer, an increase in volume takes place leading to transport of this mixture to the surface. This mixture then flows laterally, and some patterns are formed due to viscosity difference [114,182,245]. Most of the ZrO<sub>2</sub> stays at the center while the glassy scale flows. As the scale flows, B<sub>2</sub>O<sub>3</sub> starts to evaporate as its vapor pressure on the surface is much higher than SiO<sub>2</sub> (233 Pa for B<sub>2</sub>O<sub>3</sub>, 3 x  $10^{-4}$  for SiO<sub>2</sub>) [182,245]. B<sub>2</sub>O<sub>3</sub> evaporation results in viscosity during the flow leaving floral patterns behind. The darker regions show B<sub>2</sub>O<sub>3</sub>, and relatively brighter regions show SiO<sub>2</sub>-rich scale. At this stage, Ce also migrates to the top. These convection cells were not observed on the surface at

the end of 10 h due to formation of protective SiO<sub>2</sub>-rich scale at the top. At some regions, ZrO<sub>2</sub> particles were also observed.

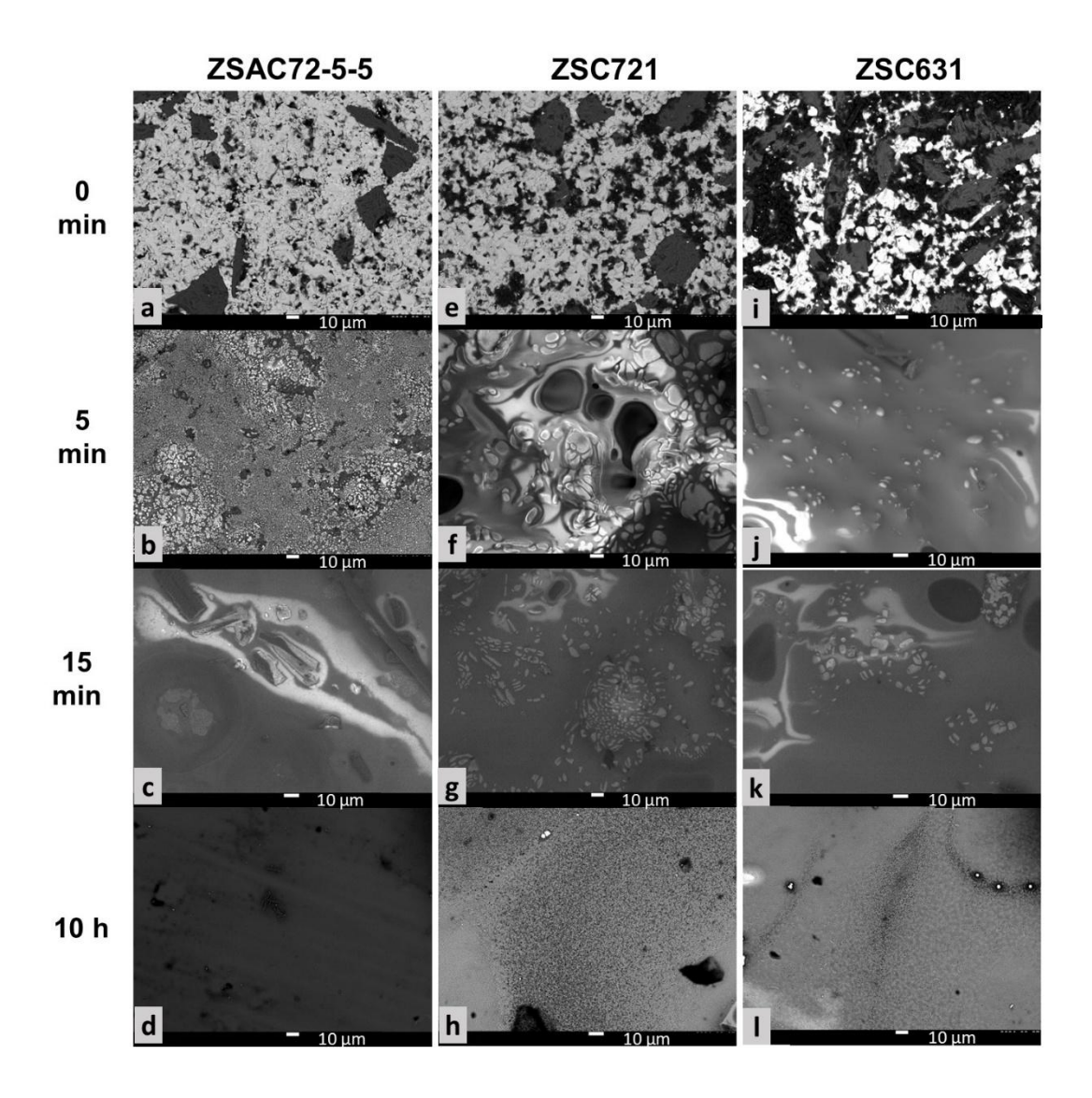


Figure 6.6. Surface microstructures of UHTCs using BSE imaging prior to oxidation and post oxidation for 5 min, 15 min and 10 h. (a)-(d) ZSAC72-5-5, (e)-(h) ZSC721, (i)-(l) ZSC631

Samples ZSC721 and ZSC631 initially formed SiO<sub>2</sub> glass with ZrO<sub>2</sub> agglomerates. The ZrO<sub>2</sub> agglomerates were smaller in size and lesser in amount on ZSC631 surface as compared to ZSC721. As ZSC631 had higher SiC content and lower ZrB<sub>2</sub> content, it led to the formation of more SiO<sub>2</sub> during oxidation. At the end of 10 h, a uniform SiO<sub>2</sub> layer was observed on both samples. When oxidation started in these two samples, SiO<sub>2</sub> and ZrO<sub>2</sub> formed. Now, as CeO<sub>2</sub> was also present, it results in the formation of NBOs in SiO<sub>2</sub>. Presence of NBOs can make the oxygen diffusion faster and this phenomenon was also observed in our previous work [241]. Increased oxygen diffusion increases oxidation

resulting in more  $SiO_2$  formation. According to volatility diagram calculations, SiC can oxidize to  $SiO_2$  at lower  $P_{O2}$  values than that required for  $ZrB_2$  to  $ZrO_2$  formation. This suggests that SiC can oxidize as soon as small oxygen concentration gets available at the substrate oxide interface. The  $SiO_2$  glassy scale then moves outwards along with Ce covering the underlying oxide at the end of 10 h of oxidation.

#### 6.4.2 Oxide scale cross sectional microstructures

The alloy ZSA721 containing 10 vol% Al, showed mass gain of ~58 mg/cm<sup>2</sup> at the end of 10 h of exposure at 1600 °C with average oxide layer thickness of  $1388 \pm 100 \, \mu m$ . The cross section after oxidation is shown in Figure 6.7. The sample formed a thick and porous layer consisting of mostly ZrO<sub>2</sub> columns with SiO<sub>2</sub>-rich scale trapped within the pores. The UHTC ZSAT72-5-5 with addition of 5 vol% TaC resulted in the formation of thick and porous oxide layer of  $1357 \pm 100 \, \mu m$  (Figure 6.8). A minute glassy SiO<sub>2</sub>-rich layer with thickness of ~25 µm was found at the top resulting in continuous oxidation. If we compare the cross section with the surface after 10 h of oxidation, the surface shows coarsening of ZrO<sub>2</sub> (Figure 6.5) and smooth SiO<sub>2</sub>-rich scale in smaller region. This suggests that the addition of Ta has slightly increased the scale viscosity. However, the microstructures reveal the formation of nonprotective oxide scale formation and the improvement in oxidation resistance was not observed. The sample ZST631 containing only TaC, suffered the maximum damage. It formed a highly porous and thick oxide layer of around  $1477 \pm 200 \,\mu m$  thickness showing a mass gain of 69 mg/cm<sup>2</sup>. The oxide layer consisted of long ZrO<sub>2</sub> grains filled with SiO<sub>2</sub> without any protective SiO<sub>2</sub> scale at the top (Figure 6.9).

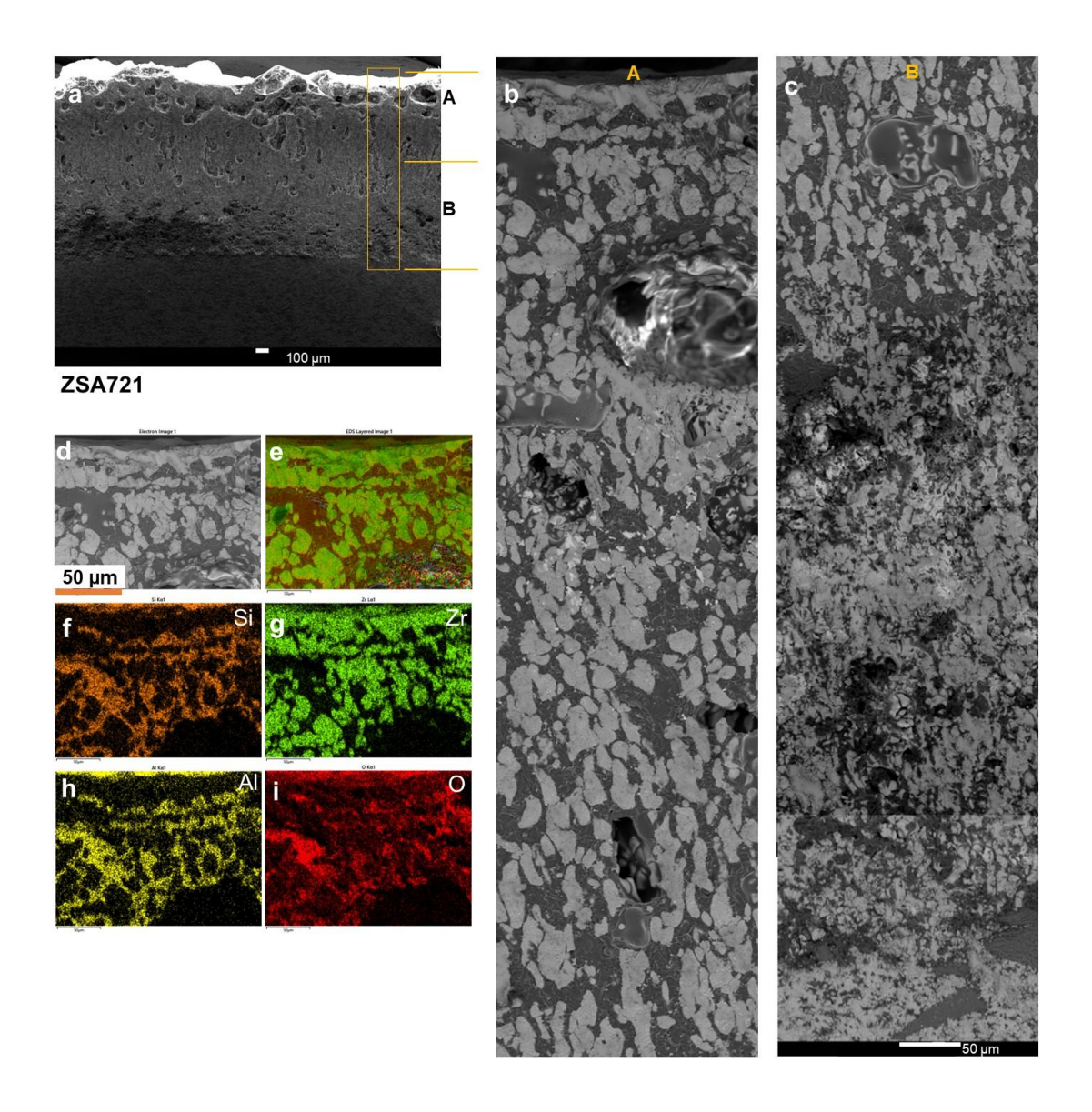


Figure 6.7. a) Cross section of sample ZSA721 after oxidation for 10h, b), c) magnified view of the cross section, d) electron image of upper region of the cross section for elemental mapping, e) layered image, f)-O) elemental mapping.

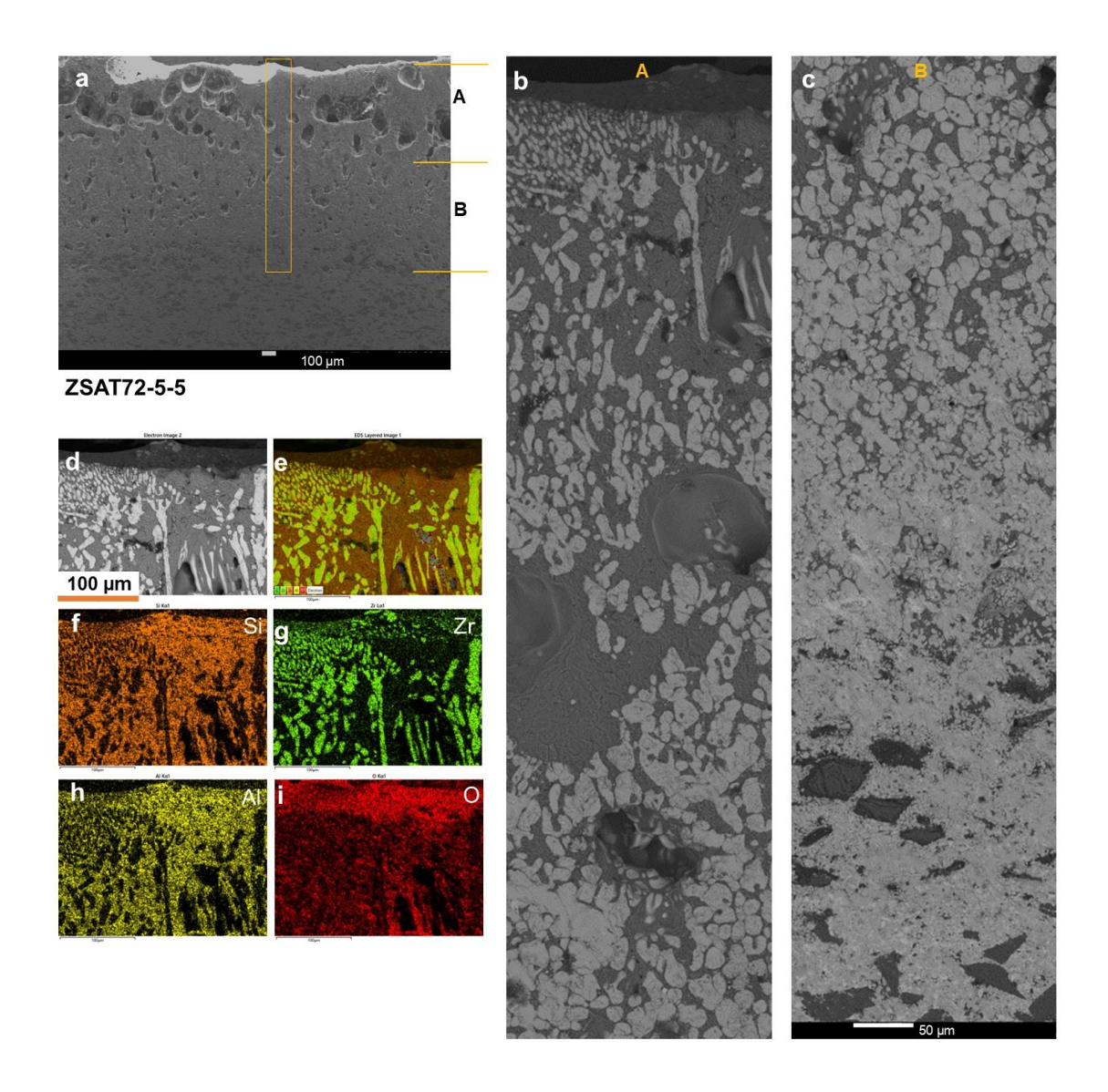


Figure 6.8. a) Cross section of ZSAT72-5-5 sample after oxidation at 1600  $^{\circ}$ C for 10 h, b), c) magnified view the cross section obtained by stitching the images together from top to bottom, d)-i) EDS elemental mapping of the upper region.

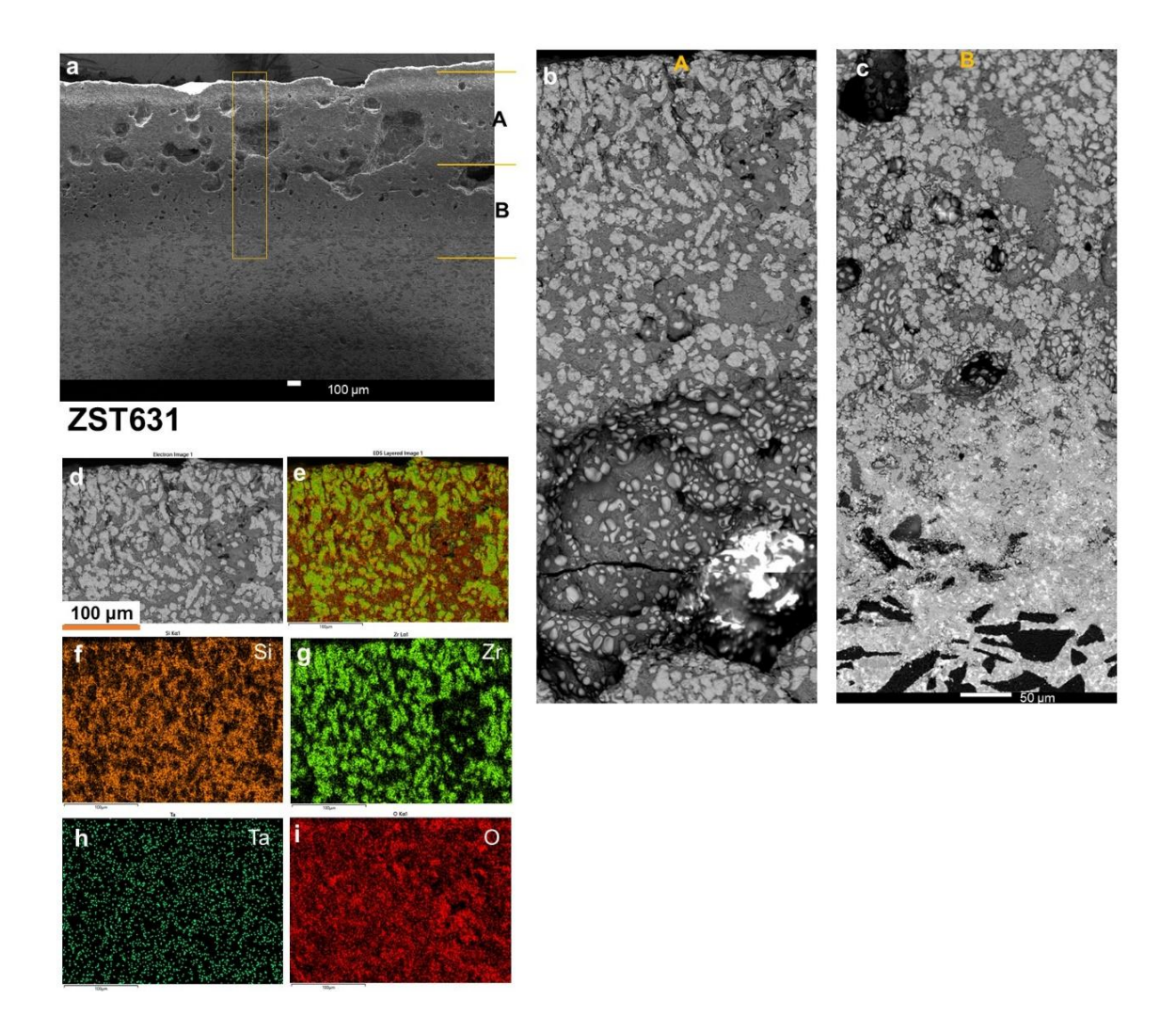


Figure 6.9. a) Cross section of ZST631 sample after oxidation at 1600 for 10 h, b),c) magnified view the cross section obtained by stitching the images together from top to bottom, c)-h) EDS elemental mapping of the upper region.

In alloy ZSAC72-5-5, when 5 vol% CeO<sub>2</sub> was added at the expense of Al, the oxide layer thickness was  $550 \pm 75 \, \mu m$ . The cross section of oxidized ZSAC72-5-5 as shown in Figure 6.10 revealed the formation of glassy SiO<sub>2</sub> scale at the top with ZrO<sub>2</sub> fingers beneath it. The channels between ZrO<sub>2</sub> fingers were filled with SiO<sub>2</sub>-rich glass. ZrO<sub>2</sub> changed from finger-like structure to globular on moving to the depth. Below ZrO<sub>2</sub>, SiC depleted zone was also observed. The SiO<sub>2</sub> top layer was smooth and dense with some pits indicating bubbling during oxidation. EDS maps showed fine Ce particles homogeneously dispersed in SiO<sub>2</sub> top layer indicating presence of CeO<sub>2</sub>.

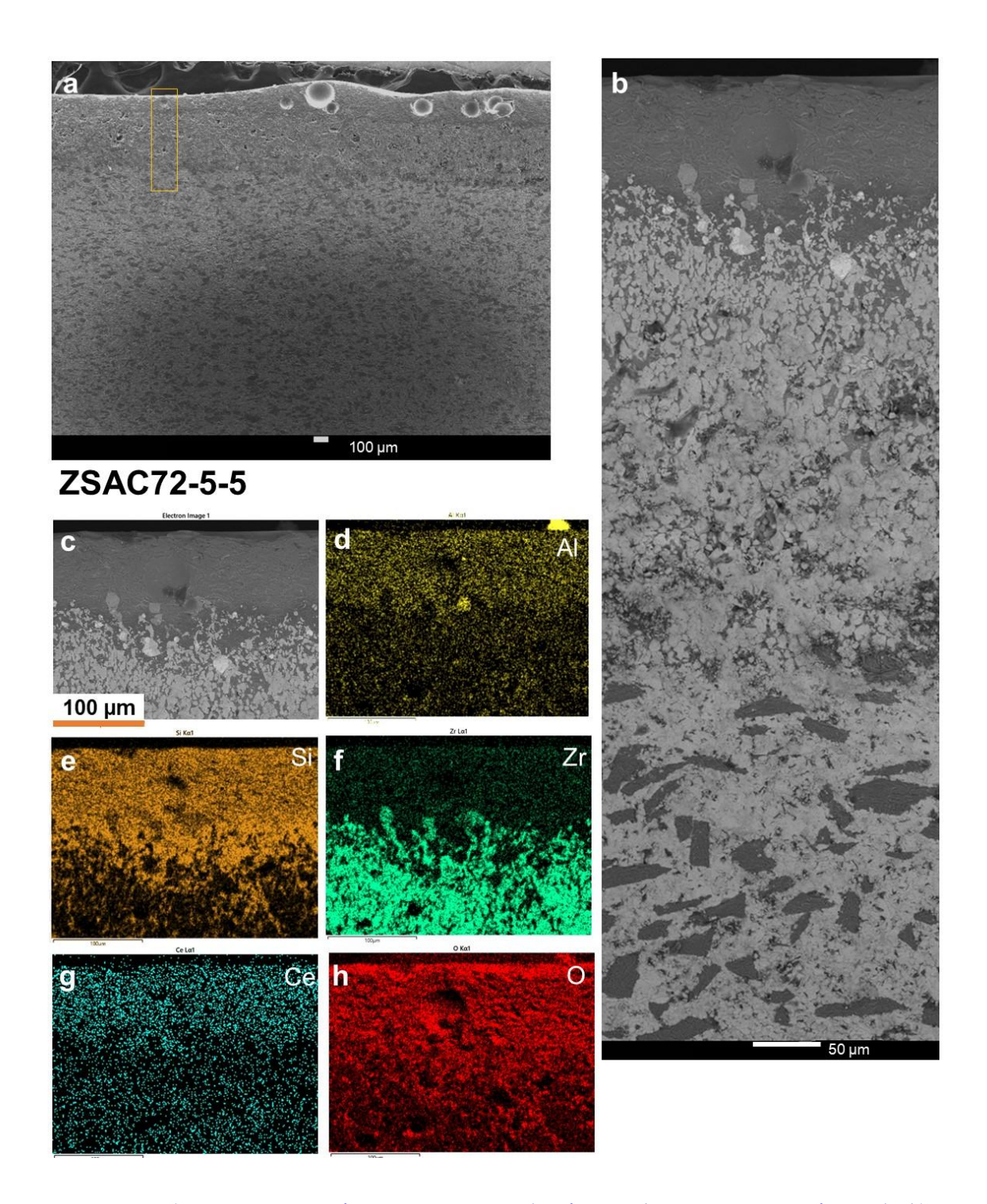


Figure 6.10 a) Cross section of ZSAC72-5-5 sample after oxidation at 1600 °C for 10 h, b) magnified view the cross section obtained by stitching the images together from top to bottom, c)-h) EDS elemental mapping of the upper region.

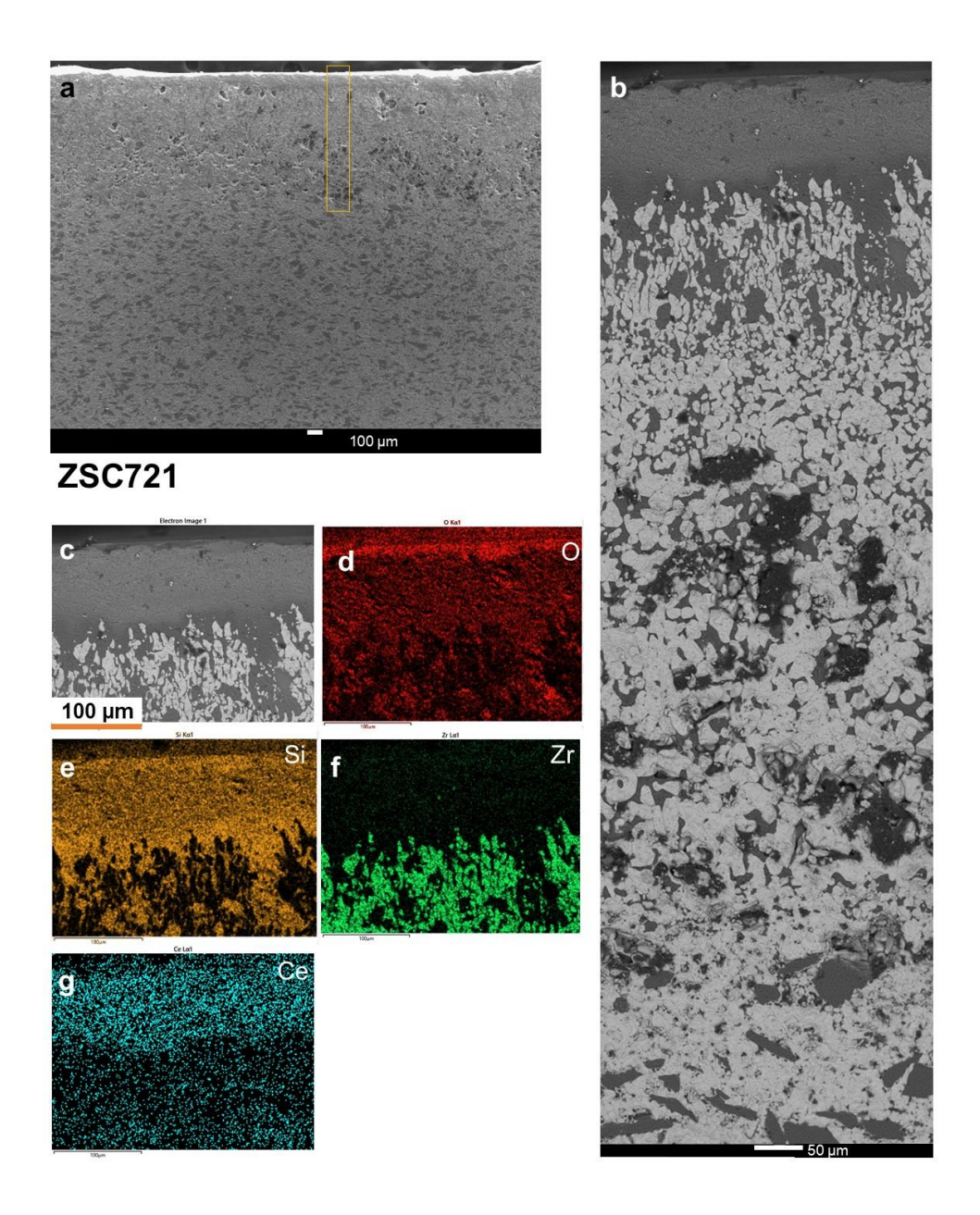


Figure 6.11 a) Cross section of ZSC721 sample after oxidation at 1600 for 10 h, b) magnified view the cross section obtained by stitching the images together from top to bottom, c)-g) EDS elemental mapping of the upper region.

Sample ZSC721 and ZSC631 oxidized to form ZrO<sub>2</sub> and SiO<sub>2</sub> oxide layers. CeO<sub>2</sub> was uniformly dispersed in SiO<sub>2</sub> top layer, and this mixture was also filled in the gaps between ZrO<sub>2</sub> fingers. The oxide scale present on ZSC721 did not show significant pores, while the oxide scale on ZSC631 was porous as can be seen from Figure 6.12. But these pores or cavities were not seen in the top SiO<sub>2</sub> layer. As the latter UHTC had more SiC content (i.e., 30 vol%), the pores could be due to higher SiO<sub>2</sub> and CO formation resulting in cavities as the gases escape. There was not much difference in the mass gain of these two samples and the oxide

layer that formed on ZSC631 was slightly thinner with an average thickness of about  $623 \pm 40 \, \mu m$ . As SiC content is higher in ZSC631, SiO<sub>2</sub>-rich layer probably has formed relatively faster and in larger amount than that in ZSC721. Similar observation was made by Williams et al. [249] for high silicon content in the samples. The thickness of SiC-depleted zone in ZSC721 with lower Si (20vol%) content than ZSC631 (30vol%) was less and ZrO<sub>2</sub> was denser. The oxidation mechanism seems similar in both ZSC721 and ZSC631, but the oxide structure in terms of thickness of various layers is slightly different. We assume that this difference is due to the varying ZrB<sub>2</sub> and SiC contents in the two samples.

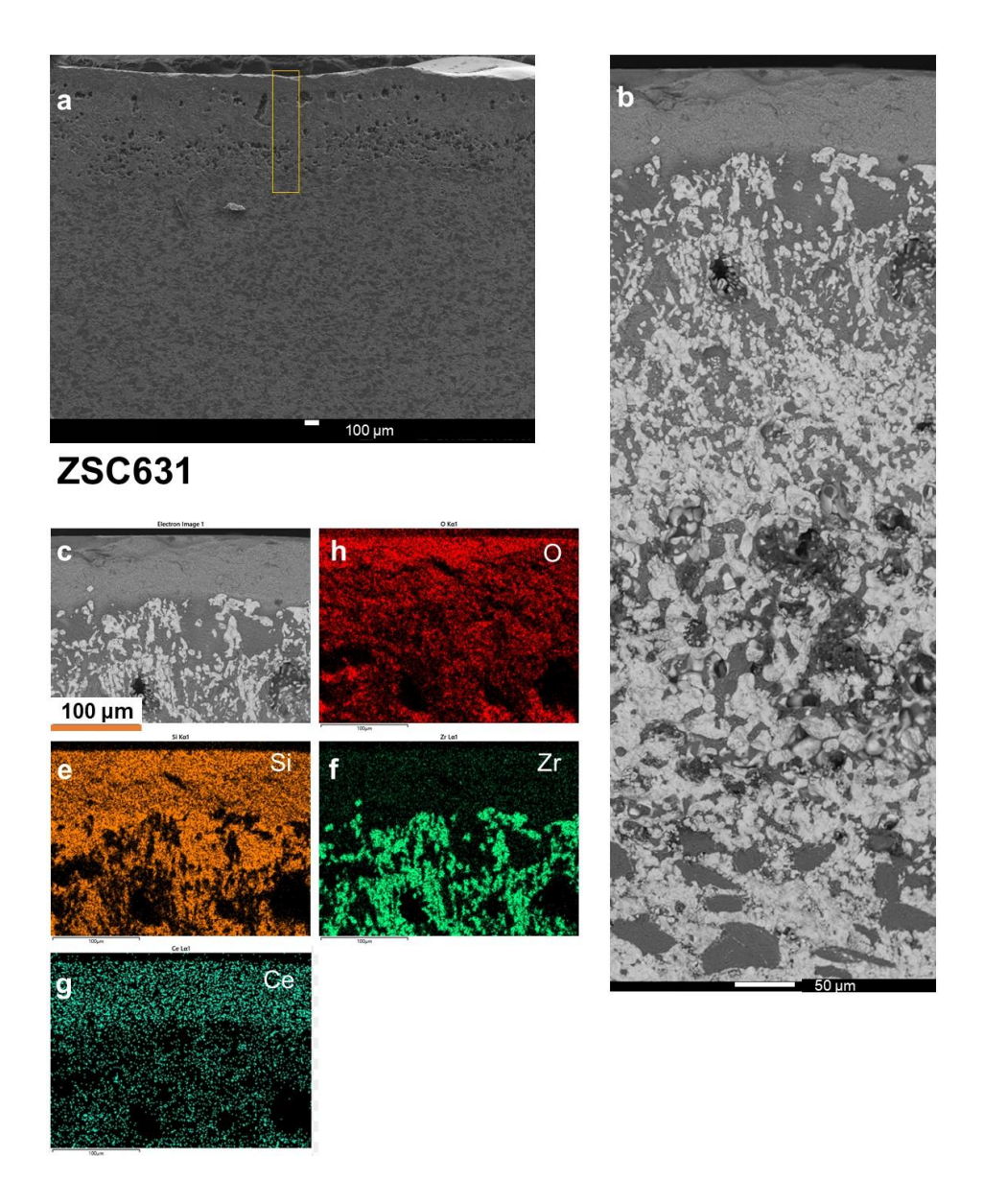


Figure 6.12. a) Cross section of ZSC631 sample after oxidation at 1600 for 10h, b) magnified view the cross section obtained by stitching the images together from top to bottom, c)-g) EDS elemental mapping of the upper region.

#### 6.4.3 Oxidation kinetics

Mass gain and average thickness of oxide layer at the end of 10 h of oxidation for UHTC samples is mentioned in Table 6.2. The alloy ZSA721 showed mass gain of ~58 mg/cm<sup>2</sup> at the end of 10 h of exposure at 1600 °C. The mass gain was mostly due to the formation of ZrO<sub>2</sub> fingers and silica-rich scale trapped within those fingers. The stable oxide layer was not found which would have prevented the oxidation XRD analysis as shown in Figure 6.13 shows only ZrO<sub>2</sub> peaks as SiO<sub>2</sub> peaks were absent due to its amorphous nature. On adding TaC, a slight reduction in oxidation rate and overall mass gain was observed as shown in Figure 6.14. A thin SiO<sub>2</sub>-rich layer of ~25 μm was observed. However, the surface microstructure showed coarse ZrO2 on the surface embedded in silica-rich scale. This indicates that the formation of protective SiO<sub>2</sub>-rich oxide scale occurred, but it was not stable and insufficient in preventing diffusion of species across it. The viscosity was low enough for ZrO2 formation and its migration to the surface. XRD analysis after oxidation confirmed that the coarse particles present on the surface are ZrO<sub>2</sub> particles. The sample ZST631 with only TaC (10 vol%) showed the maximum mass gain with a thick and porous oxide layer (~1477 µm). The mass change plot shows fast mass gain which could be attributed to the porous scale which enhanced oxygen diffusion and faster oxidation.

Table 6.2. Mass gain and average oxide layer thickness after 10 h of exposure at 1600 °C.

Sample	Mass gain	Average oxide	SiO <sub>2</sub>	SiC
	(mg/cm <sup>2</sup> )	layer thickness	thickness	depleted
		(µm)	(µm)	zone (µm)
ZSA721	58	$1388 \pm 100$	~ 5	156 ± 12
ZSAC72-5-5	40	$550 \pm 75$	82 ± 10	200 ± 15
ZSAT72-5-5	45	$1357 \pm 100$	25 ± 5	240 ± 15
ZSC721	56	$754 \pm 36$	91 ± 10	$380 \pm 25$
ZSC631	54	$623 \pm 40$	$72 \pm 10$	$266 \pm 25$
ZST631	69	$1477\pm200$	-	258 ± 10

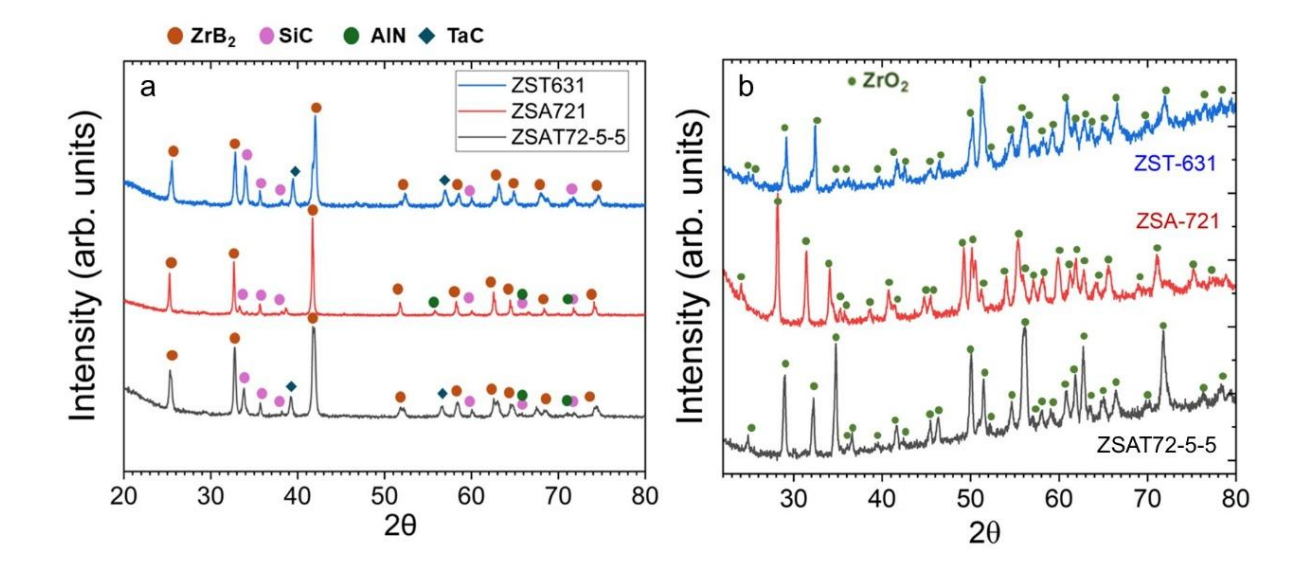


Figure 6.13. XRD analysis of samples ZSA721, ZSAT72-5-5 and ZST631 (a) before oxidation (b) after oxidation for 10 h at  $1600 \, ^{\circ}$ C.

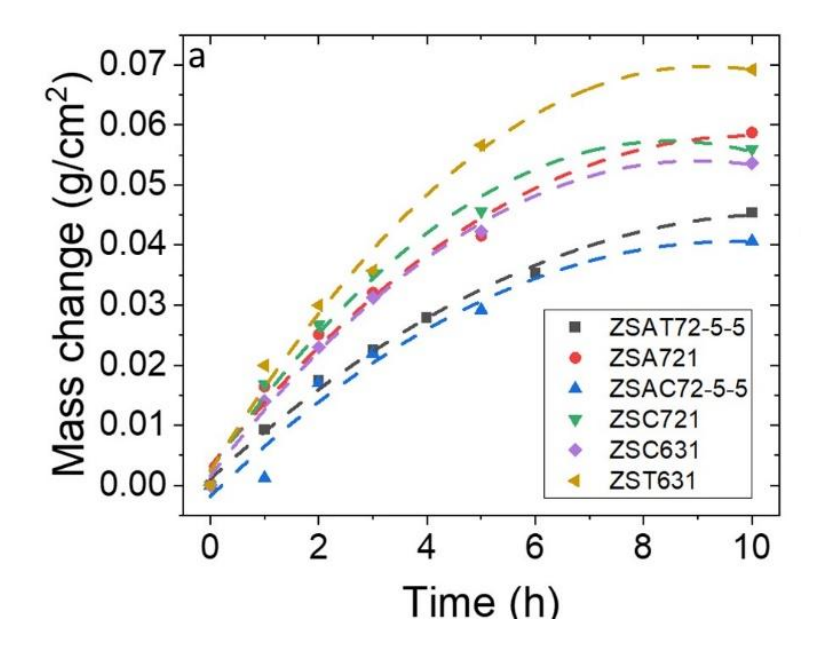


Figure 6.14 (a) Mass change per unit area during oxidation at 1600 °C after 10 h of oxidation.

In alloy ZSAC72-5-5, in which 5 vol% CeO<sub>2</sub> was added at the expense of Al, the mass gain reduced to  $\sim 40 \text{ mg/cm}^2$  and the mass gain rate was minimum. The cross section shows SiO<sub>2</sub>-rich scale at the top which reduced the oxygen diffusion and oxide rate formation resulting in slow mass gain. In samples ZSC721 and ZSC631, there was not much difference in mass gain; however, it was much higher than the sample containing both AlN and CeO<sub>2</sub>. This indicates that initially, the oxidation rate was faster which is also evident from the surface microstructures taken at short durations. After 15 min of oxidation

ZSAC72-5-5 showed formation of SiO<sub>2</sub>-rich scale with convection cells at some regions, while the samples ZSC721 and ZSC631 showed formation of SiO<sub>2</sub>-rich glass with coarse ZrO<sub>2</sub> particles. However, at the end of 10 h, stable oxide layer was observed on all the samples.

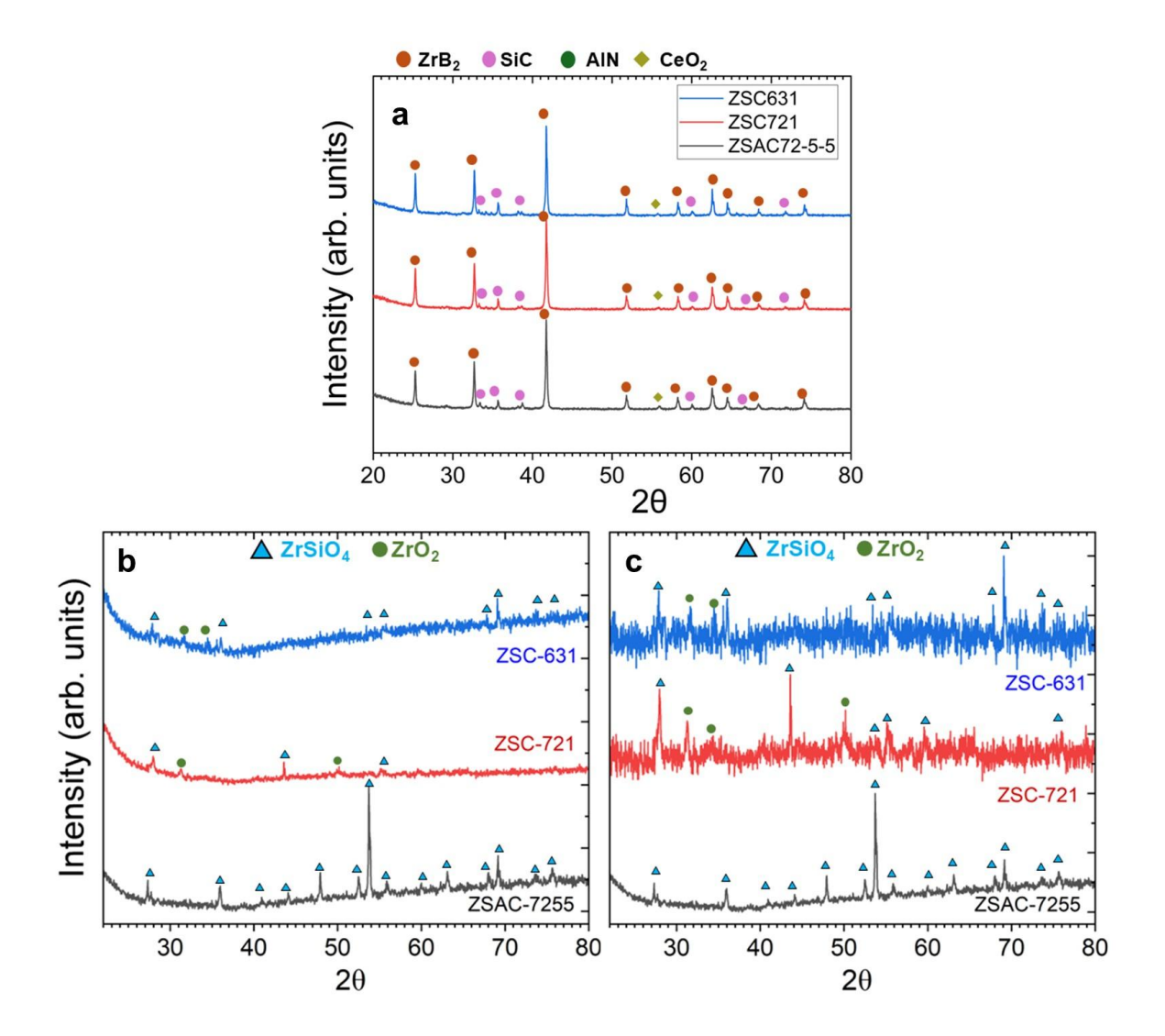


Figure 6.15. XRD analysis of samples containing  $CeO_2$  (a) before oxidation (b) & (c) after oxidation for 10 h at 1600 °C. (b) shows the results with background and (c) shows the results after background removal from ZSC721 and ZSC631 for better visibility of peaks.

The mass change plot (Figure 6.14) shows slower mass gain in ZSC631 as compared to ZSC721 which could be due to early formation of SiO<sub>2</sub> layer and less amount of ZrO<sub>2</sub>. XRD analysis in Figure 6.15 shows formation of ZrSiO<sub>4</sub> in samples ZSAC72-5-5 which is reported to reduce oxidation rate by enhancing the thermal stability of SiO<sub>2</sub>-rich scale [119]. Some ZrSiO<sub>4</sub> peaks were also observed in ZSC721 and ZSC 631 samples and we speculate its formation in

minor quantities, but it is difficult to say conclusively. Therefore, a detailed analysis was done using EDS-PhaSe software developed by Beniwal et al. [250]. The SEM and EDS images were used to generate masks at the regions where Zr, Si and O compositions match the stoichiometry of ZrSiO<sub>4</sub>, and the area was calculated to approximate its amount. The role of ZrSiO<sub>4</sub> on oxidation behaviour is explained in detail in the next section.

### 6.4.4 Phenomenological model and oxidation pathways

For UHTC ZSA721, oxidized surface at the end of 10 h was covered with ZrO<sub>2</sub> agglomerates with small amount SiO<sub>2</sub>-rich scale. The cross section of the same sample showed a very thin layer of SiO<sub>2</sub>-rich scale approximately 5 µm. As AlN is known to reduce scale viscosity, it is proposed that for this composition the viscosity is low due to the formation of aluminosilicate glass resulting in upward migration of Zr and more ZrO<sub>2</sub> fingers. ZrO<sub>2</sub> doesn't form continuously, allowing for easier oxygen ingress resulting in massive oxidation of underlying substrate. When 5 vol% CeO<sub>2</sub> is added along with 5 vol% AlN (ZSAC72-5-5), the surface microstructure and cross section of oxidized sample showed formation of dense SiO<sub>2</sub>-rich scale at the top.

The addition of Ce massively reduces the Si depleted zone. Also, with a lower Al content coupled with Ce (more electropositive element than Zr), the silica scale forms continuously at the top. EDS maps would suggest that alumino-SiO<sub>2</sub> is intimately mixed with Ce. XRD analysis of the oxidized surface showed ZrSiO<sub>4</sub> peaks instead of ZrO<sub>2</sub>. Generally, it appears the highly electropositive Ce preferentially diffuses upwards resulting in suppressed Zr upward diffusion. This results in a subsurface layer which is enriched in Zr, Si and O where the ZrSiO<sub>4</sub> forms. The Si/Zr overlap is more in ZSAC compared to ZSC (where it is almost non-existent) showing a greater possibility of ZrSiO<sub>4</sub> formation in ZSAC but not in ZSC721 and ZSC631. It was difficult to clearly find Zr/Si overlaps from EDS maps, therefore, EDS-PhaSe software [250] was used to create ZrSiO<sub>4</sub> masks which represent the regions that correspond to stoichiometry of ZrSiO<sub>4</sub> on ZSAC72-5-5, ZSC721 and ZSC631 samples as shown

in Figure 6.16. For sample containing both Al and Ce, this area is approximately 10.25 %. For ZSC 721, a very small area of 4.64 % shows the presence of ZrSiO<sub>4</sub>.

The presence of ZrSiO<sub>4</sub> in SiO<sub>2</sub>-rich glasses affects oxide scale structure and thermal stability. According to Lin and Hwang [248], Al present in CeO<sub>2</sub>-Al<sub>2</sub>O<sub>3</sub>-SiO<sub>2</sub> (CAS) glasses, can act as either network former or network modifier depending on the glass composition. In presence of CeO<sub>2</sub>, Al ions tend to stay in Al(6) instead of Al(4) coordination. When it exists in Al(4) coordination forming [AlO<sub>4</sub>]- tetrahedra similar to SiO<sub>2</sub> tetrahedra, it acts as network former, whereas in Al(6) coordination when it forms [AlO<sub>6</sub>]<sup>3-</sup>, distortion occurs in Si-O network, and it acts as network modifier. As Ce cations have larger size, it becomes difficult for Ce to coordinate tetrahedrally, therefore it acts as charge balancer. Since Ce cations have +4 or +3 charge in glasses and to balance the excess charge of Ce cations, [AlO<sub>6</sub>]<sup>3-</sup> units are easily created than [AlO<sub>4</sub>]- units. The formation of [AlO<sub>6</sub>]<sup>3-</sup> units creates NBOs in CAS glasses. Now, as NBOs are present in SiO<sub>2</sub> glass Zr can bond easily with SiO<sub>2</sub> units to form ZrSiO<sub>4</sub>. Formation of ZrSiO<sub>4</sub> also depends on ZrO<sub>2</sub>+SiO<sub>2</sub>+B<sub>2</sub>O<sub>3</sub> composition.

When B<sub>2</sub>O<sub>3</sub> evaporates from this mixture and the composition is such that it moves to two phase ZrO<sub>2</sub>+SiO<sub>2</sub> region in the phase diagram where ZrSiO<sub>4</sub> forms [182]. Wang et al. [119] suggested that the formation of ZrSiO<sub>4</sub> in SiO<sub>2</sub> retards inward oxygen diffusion resulting in reduced oxidation. Additionally, ZrSiO<sub>4</sub> present in SiO<sub>2</sub>, releases Zr into SiO<sub>2</sub> which occupies either interstitial site or substitutes Si atom in SiO<sub>2</sub>. Presence of Zr in SiO<sub>2</sub> increases Si-O bond strength and improves its high temperature stability [186]. These observations indicate that Ce and Al atoms addition to ZrB<sub>2</sub>-SiC UHTCs promote the formation of ZrSiO<sub>4</sub> in oxide scale which improves oxidation resistance at 1600 °C in air.

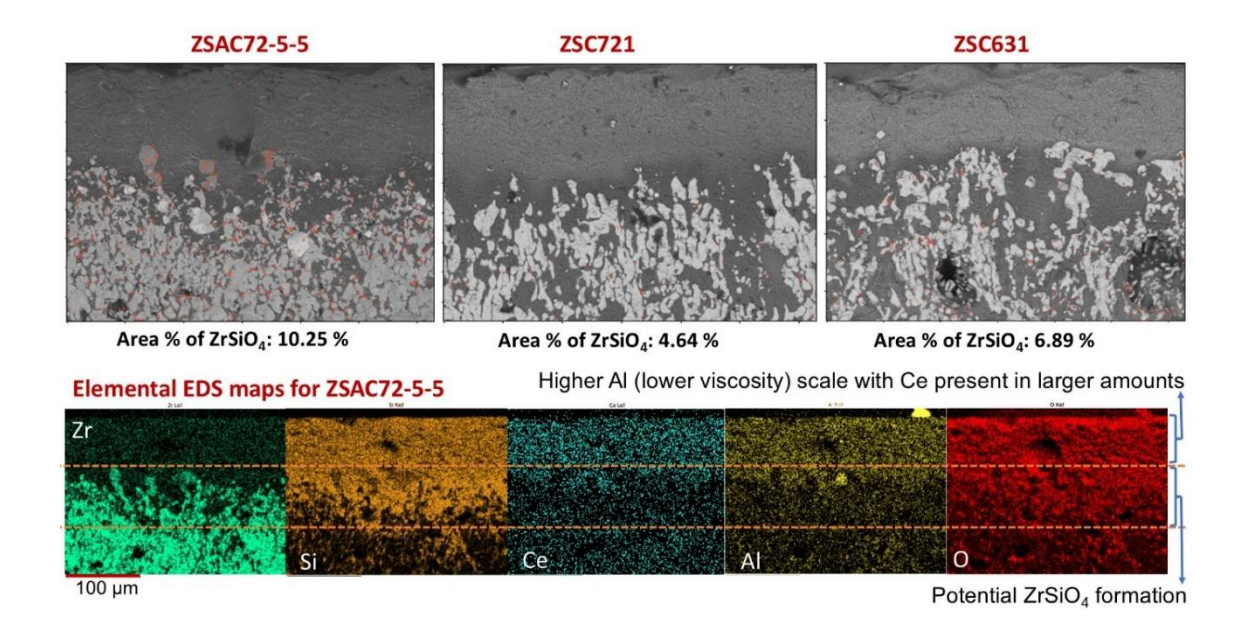


Figure 6.16. Masks showing regions where the composition matches the ZrSiO<sub>4</sub> stoichiometry. Maske were generated through quantitative analysis of EDS maps using EDS-PhaSe software [250].

### 6.5 Summary

ZrB<sub>2</sub>-SiC UHTCs containing AlN, TaC, CeO<sub>2</sub> in different concentrations were oxidized at 1600 °C in stagnant air. Figure 6.17 shows the effect of these additions on oxidation mechanism, overall mass change and thickness of outermost SiO<sub>2</sub>-rich scale. Sample ZSA721 (10 vol% AlN) showed poor oxidation resistance which could be due to lower scale viscosity through which oxygen can easily diffuse and enhance oxidation. Al present in SiO2 scale reduces the scale viscosity. It also allows the upward Zr migration leading to ZrO<sub>2</sub> coarsening which is evident from the microstructures. A stable silica scale could not form on this sample. Addition of 5 vol% TaC combined with 5 vol% AlN (sample ZSAT72-5-5) did not improve any oxidation resistance, but CeO<sub>2</sub> addition (ZSAC72-5-5) improved oxidation resistance. Ce migrated at the top with SiO<sub>2</sub>-rich glass as can be seen from cross section microstructures and EDS analysis. The presence of Ce in the scale helps in viscosity reduction as well. This aided the scale flow resulting in a uniform scale. As Ce preferentially moves upwards, it suppresses Zr upward movement. The available Zr in the sublayer can react with O and Si present there resulting in formation of ZrSiO<sub>4</sub>. ZrSiO<sub>4</sub> was formed during its oxidation as confirmed by XRD. ZrSiO<sub>4</sub> densifies ZrO<sub>2</sub> pores and helps in reducing oxygen permeation to the substrate. ZrSiO<sub>4</sub> also improves SiO<sub>2</sub> stability at high temperatures. Oxidation of ZSC721 and ZSC631 also showed improvement in oxidation resistance by forming protective SiO<sub>2</sub>-rich layer. TaC addition resulted in cavities and pores formation at the top indicating degradation of oxidation resistance. It can be concluded that CeO<sub>2</sub> addition with and without AlN addition improved oxidation resistance of ZrB<sub>2</sub>-70vol% SiC. Therefore, it is suggested that more compositions containing AlN and CeO<sub>2</sub> should be explored.

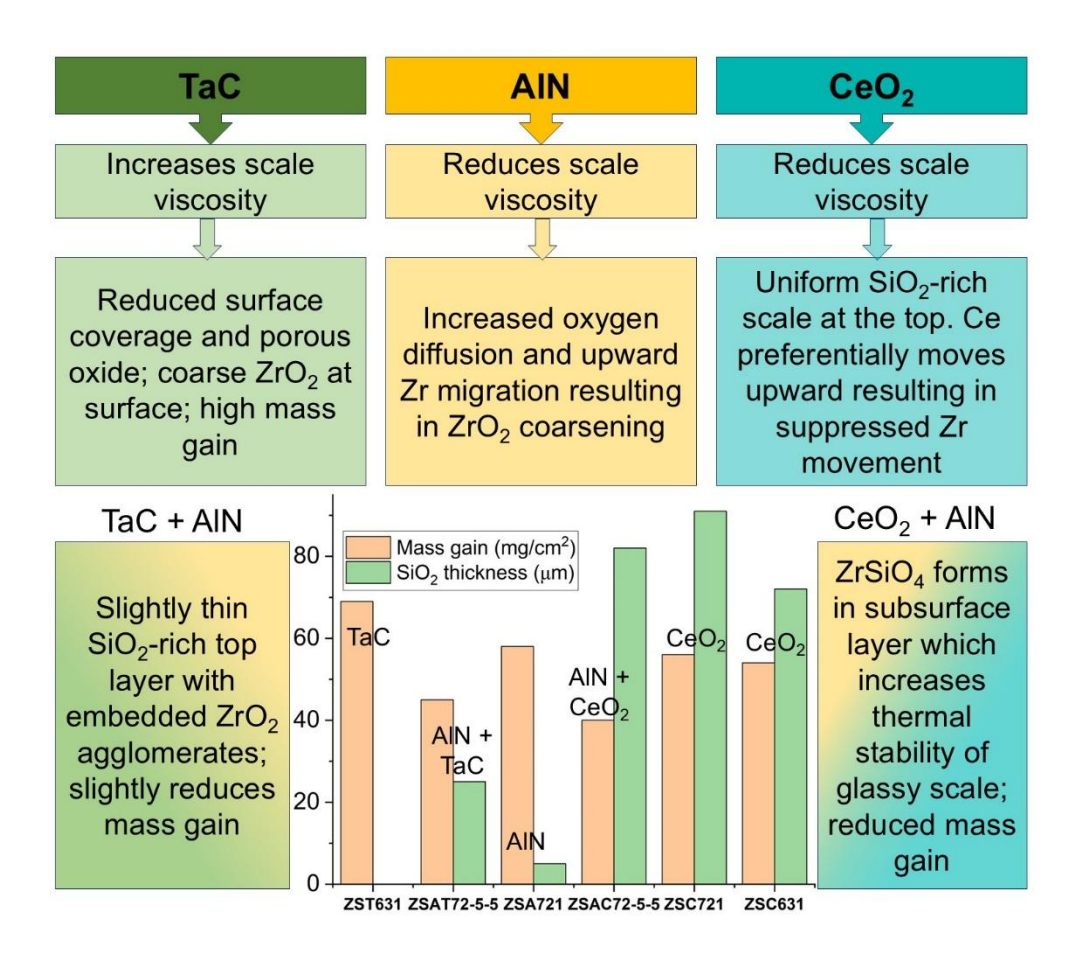


Figure 6.17. A visual summary of key insights into the oxidation mechanisms along with the bar chart showing oxide scale thickness and silica-rich scale thickness at the top

# **Chapter 7 Conclusion**

### 7.1 General conclusions from the thesis

- The first part of this work involves determination of the self-diffusivity of Si and O in amorphous SiO<sub>2</sub> using molecular dynamics simulations using different interatomic potentials in the temperature range of 1200-1700 °C. The addition of Hf to SiO<sub>2</sub> resulted in increased diffusion kinetics as well as increased activation energy. Hf addition increases SiO bond strength which makes it difficult to break resulting in high activation energy. Higher diffusivity values could be due to formation of low melting eutectic (which forms at ~2 mol% HfO<sub>2</sub> in SiO<sub>2</sub>) facilitating easy movement of diffusing elements. An optimum amount of Al addition (3 at%) resulted in increased diffusivity values indicating reduction in scale viscosity. According to SiO<sub>2</sub>-Al<sub>2</sub>O<sub>3</sub> phase diagram, eutectic phase forms at 3.02 mol% of Al<sub>2</sub>O<sub>3</sub> resulting in lower melting point and easy mobility of species.
- In Chapter 4, predictive framework through a combination of mathematical modelling and Cellular Automata was developed. This model simulates the transient oxidation phenomenon which captures microstructural changes and calculates mass change at each time-step for the Mo-Si-B alloys. The model effectively shows the role of the microstructure scale on borosilica scale formation and oxidation resistance, which is a function of chemistry, phase connectivity and spatial distribution.
- In Chapter 5, experimental studies on oxidation behaviour of Mo-Si-B alloys with the effect of Si/B ratio, Mo content and alloying additions including W, Ta and Al were conducted. Silica-rich scale is protective but high Si content in the alloy is not the only factor that can improve oxidation resistance. The addition of W to the alloy worsens the oxidation resistance even if there is formation of silica rich scale. When

W forms WO<sub>3</sub> on the surface at these temperatures, it impedes borosilica flow resulting in poor surface coverage and poor oxidation resistance. Al addition reduces the risk of pesting at moderate temperatures, but at higher temperatures, it lowers the protective scale viscosity allowing greater oxygen ingress and accelerated oxidation. The addition of small amounts of Ta (5 at%) increases scale viscosity and improves oxidation resistance without significant mass loss.

• The oxidation behaviour of ZrB<sub>2</sub>-SiC UHTCs with AlN, TaC and CeO<sub>2</sub> additions was studied at 1600 °C and presented in Chapter 6. Addition of TaC showed degradation in the oxidation properties as evident from the microstructures and mass change plots. However, CeO<sub>2</sub> addition alone and in tandem with AlN showed reduced mass loss and formation of uniform glassy scale at the top surface indicating improvement in oxidation resistance. CeO<sub>2</sub> in presence of AlN promoted ZrSiO<sub>2</sub> formation that improves thermal stability SiO<sub>2</sub>-rich scale.

## 7.2 Scope for future work

- The diffusion modelling using Molecular Dynamics was done for only SiO<sub>2</sub> glasses with additives. The work can be extended for predicting diffusion coefficients and activation energy was borosilica glasses with elemental additions such as Ce, W and Ta, with the goal of obtaining a rationale for selecting the appropriate elements. It is worth finding the diffusivity values for these systems for their further use to model oxidation.
- In the present work, the experimental studies for oxidation of Mo-Si-B alloys were carried out at 1100 and 1350 °C. These alloys specifically with W addition must be studied above 1400 °C because WO<sub>3</sub> is volatile in the 1300-1400 °C temperature regime. As it won't impede the borosilica scale flow, it may show improved oxidation resistance.
- In the present work, when TaC was added along with AlN in ZrB<sub>2</sub>-SiC composite, it improved oxidation properties slightly. However, the addition of TaC alone drastically degraded oxidation properties of UHTCs. In Mo-Si-B alloys, Ta addition improved oxidation resistance. Due to this contrasting behaviour of Ta in Mo-Si-B alloys and UHTCs, more compositions with TaC additions or other forms of Ta such as TaSi<sub>2</sub> along with AlN must be studied in future.
- The studies that can replicate the actual environmental conditions encountered by these materials can be done. For example, UHTCs for

hypersonic and aerospace applications experience shock waves, high velocity (Mach 7-8) and surface temperatures ~3000-4000 °C. Low-cost testing facilities must be developed for better design of ultra-high temperature materials. The use and development of computational modelling approaches for such studies can be beneficial and may complement the existing test techniques.

# References

- [1] S.-C. Yu, L. Chen, Y. Zhao, H.-X. Li, X.-R. Zhang, A brief review study of various thermodynamic cycles for high temperature power generation systems, Energy Conversion and Management 94 (2015) 68–83. https://doi.org/10.1016/j.enconman.2015.01.034.
- [2] Q. Zeng, X. Chen, Combustor technology of high temperature rise for aero engine, Progress in Aerospace Sciences 140 (2023) 100927. https://doi.org/10.1016/j.paerosci.2023.100927.
- [3] D.M. Van Wie, D.G. Drewry, D.E. King, C.M. Hudson, The hypersonic environment: Required operating conditions and design challenges, Journal of Materials Science 39 (2004) 5915–5924. https://doi.org/10.1023/B:JMSC.0000041688.68135.8b.
- [4] R.C. Reed, The Superalloys: Fundamentals and Applications, Cambridge University Press, Cambridge, 2006. https://doi.org/10.1017/CBO9780511541285.
- [5] W.G. Fahrenholtz, G.E. Hilmas, Ultra-high temperature ceramics: Materials for extreme environments, Scripta Materialia 129 (2017) 94–99. https://doi.org/10.1016/j.scriptamat.2016.10.018.
- [6] J.H. Perepezko, High temperature environmental resistant Mo-Si-B based coatings, International Journal of Refractory Metals and Hard Materials 71 (2018) 246–254. https://doi.org/10.1016/j.ijrmhm.2017.11.033.
- [7] A. Misra, 12 Composite materials for aerospace propulsion related to air and space transportation, in: J. Njuguna (Ed.), Lightweight Composite Structures in Transport, Woodhead Publishing, 2016: pp. 305–327. https://doi.org/10.1016/B978-1-78242-325-6.00012-8.
- [8] T.H. Squire, J. Marschall, Material property requirements for analysis and design of UHTC components in hypersonic applications, Journal of the European Ceramic Society 30 (2010) 2239–2251. https://doi.org/10.1016/j.jeurceramsoc.2010.01.026.
- [9] A. Aprovitola, L. Iuspa, G. Pezzella, A. Viviani, Phase-A design of a reusable re-entry vehicle, Acta Astronautica 187 (2021) 141–155. https://doi.org/10.1016/j.actaastro.2021.06.034.

- [10] W. Betteridge, S.W.K. Shaw, Development of superalloys, Materials Science and Technology 3 (1987) 682–694. https://doi.org/10.1179/mst.1987.3.9.682.
- [11] C.T. Sims, N.S. Stoloff, W.C. Hagel, Superalloys II: High-Temperature Materials for Aerospace and Industrial Power | Wiley, in: Wiley.Com, John Wiley and Sons, New York, 1987. https://www.wiley.com/en-us/Superalloys+II%3A+High+Temperature+Materials+for+Aerospace+and+Industrial+Power-p-9780471011477 (accessed March 9, 2024).
- [12] V. Behrani, A.J. Thom, M.J. Kramer, M. Akinc, Microstructure and oxidation behavior of Nb–Mo–Si–B alloys, Intermetallics 14 (2006) 24–32. https://doi.org/10.1016/j.intermet.2005.03.007.
- [13] J.H. Perepezko, R. Sakidja, S. Kim, Phase Stability in Processing and Microstructure Control in High Temperature Mo-Si-B Alloys, MRS Online Proceedings Library (OPL) 646 (2000) N4.5.1. https://doi.org/10.1557/PROC-646-N4.5.1.
- [14] A.K. Vasudévan, J.J. Petrovic, A comparative overview of molybdenum disilicide composites, Materials Science and Engineering: A 155 (1992) 1–17. https://doi.org/10.1016/0921-5093(92)90308-N.
- [15] D.M. Shah, D. Berczik, D.L. Anton, R. Hecht, Appraisal of other silicides as structural materials, Materials Science and Engineering: A 155 (1992) 45–57. https://doi.org/10.1016/0921-5093(92)90311-N.
- [16] G. Ouyang, P.K. Ray, S. Thimmaiah, M.J. Kramer, M. Akinc, P. Ritt, J.H. Perepezko, Oxidation resistance of a Mo-W-Si-B alloy at 1000–1300 °C: The effect of a multicomponent Mo-Si-B coating, Applied Surface Science 470 (2019) 289–295. https://doi.org/10.1016/j.apsusc.2018.11.167.
- [17] F.A. Rioult, S.D. Imhoff, R. Sakidja, J.H. Perepezko, Transient oxidation of Mo–Si–B alloys: Effect of the microstructure size scale, Acta Materialia 57 (2009) 4600–4613. https://doi.org/10.1016/j.actamat.2009.06.036.
- [18] M.G. Mendiratta, T.A. Parthasarathy, D.M. Dimiduk, Oxidation behavior of αMo–Mo3Si–Mo5SiB2 (T2) three phase system, Intermetallics 10 (2002) 225–232. https://doi.org/10.1016/S0966-9795(01)00118-2.
- [19] A. Misra, 12 Composite materials for aerospace propulsion related to air and space transportation, in: J. Njuguna (Ed.), Lightweight Composite Structures in Transport, Woodhead Publishing, 2016: pp. 305–327. https://doi.org/10.1016/B978-1-78242-325-6.00012-8.
- [20] J.E. Grady, CMC Technology Advancements for Gas Turbine Engine Applications, (2013). https://ntrs.nasa.gov/citations/20140000458 (accessed February 6, 2024).
- [21] D.B. Marshall, B.N. Cox, Integral Textile Ceramic Structures, Annual Review of Materials Research 38 (2008) 425–443. https://doi.org/10.1146/annurev.matsci.38.060407.130214.
- [22] Y.D. Blum, J. Marschall, D. Hui, S. Young, Thick Protective UHTC Coatings for SiC-Based Structures: Process Establishment, Journal of the American Ceramic Society 91 (2008) 1453–1460. https://doi.org/10.1111/j.1551-2916.2008.02360.x.

- [23] E.L. Corral, R.E. Loehman, Ultra-High-Temperature Ceramic Coatings for Oxidation Protection of Carbon-Carbon Composites, Journal of the American Ceramic Society 91 (2008) 1495–1502. https://doi.org/10.1111/j.1551-2916.2008.02331.x.
- [24] M.K. Meyer, M. Akinc, Oxidation Behavior of Boron-Modified Mo5Si3 at 800°–1300°C, Journal of the American Ceramic Society 79 (1996) 938–944. https://doi.org/10.1111/j.1151-2916.1996.tb08528.x.
- [25] M. Meyer, M. Kramer, M. Akinc, Boron-doped molybdenum silicides, Advanced Materials 8 (1996) 85–88. https://doi.org/10.1002/adma.19960080118.
- [26] M.K. Meyer, A.J. Thom, M. Akinc, Oxide scale formation and isothermal oxidation behavior of Mo–Si–B intermetallics at 600–1000°C, Intermetallics 7 (1999) 153–162. https://doi.org/10.1016/S0966-9795(98)00058-2.
- [27] H. Nowotny, E. Dimakopoulou, H. Kudielka, Untersuchungen in den Dreistoffsystemen: Molybdän-Silizium-Bor, Wolfram-Silizium-Bor und in dem System: VSi2-TaSi2, Monatshefte für Chemie 88 (1957) 180-192. https://doi.org/10.1007/BF00901624.
- [28] C.A. Nunes, R. Sakidja, Z. Dong, J.H. Perepezko, Liquidus projection for the Mo-rich portion of the Mo-Si-B ternary system, Intermetallics 8 (2000) 327–337. https://doi.org/10.1016/S0966-9795(99)00088-6.
- [29] D.M. Berczik, Method for enhancing the oxidation resistance of a molybdenum alloy, and a method of making a molybdenum alloy, US5595616A, 1997. https://patents.google.com/patent/US5595616A/en (accessed February 18, 2025).
- [30] M. Akinc, M.K. Meyer, M.J. Kramer, A.J. Thom, J.J. Huebsch, B. Cook, Boron-doped molybdenum silicides for structural applications, Materials Science and Engineering: A 261 (1999) 16–23. https://doi.org/10.1016/S0921-5093(98)01045-4.
- [31] J.H. Schneibel, R.O. Ritchie, J.J. Kruzic, P.F. Tortorelli, Optimizaton of Mo-Si-B Intermetallic Alloys, METALLURGICAL AND MATERIALS TRANSACTIONS A (2005) 525–531.
- [32] J.A. Lemberg, R.O. Ritchie, Mo-Si-B Alloys for Ultrahigh-Temperature Structural Applications, Advanced Materials 24 (2012) 3445–3480. https://doi.org/10.1002/adma.201200764.
- [33] I. Rosales, J.H. Schneibel, Stoichiometry and mechanical properties of Mo3Si, Intermetallics 8 (2000) 885–889. https://doi.org/10.1016/S0966-9795(00)00058-3.
- [34] D.H. Templeton, C.H. Dauben, The crystal structure of Mo3Si, Acta Cryst 3 (1950) 261–262. https://doi.org/10.1107/S0365110X50000689.
- [35] G.R. Johnson, D.H. Douglass, A-15 phases: Occurrence, Geller radii, and electronic structure, J Low Temp Phys 14 (1974) 565–573. https://doi.org/10.1007/BF00658881.
- [36] W. Speier, L. Kumar, D.D. Sarma, R.A. de Groot, J.C. Fuggle, The electronic structure of 4d and 5d silicides, J. Phys.: Condens. Matter 1 (1989) 9117. https://doi.org/10.1088/0953-8984/1/46/006.

- [37] C.L. Fu, X. Wang, Y.Y. Ye, K.M. Ho, Phase stability, bonding mechanism, and elastic constants of Mo5Si3 by first-principles calculation, Intermetallics 7 (1999) 179–184. https://doi.org/10.1016/S0966-9795(98)00018-1.
- [38] R. Sakidja, J.H. Perepezko, S. Kim, N. Sekido, Phase stability and structural defects in high-temperature Mo–Si–B alloys, Acta Materialia 56 (2008) 5223–5244. https://doi.org/10.1016/j.actamat.2008.07.015.
- [39] S. Kim, J.H. Perepezko, Interdiffusion kinetics in the Mo5SiB2 (T2) phase, JPED 27 (2006) 605–613. https://doi.org/10.1007/BF02736562.
- [40] K. Yakang, C. Wang, X. Chen, Y. Qu, J. Yu, H. Ju, X. Yilei, Review of Research Progress on Mo–Si–B Alloys, Materials 16 (2023) 5495. https://doi.org/10.3390/ma16155495.
- [41] P. Villars, L.D. Calvert, W.D. Pearson, Pearson's handbook of crystallographic data for intermetallic phases, n.d.
- [42] Materials Project, Materials Project (n.d.). https://next-gen.materialsproject.org/ (accessed May 19, 2025).
- [43] J.H. Schneibel, High temperature strength of Mo–Mo3Si–Mo5SiB2 molybdenum silicides, Intermetallics 11 (2003) 625–632. https://doi.org/10.1016/S0966-9795(03)00044-X.
- [44] A.S. for Metals, Theory of Alloy Phases: A Seminar on Theory of Alloy Phases Held During the Thirty-seventh National Metal Congress and Exposition, Philadelphia, October 15 to 21, 1955, American Society for Metals, 1956.
- [45] T.A. Parthasarathy, M.G. Mendiratta, D.M. Dimiduk, Oxidation mechanisms in Mo-reinforced Mo5SiB2(T2)–Mo3Si alloys, Acta Materialia 50 (2002) 1857–1868. https://doi.org/10.1016/S1359-6454(02)00039-3.
- [46] K. Pan, Y. Yang, S. Wei, H. Wu, Z. Dong, Y. Wu, S. Wang, L. Zhang, J. Lin, X. Mao, Oxidation behavior of Mo-Si-B alloys at medium-to-high temperatures, Journal of Materials Science & Technology 60 (2021) 113–127. https://doi.org/10.1016/j.jmst.2020.06.004.
- [47] S. Majumdar, B. Gorr, H.-J. Christ, D. Schliephake, M. Heilmaier, Oxidation mechanisms of lanthanum-alloyed Mo-Si-B, Corrosion Science 88 (2014) 360–371. https://doi.org/10.1016/j.corsci.2014.07.058.
- [48] S. Majumdar, B. Dönges, B. Gorr, H.-J. Christ, D. Schliephake, M. Heilmaier, Mechanisms of oxide scale formation on yttrium-alloyed Mo-Si-B containing fine-grained microstructure, Corrosion Science 90 (2015) 76–88. https://doi.org/10.1016/j.corsci.2014.09.017.
- [49] R. Sakidja, J.S. Park, J. Hamann, J.H. Perepezko, Synthesis of oxidation resistant silicide coatings on Mo-Si-B alloys, Scripta Materialia 53 (2005) 723-728. https://doi.org/10.1016/j.scriptamat.2005.05.015.
- [50] S. Burk, B. Gorr, V.B. Trindade, H.-J. Christ, Effect of Zr Addition on the High-Temperature Oxidation Behaviour of Mo–Si–B Alloys, Oxid Met 73 (2010) 163–181. https://doi.org/10.1007/s11085-009-9175-9.

- [51] M. Zhao, W. Ye, M. Zhu, Y. Gui, W. Guo, S. Wu, Y. Yan, From Mo-Si-B to Mo-Ti-Si-B Alloys: A Short Review, Materials 16 (2023) 3. https://doi.org/10.3390/ma16010003.
- [52] D. Schliephake, M. Azim, K. von Klinski-Wetzel, B. Gorr, H.-J. Christ, H. Bei, E.P. George, M. Heilmaier, High-Temperature Creep and Oxidation Behavior of Mo-Si-B Alloys with High Ti Contents, Metall Mater Trans A 45 (2014) 1102–1111. https://doi.org/10.1007/s11661-013-1944-z.
- [53] S. Paswan, R. Mitra, S.K. Roy, Isothermal oxidation behaviour of Mo–Si–B and Mo–Si–B–Al alloys in the temperature range of 400–800°C, Materials Science and Engineering: A 424 (2006) 251–265. https://doi.org/10.1016/j.msea.2006.03.014.
- [54] S. Paswan, R. Mitra, S.K. Roy, Oxidation behaviour of the Mo–Si–B and Mo–Si–B–Al alloys in the temperature range of 700–1300°C, Intermetallics 15 (2007) 1217–1227. https://doi.org/10.1016/j.intermet.2007.02.012.
- [55] T. Karahan, G. Ouyang, P.K. Ray, M.J. Kramer, M. Akinc, Oxidation mechanism of W substituted Mo-Si-B alloys, Intermetallics 87 (2017) 38– 44. https://doi.org/10.1016/j.intermet.2017.04.005.
- [56] J. Wang, B. Li, R. Li, X. Chen, T. Wang, G. Zhang, Unprecedented oxidation resistance at 900 °C of Mo–Si–B composite with addition of ZrB2, Ceramics International 46 (2020) 14632–14639. https://doi.org/10.1016/j.ceramint.2020.02.264.
- [57] M. Wang, N.M. Anoop Krishnan, B. Wang, M.M. Smedskjaer, J.C. Mauro, M. Bauchy, A new transferable interatomic potential for molecular dynamics simulations of borosilicate glasses, Journal of Non-Crystalline Solids 498 (2018) 294–304. https://doi.org/10.1016/j.jnoncrysol.2018.04.063.
- [58] M.M. Smedskjaer, J.C. Mauro, R.E. Youngman, C.L. Hogue, M. Potuzak, Y. Yue, Topological Principles of Borosilicate Glass Chemistry, J. Phys. Chem. B 115 (2011) 12930–12946. https://doi.org/10.1021/jp208796b.
- [59] B.A. Pint, Experimental observations in support of the dynamic-segregation theory to explain the reactive-element effect, Oxid Met 45 (1996) 1–37. https://doi.org/10.1007/BF01046818.
- [60] A.K. Mohanty, Rate Processes in Metallurgy, 3rd ed., PHI Learning Private Limited, New Delhi, 2009.
- [61] I.J. Bennett, W.G. Sloof, Modelling the influence of reactive elements on the work of adhesion between a thermally grown oxide and a bond coat alloy, Materials and Corrosion 57 (2006) 223–229. https://doi.org/10.1002/maco.200503928.
- [62] S. Paswan, R. Mitra, S.K. Roy, Nonisothermal and Cyclic Oxidation Behavior of Mo-Si-B and Mo-Si-B-Al Alloys, Metall Mater Trans A 40 (2009) 2644–2658. https://doi.org/10.1007/s11661-009-9946-6.
- [63] P.K. Ray, Y.Y. Ye, M. Akinc, M.J. Kramer, Effect of Nb and W substitutions on the stability of the A15 Mo3Si phase, Journal of Alloys and Compounds 537 (2012) 65–70. https://doi.org/10.1016/j.jallcom.2012.04.109.

- [64] L. Yu, F. Shen, T. Fu, Y. Zhang, K. Cui, J. Wang, X. Zhang, Microstructure and Oxidation Behavior of Metal-Modified Mo-Si-B Alloys: A Review, Coatings 11 (2021) 1256. https://doi.org/10.3390/coatings11101256.
- [65] M. Azimovna Azim, S. Burk, B. Gorr, H.-J. Christ, D. Schliephake, M. Heilmaier, R. Bornemann, P.H. Bolívar, Effect of Ti (Macro-) Alloying on the High-Temperature Oxidation Behavior of Ternary Mo-Si-B Alloys at 820-1,300 °C, Oxid Met 80 (2013) 231-242. https://doi.org/10.1007/s11085-013-9375-1.
- [66] F. Shen, Y. Zhang, L. Yu, T. Fu, J. Wang, H. Wang, K. Cui, Microstructure and Oxidation Behavior of Nb-Si-Based Alloys for Ultrahigh Temperature Applications: A Comprehensive Review, Coatings 11 (2021) 1373. https://doi.org/10.3390/coatings11111373.
- [67] S. Zhang, W. Liu, J. Sha, Microstructural evolution and mechanical properties of Nb-Si-Cr ternary alloys with a tri-phase Nb/Nb5Si3/Cr2Nb microstructure fabricated by spark plasma sintering, Progress in Natural Science: Materials International 28 (2018) 626–634. https://doi.org/10.1016/j.pnsc.2018.09.001.
- [68] Y. Guo, Z. Li, J. He, H. Su, L. Jia, J. Zhang, L. Liu, H. Zhang, Surface microstructure modification of hypereutectic Nb-Si based alloys to improve oxidation resistance without damaging fracture toughness, Materials Characterization 159 (2020) 110051. https://doi.org/10.1016/j.matchar.2019.110051.
- [69] Y. Ge, Y. Wang, J. Chen, Y. Zou, L. Guo, J. Ouyang, D. Jia, Y. Zhou, An Nb2O5-SiO2-Al2O3/NbSi2/Nb5Si3 multilayer coating on Nb-Hf alloy to improve oxidation resistance, Journal of Alloys and Compounds 745 (2018) 271–281. https://doi.org/10.1016/j.jallcom.2018.02.107.
- [70] S. Zhang, X. Guo, Effects of B addition on the microstructure and properties of Nb silicide based ultrahigh temperature alloys, Intermetallics 57 (2015) 83–92. https://doi.org/10.1016/j.intermet.2014.10.007.
- [71] K.S. Thomas, S.K. Varma, Oxidation response of three Nb–Cr–Mo–Si–B alloys in air, Corrosion Science 99 (2015) 145–153. https://doi.org/10.1016/j.corsci.2015.06.026.
- [72] S. Zhang, X. Guo, Alloying effects on the microstructure and properties of Nb–Si based ultrahigh temperature alloys, Intermetallics 70 (2016) 33–44. https://doi.org/10.1016/j.intermet.2015.12.002.
- [73] L. Su, L. Jia, J. Weng, Z. Hong, C. Zhou, H. Zhang, Improvement in the oxidation resistance of Nb–Ti–Si–Cr–Al–Hf alloys containing alloyed Ge and B, Corrosion Science 88 (2014) 460–465. https://doi.org/10.1016/j.corsci.2014.08.006.
- [74] V. Behrani, A.J. Thom, M.J. Kramer, M. Akinc, Chlorination treatment to improve the oxidation resistance of Nb-Mo-Si-B alloys, Metall Mater Trans A 36 (2005) 609–615. https://doi.org/10.1007/s11661-005-0176-2.
- [75] M.M. Opeka, I.G. Talmy, E.J. Wuchina, J.A. Zaykoski, S.J. Causey, Mechanical, Thermal, and Oxidation Properties of Refractory Hafnium and

- zirconium Compounds, Journal of the European Ceramic Society 19 (1999) 2405–2414. https://doi.org/10.1016/S0955-2219(99)00129-6.
- [76] W.B. Hillig, Prospects for Ultra-High-Temperature Ceramic Composites, in: R.E. Tressler, G.L. Messing, C.G. Pantano, R.E. Newnham (Eds.), Tailoring Multiphase and Composite Ceramics, Springer US, Boston, MA, 1986: pp. 697–712. https://doi.org/10.1007/978-1-4613-2233-7\_55.
- [77] M.M. Opeka, I.G. Talmy, J.A. Zaykoski, Oxidation-based materials selection for 2000°C + hypersonic aerosurfaces: Theoretical considerations and historical experience, Journal of Materials Science 39 (2004) 5887–5904. https://doi.org/10.1023/B:JMSC.0000041686.21788.77.
- [78] E. Wuchina, E. Opila, M. Opeka, B. Fahrenholtz, I. Talmy, UHTCs: Ultra-High Temperature Ceramic Materials for Extreme Environment Applications, Electrochem. Soc. Interface 16 (2007) 30–36. https://doi.org/10.1149/2.F04074IF.
- [79] W.G. Fahrenholtz, G.E. Hilmas, I.G. Talmy, J.A. Zaykoski, Refractory Diborides of Zirconium and Hafnium, Journal of the American Ceramic Society 90 (2007) 1347–1364. https://doi.org/10.1111/j.1551-2916.2007.01583.x.
- [80] S.-Q. Guo, Densification of ZrB2-based composites and their mechanical and physical properties: A review, Journal of the European Ceramic Society 29 (2009) 995–1011. https://doi.org/10.1016/j.jeurceramsoc.2008.11.008.
- [81] B.R. Golla, A. Mukhopadhyay, B. Basu, S.K. Thimmappa, Review on ultra-high temperature boride ceramics, Progress in Materials Science 111 (2020) 100651. https://doi.org/10.1016/j.pmatsci.2020.100651.
- [82] E.D. Case, J.R. Smyth, O. Hunter, Grain-size dependence of microcrack initiation in brittle materials, J Mater Sci 15 (1980) 149–153. https://doi.org/10.1007/BF00552439.
- [83] W.D. Kingery, H.K. Bowen, D.R. Uhlmann, Introduction to Ceramics, 2nd Edition | Wiley, 2nd ed., Wiley, 1976. https://www.wiley.com/enus/Introduction+to+Ceramics%2C+2nd+Edition-p-9780471478607 (accessed May 19, 2025).
- [84] A.L. Chamberlain, W.G. Fahrenholtz, G.E. Hilmas, Pressureless Sintering of Zirconium Diboride, Journal of the American Ceramic Society (2006) 450. https://doi.org/10.1111/j.1551-2916.2005.00739.x.
- [85] H.-B. Ma, H.-L. Liu, J. Zhao, F.-F. Xu, G.-J. Zhang, Pressureless sintering, mechanical properties and oxidation behavior of ZrB2 ceramics doped with B4C, Journal of the European Ceramic Society 35 (2015) 2699–2705. https://doi.org/10.1016/j.jeurceramsoc.2015.03.030.
- [86] M. Mashhadi, M. Shambuli, S. Safi, Effect of MoSi2 addition and particle size of SiC on pressureless sintering behavior and mechanical properties of ZrB2–SiC–MoSi2 composites, Journal of Materials Research and Technology 5 (2016) 200–205. https://doi.org/10.1016/j.jmrt.2015.10.003.
- [87] T. Nishimura, X. Xu, K. Kimoto, N. Hirosaki, H. Tanaka, Fabrication of silicon nitride nanoceramics—Powder preparation and sintering: A review,

- Science and Technology of Advanced Materials 8 (2007) 635–643. https://doi.org/10.1016/j.stam.2007.08.006.
- [88] R. Orrù, R. Licheri, Consolidation/synthesis of materials by electric current activated/assisted sintering ScienceDirect, (n.d.). https://www.sciencedirect.com/science/article/pii/S0927796X08000995 (accessed January 10, 2025).
- [89] V. Zamora, A.L. Ortiz, F. Guiberteau, M. Nygren, Spark-plasma sintering of ZrB2 ultra-high-temperature ceramics at lower temperature via nanoscale crystal refinement, Journal of the European Ceramic Society 32 (2012) 2529–2536. https://doi.org/10.1016/j.jeurceramsoc.2012.02.023.
- [90] M. Cologna, B. Rashkova, R. Raj, Flash Sintering of Nanograin Zirconia in <5 s at 850°C, Journal of the American Ceramic Society 93 (2010) 3556–3559. https://doi.org/10.1111/j.1551-2916.2010.04089.x.
- [91] J. Gonzalez-Julian, K. Jähnert, K. Speer, L. Liu, J. Räthel, M. Knapp, H. Ehrenberg, M. Bram, O. Guillon, Effect of Internal Current Flow During the Sintering of Zirconium Diboride by Field Assisted Sintering Technology, Journal of the American Ceramic Society 99 (2016) 35–42. https://doi.org/10.1111/jace.13931.
- [92] S. Grasso, E.-Y. Kim, T. Saunders, M. Yu, A. Tudball, S.-H. Choi, M. Reece, Ultra-Rapid Crystal Growth of Textured SiC Using Flash Spark Plasma Sintering Route, Crystal Growth & Design 16 (2016) 2317–2321. https://doi.org/10.1021/acs.cgd.6b00099.
- [93] T.A. Parthasarathy, R.A. Rapp, M. Opeka, R.J. Kerans, A model for the oxidation of ZrB2, HfB2 and TiB2, Acta Materialia 55 (2007) 5999–6010. https://doi.org/10.1016/j.actamat.2007.07.027.
- [94] T.A. Parthasarathy, R.A. Rapp, M. Opeka, R.J. Kerans, A model for the oxidation of ZrB2, HfB2 and TiB2, Acta Materialia 55 (2007) 5999–6010. https://doi.org/10.1016/j.actamat.2007.07.027.
- [95] A.K. Kuriakose, J.L. Margrave, The Oxidation Kinetics of Zirconium Diboride and Zirconium Carbide at High Temperatures, J. Electrochem. Soc. 111 (1964) 827. https://doi.org/10.1149/1.2426263.
- [96] J.B. Berkowitz-Mattuck, HIGH-TEMPERATURE OXIDATION. III. ZIRCONIUM AND HAFNIUM DIBORIDES, Journal of the Electrochemical Society (U.S.) Absorbed Electrochem. Technol. Vol: 113 (1966). https://doi.org/10.1149/1.2424154.
- [97] W.C. Tripp, H.C. Graham, Thermogravimetric study of the oxidation of ZrB2 in the temperature range of 8000 to 15000C, Journal of the Electrochemical Society 118 (1971) 1195–1199.
- [98] L. Kaufman, E.V. Clougherty, J.B. Berkowitz-Mattuck, OXIDATION CHARACTERISTICS OF HAFNIUM AND ZIRCONIUM DIBORIDE., Trans. Met. Soc. AIME, 239: 458-66(Apr. 1967). (1967). https://www.osti.gov/biblio/4405185-oxidation-characteristics-hafnium-zirconium-diboride (accessed December 5, 2021).
- [99] R.J. Irving, I.G. Worsley, OXIDATION OF TITANIUM DIBORIDE AND ZIRCONIUM DIBORIDE AT HIGH TEMPERATURES., J. Less-

- Common Metals, 16: 103-12(Oct. 1968). (1968). https://doi.org/10.1016/0022-5088(68)90067-2.
- [100]F. Monteverde, A. Bellosi, Oxidation of ZrB2-Based Ceramics in Dry Air, J. Electrochem. Soc. 150 (2009) 8.
- [101] W.G. Fahrenholtz, Thermodynamic Analysis of ZrB2–SiC Oxidation: Formation of a SiC-Depleted Region, Journal of the American Ceramic Society 90 (2007) 143–148. https://doi.org/10.1111/j.1551-2916.2006.01329.x.
- [102] W.G. Fahrenholtz, The ZrB2 Volatility Diagram, Journal of the American Ceramic Society 88 (2005) 3509–3512. https://doi.org/10.1111/j.1551-2916.2005.00599.x.
- [103]G. Hilmas, W. Fahrenholtz, A. Chamberlain, D. Ellerby, Oxidation of ZrB<sub>2</sub>-SiC Ceramics under Atmospheric and Reentry Conditions, Materials Science and Engineering Faculty Research & Creative Works (2005). https://scholarsmine.mst.edu/matsci\_eng\_facwork/608.
- [104] E. Wuchina, M. Opeka, S. Causey, K. Buesking, J. Spain, A. Cull, J. Routbort, F. Guitierrez-Mora, Designing for ultrahigh-temperature applications: The mechanical and thermal properties of HfB2, HfCx, HfNx and Hf(N), Journal of Materials Science 39 (2004) 5939–5949. https://doi.org/10.1023/B:JMSC.0000041690.06117.34.
- [105] W.C. Tripp, H.H. Davis, H.C. Graham, Effect of an SiC addition on the oxidation of ZrB2, Amer Ceram Soc Bull 52 (1973) 612–616.
- [106] E.J. Opila, M.C. Halbig, Oxidation of ZrB2-SiC, in: 2001: p. 221. https://scholar.google.com/citations?view\_op=view\_citation&hl=en&user=RiXqXbQAAAAJ&citation\_for\_view=RiXqXbQAAAAJ:WF5omc3n YNoC (accessed December 6, 2021).
- [107] E.V. Clougherty, R.L. Pober, L. Kaufman, SYNTHESIS OF OXIDATION RESISTANT METAL DIBORIDE COMPOSITES., Trans. Met. Soc. AIME, 242: 1077-82(June 1968). (1968). https://www.osti.gov/biblio/4519412-synthesis-oxidation-resistant-metal-diboride-composites (accessed December 6, 2021).
- [108]G. Ouyang, P.K. Ray, M.J. Kramer, M. Akinc, High-Temperature Oxidation of ZrB2 –SiC–AlN Composites at 1600°C, J. Am. Ceram. Soc. 99 (2016) 808–813. https://doi.org/10.1111/jace.14039.
- [109]S.N. Karlsdottir, J.W. Halloran, C.E. Henderson, Convection Patterns in Liquid Oxide Films on ZrB2–SiC Composites Oxidized at a High Temperature, Journal of the American Ceramic Society 90 (2007) 2863– 2867. https://doi.org/10.1111/j.1551-2916.2007.01784.x.
- [110]K. Shugart, S. Liu, F. Craven, E. Opila, Determination of Retained B2O3 Content in ZrB2-30 vol% SiC Oxide Scales, Journal of the American Ceramic Society 98 (2015) 287–295. https://doi.org/10.1111/jace.13236.
- [111]K. Shugart, W. Jennings, E. Opila, Initial Stages of ZrB2–30 vol% SiC Oxidation at 1500°C, Journal of the American Ceramic Society 97 (2014) 1645–1651. https://doi.org/10.1111/jace.12843.

- [112]S.N. Karlsdottir, J.W. Halloran, Rapid Oxidation Characterization of Ultra-High Temperature Ceramics, Journal of the American Ceramic Society 90 (2007) 3233–3238. https://doi.org/10.1111/j.1551-2916.2007.01861.x.
- [113]S.N. Karlsdottir, J.W. Halloran, Oxidation of ZrB2-SiC: Influence of SiC Content on Solid and Liquid Oxide Phase Formation, Journal of the American Ceramic Society 92 (2009) 481-486. https://doi.org/10.1111/j.1551-2916.2008.02874.x.
- [114]S.N. Karlsdottir, J.W. Halloran, Formation of Oxide Scales on Zirconium Diboride–Silicon Carbide Composites During Oxidation: Relation of Subscale Recession to Liquid Oxide Flow, Journal of the American Ceramic Society 91 (2008) 3652–3658. https://doi.org/10.1111/j.1551-2916.2008.02639.x.
- [115]S.N. Karlsdottir, J.W. Halloran, A.N. Grundy, Zirconia Transport by Liquid Convection during Oxidation of Zirconium Diboride–Silicon Carbide, Journal of the American Ceramic Society 91 (2008) 272–277. https://doi.org/10.1111/j.1551-2916.2007.02142.x.
- [116]F. Monteverde, A. Bellosi, Beneficial Effects of AlN as Sintering Aid on Microstructure and Mechanical Properties of Hot-pressed ZrB2, Advanced Engineering Materials 5 (2003) 508–512. https://doi.org/10.1002/adem.200300349.
- [117] W. Han, G. Li, X. Zhang, J. Han, Effect of AlN as sintering aid on hot-pressed ZrB2–SiC ceramic composite, Journal of Alloys and Compounds 471 (2009) 488–491. https://doi.org/10.1016/j.jallcom.2008.03.135.
- [118]G. Ouyang, P.K. Ray, M.J. Kramer, M. Akinc, Effect of AlN Substitutions on the Oxidation Behavior of ZrB2–SiC Composites at 1600°C, Journal of the American Ceramic Society 99 (2016) 3389–3397. https://doi.org/10.1111/jace.14345.
- [119]Y. Wang, B. Ma, L. Li, L. An, Oxidation Behavior of ZrB2–SiC–TaC Ceramics, Journal of the American Ceramic Society 95 (2012) 374–378. https://doi.org/10.1111/j.1551-2916.2011.04945.x.
- [120]I.G. Talmy, J.A. Zaykoski, M.M. Opeka, High-Temperature Chemistry and Oxidation of ZrB2 Ceramics Containing SiC, Si3N4, Ta5Si3, and TaSi2, Journal of the American Ceramic Society 91 (2008) 2250–2257. https://doi.org/10.1111/j.1551-2916.2008.02420.x.
- [121]F. Peng, R.F. Speyer, Oxidation Resistance of Fully Dense ZrB2 with SiC, TaB2, and TaSi2 Additives, Journal of the American Ceramic Society 91 (2008) 1489–1494. https://doi.org/10.1111/j.1551-2916.2008.02368.x.
- [122] E. Opila, S. Levine, J. Lorincz, Oxidation of ZrB2- and HfB2-based ultrahigh temperature ceramics: Effect of Ta additions, Journal of Materials Science 39 (2004) 5969–5977. https://doi.org/10.1023/B:JMSC.0000041693.32531.d1.
- [123] S.C. Zhang, G.E. Hilmas, W.G. Fahrenholtz, Improved Oxidation Resistance of Zirconium Diboride by Tungsten Carbide Additions, Journal

- of the American Ceramic Society 91 (2008) 3530–3535. https://doi.org/10.1111/j.1551-2916.2008.02713.x.
- [124] P. Sengupta, I. Manna, Role of TiC and WC Addition on the Mechanism and Kinetics of Isothermal Oxidation and High-Temperature Stability of ZrB2–SiC Composites, High Temperature Corrosion of Mater. 101 (2024) 57–83. https://doi.org/10.1007/s11085-024-10234-1.
- [125] T.S. Gates, G.M. Odegard, S.J.V. Frankland, T.C. Clancy, Computational materials: Multi-scale modeling and simulation of nanostructured materials, Composites Science and Technology 65 (2005) 2416–2434. https://doi.org/10.1016/j.compscitech.2005.06.009.
- [126]H. Chan, B. Narayanan, M.J. Cherukara, F.G. Sen, K. Sasikumar, S.K. Gray, M.K.Y. Chan, S.K.R.S. Sankaranarayanan, Machine Learning Classical Interatomic Potentials for Molecular Dynamics from First-Principles Training Data, J. Phys. Chem. C 123 (2019) 6941–6957. https://doi.org/10.1021/acs.jpcc.8b09917.
- [127] A. van de Walle, M. Asta, High-throughput calculations in the context of alloy design, MRS Bulletin 44 (2019) 252–256. https://doi.org/10.1557/mrs.2019.71.
- [128]H. Mehrer, Diffusion: Introduction and Case Studies in Metals and Binary Alloys, in: P. Heitjans, J. Kärger (Eds.), Diffusion in Condensed Matter: Methods, Materials, Models, Springer, Berlin, Heidelberg, 2005: pp. 3–63. https://doi.org/10.1007/3-540-30970-5\_1.
- [129]Z. Wei, J. Yu, Y. Lu, J. Han, C. Wang, X. Liu, Prediction of diffusion coefficients in fcc, bcc and hcp phases remained stable or metastable by the machine-learning methods, Materials & Design 198 (2021) 109287. https://doi.org/10.1016/j.matdes.2020.109287.
- [130]R. LeSar, Introduction to Computational Materials Science: Fundamentals to Applications, Cambridge University Press, Cambridge, 2013. https://doi.org/10.1017/CBO9781139033398.
- [131] J.E. Jones, A.E. Ingham, S. Chapman, On the calculation of certain crystal potential constants, and on the cubic crystal of least potential energy, Proceedings of the Royal Society of London. Series A, Containing Papers of a Mathematical and Physical Character 107 (1997) 636–653. https://doi.org/10.1098/rspa.1925.0047.
- [132] F.H. Stillinger, T.A. Weber, Computer simulation of local order in condensed phases of silicon, Phys. Rev. B 31 (1985) 5262–5271. https://doi.org/10.1103/PhysRevB.31.5262.
- [133] P. Vashishta, R.K. Kalia, J.P. Rino, I. Ebbsjö, Interaction potential for SiO2: A molecular-dynamics study of structural correlations, Phys. Rev. B 41 (1990) 12197–12209. https://doi.org/10.1103/PhysRevB.41.12197.
- [134]H. Rafii-Tabar, A.P. Sulton, Long-range Finnis-Sinclair potentials for f.c.c. metallic alloys, Philosophical Magazine Letters 63 (1991) 217–224. https://doi.org/10.1080/09500839108205994.

- [135] M.S. Daw, M.I. Baskes, Embedded-atom method: Derivation and application to impurities, surfaces, and other defects in metals, Phys. Rev. B 29 (1984) 6443–6453. https://doi.org/10.1103/PhysRevB.29.6443.
- [136] M.I. Baskes, Modified embedded-atom potentials for cubic materials and impurities, Phys. Rev. B 46 (1992) 2727–2742. https://doi.org/10.1103/PhysRevB.46.2727.
- [137]G.C. Abell, Empirical chemical pseudopotential theory of molecular and metallic bonding, Phys. Rev. B 31 (1985) 6184–6196. https://doi.org/10.1103/PhysRevB.31.6184.
- [138] J. Tersoff, New empirical approach for the structure and energy of covalent systems, Phys. Rev. B 37 (1988) 6991–7000. https://doi.org/10.1103/PhysRevB.37.6991.
- [139] J. Tersoff, Empirical Interatomic Potential for Carbon, with Applications to Amorphous Carbon, Phys. Rev. Lett. 61 (1988) 2879–2882. https://doi.org/10.1103/PhysRevLett.61.2879.
- [140] D.W. Brenner, O.A. Shenderova, J.A. Harrison, S.J. Stuart, B. Ni, S.B. Sinnott, A second-generation reactive empirical bond order (REBO) potential energy expression for hydrocarbons, Journal of Physics Condensed Matter 14 (2002) 783–802. https://doi.org/10.1088/0953-8984/14/4/312.
- [141] D.G. Pettifor, I.I. Oleynik, Interatomic bond-order potentials and structural prediction, Progress in Materials Science 49 (2004) 285–312. https://doi.org/10.1016/S0079-6425(03)00024-0.
- [142] M.I. Mendelev, H. Zhang, D.J. Srolovitz, Grain boundary self-diffusion in Ni: Effect of boundary inclination, Journal of Materials Research 20 (2005) 1146–1153. https://doi.org/10.1557/JMR.2005.0177.
- [143] A. Gotte, D. Spångberg, K. Hermansson, M. Baudin, Molecular dynamics study of oxygen self-diffusion in reduced CeO2, Solid State Ionics 178 (2007) 1421–1427. https://doi.org/10.1016/j.ssi.2007.08.003.
- [144]G.M. Poletaev, I.V. Zorya, D.V. Novoselova, M.D. Starostenkov, Molecular dynamics simulation of hydrogen atom diffusion in crystal lattice of fcc metals, International Journal of Materials Research 108 (2017) 785–790. https://doi.org/10.3139/146.111556.
- [145]L.V. Woodcock, C.A. Angell, P. Cheeseman, Molecular dynamics studies of the vitreous state: Simple ionic systems and silica, J. Chem. Phys. 65 (1976) 1565–1577. https://doi.org/10.1063/1.433213.
- [146] N.V. Doan, Molecular dynamics study of irradiation-induced defects in vitreous silica, Philosophical Magazine A, Physics of Condensed Matter Defects and Mechanical Properties 49 (1984) 683–687.
- [147] C.A. Angell, P.A. Cheeseman, C.C. Phifer, Dynamics of Compressed and Stretched Liquid SiO2, and the Glass Transition, MRS Online Proceedings Library (OPL) 63 (1985). https://doi.org/10.1557/PROC-63-85.
- [148] T.F. Soules, A molecular dynamic calculation of the structure of B2O3 glass, J. Chem. Phys. 73 (1980) 4032–4036. https://doi.org/10.1063/1.440632.

- [149]S.H. Garofalini, Molecular dynamics simulation of the frequency spectrum of amorphous silica, J. Chem. Phys. 76 (1982) 3189–3192. https://doi.org/10.1063/1.443363.
- [150] J.D. Kubicki, A.C. Lasaga, Molecular dynamics simulations of SiO 2 melt and glass; ionic and covalent models, American Mineralogist 73 (1988) 941– 955.
- [151] R.G. Della Valle, H.C. Andersen, Molecular dynamics simulation of silica liquid and glass, J. Chem. Phys. 97 (1992) 2682–2689. https://doi.org/10.1063/1.463056.
- [152]B.P. Feuston, S.H. Garofalini, Empirical three-body potential for vitreous silica, J. Chem. Phys. 89 (1988) 5818–5824. https://doi.org/10.1063/1.455531.
- [153]B. Vessal, M. Amini, D. Fincham, C.R.A. Catlow, Water-like melting behaviour of SiO2 investigated by the molecular dynamics simulation technique, Philosophical Magazine B 60 (1989) 753–775. https://doi.org/10.1080/13642818908209741.
- [154]S. Tsuneyuki, M. Tsukada, H. Aoki, Y. Matsui, First-Principles Interatomic Potential of Silica Applied to Molecular Dynamics, Phys. Rev. Lett. 61 (1988) 869–872. https://doi.org/10.1103/PhysRevLett.61.869.
- [155]B. Guillot, N. Sator, A computer simulation study of natural silicate melts. Part I: Low pressure properties, Geochimica et Cosmochimica Acta 71 (2007) 1249–1265. https://doi.org/10.1016/j.gca.2006.11.015.
- [156]R. Kubo, The fluctuation-dissipation theorem, Rep. Prog. Phys. 29 (1966) 255. https://doi.org/10.1088/0034-4885/29/1/306.
- [157] P. Cao, D. Wells, M. Philip Short, Anisotropic ion diffusion in α-Cr 2 O 3: an atomistic simulation study, Physical Chemistry Chemical Physics 19 (2017) 13658–13663. https://doi.org/10.1039/C7CP00838D.
- [158]I. Roy, P.K. Ray, G. Balasubramanian, Diffusion of multi-principal elements through stable Cr2O3 and Al2O3 scales, Materialia 24 (2022) 101497. https://doi.org/10.1016/j.mtla.2022.101497.
- [159]H.J.T. Ellingham, Reducibility of oxides and sulphides in metallurgical processes, Journal of the Society of Chemical Industry 63 (1944) 125–160. https://doi.org/10.1002/jctb.5000630501.
- [160] L. Kaufman, E.V. Clougherty, J.B. Berkowitz-Mattuck, OXIDATION CHARACTERISTICS OF HAFNIUM AND ZIRCONIUM DIBORIDE., Trans. Met. Soc. AIME, 239: 458-66(Apr. 1967). (1967). https://www.osti.gov/biblio/4405185-oxidation-characteristics-hafnium-zirconium-diboride (accessed December 5, 2021).
- [161] N.S. Jacobson, D.L. Myers, Active Oxidation of SiC, Oxid Met 75 (2011) 1–25. https://doi.org/10.1007/s11085-010-9216-4.
- [162] J. Roy, S. Chandra, S. Das, S. Maitra, OXIDATION BEHAVIOUR OF SILICON CARBIDE A REVIEW, (n.d.).
- [163] J.D. Bull, D.J. Rasky, J.C. Karika, Stability characterization of diboride composites under high velocity atmospheric flight conditions, SAMPE, United States, 1992.

- [164]M. Gasch, D. Ellerby, E. Irby, S. Beckman, M. Gusman, S. Johnson, Processing, properties and arc jet oxidation of hafnium diboride/silicon carbide ultra high temperature ceramics, Journal of Materials Science 39 (2004) 5925–5937. https://doi.org/10.1023/B:JMSC.0000041689.90456.af.
- [165] W.C. Tripp, H.H. Davis, H.C. Graham, Effect of an SiC addition on the oxidation of ZrB2, Amer Ceram Soc Bull 52 (1973) 612–616.
- [166] A. Momozawa, R. Tu, T. Goto, Y. Kubota, H. Hatta, K. Komurasaki, Quantitative evaluation of the oxidation behavior of ZrB2-15 vol.%SiC at a low oxygen partial pressure, Vacuum 88 (2013) 98–102. https://doi.org/10.1016/j.vacuum.2012.04.004.
- [167] A. Rezaie, W.G. Fahrenholtz, G.E. Hilmas, Evolution of structure during the oxidation of zirconium diboride—silicon carbide in air up to 1500 °C, Journal of the European Ceramic Society 27 (2007) 2495–2501. https://doi.org/10.1016/j.jeurceramsoc.2006.10.012.
- [168] T.A. Parthasarathy, R.A. Rapp, M. Opeka, M.K. Cinibulk, Modeling Oxidation Kinetics of SiC-Containing Refractory Diborides, Journal of the American Ceramic Society 95 (2012) 338–349. https://doi.org/10.1111/j.1551-2916.2011.04927.x.
- [169]S.R. Levine, E.J. Opila, M.C. Halbig, J.D. Kiser, M. Singh, J.A. Salem, Evaluation of ultra-high temperature ceramics foraeropropulsion use, Journal of the European Ceramic Society 22 (2002) 2757–2767. https://doi.org/10.1016/S0955-2219(02)00140-1.
- [170] C.M. Carney, P. Mogilvesky, T.A. Parthasarathy, Oxidation Behavior of Zirconium Diboride Silicon Carbide Produced by the Spark Plasma Sintering Method, Journal of the American Ceramic Society 92 (2009) 2046–2052. https://doi.org/10.1111/j.1551-2916.2009.03134.x.
- [171] P. Zeman, J. Musil, R. Daniel, High-temperature oxidation resistance of Ta–Si–N films with a high Si content, Surface and Coatings Technology 200 (2006) 4091–4096. https://doi.org/10.1016/j.surfcoat.2005.02.097.
- [172] M. Nascimento, E. Zanotto, Diffusion Processes in Vitreous Silica Revisited, Physics and Chemistry of Glasses - European Journal of Glass Science and Technology Part B 48 (2007).
- [173]S. Ochiai, Influence of the addition of Cr and Al elements to the Mo3Si intermetallic alloy on the phase construction and the oxidation behavior, Materials Science Forum 426–432 (2003) 1771–1776.
- [174] F. Monteverde, L. Scatteia, Resistance to Thermal Shock and to Oxidation of Metal Diborides—SiC Ceramics for Aerospace Application, Journal of the American Ceramic Society 90 (2007) 1130–1138. https://doi.org/10.1111/j.1551-2916.2007.01589.x.
- [175]M.M. Opeka, I.G. Talmy, J.A. Zaykoski, Oxidation-based materials selection for 2000°C + hypersonic aerosurfaces: Theoretical considerations and historical experience, Journal of Materials Science 39 (2004) 5887–5904. https://doi.org/10.1023/B:JMSC.0000041686.21788.77.
- [176]G. Ouyang, M. Besser, M. Kramer, M. Akinc, P. Ray, Designing oxidation resistant ultra-high temperature ceramics through the development of an

- adherent native thermal barrier, Journal of Alloys and Compounds 790 (2019) 1119–1126. https://doi.org/10.1016/j.jallcom.2019.03.250.
- [177] M. Meyer, M. Kramer, M. Akinc, Boron-doped molybdenum silicides, Advanced Materials 8 (1996) 85–88. https://doi.org/10.1002/adma.19960080118.
- [178] E.J. Opila, M.K. Boyd, Oxidation of SiC Fiber-Reinforced SiC Matrix Composites with a BN Interphase, MSF 696 (2011) 342–347. https://doi.org/10.4028/www.scientific.net/MSF.696.342.
- [179] W.G. Fahrenholtz, G.E. Hilmas, I.G. Talmy, J.A. Zaykoski, Refractory Diborides of Zirconium and Hafnium, Journal of the American Ceramic Society 90 (2007) 1347–1364. https://doi.org/10.1111/j.1551-2916.2007.01583.x.
- [180]S.N. Karlsdottir, J.W. Halloran, Rapid Oxidation Characterization of Ultra-High Temperature Ceramics, Journal of the American Ceramic Society 90 (2007) 3233–3238. https://doi.org/10.1111/j.1551-2916.2007.01861.x.
- [181]S.N. Karlsdottir, J.W. Halloran, Oxidation of ZrB2–SiC: Influence of SiC Content on Solid and Liquid Oxide Phase Formation, Journal of the American Ceramic Society 92 (2009) 481–486. https://doi.org/10.1111/j.1551-2916.2008.02874.x.
- [182]S.N. Karlsdottir, J.W. Halloran, A.N. Grundy, Zirconia Transport by Liquid Convection during Oxidation of Zirconium Diboride–Silicon Carbide, Journal of the American Ceramic Society 91 (2008) 272–277. https://doi.org/10.1111/j.1551-2916.2007.02142.x.
- [183]S.N. Karlsdottir, J.W. Halloran, C.E. Henderson, Convection Patterns in Liquid Oxide Films on ZrB2–SiC Composites Oxidized at a High Temperature, Journal of the American Ceramic Society 90 (2007) 2863–2867. https://doi.org/10.1111/j.1551-2916.2007.01784.x.
- [184] G. Urbain, Y. Bottinga, P. Richet, Viscosity of liquid silica, silicates and alumino-silicates, Geochimica et Cosmochimica Acta 46 (1982) 1061–1072. https://doi.org/10.1016/0016-7037(82)90059-X.
- [185] C. Cheng, W. Xie, H. Li, Q. Fu, Evaporation behavior of SiO2 glass doped with various transition metal oxides, Journal of the American Ceramic Society 104 (2021) 3130–3138. https://doi.org/10.1111/jace.17710.
- [186] C. Cheng, H. Li, Q. Fu, L. Guo, J. Sun, X. Yin, Effect of Zr doping on the high-temperature stability of SiO2 glass, Computational Materials Science 147 (2018) 81–86. https://doi.org/10.1016/j.commatsci.2018.01.051.
- [187] F.J. Norton, Permeation of gaseous oxygen through vitreous silica, Nature 191 (1961) 701–701.
- [188] R. Haul, G. Dumbgen, Oxygen mobility in TiO2, SiO2 and fused quartz by heterogeneous isotopic exchange, Z. Elektrochem (1962) 636.
- [189] E.L. Williams, Diffusion of Oxygen in Fused Silica, Journal of the American Ceramic Society 48 (1965) 190–194. https://doi.org/10.1111/j.1151-2916.1965.tb14710.x.

- [190] J.C. Mikkelsen, Self-diffusivity of network oxygen in vitreous SiO2, Appl. Phys. Lett. 45 (1984) 1187–1189. https://doi.org/10.1063/1.95086.
- [191] J.D. Cawley, R.S. Boyce, A solution of the diffusion equation for double oxidation in dry oxygen including lazy exchange between network and interstitial oxygen, Philosophical Magazine A 58 (1988) 589–601. https://doi.org/10.1080/01418618808209939.
- [192] A. Einstein, On the Motion of Small Particles Suspended in Liquids at Rest Required by the Molecular-Kinetic Theory of Heat, Annalen Der Physik 17 (1905) 549–560.
- [193] A. Gotte, D. Spångberg, K. Hermansson, M. Baudin, Molecular dynamics study of oxygen self-diffusion in reduced CeO2, Solid State Ionics 178 (2007) 1421–1427. https://doi.org/10.1016/j.ssi.2007.08.003.
- [194] C.-L. Liu, S.J. Plimpton, Molecular dynamics simulations of grain boundary diffusion in Al using embedded atom method potentials, Journal of Materials Research 10 (1995) 1589–1592. https://doi.org/10.1557/JMR.1995.1589.
- [195]P. Hirel, Atomsk: A tool for manipulating and converting atomic data files, Computer Physics Communications 197 (2015) 212–219. https://doi.org/10.1016/j.cpc.2015.07.012.
- [196] A.P. Thompson, H.M. Aktulga, R. Berger, D.S. Bolintineanu, W.M. Brown, P.S. Crozier, P.J. in 't Veld, A. Kohlmeyer, S.G. Moore, T.D. Nguyen, R. Shan, M.J. Stevens, J. Tranchida, C. Trott, S.J. Plimpton, LAMMPS a flexible simulation tool for particle-based materials modeling at the atomic, meso, and continuum scales, Computer Physics Communications 271 (2022) 108171. https://doi.org/10.1016/j.cpc.2021.108171.
- [197]S. Munetoh, T. Motooka, K. Moriguchi, A. Shintani, Interatomic potential for Si–O systems using Tersoff parameterization, Computational Materials Science 39 (2007) 334–339. https://doi.org/10.1016/j.commatsci.2006.06.010.
- [198] A.C. Wright, The comparison of molecular dynamics simulations with diffraction experiments, Journal of Non-Crystalline Solids 159 (1993) 264–268. https://doi.org/10.1016/0022-3093(93)90232-M.
- [199] T.-R. Shan, B.D. Devine, T.W. Kemper, S.B. Sinnott, S.R. Phillpot, Charge-optimized many-body potential for the hafnium/hafnium oxide system, Phys. Rev. B 81 (2010) 125328. https://doi.org/10.1103/PhysRevB.81.125328.
- [200] T.-R. Shan, B.D. Devine, J.M. Hawkins, A. Asthagiri, S.R. Phillpot, S.B. Sinnott, Second-generation charge-optimized many-body potential for Si/SiO2 and amorphous silica, Phys. Rev. B 82 (2010) 235302. https://doi.org/10.1103/PhysRevB.82.235302.
- [201] P.A.V. Johnson, A.C. Wright, R.N. Sinclair, Neutron scattering from vitreous silica II. Twin-axis diffraction experiments, Journal of Non-Crystalline Solids 58 (1983) 109–130. https://doi.org/10.1016/0022-3093(83)90107-2.

- [202] J. Sarnthein, A. Pasquarello, R. Car, Model of vitreous SiO2 generated by an ab initio molecular-dynamics quench from the melt, Phys. Rev. B 52 (1995) 12690–12695. https://doi.org/10.1103/PhysRevB.52.12690.
- [203] D. Beniwal, Jhalak, P.K. Ray, Data-Driven Phase Selection, Property Prediction and Force-Field Development in Multi-Principal Element Alloys, in: A. Verma, S. Mavinkere Rangappa, S. Ogata, S. Siengchin (Eds.), Forcefields for Atomistic-Scale Simulations: Materials and Applications, Springer Nature, Singapore, 2022: pp. 315–347. https://doi.org/10.1007/978-981-19-3092-8 16.
- [204] J.D. Kalen, R.S. Boyce, J.D. Cawley, Oxygen Tracer Diffusion in Vitreous Silica, Journal of the American Ceramic Society 74 (1991) 203–209. https://doi.org/10.1111/j.1151-2916.1991.tb07318.x.
- [205]Y. Limoge, G. Brebec, Relation between viscosity and diffusion in amorphous metallic alloys, Acta Metallurgica 36 (1988) 665–673. https://doi.org/10.1016/0001-6160(88)90100-9.
- [206] Ellingham Diagrams, (n.d.). https://www.doitpoms.ac.uk/tlplib/ellingham\_diagrams/index.php (accessed April 7, 2023).
- [207] V.N. Parfenenkov, R.G. Grebenshikov, N.A. Toropov, Phase equilibriums in the hafnium dioxide–silicon dioxide system, in: Dokl. Akad. Nauk SSSR, 1969: pp. 840–842.
- [208] R. A Dunlap, The Symmetry and Packing Fraction of The Body Centered Tetragonal Structure, European J of Physics Education 3 (2012) 19–24.
- [209]B. deB. Darwent, Bond dissociation energies in simple molecules, (1970). https://srd.nist.gov/NSRDS/NSRDS-NBS31.pdf.
- [210] T.L. Cottrell, The strengths of chemical bonds, 2d ed, Butterworths, London, 1958. http://books.google.com/books?id=HKg6AAAAMAAJ (accessed March 18, 2023).
- [211] M. Bauchy, B. Guillot, M. Micoulaut, N. Sator, Viscosity and viscosity anomalies of model silicates and magmas: A numerical investigation, Chemical Geology 346 (2013) 47–56. https://doi.org/10.1016/j.chemgeo.2012.08.035.
- [212] J.D. Mackenzie, THE PHYSICAL CHEMISTRY OF SIMPLE MOLTEN GLASSES, Chemical Reviews 56 (1956) 455–470.
- [213] W.G. Fahrenholtz, Thermodynamic Analysis of ZrB2–SiC Oxidation: Formation of a SiC-Depleted Region, Journal of the American Ceramic Society 90 (2007) 143–148. https://doi.org/10.1111/j.1551-2916.2006.01329.x.
- [214]B.H. Toby, R.B. Von Dreele, GSAS-II: the genesis of a modern open-source all purpose crystallography software package, J Appl Cryst 46 (2013) 544–549. https://doi.org/10.1107/S0021889813003531.
- [215] J. Schindelin, I. Arganda-Carreras, E. Frise, V. Kaynig, M. Longair, T. Pietzsch, S. Preibisch, C. Rueden, S. Saalfeld, B. Schmid, J.-Y. Tinevez, D.J. White, V. Hartenstein, K. Eliceiri, P. Tomancak, A. Cardona, Fiji: an

- open-source platform for biological-image analysis, Nat Methods 9 (2012) 676–682. https://doi.org/10.1038/nmeth.2019.
- [216] Thomas C. Allison, NIST-JANAF Thermochemical Tables SRD 13, (2013). https://doi.org/10.18434/T42S31.
- [217] P.K. Ray, Microstructures and oxidation behavior of some Molybdenum based alloys, 2011. https://doi.org/10.2172/1037978.
- [218] D.M. Dimiduk, J.H. Perepezko, Mo-Si-B Alloys: Developing a Revolutionary Turbine-Engine Material, MRS Bulletin 28 (2003) 639–645. https://doi.org/10.1557/mrs2003.191.
- [219] J.J. Petrovic, A.K. Vasudevan, Key developments in high temperature structural silicides, Materials Science and Engineering: A 261 (1999) 1–5. https://doi.org/10.1016/S0921-5093(98)01043-0.
- [220]I. Rosales, J.H. Schneibel, L. Heatherly, J.A. Horton, L. Martinez, B. Campillo, High temperature deformation of A15 Mo3Si single crystals, Scripta Materialia 48 (2003) 185–190. https://doi.org/10.1016/S1359-6462(02)00360-3.
- [221]S. Ochiai, Improvement of the oxidation-proof property and the scale structure of Mo3Si intermetallic alloy through the addition of chromium and aluminum elements, Intermetallics 14 (2006) 1351–1357. https://doi.org/10.1016/j.intermet.2006.01.059.
- [222]R. Sakidja, J.H. Perepezko, Phase stability and alloying behavior in the Mo-Si-B system, Metall Mater Trans A 36 (2005) 507–514. https://doi.org/10.1007/s11661-005-0164-6.
- [223] T. Geng, C. Li, X. Zhao, H. Xu, Z. Du, C. Guo, Thermodynamic assessment of the Nb–Si–Mo system, Calphad 34 (2010) 363–376. https://doi.org/10.1016/j.calphad.2010.07.003.
- [224] K. Ihara, K. Ito, K. Tanaka, M. Yamaguchi, Mechanical properties of Mo5SiB2 single crystals, Materials Science and Engineering: A 329–331 (2002) 222–227. https://doi.org/10.1016/S0921-5093(01)01575-1.
- [225] J.J. Kruzic, J.H. Schneibel, R.O. Ritchie, Fracture and fatigue resistance of Mo–Si–B alloys for ultrahigh-temperature structural applications, Scripta Materialia 50 (2004) 459–464. https://doi.org/10.1016/j.scriptamat.2003.11.002.
- [226] J.H. Schneibel, M.J. Kramer, D.S. Easton, A Mo–Si–B intermetallic alloy with a continuous  $\alpha$ -Mo matrix, Scripta Materialia 46 (2002) 217–221. https://doi.org/10.1016/S1359-6462(01)01227-1.
- [227] Z. Lin, M. Li, J. He, M. Li, G. Wang, Y. Li, Y. Zeng, J. Han, J. Liu, Effect of Ta2O5 addition on the structure, crystallization mechanism, and properties of CaO-B2O3-SiO2 glasses for LTCC applications, Ceramics International 49 (2023) 4872–4880. https://doi.org/10.1016/j.ceramint.2022.09.378.
- [228] A. Yamauchi, K. Yoshimi, Y. Murakami, K. Kurokawa, S. Hanada, Oxidation Behavior of Mo-Si-B In Situ Composites, Solid State Phenomena 127 (2007) 215–220. https://doi.org/10.4028/www.scientific.net/SSP.127.215.

- [229] H. Bakker, Enthalpies in Alloys: Miedema's Semi-empirical Model, Trans Tech Publications, 1998.
- [230] A.K. Niessen, F.R. de Boer, R. Boom, P.F. de Châtel, W.C.M. Mattens, A.R. Miedema, Model predictions for the enthalpy of formation of transition metal alloys II, Calphad 7 (1983) 51–70. https://doi.org/10.1016/0364-5916(83)90030-5.
- [231] F.R. de Boer, W.C.M. Mattens, R. Boom, A.R. Miedema, A.K. Niessen, Cohesion in metals. Transition metal alloys, 1 (1988). https://www.osti.gov/etdeweb/biblio/5556327 (accessed August 20, 2024).
- [232] K. Yoshimi, S. Nakatani, T. Suda, S. Hanada, H. Habazaki, Oxidation behavior of Mo5SiB2-based alloy at elevated temperatures, Intermetallics 10 (2002) 407–414. https://doi.org/10.1016/S0966-9795(02)00013-4.
- [233] D.A. Helmick, G.H. Meier, F.S. Pettit, The development of protective borosilicate layers on a Mo-3Si-1B (weight percent) alloy, Metall Mater Trans A 36 (2005) 3371–3383. https://doi.org/10.1007/s11661-005-0011-9.
- [234] J.H. Perepezko, R. Sakidja, Oxidation-resistant coatings for ultra-high-temperature refractory Mo-based alloys, JOM 62 (2010) 13–19. https://doi.org/10.1007/s11837-010-0148-x.
- [235]E.F. Riebling, Structure of Borosilicate and Borogermanate Melts at 1300°C; a Viscosity and Density Study, Journal of the American Ceramic Society 47 (1964) 478–483. https://doi.org/10.1111/j.1151-2916.1964.tb13794.x.
- [236] O.J. Lu-Steffes, R. Sakidja, J. Bero, J.H. Perepezko, Multicomponent coating for enhanced oxidation resistance of tungsten, Surface and Coatings Technology 207 (2012) 614–619. https://doi.org/10.1016/j.surfcoat.2012.08.011.
- [237] J.-K. Yoon, K.-W. Lee, S.-J. Chung, I.-J. Shon, J.-M. Doh, G.-H. Kim, Growth kinetics and oxidation behavior of WSi2 coating formed by chemical vapor deposition of Si on W substrate, Journal of Alloys and Compounds 420 (2006) 199–206. https://doi.org/10.1016/j.jallcom.2005.11.002.
- [238] I.G. Talmy, J. Zaykoski, M. Opeka, S. Dallek, Oxidation of ZrB2 ceramics modified with SiC and group IV-VI transition metal diborides, Electrochem. Soc. Proc. 12 (2001) 144–158.
- [239] W. Vogel, ed., Glass Chemistry, Springer, Berlin, Heidelberg, 1994. https://doi.org/10.1007/978-3-642-78723-2.
- [240] WebElements Periodic Table » Periodicity » Electronegativity (Pauling) » Periodic table gallery, (n.d.). https://www.webelements.com/periodicity/eneg\_pauling/ (accessed January 29, 2025).
- [241] Jhalak, G. Balasubramanian, P.K. Ray, Effect of Hf and Al on Self-Diffusion in Amorphous Silica Using Molecular Dynamics, JOM (2023). https://doi.org/10.1007/s11837-023-06323-2.
- [242] M.M. Opeka, I.G. Talmy, J.A. Zaykoski, Oxidation-based materials selection for 2000°C + hypersonic aerosurfaces: Theoretical considerations

- and historical experience, Journal of Materials Science 39 (2004) 5887–5904. https://doi.org/10.1023/B:JMSC.0000041686.21788.77.
- [243] P. Kolodziej, A. Research, Aerothermal Performance Constraints for Hypervelocity, NASA Technical Memorandum 112204 (1997).
- [244] T.H. Squire, J. Marschall, Material property requirements for analysis and design of UHTC components in hypersonic applications, Journal of the European Ceramic Society 30 (2010) 2239–2251. https://doi.org/10.1016/j.jeurceramsoc.2010.01.026.
- [245]S.N. Karlsdottir, J.W. Halloran, C.E. Henderson, Convection Patterns in Liquid Oxide Films on ZrB2-SiC Composites Oxidized at a High Temperature, Journal of the American Ceramic Society 90 (2007) 2863– 2867. https://doi.org/10.1111/j.1551-2916.2007.01784.x.
- [246] L. Silvestroni, G. Meriggi, D. Sciti, Oxidation behavior of ZrB2 composites doped with various transition metal silicides, Corrosion Science 83 (2014) 281–291. https://doi.org/10.1016/j.corsci.2014.02.026.
- [247] WebElements Periodic Table » Periodicity » Radius metallic (12) » Periodic table gallery, (n.d.). https://www.webelements.com/periodicity/metallic\_radius/ (accessed January 14, 2024).
- [248]S.-L. Lin, C.-S. Hwang, Structures of CeO2\(\times\)Al2O3\(\times\)SiO2 glasses, Journal of Non-Crystalline Solids 202 (1996) 61–67. https://doi.org/10.1016/0022-3093(96)00138-X.
- [249] P.A. Williams, R. Sakidja, J.H. Perepezko, P. Ritt, Oxidation of ZrB2–SiC ultra-high temperature composites over a wide range of SiC content, Journal of the European Ceramic Society 32 (2012) 3875–3883. https://doi.org/10.1016/j.jeurceramsoc.2012.05.021.
- [250] D. Beniwal, V. Shivam, O. Palasyuk, M.J. Kramer, G. Phanikumar, P.K. Ray, EDS-PhaSe: Phase Segmentation and Analysis from EDS Elemental Map Images Using Markers of Elemental Segregation, Metallogr. Microstruct. Anal. 12 (2023) 924–933. https://doi.org/10.1007/s13632-023-01020-7.